Investigating the Influence of Bacterial Cell Characteristics on M13 Phage Infection Process

by

Seyedeh Sara Haghayegh Khorasani

A thesis
presented to the University of Waterloo
in fulfillment of the
thesis requirement for the degree of
Doctor of Philosophy
in
Chemical Engineering

Waterloo, Ontario, Canada, 2024

© Seyedeh Sara Haghayegh Khorasani 2024

Examining Committee Membership

The following served on the Examining Committee for this thesis. The decision of the Examining Committee is by majority vote.

External Examiner:	Dominic Sauvageau Associate Professor, Dept. of Chemical Engineering, University of Alberta
Supervisor(s):	Marc Aucoin Professor, Dept. of Chemical Engineering, University of Waterloo Brian Ingalls Professor, Dept. of Applied Mathematics, University of Waterloo
Internal Member:	Hector Budman Professor, Dept. of Chemical Engineering, University of Waterloo
Internal Member:	Valerie Ward Assistant Professor, Dept. of Chemical Engineering, University of Waterloo
Internal-External Member:	Brian Dixon Professor, Dept. of Biology, University of Waterloo

Author's Declaration

I hereby declare that I am the sole author of this thesis. This is a true copy of the thesis, including any required final revisions, as accepted by my examiners.

I understand that my thesis may be made electronically available to the public.

Abstract

Microbial communities are fundamental to ecosystem health and biodiversity, affecting environments from soil to human microbiomes. Bacteriophages, or phages, are vital components of these communities, shaping bacterial dynamics and genetic diversity through mechanisms like gene transfer. Traditional population-level studies, while informative, can obscure the detailed behaviors and interactions present at the individual cell level. This research seeks to mitigate this oversight by applying single-cell analysis techniques to explore the M13 phage infection process.

Focusing specifically on the interactions between the M13 bacteriophage and *E. coli*, this research employs time-lapse microscopy to investigate how individual bacterial cell characteristics— size, elongation rate, and spatial positioning—impact phage infection susceptibility. The experimental approach incorporates both microfluidic devices and agar pads to compare the effects of direct phage introduction versus *in-situ* phage production within mixed bacterial cultures. Image processing was conducted using the Ilastik and CellProfiler software, extracting vital cellular metrics, such as size, shape, elongation rate, and spatial distribution, for analysis. Subsequent post-processing, performed with custom MATLAB scripts, generated lineage trees for individual cells, enabling tracking and analysis of cellular behavior over time.

Experimental results demonstrate that *E. coli* cells exhibiting higher elongation rates and larger sizes were notably more susceptible to M13 phagemid infection. This correlation underscores the significance of physical and physiological cell properties in the infection process. Moreover, this research extends its analysis through computational simulations employing the CellModeller platform, to investigate the M13 bacteriophage infection process beyond what is observable in laboratory experiments. The simulations are particularly concentrated on assessing how variations in phage diffusion rates impact the spatial patterns of infection, especially regarding the proximity of infected cells to those producing phages. The simulation results from this study highlight that an increase in the phage diffusion rate leads to a decrease in the distance between infected cells and those producing phages, suggesting that higher diffusion rates facilitate wider spread and more uniform distribution of the phage within the bacterial population. This pattern is consistent with the hypothesis that phage mobility plays a critical role in the dynamics of infection spread.

Acknowledgments

I am deeply grateful for the guidance, encouragement, and support I have received throughout my PhD journey. This experience has been immeasurably enriched by the individuals around me.

First and foremost, I extend my deepest appreciation to my co-supervisors, Marc Aucoin and Brian Ingalls. Your combined leadership, mentorship, and wisdom have been the driving forces behind my academic progress. The collaborative environment you fostered allowed me to explore innovative ideas, face challenges with perseverance, and pursue excellence with integrity.

I extend my heartfelt gratitude to Brian Ingalls for his unwavering trust, boundless support, and remarkable patience throughout this journey. Your confidence in my abilities has shaped my research and profoundly influenced my personal and professional growth. I am deeply thankful for your belief in my potential and the invaluable opportunities you have provided.

My family's unwavering love, encouragement, and sacrifice have been the foundation of my achievements. Your constant support and belief in my dreams have been the source of my strength. To Mehrdad, whose calming presence and unwavering support during stressful times have meant the world to me.

To my peers in the Applied Virus and Complex Biologics Bioprocessing Research Lab—Reza, Lisa, Madhuja, Jacqueline, Chris Sung, Chris Nogueira, Mark, Scott, and Sara—thank you for the friendship, laughter, and unwavering support. The environment of mutual respect and collaboration we shared has been instrumental in my growth as both a scientist and a colleague.

To everyone who has contributed to my journey, your impact extends beyond words. I am deeply thankful for your role in shaping my PhD experience and for all the lessons learned along the way.

Dedication

This work is dedicated to my beloved family. To my parents, Zohreh and Hossein, whose unwavering love, guidance, and sacrifices have not only shaped my academic journey but also the person I am today. Your constant support has been my foundation.

To my siblings, Zahra and Mohsen, thank you for cheering me on and always believing in me. To Mariam, your advice and support during difficult times have been invaluable. And to Amir, your advice and boundless support have been a constant source of strength. Each of you has played a unique and irreplaceable role in my life, and I am forever grateful.

Table of Contents

Examining Committee Membership ii

Author's Declaration iii

Abstract iv

Acknowledgments v

Dedication vi

List of Figures xii

List of Tables xxiii

1 Introduction 1

2 Background 3

2.1 Bacteriophage 3

2.1.1 Filamentous Bacteriophage 5

2.2 M13 Bacteriophage 5

2.2.1 Assembly-Infection-Life Cycle 7

2.2.2 Vector Systems in M13 Phage Production: Phage Versus Phagemid Approaches 9

2.3 M13 Applications 11

2.3.1 Phage therapy . . . 12
2.3.2 Phage display . . . 13
2.3.3 Harnessing Bacteriophages for Microbial Community Engineering . 14
2.4 Spatiotemporal analysis of M13 bacteriophage infection process at single level 15
2.4.1 Image Processing and Segmentation . . . 19
2.4.2 Cultivation methods under Microscope . . . 20
2.5 Simulation . . . 31
2.5.1 Mathematical and computational modelling of phage-bacteria interaction . . . 31
2.5.2 Agent based modelling in the study of phage . . . 35
2.5.3 CellModeller . . . 36

3 Project hypothesis and objectives 38

4 Design, Development, and Validation of Microfluidic and Agar Pad Systems for Studying Bacterial Dynamics 41
4.1 Introduction . . . 41
4.1.1 Time-lapse Experiments . . . 41
4.1.2 Image Processing . . . 42
4.2 Material and Methods . . . 42
4.2.1 Time-lapse Experiments . . . 44
4.2.2 Agar Pad Setup . . . 44
4.2.3 Microfluidic Device . . . 44
4.2.4 Microfluidic Device Preparation for Time-lapse Experiments . . . 47
4.3 Image Segmentation . . . 49
4.3.1 Segmenting Microfluidic Device Images . . . 50
4.4 MATLAB Script for Analyzing Microscopy Data and Cell Lineages . . . 55
4.5 Protocol for Unperturbed Monoculture Growth . . . 57
4.6 Results . . . 58

4.6.1 Chamber seeding . . . 58
4.6.2 Assessment of cell features through time . . . 59
4.7 Discussion . . . 66

5 Spatiotemporal Dynamics of M13 Phage Infection **68**
5.1 Introduction . . . 68
5.2 Materials and Methods . . . 70
5.2.1 Phagemid Construction . . . 71
5.2.2 Phage amplification and purification . . . 74
5.2.3 Phage Quantification . . . 74
5.2.4 Microscopy . . . 75
5.2.5 Agar pad setup . . . 76
5.2.6 Image Segmentation and Data analysis . . . 78
5.3 Results and Discussion . . . 81
5.3.1 Quantification and Infectivity Assessment of Engineered Phages . . . 81
5.3.2 Direct Introduction of phage . . . 82
5.3.3 Microfluidic device: Distribution of Infection Events . . . 83
5.3.4 Distribution of phage infection events across cell states . . . 86
5.3.5 *In-situ* production of phage . . . 95
5.3.6 Results . . . 96
5.3.7 Conclusion . . . 108
5.3.8 Direct Application of Phage . . . 109
5.4 Simulating of M13 infection process . . . 115
5.4.1 Introduction . . . 116
5.4.2 Deconvolution Technique . . . 117
5.4.3 Methods . . . 119
5.4.4 Results . . . 124
5.4.5 Discussion and conclusion . . . 128

6 Conclusion and Future Work **131**

6.1 Conclusion . . . 131

6.2 Future work . . . 133

6.2.1 Enhancement of Image Processing and Tracking Capabilities . . . 133

6.2.2 Optimization of Microfluidic Device Design . . . 133

6.2.3 Investigation of GFP-tagged Phage Particles . . . 134

6.2.4 M13 Phage Interaction with Gut Microbiome Cultures . . . 134

References **135**

A Media Recipes **193**

B Single-cell analysis **194**

C Lineage Tree **197**

D Segmentation **199**

D.1 Segmenting Limitation in Agar Pad Setup . . . 205

D.2 Ilastik Pipeline . . . 209

D.2.1 Population . . . 209

D.2.2 Segmentation . . . 210

D.3 CellProfiler pipeline . . . 210

E Diffusion Variables **212**

F GFP threshold **213**

G Different Delay Time **214**

H Simulation **215**

H.1 Simulation Code . . . 215

H.1.1 Calibration code . . . 215

H.1.2 Wrapper code . . . 223

H.1.3 MATLAB code . . . 228

I Phage Display **234**

I.1 Introduction . . . 234

I.2 Phage Display Overview . . . 235

I.2.1 Display on pIII . . . 236

I.2.2 Display Domains . . . 236

I.3 Materials and Methods . . . 237

I.3.1 Phagemid Preparation and Amplification . . . 238

I.4 Results . . . 238

I.5 Discussions . . . 238

J Evaluating M13 Phage Infectivity within Gut Microbiome Cultures: Single-Species and Co-Culture **240**

J.1 Introduction . . . 240

J.2 Material and methods . . . 240

J.2.1 Protocol . . . 241

J.3 Results . . . 242

J.3.1 Microbiome Culture Analysis: Growth Behaviors of Different Strains in Varying Culture Conditions. . . . 243

J.3.2 Susceptibility to M13 phage . . . 247

J.3.3 Impact of Co-culturing Wild Type Culture with Lab Strain ER2738 on M13 phage Infectivity . . . 249

J.4 Discussion . . . 250

J.5 conclusion . . . 254

List of Figures

2.1 Schematic Diagram of M13 Bacteriophage Structure and Protein Functions 6

2.2 M13 Bacteriophage Infection and Replication Cycle. This diagram depicts the sequential steps in the M13 lifecycle, beginning with the attachment of the phage to the F pilus of the host cell, the subsequent injection of ssDNA into the cytoplasm, replication and expression of phage DNA within the host, and the assembly of new phage particles in the periplasm before being released outside the cell. 8

2.3 Different M13 display types. The diagram illustrates the three main categories of M13 viral vectors based on their gene III and VIII display capabilities: Type 3, Type 33, and Type 3+3 [34, 485]. Type 3 vectors are phagemid-based and carry gene III, allowing for the display of one fusion protein per phage particle, which does not impede infectivity and is advantageous during selection processes [554]. Type 33 vectors are phage-based and carry two copies of gene III, accommodating both wild-type and recombinant proteins on the phage surface. Type 3+3 vectors employ a dual-system approach where the recombinant gene is incorporated into a phagemid and a 'helper' phage introduces an extra copy of the wild-type gene III, enabling the assembled phages to exhibit both traditional and engineered proteins while maintaining their ability to replicate in the presence of foreign sequences [511]. These systems have been developed in response to the challenges posed to phage assembly, stability, and infectivity by certain sequences when displayed on the phage exterior. The figure delineates the structural components of phage vectors, helper plasmids, and phagemids, providing a visual guide to the vector configurations employed in M13 phage display technology [554]. 10

4.1 Agar pad setup. (a) 1µL of bacteria was dispensed onto the dish and covered with an agar pad. (b) The dish's lid was closed and sealed with parafilm. It was then placed in the microscopy chamber, positions were chosen, and imaging was initiated. 45

4.2 Microfluidic Design prepared by Matthew Courtney. The figure depicts a single chip containing multiple microfluidic devices. Each device has multiple rectangular one open-ended chambers 46

4.3 Microfluidic Device Under the Microscope at 10x Resolution. The chambers were successfully formed and connected to the main channel. 47

4.4 Microfluidic Operation (Matthew Courtney, 2023) 48

4.5 Microfluidic setup: cultures, as detailed in Section 4.2, were transferred into the device. Upon attachment of waste and nutrient vials, the setup was placed within the microscopy incubator chamber to commence the experiment promptly. 49

4.6 Microscopy images for a single frame in different channels. Scale bar: 20 micrometers. Left: phase channel; middle: EGFP channel represents GFP signal; right: mCherry channel represents RFP signal. 50

4.7 Time-lapse images of the frame with medium population density, magnified by 600x. A scale bar within the image indicates a length of 20 micrometers. Microfluidic Segmentation: Cells grew closely, yet with enough intercellular space to maintain a discernible contrast between cell and background pixel intensities. Blue arrows indicate cell pixels, while red arrows represent background pixels. 51

4.8 Image with high population density, magnified by 600x. Blue arrows indicate cell pixels, while red arrows represent background pixels.In the magnified part, cells displayed pixel intensities that closely aligned with the boundaries between cells, making cell identification notably challenging; hence after reaching these types of images, segmentation stopped. 52

4.9 Segmented images in Ilastik. A scale bar within the image indicates a length of 20 micrometers. Above: Original image captured by the microscope. Below: Image showing identified objects after segmentation. 53

4.10 Tracked images using CellProfiler. A scale bar within the image indicates a length of 20 micrometers. Lineages are color-coded (images taken every 10 minutes a subset are shown). 54

4.11 Tracked cell images. The numbers displayed within each cell represent their lineage label, which remained consistent throughout the experiment, serving as a unique identifier for each lineage. 55

4.12 Lineage tree describing the progression of growth from an ancestor cell during an experiment. Each node is assigned a unique index as indicated. Each node is assigned a collection of parameters as indicated. 56

4.13 Initial cell seeding density at the start of each experiment. Above each graph: Microscopy image depicting the actual chamber positions during imaging. The red arrow indicates the flow direction in the device, originating from the lower location. In the bottom right corner, there's an individual image representing a single chamber from the device specific to that experiment. 59

4.14 Spatiotemporal trends in cell radius. a) Change over time for agar set-up; b) hang over time for microfluidic devices. (c) The variation in space for microfluidic devices. Mean and standard deviation (bars) are shown. Best fit trend lines to the mean are shown along with slope, R squared values and sample size (n). Here, individual cells in each chamber occupy diverse positions, leading to varying depth levels within the device. The data in (c) has been binned into 10 µm intervals. 61

4.15 The figure illustrates the spatiotemporal changes in the average length, displaying (a) and (b) the changes over time for agar and microfluidic device respectively. (c) The variations in space for microfluidic device. Here, individual cells in each chamber occupy diverse positions, leading to varying depth levels within the device. The data has been binned into 10 µm intervals, with bars indicating the standard deviation. Best fit trend lines to the mean are shown along with slope, R squared values and sample size (n). Linear regression analysis revealed no significant trend in the length over time and space. 63

4.16 The figure illustrates the spatiotemporal changes in the average elongation rate (um/min), displaying (a) and (b) the changes over time for agar and microfluidic device respectively. (c) The variations in space for microfluidic device. Here, individual cells in each chamber occupy diverse positions, leading to varying depth levels within the device. Best fit trend lines to the mean are shown along with slope, R squared values and sample size (n). The data has been binned into 10 µm intervals, with bars indicating the standard deviation. 65

4.17 Temporal trends in RFP Intensity for cells in microfluidic device. 66

5.1 The two approaches used in this study to introduce phage to the microbial community, a) Direct phage introduction into the environment. b) *In-situ* production of phage 69

5.2 Preparation of the pBlueGFP phagemid. (a) Step 1. phagemid design; (b) Step 2. Amplification of sequence and electrophoresis; (c) Step 3. Gibson assembly and plasmid transformation. Colonies were examined under blue light to validate the presence of GFP within the bacteria. Additionally, these colonies were cultured and amplified using the same primers as in the previous method to verify that the plasmids retained the desired sequence and size. 73

5.3 Steps required to run the experiment in the microfluidic device with direct Introduction of phage 76

5.4 Steps required to run the experiment in the microfluidic device for cell to cell approach 77

5.5 Comparing fluorescent images with phase contrast image. Fluorescent images allow for distinctly delineating cell boundaries during the segmentation process. 78

5.6 This lineage tree illustrates the progression of cells that underwent infection during the experiment. Initially, host cells contain a red fluorescent protein (RFP) plasmid, represented in red on the tree, indicating their uninfected state. Upon infection by the phage, which carries a green fluorescent protein (GFP) gene, these cells commence expressing GFP, depicted in green, signifying an infected status. This color-coding directly corresponds to the real fluorescent signals observed. Consistent with descriptions in Chapter 4, each node within the tree is uniquely indexed, denoted by numbers for easy reference. 80

5.7 Phage Quantification results. a) Results of Spot test. 6th dilution is last dilution showing infection b) Colony counting assay results c) Plaque assay results. 81

5.8 Distribution of above-threshold GFP signal appearance timing for direct phage introduction A: agar pad, B: microfluidic device. From the results in (B) we inferred a 25 minutes delay from infection to above-threshold GFP signal appearance. 83

5.9 Distribution of Infection Events in Experimental Chambers: Plots show the number of infection events that occurred within each chamber. On the top left of each plot, an image displays the placement of the chambers; the red arrow indicates the direction of flow. 84

5.10 Histogram plot for Number of Infection event over total number of cells presents in the chamber at the inferred time of infection. 85

5.11 Spatial distribution of infection events within the chambers at the time of infection. 86

5.12 a) to d) distribution of cell radius a) and b) infection events in agar pad and microfluidic setups, and c) and d) cell-objects that were not involved in infection events. e) and f) average cell radius for infection events, and non-infection events. T-test significance is shown. Error bars represent standard deviations as described in the main text. n-values represent populations. . 87

5.13 a) to d) Distribution of cell length. a) and b) infection events in agar pad and microfluidic setups,and c) and d) cell-objects that were not involved in infection events. e) and f) average cell length for infection events, and non-infection events. T-test significance is shown. Error bars represent standard deviations as described in the main text. n-values represent populations. . 89

5.14 a) to d) distribution of elongation rate at the inferred moment of infection. a) and b) infection events in agar pad and microfluidic setups,and c) and d) cell-objects at the same time-point as (a)-(b) but in cell objects that were not involved in infection events. e) and f) illustrate the average cell elongation rate for both infected and non-infected cell objects, respectively, with t-test significance indicated. Error bars denote standard deviations, as detailed in the main text. The sample sizes (n-values) represent the populations of the cells examined. 91

5.16 a) to d) Distribution of cell length. a) and b) infection events in agar pad and microfluidic setups,and c) and d) cell-objects that were not involved in infection events. e) and f) average cell length for infection events, and non-infection events. T-test significance is shown. Error bars represent standard deviations as described in the main text. n-vlaues representing the populations of the cells. 99

5.17 a) to d) distribution of elongation rates. a) and b) infection events in agar pad and microfluidic setups,and c) and d) cell-objects that were not involved in infection events. e) and f) illustrate the average cell elongation rate for both infected and non-infected cell objects, respectively, with t-test significance indicated. Error bars denote standard deviations, as detailed in the main text. The sample sizes (n-values) represent the populations of the cells examined. 101

5.18 Figures a) to d) depict histograms showing the minimum distance from phage producers at the time of infection. a) and b) showcase the distribution for infection events in agar pad and microfluidic setups, while c) and d) illustrate the distribution for non infection events. Figures e) and f) are box graphs displaying the average aggregated proximity for infection events, and non-infection events. T-tests were utilized, and error bars represent standard deviations. P-values below 0.5 were considered statistically significant. . . 103

5.19 Aggregated proximity from phage producers at the time of infection. Figures a) to d) depict histograms showing the aggregated proximity from phage producers at the inferred moment of infection. a) and b) showcase the distribution for infection events in agar pad and microfluidic setups, while c) and d) illustrate the distribution for non infection events. Figures e) and f) are box graphs displaying the average aggregated proximity for infection events, and non-infection events. T-tests were utilized, and error bars represent standard deviations. 105

5.20 The figure shows the radius, length and elongation rate for cells containing helper plasmid at the infection time. in panel g, h and i) Atop each bar, the number of lineages in each category is displayed, with corresponding p-values determined. Similar to the hosts without helper plasmid, cells with larger length and radius, and higher elongation rate demonstrated a higher likelihood of getting infected by phages. 110

5.21 The figure consists of two key sections: (a) and (b) display histograms illustrating the distribution of radii for both infected and non-infected cells throughout the experiment; (c) features a box graph comparing the average radii of the two groups. T-tests were applied to analyze the data, and error bars indicate standard deviations. P-values below 0.05 were deemed statistically significant. The data clearly show that infected cells exhibit a decrease in radius in comparison to non-infected cells, highlighting a statistically significant difference between the groups. 111

5.22 The figure comprises two key elements: (a) and (b) depict histograms illustrating the distribution of cell length among infected and non-infected cells throughout the experiment. Additionally, (c) features a box graph comparing average length. T-tests were applied to analyze the data, and error bars indicate standard deviations. Statistically significant p-values below 0.5 were observed. It's evident that infected cells exhibited lower length compared to non-infected cells, and the accompanying statistical analysis confirms this significant difference. 112

5.23 The figure comprises two key elements: (a) and (b) depict histograms illustrating the distribution of cell elongation rate among infected and non-infected cells throughout the experiment. Additionally, (c) features a box graph comparing average elongation rate. T-tests were applied to analyze the data, and error bars indicate standard deviations. A highly significant difference was observed between infected and non-infected cells, with a p-value of less than 0.001. 113

5.24 a) Experiment b) Simulation environment 120

5.25 Simulation of Phage Diffusion: In the simulation environment, green cells represent phage-producing cells, red cells indicate host cells and yellow cells represent infected cells. The surrounding red cloud illustrates the concentration and spread of phage particles emanating from the producer cells, depicting their diffusion throughout the environment. 121

5.26 Deconvolution results for elongation rate. The green line represents the PDF of uninfected cells, the red line represents the PDF of infected cells, and the blue dashed line represents the estimated kernel PDF (K_1) (deconvolved and smoothed). 125

5.27 Deconvolution results for cell length. The green line represents the PDF of uninfected cells, the red line represents the PDF of infected cells, and the blue dashed line represents the estimated kernel PDF (K_2)) (deconvolved and smoothed). 126

5.28 3D surface plot depicting the relationship between uptake scaling factor (K_3), the diffusion coefficient ($\mu m^2/min$), and the square difference of the average minimum distance. The plot identifies the optimal ranges for K_3 and the diffusion coefficient, where the simulation results most closely match the experimental data. Lower values on the Z-axis indicate a better fit. The optimal diffusion coefficient is found to be in the range of 250 to 300 $\mu m^2/min$, and the optimal K_3 value is around 15 to 20. Higher diffusion coefficients lead to increased square differences and instability in the simulation, while moderate values ensure accurate phage spread and infection dynamics. Each value was tested over 10 runs. 128

B.1 The figure illustrates average radius in all the experiments analysed for control section 195

B.2 The figure displays the average length across all three experiments that were utilized for the analysis. 195

B.3 Consistent Average Elongation Rate across all experiments 196

C.1 This lineage tree provides a visual representation of the phenotypes associated with the points of interest. The highlighted node is the presumed point of infection origin, characterized by a GFP level exceeding a specified threshold. The "Infection Initiation" designates this node as the starting point for infection. Consequently, all connected nodes, including its descendants, inherit an "Infection Spread" characteristic. The rectangular black boxes highlight the branches displaying the "Infection Spread" within this lineage tree. 198

D.1 Initial step of Segmention in Ilastik: Measuring Intensity Density (a) Density of Cells Intenity, a, b and c representing low populated, medium populated and over populated frames, respectively (b) Fluctuation in the intensity density of the current frame compared to its previous frame 200

D.2 Image with low population density, magnified by 600x. A scale bar within the image indicates a length of 20 micrometers. Blue arrows denote cell pixels, while red arrows indicate background pixels. Evidently, the pixel intensity of cells starkly contrasts with that of the background, rendering the differentiation between cells and background straightforward in this image type. 201

D.3 Image with medium population density, magnified by 600x. A scale bar within the image indicates a length of 20 micrometers. Blue arrows indicate cell pixels, while red arrows represent background pixels. Cells in this context exhibited close adjacency, maintaining enough intercellular space for distinct differentiation between cell and background pixel intensities. . . . 202

D.4 Image with medium population density, magnified by 600x. A scale bar within the image indicates a length of 20 micrometers. Blue arrows indicate cell pixels, while red arrows represent background pixels. Certain cells displayed intensities resembling the background, highlighting the need for meticulous training to achieve accurate segmentation. 202

D.5 Image with high population density, magnified by 600x. Blue arrows indicate cell pixels, while red arrows represent background pixels. In this instance, specific cells displayed pixel intensities that closely aligned with the boundaries between cells, making cell identification notably challenging and largely unattainable. 203

D.6 Segmented images in Ilastik. (a) Microfluidic Segmentation: 1)Original phase image obtained through microscopy. 2) Pixel-classified image, where cells are denoted in yellow, while background pixels are marked in blue. 3) After the object filtration stage, cells within a defined size range were identified as primary objects, while those outside this range, like chambers walls, were excluded and not considered as objects. (b) Agar pad Segmentation: 1) Successful Segmentation of image 2, where the background is represented in blue and individual cells are colorfully differentiated. 204

D.7 Agar Experiment Segmentation Challenge: Middle Image: Represents the raw image captured during the agar experiment.Left Image: Depicts a scenario where cells are situated too closely to each other, complicating their differentiation based on pixel intensity.Right Image: Illustrates a situation where cells at the center of the colony have moved out of the focal plane, making their accurate segmentation challenging. 206

D.8 Figure illustrating the Impact of Variable Z-locations of Cells within a Colony 207

D.9 This figure illustrates the Formation of Multilayers in the Agar Experiment. As evident in the figure, the overlapping cell layers make it challenging to distinguish individual cells.A scale bar within the image indicates a length of 20 micrometers. 208

D.10 Right: Successful Segmentation of Left Images, where the background is represented in blue and individual cells are colorfully differentiated. A scale bar within the image indicates a length of 20 micrometers. 209

F.1 The information was processed using different GFP thresholds to examine: a) The mean cell radius b) The mean cell length c) The average rate of elongation d) Time-lapse sequences capturing cell growth and phage infection, with images captured in the EGFP channel. The EGFP intensity was quantified for individual cells, indicated by an orange arrow. As the GFP levels rose within the cell, its intensity also increased. The initial detectable GFP intensity was selected as a threshold for subsequent measurements. . 213

G.1 The information was processed using three different delay time to examine: a) The mean cell radius b) The mean cell length c) The average rate of elongation 214

I.1 The figure offers an observation of small green fluorescent particles in the direct introduction of phage approach within the agar experiment. This observation is made under 63x resolution in both the phase and EGFP channels. Images were taken using Zeiss Fluorescence Microscopy (Carl Zeiss Promenade, Germany) 235

I.2 The figures represent: Left: 1uL of phage lysate used in the experiments, Right: Results of surface panning of the same stock phage lysate. As depicted in the figure, the concentration of green particles has decreased, but they are still observable under the 63x objective in the EGFP channel. Images were taken using Zeiss Fluorescence Microscopy (Carl Zeiss Promenade, Germany) 239

J.1 Growth Behavior and Microscopic Image of Strain 4 (*Brevibacillus agri*). a) OD600 growth curves of strain 4 when cultivated individually and in co-culture with one or two additional bacterial strains. b) Microscopic image of strain 4, shown at a scale bar of 20 µm. The images correspond with those documented in previous research on Brevibacillus species [309]. 243

J.2 Growth Behavior and Microscopic Image of Strain 6 (*Klebsiella aerogenes*). a) OD600 growth curves of strain 6 when cultivated individually and in co-culture with one or two additional bacterial strains. b) Microscopic image of strain 6, shown at a scale bar of 20 µm. The images correspond with those documented in previous research on the Klebsiella aerogenes [4]. 244

J.3 Growth Behavior and Microscopic Image of Strain 9 (*Staphylococcus capitis*). a) OD600 growth curves of strain 6 when cultivated individually and in co-culture with one or two additional bacterial strains. b) Microscopic image of strain 9, shown at a scale bar of 20 µm. The images correspond with those documented in previous research on the Staphylococcus capitis [310]. . . 245

J.4 Growth Behavior and Microscopic Image of Strain 10 (*Escherichia fergusonii*). a) OD600 growth curves of strain 10 when cultivated individually and in co-culture with one or two additional bacterial strains. b) Microscopic image of strain 10, shown at a scale bar of 20 µm. 245

J.5 Growth Behavior and Microscopic Image of Strain 15 (*Parastutterella excrementihon*). a) OD600 growth curves of strain 15 when cultured individually and in co-culture with one or two additional bacterial strains. b) Microscopic image of strain 15, displayed with a scale bar of 20 µm. 246

J.6 Figure: Growth Behavior and Microscopic Image of Strain *E. coli* ER2738. a) OD600 growth curves illustrating the growth patterns of strain ER2738 when cultured individually and in co-culture with one or two additional bacterial strains. b) Microscopic image showcasing ER2738, with a scale bar of 20 µm for reference 247

J.7 Results of M13 Phage Infection. a) Cultures of wild-type *E. coli* and b) *E. coli* ER2738. c) Overnight growth of Strain 10 on Sorbitol-MacConkey Agar. Red colonies indicate sorbitol fermentation, distinguishing it from pathogenic *E. coli* 0157:H7, which ferments lactose but not sorbitol. d) Aquavill test for lactose fermentation. *E. fergusonii* does not ferment lactose, thus strain 10 classified as *E. coli*. e) Plasmid alignment results from Strain 10 against pVR50. These plasmids exhibit a 99.9% similarity, differing in only one base. 248

J.8 Infectivity of M13 Phage. The left and center plates depict the growth of the culture without the presence of phage. The right plate in each panel illustrates the co-culture's growth in the presence of M13 phage. Shiny colonies observed in the right plate represent instances of infection by Phagemid-EGFP phage. The bar graph shows the number of green colonies in each culture. *E. coli* ER2738 is the strain that can infected with phage. rests are the wt gut microbiom 249

List of Tables

2.1 Modelling techniques used to study phage–bacteria dynamics. 32

4.1 Bacterial strains and phages used in this study 43
4.2 Experiment Information for Unperturbed Monoculture Growth Experiment 57

5.1 Bacterial strains and phages used in this study 70
5.2 Plasmids used in the characterization of phages 71
5.3 Primers used in this study 72
5.4 Experiment summary: Direct phage introduction, agar pad growth conditions 82
5.5 Direct introduction of phage experiment information 82
5.6 '*In-situ* production of phage' experiment Information for agar pad setup . 95
5.7 '*In-situ* production of phage' experiment Information for Microfluidic Devices 95
5.8 Direct approach, experiment information for agar experiments 109

A.1 Media used in this study and their formulation 193

I.1 Bacterial strain 237
I.2 Phage used in this study 237
I.3 Plasmids used in this study 237

J.1 Bacteria culture used in this section 241
J.2 Phages used in this section 241
J.3 Results of Control and Phage susceptibility experiments 248
J.4 Factors Influencing OD Changes in Bacterial Cultures 252

Chapter 1

Introduction

Understanding the dynamics of microbial interactions at the single-cell level offers insights into biological processes that are often obscured in population-level studies [21]. This perspective is especially critical when examining bacteriophage (phage) infections, where individual bacterial responses can vary widely, even within genetically identical populations [177]. Single-cell analysis enables the observation of these variations, providing a deeper understanding of phage-host interactions beyond average population responses.

Bacteriophages are viruses that specifically infect bacteria. They play significant roles in modulating bacterial populations [163, 69], driving gene transfer, and shaping microbial communities [18, 106]. The phage M13, characterized for its filamentous shape and non-lytic infection cycle [224], serves as a valuable model for studying phage-host interactions due to its well-characterized genetics and life cycle. Previous studies on M13 phage infection have primarily employed population-based data, significantly advancing our understanding of its infection process. However, as mentioned earlier, even within homogeneous cultures, individual cells exhibit distinct behaviors and responses.

In light of this, this research adopts a single-cell perspective to study the M13 phage infection process. In this context, the research employed time-lapse microscopy techniques within microfluidic devices and agar pad setups to observe the dynamic interactions between M13 phagemid—capable of infecting hosts but unable to replicate without a helper plasmid— and *Escherichia coli* ER2738 culture at an individual cell level. This investigative approach focused on examining specific cell characteristics that impact their susceptibility to phage infection: size, elongation rate, and proximity. The study employed two main methods of phage introduction: the direct application of phage supernatant and *in-situ* production within mixed cultures.

By integrating single-cell microscopy techniques with computational modeling, the research provided an understanding of M13 phage infection process. This approach allowed for the visualization and quantification of individual bacterial cell responses to phage exposure.

The thesis is divided into five chapters:

In **Chapter 2** an overview of single-cell methods is provided, focusing on microscopy techniques relevant to the current research. The discussion includes batch and continuous approaches, with specific attention to agar and microfluidic devices employed herein. Additionally, this chapter reviews bacteriophages, highlighting their applications, life cycles, and studies at the single-cell level. Special emphasis is placed on the M13 phage, which is the primary bacteriophage investigated in this study.

Chapter 3 outlines the hypotheses and objectives of each subsequent chapter.

Chapter 4 introduces the initial experimental findings, concentrating on bacterial monocultures to assess their interactions within microfluidic and agar environments. This chapter elaborates on the experimental designs, methods, and the establishment of an image analysis framework designed for single-cell data examination. The experiments and subsequent analyses seek to explore the growth dynamics and response characteristics of bacteria - radius, length, and elongation rate - under microfluidic and agar pad setups, setting the groundwork for further investigations into phage infection detailed in Chapter 4.

Chapter 5 serves as a pivotal section of the thesis, where the phage infection process is examined. Utilizing microfluidic and agar cultivation methods, as outlined in Chapter 3, this chapter delves into the effects of direct and in-situ phage introduction on individual bacterial cells. The chapter details how these approaches influence the infectivity rates of M13 phages on two separate host bacterial strains—one capable of phage replication due to the presence of a helper plasmid and the other incapable. The analysis centers on how the size, and elongation rate of bacterial cells affect their susceptibility to phage infection. The outcomes from both experimental setups are compared to understand the differential impacts of phage introduction methods on bacterial hosts. Furthermore, this chapter extends its exploration by integrating simulation studies using CellModeller to mirror the M13 phage infection process. This simulation aims to bridge gaps left by experimental limitations, particularly in understanding the interplay between phage diffusion rates and the spatial distribution of infected cells in proximity to phage producers.

Chapter 2

Background

2.1 Bacteriophage

Bacteriophages, also known as phages, are the most numerous biological entities on Earth [388], playing a crucial role in the microbial dynamics of various habitats [18]. Their applications extend across a broad spectrum, beginning with phage therapy [218, 294, 328]—a promising approach to targeting pathogenic bacteria selectively while preserving beneficial microbiota [296, 323, 328]. This method exhibits adaptability, as phages can evolve to counter bacterial defense mechanisms, potentially offering a solution to antibiotic resistance [397]. This specificity is particularly valuable in combating antibiotic-resistant strains, as phages can adapt to overcome bacterial defenses [397], potentially enhancing treatment efficacy through their ability to self-amplify within the host [6, 5]. Their diversity allows for targeting a wide array of bacterial species [48]. Furthermore, the integration of phages with antibiotics or other therapeutic agents may improve treatment outcomes, mitigating resistance development [505, 315]. Phages are environmentally friendly, as they are natural entities that target bacteria without harming other organisms or causing pollution [284]. They also demonstrate effectiveness in clearing biofilms and exhibit a narrower potential for inducing resistance compared to antibiotics [267]. With these inherent advantages, it comes as no surprise that phages are increasingly employed as therapeutic agents across a diverse spectrum of applications, encompassing both bacterial and eukaryotic realms. Their adaptability and specificity, coupled with their ability to multiply within their host cells, make them highly versatile tools for addressing a multitude of challenges and opportunities in medicine, microbiology, and beyond [186, 284, 328].

Beyond medical applications, phages are employed in biocontrol strategies to ensure food safety by targeting foodborne pathogens [338, 276, 359], offering an eco-friendly alter-

native to traditional methods [531]. In agriculture and aquaculture, phage-based biocontrol helps manage bacterial diseases, supporting sustainable practices [504, 143]. The versatility of phages is further demonstrated in biotechnological applications, such as phage display [45, 102, 251], phage engineering for bioremediation [375, 411], phage-mediated gene transfer [282], and the development of phage-based biosensors for rapid detection of pathogens and biomarkers [160, 565, 159, 405, 302]. These biosensors stand out for their high specificity, reliability, and cost-effectiveness [159].

Phages are categorized based on their morphology and genetic composition, which within the International Committee on Taxonomy of Viruses (ICTV), are classified into one single order and 13 families [13]. Phages can be broadly categorized as either tailed or having polyhedral, filamentous, or pleomorphic shapes [14], with the majority of them (accounting for 96% [109, 14]) belonging to the tailed phages category [60, 335, 13]. These tailed phages possess double-stranded DNA genomes [15]. Within the Caudovirales order, classification is based on the nature of their tail, categorized into Siphoviridae (long and non-contractile tails), Myoviridae (long and contractile tails), or Podoviridae (short tails). In contrast, a minority of bacterial viruses, specifically polyhedral-shaped phages (possessing genomes of either ssDNA, dsDNA, or ssRNA), filamentous-shaped phages (with genomes of either ssDNA or dsDNA), and pleomorphic-shaped phages (with dsDNA genomes), collectively comprising less than 4% of bacterial viruses [13]. These phages are categorized into ten distinct families, each distinguished by unique fundamental traits, such as the presence of an icosahedral capsid, the presence of an envelope, and the presence of lipids, among other distinguishing features [13].

Filamentous-shaped phages are categorized into three families: *Inoviridae*, *Lipothrixviridae*, and *Rudiviridae* [13]. Within these families, the *Inoviridae* family comprises various phage sub-families, each distinguished by unique structures and lifestyles. Filamentous phages, found within these subgroups, have been extensively studied, primarily through the investigation of closely related *Escherichia coli* phages collectively known as Ff filamentous phages, referred to as M13, fd, and f1 [219].

In terms of their life cycle, phages can be classified into three main types: strictly virulent (also known as lytic), temperate and chronic. Strictly virulent phages undergo a lytic life cycle, while temperate phages initiate a lysogenic cycle and can sporadically transition into a lytic cycle under specific circumstances [137]. During the lytic cycle, lytic phages employ key proteins, such as holins and lysins, to effectively disrupt and destroy the host cells they infect [190]. Certain filamentous phages and archaeal viruses have been found to exhibit chronic life cycle, where progeny virions are released slowly and continuously from the cell surface instead of being released in a single burst event [137]. This unique characteristic sets them apart from other families of phages, making them

easily distinguishable [463].

In the subsequent chapters, our focus will shift to the comprehensive exploration of filamentous bacteriophages, with particular emphasis on the M13 phage, a ssDNA phage with chronic life cycle. The details of their infection process and the current understanding and knowledge surrounding this phage will be discussed.

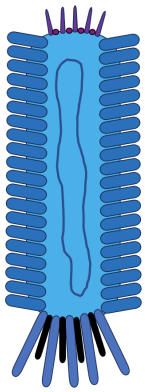
2.1.1 Filamentous Bacteriophage

Filamentous phages belong to the *Invirodae* family [577], and contain a single-stranded DNA genome surrounded by structural proteins [90]. Filamentous phages, often referred to as Ff phages, infect Gram-negative bacteria bearing a F plasmid [441, 234, 233, 537], and does not bind to other pili found on the surface of these cells [425]. Ff phages share about 98% DNA sequence identity and possess identical replication mechanisms [289]. Within an infected host, following the assembly of phage particles, they are consistently released from the bacterial membranes without accumulating within the bacterial cytoplasm or causing host cell lysis. This continuous release of phage particles subsequently leads to a decreased growth rate in the host cells [45]. As a result, infected *E. coli* cells can be distinguished visually on a lawn of bacteria by the presence of turbid plaques, which indicate zones of reduced growth [537]. This robust replication process also enables them to reach high titers, often reaching concentrations of up to 10^{13} phages per milliliter of culture [3].

In this thesis, the focus will be on M13 phages, which have garnered significant attention owing to their distinctive biological advantages and remarkable engineering capabilities. Researchers have explored novel engineering approaches to enhance the versatility and potential applications of M13 phages [90]. As a result, these phages have found successful utilization in various therapeutic areas such as drug delivery [185, 333], biodetection [568, 404], tissue regeneration [90, 258], and targeted cancer therapy [66]. The subsequent sections will provide detailed discussions on M13 phage, its applications and life cycle.

2.2 M13 Bacteriophage

The M13 bacteriophage, a filamentous virus that infects *E. coli*, has carved a notable niche within the field of molecular biology and biotechnology since its discovery in the sewers of Munich in 1963 [234]. Characterized by its unique semi-flexible structure [90], the M13 phage has a profound relationship between its length and genomic size, encapsulating a single-stranded DNA genome within a protective coat composed of structural proteins [256,



	Protein Name	Function
	pI	Assembly
	pII	Replication
	pIII	Adsorption and extrusion
	pIV	Assembly (exit channel)
	pV	Replication
	pVI	Virion component
	pVII	Virion component
	pVIII	Virion component
	pIX	Assembly and budding
	pX	Replication
	pXI	Assembly

Figure 2.1: Schematic Diagram of M13 Bacteriophage Structure and Protein Functions

422]. This phage's lifecycle, notably non-lytic, allows it to replicate within its host without causing cellular destruction, distinguishing it from many other bacteriophages with lytic cycles [441]. The wild type (wt) virus particles contain a 6.6 Kbp single-stranded DNA that is encapsulated with five structural proteins: major coat protein pVIII, and minor coat proteins pIII, pVI, pVII, and pIX. Six other proteins coded in the M13 genome facilitate DNA replication, assembly and packaging of new virions [573] (Figure 2.1), which are then extruded from the host cell through a process that preserves cell viability (chronic life style). This feature, along with its ability to be genetically manipulated, has made M13 a versatile tool in research laboratories around the world.

Use of M13 bacteriophage extends beyond basic research into practical applications. Its ability to display peptides and proteins on its surface has been harnessed for phage display technologies [473], contributing to antibody engineering [241], vaccine development [133], and the identification of protein interactions [2]. Moreover, the phage's single-stranded DNA serves as a template for mutagenesis and sequencing, further underscoring its utility in genetic engineering and synthetic biology [251]. The ongoing study and utilization of M13 continue to unveil its vast capabilities, promising further innovations in medical, environmental, and industrial fields.

Expanding on the basic insights into the M13 bacteriophage, the following sections will explore its lifecycle and wide-ranging applications in greater detail.

2.2.1 Assembly-Infection-Life Cycle

The life cycle of M13 phages, which is distinct for its chronic nature and non-lytic approach to host interaction, allows for the production of high phage titers without destroying the host cell. While the infection process has been extensively studied elsewhere [441, 483, 482], for the purpose of this research, we will provide a simplified overview of this process (See Figure 2.2).

Initiation of infection begins when the M13 phage's minor coat protein, pIII, attaches to the F pilus of the host cell, facilitating the injection of the phage's single-stranded DNA (ssDNA) into the bacterial cytoplasm. During this entry, the phage coat proteins are depolymerised, and the ssDNA is released into the host's cytoplasm. Once inside, the ssDNA is converted into a double-stranded replicative form (RF) with the assistance of host cell enzymes, employing a rolling-circle replication mechanism [441]. This process allows for the production of multiple copies of the phage genome.

As replication progresses, an increase in the concentration of the protein pV leads to a pivotal shift [483]; it begins to bind newly synthesized ssDNA, forming ssDNA-pV complexes, preventing its conversion into the RF. This binding exposes a packaging signal, which is recognized by proteins pIV, pXI, and pI, integral to the phage assembly line within the host membrane. pIV plays a crucial role by creating a channel through which the nascent phage particles are assembled and eventually extruded. During assembly, either host or phage proteins displace pV from the ssDNA-pV complex, allowing the major coat protein pVIII to encapsulate the ssDNA. This encapsulation process involves the sequential addition of phage proteins at specific sites: pVII and pIX at one end of the DNA strand, preparing it for packaging, and pIII and pVI at the other end, readying the phage for release [441].

The final stage sees the assembled M13 phage particle being extruded from the host cell through the pIV-created channel. Finally, the C-terminal domain of pIII facilitates the release of the new virion from the host cell. Notably, this process does not result in cell lysis, allowing the host cell to remain alive and continue producing more phage particles. This chronic lifecycle of M13 not only underscores its unique relationship with its host but also its potential utility in biotechnological applications, where continuous phage production is advantageous.

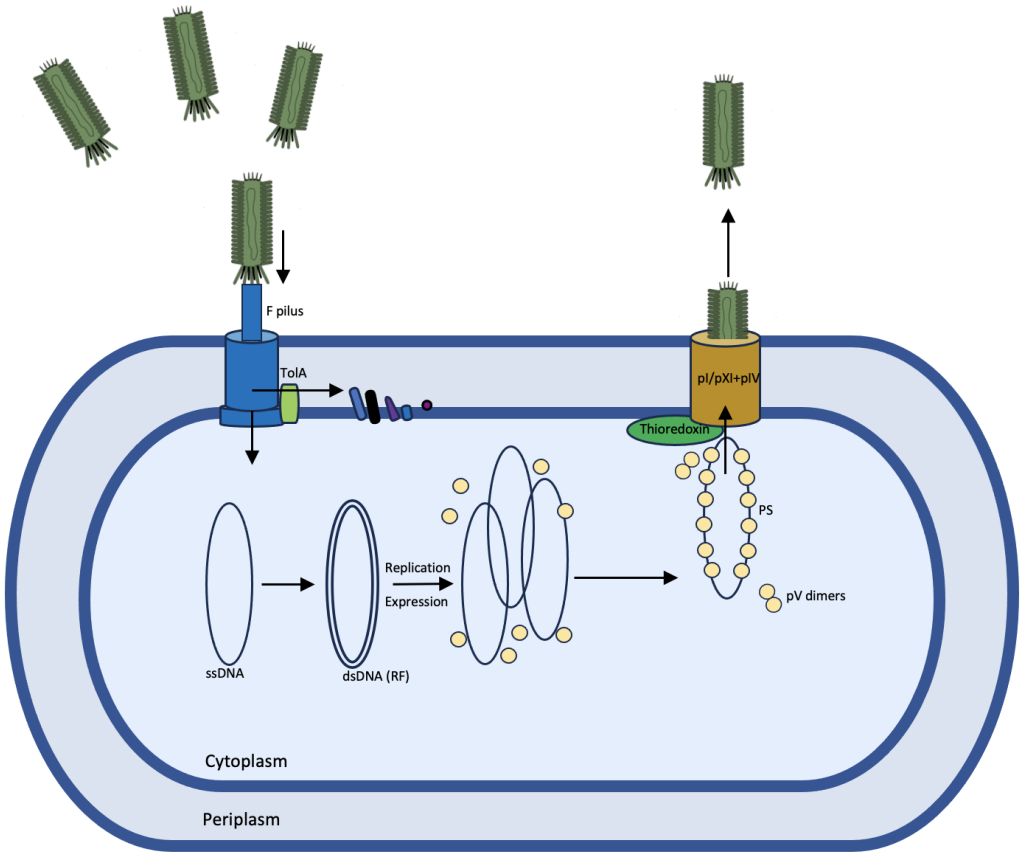


Figure 2.2: M13 Bacteriophage Infection and Replication Cycle. This diagram depicts the sequential steps in the M13 lifecycle, beginning with the attachment of the phage to the F pilus of the host cell, the subsequent injection of ssDNA into the cytoplasm, replication and expression of phage DNA within the host, and the assembly of new phage particles in the periplasm before being released outside the cell.

2.2.2 Vector Systems in M13 Phage Production: Phage Versus Phagemid Approaches

In the following section, we will detail the two primary vector systems utilized in M13 phage production: the phage vector system and the phagemid system [91]. These systems are foundational to the manipulation and production of M13 for a variety of applications, such as phage display, molecular cloning and sequencing. Understanding their distinctions is crucial for selecting the appropriate system for specific research requirements. Phage vector systems are derived directly from the genomes of filamentous phages, such as M13, f1, or fd, and contain all the necessary proteins for replication and assembly of the phage particles [407]. In contrast, the phagemid system uses a plasmid-based vector that carries the M13 phage origin of replication and packaging signal, allowing the production of single-stranded DNA in a phage-like particle upon superinfection with a helper phage[1] which provides the necessary proteins for phagemid replication, packaging, and phage coat formation [407, 232, 423].

This bifurcation into phage and phagemid systems is pivotal because each class offers distinct advantages depending on the research or application goals. For instance, the phage vector system is characterized by the integration of a gene encoding the displayed protein directly into the phage genome. This leads to the consistent display of the recombinant protein across all phage particles produced from a single clone, ensuring genotype-phenotype congruence [91] (Figure 2.3a). However, this system has limitations, especially when dealing with large protein fusions that may affect phage assembly and infectivity [337]. On the other hand, phagemids, are particularly useful in phage display technologies due to their ability to produce large libraries of variants with high diversity, which is essential for the selection and evolution of peptides, proteins, and antibody fragments with desired binding properties. Also, upon infection of a bacterium with a helper phage, the impaired packaging signal does not hinder the production of helper phage particles. However, when the bacterium is co-infected with both a phagemid and a helper phage, the phagemid DNA containing an intact packaging signal is preferentially packaged. Consequently, the resulting phagemid preparations exhibit heterogeneity in terms of both phenotype and genotype [91] (Figure 2.3b). The different genotypes of phage particles include those carrying

[1]Helper phages, which are instrumental in phagemid-based phage display systems, are modified versions of Ff phage genomes designed to improve the production of phage particles containing the phagemid DNA. These modifications include the incorporation of an alternative origin of replication and the introduction of antibiotic resistance genes. The latter serves a dual purpose: it enables the selection and maintenance of the helper phage within the host bacteria and ensures the propagation of the phagemid vector. Additionally, modifications are made to weaken the helper phage's own packaging signal [440], thus preferentially directing the packaging machinery towards the phagemid DNA [407, 570, 559].

the phagemid genome and those carrying the helper phage genome [407]. Regardless of the genotype, phagemid-based display systems typically yield hybrid phages that display both the wild-type and fusion coat proteins on the same particle [407]. In summary, phagemids are particularly beneficial for DNA-level applications, offering ease of preparation, cloning, and high transfection efficiency, which allows for the creation of extensive libraries [91]. They also provide greater resistance to deletions, ensuring genetic stability [570].

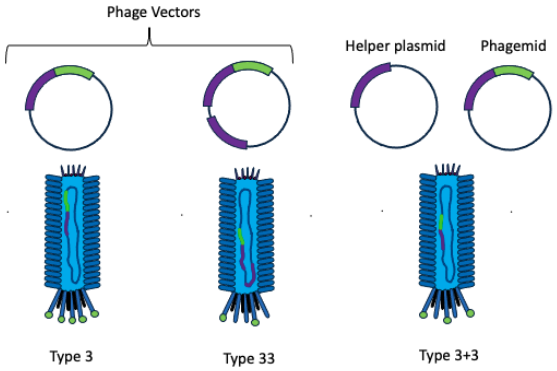


Figure 2.3: Different M13 display types. The diagram illustrates the three main categories of M13 viral vectors based on their gene III and VIII display capabilities: Type 3, Type 33, and Type 3+3 [34, 485]. Type 3 vectors are phagemid-based and carry gene III, allowing for the display of one fusion protein per phage particle, which does not impede infectivity and is advantageous during selection processes [554]. Type 33 vectors are phage-based and carry two copies of gene III, accommodating both wild-type and recombinant proteins on the phage surface. Type 3+3 vectors employ a dual-system approach where the recombinant gene is incorporated into a phagemid and a 'helper' phage introduces an extra copy of the wild-type gene III, enabling the assembled phages to exhibit both traditional and engineered proteins while maintaining their ability to replicate in the presence of foreign sequences [511]. These systems have been developed in response to the challenges posed to phage assembly, stability, and infectivity by certain sequences when displayed on the phage exterior. The figure delineates the structural components of phage vectors, helper plasmids, and phagemids, providing a visual guide to the vector configurations employed in M13 phage display technology [554].

2.3 M13 Applications

Phages have been the subject of study and utilization for over a century, particularly in the field of phage therapy as antibacterial agents [218]. Although the advent of antibiotics shifted the focus away from phages, the alarming rise of antibiotic-resistant bacteria has reignited the global interest in phage therapy [294]. Beyond their biological role, phages have been engineered for novel applications, notably in phage display technologies, which have become instrumental in the identification and characterization of peptides with therapeutic potential [452].

M13 phage has been pivotal in the advancement of phage display due to its ability to present peptides on its surface via modifications of coat protein genes. The expansive libraries of M13 phages facilitate high-throughput screening for peptide selection and purification, with the production scale-up made possible by engineered *E. coli* strains [45]. This versatility has made M13 an invaluable tool in both biotechnological applications and therapeutic development [343].

M13's specificity in binding to target receptors positions it as a prime candidate for biosensor applications, capable of detecting distinct bacteria within microbial communities. The targeted reactivity of M13 bacteriophages presents a significant advantage in diagnostic and sensor technologies [371]. Highlighted below are several key features of M13 phage that have been leveraged for various scientific and medical applications:

- M13 phage is an ideal vector for phage display technology, enabling the precise modification of surface proteins and the capacity to present a multitude of peptides, offering a multi-faceted platform for a wide array of applications [539].
- The robust capsids of M13 phage confer remarkable protection, ensuring stability and viability during drug delivery or biopanning procedures, particularly in dynamic and unpredictable physiological environments [374].
- M13 phage exhibits exceptional productivity by generating a large progeny population upon infecting host bacteria, making it an economically favorable and easily accessible 'production platform' of biomedical material [352].
- The unique nanoscale fiber-like structures of M13 phage facilitate its self-assembly into multidimensional scaffolds, enabling enhanced ligand-receptor interactions and versatile mobility for effective targeting of specific sites [75].

2.3.1 Phage therapy

Following their discovery in the early 20th century, phages were quickly utilized for the treatment of infectious diseases. However, with the emergence of antibiotics in the 1940s, research on phage therapy significantly decreased in the Western countries, while it continued to be actively pursued in the countries of the former Soviet Union [353, 530]. With the growing problem of antibiotic resistance, phage therapy has garnered renewed interest and is experiencing a well-deserved resurgence. Phages have the ability to kill both antibiotic-sensitive and antibiotic-resistant bacteria [242]. Throughout the past century, there have been numerous instances where phages have been utilized for therapeutic purposes [218].

Phage therapy entails the strategic deployment of bacteriophages to eradicate pathogenic bacteria within clinical infections, presenting a targeted approach to antimicrobial treatment [193]. This methodology capitalizes on the inherent specificity of phages, selectively attacking select bacteria and thereby preserving the beneficial constituents of the human microbiome [394]. Unlike broad-spectrum antibiotics, which can indiscriminately affect both harmful and beneficial bacteria, phage therapy offers a level of precision that mitigates the disruption of the body's microbial balance [129].

However, effectively targeting clinically relevant bacterial pathogens requires a diverse collection of well-characterized phages with specific properties. This critical selection process ensures the deployment of phages that are optimally matched to the bacterial challenge at hand. Despite this precision, bacterial resistance to phage infection remains a hurdle, potentially diminishing the therapeutic utility of even well-chosen phages. In response to these challenges, innovative strategies have been advanced to enhance the effectiveness of phage therapy. The formulation of phage cocktails, which combine multiple phage types, enhances the spectrum of action and curbs the development of resistance [207]. Phage engineering techniques have also been refined, enabling the customization of phages for heightened specificity and efficacy [553]. Additionally, combining phage therapy with traditional antibiotics offers a synergistic approach, leveraging the advantages of both modalities to tackle bacterial infections more effectively [315, 208, 242]. These methods offer potential solutions for overcoming the challenges associated with phage therapy and enhancing its efficacy in treating bacterial infections.

Early studies in phage therapy mainly explored the use of lytic phages as a therapeutic approach. However, the use of lytic phages can present clinical challenges, as it may result in rapid bacterial lysis and subsequent release of endotoxins, leading to potential side effects of phage therapy [481]. To mitigate the risk of endotoxin release and associated inflammatory responses during phage therapy, strategies have been employed to select or engineer phages that are lysis-deficient and/or non-replicative [340].

The non-lytic nature of M13 phage offer the potential to minimize the detrimental consequences associated with the release of high levels of endotoxins during bacterial cell lysis. For instance, Hagens et al., demonstrated that modified M13 phages carrying genes encoding nonlytic but lethal proteins can efficiently eliminate host bacteria while minimizing the release of endotoxins, in comparison to lytic phages [211]. In another study, M13 phage was employed to deliver DNA encoding bactericidal proteins to target bacteria. This phage-mediated delivery approach, incorporating toxins, reduced the bacterial population by several orders of magnitude [553, 373]. This innovative approach holds promise in improving the safety and efficacy of phage therapy.

2.3.2 Phage display

Phage display technology has been used in various fields including immunology, cell biology, drug discovery, pharmacology, and plant science [554]. By utilizing filamentous bacteriophages, such as fd and M13, it is possible to identify ligands with high affinity and specificity for a wide array of targets. This technology hinges on the fusion of a foreign sequence to a phage coat protein, linking the phenotype of peptide display to the genotype contained within the phage DNA [484]. It offers ease and rapidity in identifying selected molecules, making it a valuable tool in various fields of research [275, 406]. Phage display has proven to be a highly effective tool in antibody engineering, allowing for the expression of both Fab and single-chain Fv (scFv) antibody fragments on the surface of M13 viral particles without compromising their affinity and specificity [89]. Phage display technology has played a crucial role in generating more than 35 full-length human antibodies currently undergoing clinical development [349]. This powerful technique has enabled the isolation of human antibodies from patients exposed to viral pathogens, providing valuable insights into the immune response, facilitating the development of protective antibodies, and elucidating the specificity of autoimmune antibodies [349, 275]. For instance, phage display methods has been used in vaccine development by presenting protein antigens from human pathogens or cancer cells on their surface, or by encoding the genetic information for these antigens [539]. The tag system employed in phage display enables the identification of peptides that exhibit affinity for a range of biological targets, including proteins, cells, and tissues. Moreover, it has also facilitated the discovery of biomolecules that can bind to inorganic substances [224]. Phage display offers an appealing advantage as it is a straightforward, cost-effective, and fast technique that can be easily established without the need for specialized equipment, given the availability of suitable libraries [554].

2.3.3 Harnessing Bacteriophages for Microbial Community Engineering

Microbial communities are complicated and ever-changing ecosystems that hold a crucial position in diverse ecological settings, encompassing environments such as soil, marine ecosystems, and human health [432]. Advances in high-throughput sequencing have shed light on these communities' structures and functions [517] but have also highlighted the complexity of the genetic interplay that governs their ecological roles. To manipulate these communities effectively, we must overcome the current limitations in our ability to control their genetics and understand their emergent behaviors [156].

In natural settings, microbes form complex networks of interactions that are difficult to replicate in laboratory conditions [469]. Many microbes resist cultivation, which not only impedes genetic research but also our grasp of their ecological functions. The scarcity of versatile genetic tools and methods for engineering diverse microbial networks adds to the challenge, making it hard to systematically study and intentionally shape these communities [571, 496, 469].

The physiological and ecological characteristics of microbial communities rely on the spatial arrangement and temporal dynamics of their members. Spatial organization drives complex interactions and metabolic interdependencies, thereby increasing the collective's resilience and stability [550]. Microbial communities exhibit temporal dynamics characterized by fluctuations in their composition, metabolism, and function, which give rise to diverse community trajectories and phenotypes. Unraveling the underlying spatiotemporal principles governing these dynamics is essential for understanding of microbiome physiology and ecology [442, 432]. This section will explore the role of bacteriophages in engineering microbial communities, with a particular focus on their influence on the gut microbiome. Bacteriophages have the potential to significantly alter microbial ecosystems. To understand their impact on both the composition and function of these communities, a thorough examination is required.

Gut microbiome

In the past decade, there has been a growing interest in the gut microbiome and its impact on host health and disease [427, 138]. Changes in the human intestinal microbiota have been associated with gastrointestinal and liver diseases including inflammatory bowel disease [327], autism spectrum disorders [465], colorectal cancer [560], autoimmune diseases [290], metabolic syndrome [379], alcohol-associated liver disease [98], nonalcoholic fatty liver disease [304], and mental health, commonly referred to as the gut-brain axis [103].

As a result, there has been significant research into strategies for effective gut microbiome modulation.

Understanding the role of the microbiome in health and disease and applying this knowledge to therapeutic interventions has encountered significant challenges. One challenge lies in the difficulty of determining which alterations in the microbiome are causally linked to specific health outcomes [285]. Additionally, the current methods for modulating the microbiome, such as antibiotics or fecal microbiota transplants, tend to have wide-ranging effects. These broad-spectrum interventions can disrupt the delicate equilibrium of the gut flora, impacting both beneficial and harmful bacteria, which may result in adverse effects [535]. To address these issues, techniques such as transformation, conjugation, and transduction have been employed to introduce recombinant DNA into gut bacteria. Despite advancements, including the development of synthetic conjugation systems, the selective targeting of specific bacterial strains remains elusive [75]. Phage engineering, however, offers a promising avenue. Engineered phages can deliver DNA to target bacteria with high precision, akin to the specificity of viral vectors used in human gene therapy, facilitating the targeted alteration of bacterial genomes [535].

For instance, the M13 phage has been instrumental in targeting specific gut bacteria linked to colorectal cancer, and in modulating immune responses to tumors [134, 90, 378]. Engineered M13 phages have also been used to deliver gene-editing CRISPR-Cas9 systems to *E. coli* in the gut, achieving genetic modifications [303]. These phage-based techniques promise to advance our understanding and ability to manipulate the gut microbiome for therapeutic purposes.

In this study, the susceptibility of selected gut microbiome cultures to M13 phage was assessed to identify potential targets for future phage therapy or manipulation strategies (Available in Appendix J). Furthermore, the impact of the presence of various microbiome cultures on the infectivity of M13 phage within host cells (*E. coli* ER22738) was examined (Available in Appendix J).

2.4 Spatiotemporal analysis of M13 bacteriophage infection process at single level

The Significance of Single-Cell Analysis

Early research into the M13 phage infection process predominantly focused on population-level analyses. These studies provided valuable insights into the overall behavior of bacterial cultures under phage attack, measuring average growth rates [518, 444], culture

densities [286], and infection rates across entire populations [441]. Such research was crucial in building a fundamental understanding of the dynamics between phages and their bacterial hosts. However, these traditional approaches, while informative, tend to mask the complexity of individual cell behaviors, presenting a homogenized view that overlooks the diverse responses that occur within isogenic bacterial communities [150, 426].

With the advent of single-cell technologies, a more detailed picture has emerged, revealing significant diversity within isogenic bacterial communities. This cell-by-cell analysis has uncovered that individual bacteria can exhibit a wide array of responses to phage exposure, from rapid proliferation to complete inhibition, which population-level studies cannot capture due to their nature of averaging out individual behaviors [41, 41, 38]. Moreover, while a population may show a certain average growth rate, single-cell analysis might reveal a wide range of growth behaviors, from rapid proliferation to complete stasis due to phage infection. Similarly, the infection rate in a homogeneous population analysis might suggest a uniform susceptibility, yet individual cells may exhibit varying degrees of resistance or susceptibility to the phage. This disparity highlights the importance of considering individual cellular responses to fully understand the dynamics of phage-bacterial interactions.

In essence, while population-level studies have laid the essential groundwork in our understanding of M13 phage interactions with bacterial hosts, the shift towards single-cell analyses offers a more detailed view. It sheds light on the individualistic strategies and responses within bacterial communities, thereby providing a deeper understanding of the individual variations in microbial ecosystems.

Single-cell analysis illuminates the growth, metabolism, and behavior of individual cells, providing better understanding of the fundamental cellular processes [206]. This approach is invaluable in the context of phage studies, as phages can drastically alter a single microbe's state, which can affect the microbial community and its evolution [69]. By observing how individual bacteria respond to phage infection at the single-cell level, researchers can gain a better understanding of the microbial ecosystems and the detailed dynamics of phage-bacterial interactions. These insights have significant implications across various fields, including molecular biology and medicine, where they can influence the development of phage therapies and inform biotechnological processes [361, 330, 174]. In disciplines like molecular biology, systems biology, and bioprocess engineering, understanding the responses of individual cells to phages can help tailor biological systems for specific purposes, including the use of phages in combating bacterial infections or as delivery vehicles [174]. In food engineering, analyzing how microbes interact with phages at the single-cell level can lead to improved food production techniques and biotechnological manufacturing efficiency [72, 206].

Integrating single-cell analysis into phage research enriches our understanding of the

dynamics between bacteria and phages, and is instrumental in developing targeted phage therapies and advancing industrial biotechnology. The deployment of various analytical tools in microbial single-cell analysis allows for detailed observation of these interactions, each with its unique capabilities and limitations:

- **Microscopy:** Fluorescence microscopy and confocal microscopy are advanced imaging techniques employed to visualize and track individual cells, enabling the examination of specific cellular components and molecular processes [420]. They offer the advantage of observing the dynamic processes within cells over time, unlike the static analysis provided by flow cytometry, contributing to a deeper understanding of the phage infection cycle and cellular responses [543, 380].
- **Flow Cytometry:** A versatile technique for high-throughput cell analysis [178], flow cytometry excels in quantifying cell properties such as size, granularity, and fluorescence intensity, which are indicative of gene expression and other cellular processes [71]. While it's a powerful tool for profiling microbial populations, it generally provides a static snapshot of cell states and may struggle with distinguishing viable cells from debris and dealing with autofluorescence [178, 580].
- **Single-Cell Genomics and Transcriptomics:** Techniques like scRNA-seq enable the unraveling of cellular heterogeneity, providing insights into the transcriptomic landscape of individual cells. These methods are pivotal in identifying how phages may alter gene expression within a bacterium, although they face challenges related to capturing the full breadth of mRNA molecules and require sophisticated data analysis pipelines [243].
- **Mass Cytometry:** By labeling cells with heavy-metal isotopes, mass cytometry can assess multiple parameters per cell, surpassing the multiplexing capabilities of conventional flow cytometry. Although it provides a detailed cell analysis, it faces limitations in cell recovery and throughput, and may not be as sensitive as fluorescence-based methods [492].

The choice of inverted fluorescence microscopy was motivated by the need to observe and document the dynamic interactions between M13 phage and *E. coli* cells, providing real-time insights that are critical for understanding the infection process at a single-cell level.

In the context of phage research, each tool contributes uniquely to the field. Flow cytometry is often the first step in assessing the impact of phages on a microbial community. Single-cell genomics and transcriptomics provide invaluable information regarding

the changes in gene expression following phage infection at an individual cell level. They can reveal the phage's influence on bacterial gene regulation and identify potential targets for phage therapy. Microscopy allows researchers to observe the process of phage attachment, entry, and replication within single bacterial cells, a crucial aspect when studying phage-bacteria interactions or the phage life cycle. Time-lapse fluorescence microscopy, in particular, can track these dynamic processes in real time, offering a window into the phage life cycle and host interactions. Mass cytometry, though less commonly used in phage research, offers the potential for more detailed view of the cellular composition post-phage infection, especially when simultaneous measurements of various cellular markers are required. Ultimately, the importance of each method varies based on the research focus, and often, a combination of these tools is employed to gain a comprehensive understanding of phage-microbe interactions. This study primarily investigates the mechanisms of M13 bacteriophage infection and its effects on host cells, alongside the influence of cell states on infection probability. To elucidate these aspects, fluorescence microscopy was chosen as the principal investigative technique. Leveraging fluorescent labeling, this method provides the ability to closely monitor the interactions between phages and microbial cells in real-time. Through detailed visualization, we aim to gain better understanding regarding the M13 phage's life cycle and its interactions with host bacteria. The next section introduces our strategy, highlighting the critical role that microscopy plays in our investigation. It underscores how this technique is pivotal to advancing our research objectives, particularly in studying the M13 bacteriophage interactions with host bacteria.

Microscopy

Time-lapse imaging, combined with fluorescence microscopy, enables observation of bacterial cell behaviors, including changes in morphology, division rates, and intracellular movements, on a single-cell basis [512]. This technique facilitates the continuous observation of bacterial responses over time, including those to phage infection, making it indispensable for studying the phage-bacterial interactions. Fluorescence microscopy, with its use of fluorescent markers, provides a detailed view of cellular processes, gene expression patterns, and protein movements within bacterial communities [226, 336]. Time-lapse microscopy generates two primary types of images: phase channel and fluorescent channel images. Phase channel images, produced without the need for fluorescent markers, provide clear and high-contrast views of cells. This method is particularly effective for observing the overall morphology, size, and organization of cells within a population. It allows for the continuous tracking of cells in their native state, offering a broad perspective on cellular dynamics and interactions within their environment. Fluorescent channel images, in contrast, offer a targeted view by utilizing fluorescent markers to highlight specific cel-

lular components or processes [157]. This approach is invaluable for studying dynamic events within cells, such as gene expression, protein localization, and intracellular signaling [487, 417, 226, 334, 53]. For this study, fluorescence microscopy was instrumental in investigating the M13 bacteriophage's impact on host cells. It facilitated the observation of the infection process by highlighting infected cells, which become fluorescent due to fluorescent markers introduced into the phage genome. This visualization technique offers a window into the sequence of infection, showing how bacterial cells respond to phage entry and replication.

2.4.1 Image Processing and Segmentation

After capturing time-lapse images, deriving quantitative data from these visuals, such as cell division rates, spatial dynamics, or interactions [512], becomes a crucial yet demanding aspect of analysis. Previously, manual quantification was the norm, yet it quickly became apparent that this method was neither accurate nor efficient for handling the volume of data generated by microscopy [255, 487, 401]. Moreover, challenges such as low signal-to-noise ratios, overlapping cell boundaries, uneven pixel intensity, and photobleaching complicate manual analysis [145].

Computational image analysis tools have since become essential for processing microscopy images, offering solutions to these challenges [524]. They enable the handling of large datasets, provide consistent and objective analysis, and reveal details not readily apparent in raw images. These tools support advanced segmentation, tracking, and quantification methods, enhancing the exploration of cellular dynamics and behaviors over time [487, 83].

A key step in image processing is segmentation: distinguishing microbial cells from the background and accurately tracking them through the image sequence [512]. This step is foundational, allowing for the clear identification of cells, the elimination of background interference, and the reduction of noise [119]. Segmentation sets the stage for tracking, where algorithms monitor cell movements and transformations across time-lapse sequences, providing a detailed view of cellular activity [342, 512].

In recent years, various software tools incorporating statistical learning have been developed to link cellular phenotypes with image-derived metrics [487]. These tools have been individually introduced by their developers and extensively reviewed in works by Zhang [579], Jeckel [255], Smith [487], and Caicedo [83]. This thesis utilizes two prominent open-source programs: Ilastik [58] for pixel classification and cell identification, and CellProfiler [497] for morphological analysis.

CellProfiler: Developed by the Carpenter lab at the Broad Institute of MIT and Harvard, CellProfiler is a prominent open-source, Python-based software package [497]. It facilitates detailed analysis of cellular images, enabling researchers to measure cellular attributes such as size, shape, and intensity with high throughput and efficiency [497]. Despite its strengths, CellProfiler encounters limitations with phase-contrast images due to the similarity in pixel intensity between cells and their background [300]. To enhance its functionality, especially in these complex imaging scenarios, it is often paired with Ilastik [58], a machine learning tool, as suggested by its developers. This integration enhances CellProfiler's ability to navigate the challenges of phase-contrast image analysis, improving the accuracy of segmentation and quantification tasks [300].

Ilastik: Ilastik is an open-source machine learning package that stands out for its ease of use and versatility in image analysis, supported by a user-friendly interface and a suite of predefined workflows. These workflows support a range of tasks, including segmentation, object classification, counting, and tracking [58]. The pixel classification feature in Ilastik allows for the identification and differentiation of various cellular components or regions within an image. Furthermore, its object classification module facilitates the categorization of whole cells or structures based on specific attributes, aiding in the distinction between different cell types or elements within a sample [58].

2.4.2 Cultivation methods under Microscope

Maintaining stable cultivation conditions is pivotal for the success of time-lapse imaging experiments. A consistent environment ensures that observed cellular behaviors and dynamics are attributable to the biological processes under study rather than external fluctuations. This control extends to temperature, nutrient levels, and, where feasible, humidity, allowing researchers to delineate the effects of specific environmental variables on cell behavior.

The following discussion will outline the evolution of cultivation methods tailored for live-cell imaging, with an emphasis on techniques suitable for studying cellular interactions, including those influenced by phage presence. We start with traditional methods such as the agarose pad system, which facilitates the observation of cell behavior in a semi-natural setting, highlighting both cell-environment and cell-cell interactions. Despite its simplicity, the agarose pad method is versatile, supporting a range of imaging studies due to its long-standing application in microbiology. We will then explore advanced systems like microfluidic devices, which offer refined control over the experimental environment.

These systems have significantly improved live-cell imaging by allowing precise manipulation of conditions such as nutrient gradients, temperature, and atmospheric composition. Microfluidic platforms are particularly advantageous for studying dynamic interactions, such as those between phages and their host cells, under conditions that closely mimic natural physiological states. Their capability to generate dynamic culture environments, combined with the potential for high-throughput analysis and detailed manipulation of infection dynamics, underscores their value in contemporary cellular biology research.

Agarose Pad Cultivation Techniques for Live-Cell Imaging

Agarose pad cultivation techniques offer a conducive environment for observing cellular behaviors under the microscope, crucial for time-lapse microscopy studies. Traditional agar or agarose gels, known for their supportive and transparent qualities, serve as optimal substrates. These gels facilitate nutrient diffusion and are compatible with a broad spectrum of imaging methods, allowing continuous observation of cellular processes [368].

1. **Coverslip Bottom Dish Technique**: Utilizing dishes with a coverslip bottom, this approach is ideal for inverted microscopy, providing clear imaging over larger areas. An agarose layer can be added atop cells to mimic natural conditions closely [262]. Suitable for both short-term and extended studies, this technique offers less confinement than traditional agar pads, posing challenges in maintaining cell position and organization.

2. **Conventional Agar Pad Technique (agarose pad "sandwiches")** : This method involves placing a layer of agarose on a glass slide, with cells positioned for imaging under a coverslip. Its simplicity and cost-effectiveness are significant advantages, although it can be prone to drying, potentially limiting extended observation periods. Challenges include controlling environmental conditions effectively.

3. **Agarose-based microwells array Technique**: By integrating microwells into agarose pads, this approach isolates individual cells or groups for detailed study. It enhances throughput and environmental control, offering a focused analysis of cellular behaviors within each microwell [580]. Despite its benefits, the technique may necessitate specialized equipment for creating microwells [418].

4. **Hydrogel Agar Pad Technique**: Incorporating hydrogel components into agarose enhances the physiological relevance of the growth environment. This technique requires additional materials to optimize for cell compatibility, which might limit its general applicability compared to simpler agar pad methods [269].

When selecting a cultivation method for live-cell imaging, it's important to balance factors like imaging duration, need for environmental control, and cell type compatibility. The agarose pad approach is valued for its straightforward setup; however, it faces challenges such as potential desiccation and limited ability to manipulate environmental factors like temperature and gas exchange. Additionally, dense cellular growth can obscure individual cell analysis, and nutrient competition may introduce variability in growth conditions. To mitigate these issues and ensure the consistency of experimental results, imaging is typically conducted within a timeframe that supports reliable data collection, often spanning 6-8 generations [368]. This careful consideration ensures that observations remain within a controlled and scientifically meaningful context. For this study, the 'Coverslip Bottom Dish' Technique was selected for its adaptability to long-term imaging.

Phage studies using agar pad setups

Agarose pads have emerged as a prominent method for observing phage-host interactions over extended periods. Despite limitations in controlling experimental conditions, the simplicity and straightforward nature of this technique have led to its widespread utilization in phage research. St-Pierre and Endy focused on cell fate selection during phage lambda infection, uncovering mechanisms that influence cell fate determination. In their study, they employed single-cell fluorescent microscopy by integrating a GFP reporter into the phage genome to monitor the host's cell fate decisions post-infection. The imaging duration spanned at least nine hours, with an interval imaging time of 15 minutes, analyzing a population of *E. coli* cells. Their analysis primarily focused on changes in cell volume to determine the various outcomes of infection. Length measurement were processed manually using the first frame of timelapse movies. Their study indicated that cells with approximately twice the volume at the time of infection were four to five times less likely to become lysogens, indicating that variations in cell size could predict the likelihood of different infection outcomes [493].

Zeng et al., examined decision-making processes in bacteriophage infection, revealing the dynamic interactions between lambda phage particles and host cells. This study demonstrates that single-cell heterogeneity in cell-fate determination can be explained by a cascade of decisions at the sub-cellular level, showing that in bacteriophage lambda, the decision between lysis and lysogeny is initially made at the individual virus level and integrated by the cell to require unanimous viral agreement for lysogeny, thereby predicting single-cell noise. In their analysis, they utilized single-cell fluorescent microscopy, tagging the surface of phage with fluorescent markers, to visualize and record the decision-making process in real-time. Their study spanned approximately 2 hours per session with an imaging interval of 10 minutes, and involved a total of 24 experiments. They measured the fates

of *E. coli* cells confronted with phages, providing a substantial dataset for analysis. The team focused on parameters such as fluorescent intensity, viral concentration, and host growth rate, processing the data manually using MetaMorph software [578].

Rothenberg et al., studied the spatial receptor-dependent search mechanism of viruses, tracking individual viruses and their interactions with receptors [434]. They employed fluorescent microscopy, labeling the cell receptors to study the engagement between viruses and host cells in detail. Their results reveal that bacteriophage lambda locates its target receptor on *E. coli* through a unique spatial focusing process, whereby the virus moves from its initial random landing site to the cell pole, guided by interactions with LamB receptors and their spatial organization. The findings led to the development of a theoretical model that reproduces the observed target-finding behavior, with potential implications for understanding viral receptor-finding mechanisms in more complex systems. Their experimental approach captured a minimum of 1,000 images for each session, although the total duration of imaging per session is not explicitly mentioned. The analysis focused on understanding receptor displacement and intensity, employing MATLAB's image-processing toolbox for data analysis [434].

Shao et al., explored the interplay between DNA replication, negative feedback mechanisms, and gene expression in cell-fate decisions [461]. Utilizing single-cell fluorescent microscopy, they observed *E. coli* cells infected with fluorescently labeled Lambda phages. This study reveals that DNA replication significantly enhances cI (the repressor gene responsible for maintaining lysogeny) expression in bacteriophage lambda, promoting lysogenic commitment by providing additional templates, while the expression of the upstream regulator cII (the activator protein that promotes cI expression) remains robust against DNA replication due to negative autoregulation by the Cro repressor. This demonstrates how organisms use DNA replication for gene expression control and employ mechanisms like negative feedback to maintain expression stability despite DNA dosage variations. Their methodology involved continuous imaging at five-minute intervals across different channels spanning a total length of four hours. The primary focus was on quantifying the average cII mRNA level, a crucial component in the cell's decision-making during phage infection. Data analysis was performed using the MATLAB image-processing toolbox [461].

Trinh et al., focused on elucidating cell fate decisions emerging from cooperative or competitive interactions among lambda phages inside host cells. Their application of the imaging technique allowed them to capture the dynamic phage-host interactions, leading to insights into the resulting cell fate outcomes [514]. It reveals that distinct viral DNAs establish separate subcellular compartments, physically separated by the E. coli nucleoid, leading to heterogeneous viral development within single cells. These findings integrate key processes such as DNA replication, transcription, virion assembly, and resource recruitment

into a coherent spatiotemporal model of phage development, demonstrating how individual phage compartments contribute to variable molecular outcomes and coordinated development. Imaging for this study began approximately 15–20 minutes after the cells were initially placed on the substrate, with subsequent time-lapse movies captured every five minutes over a duration of around four hours. This methodology enabled the precise tracking of the number of lysed cells and phage propogation within the host. Data for this study were analyzed using Schnitzcells, supplemented by custom scripts in MATLAB [514]. They also examined the formation of heterogeneous compartments by viruses within individual bacterial cells. By utilizing time-lapse imaging, they uncovered the dynamics of virus-host interactions and the subsequent formation of distinct compartments [513].

In line with these studies, Bodner et al., genetically modified *E. coli* lysogens with fluorescent markers to facilitate the live-cell observation of prophage induction within macrophages. Their approach, which combines genetic engineering and fluorescent tagging, enables real-time visualization of prophage activation and its consequences within host cells [62]. The research demonstrates that pre-induced prophages can lyse host bacteria and propagate infection to neighboring bacteria within the same phagosome (a membrane-bound compartment within macrophages where engulfed particles are degraded). Additionally, it identifies a non-canonical pathway mediated by PhoP (a regulatory protein involved in bacterial stress response) that triggers native lambda phage induction in phagocytosed *E. coli*. Imaging sessions were conducted at regular ten-minute intervals, ensuring at least two images per pad to capture the dynamic changes over time. The study primarily focused on analyzing the fluorescence signal intensity and growth curves to understand the cellular responses to prophage activation. Data were processed and analyzed using CellTK, a Python-based image analysis software [62].

Wohlfarth et al., studied L-form conversion in Gram-positive bacteria - such as *Listeria monocytogenes* and *Enterococcus faecalis* - as a means to evade phage infection [557]. This study demonstrates that *Listeria monocytogenes* can evade phage predation by transiently converting to a cell wall-deficient L-form state in osmotically stabilized environments. This escape mechanism is triggered by phage endolysins degrading the cell wall, leading to the extrusion of viable L-form cells. These L-forms can revert to their walled state in the absence of phage predation. The research highlights this L-form conversion as a persistence mechanism at the population level to avoid complete eradication by phages. Additionally, it shows phage-mediated L-form switching in the urinary tract pathogen *Enterococcus faecalis* in human urine, suggesting the potential widespread occurrence and significant implications for phage and endolysin-based therapies. The study utilized light microscopy and confocal laser scanning microscopy to observe the structural changes during L-form conversion, especially in response to the interaction with A006 deltaLCR, an engineered

virulent derivative of temperate phage A006 lacking its lysogeny control region. Imaging sessions were carried out at various time intervals — 0, 45, 60, 75, and 120 minutes — to capture the progression of L-form conversion over time. The focus was on analyzing fluorescence signals to detect L-form transformation and assess the survival strategy against phage assault. Data analysis and processing were adeptly conducted using Fiji v1.51 software [557].

Misson et al., investigated the impact of macrophage infection on phage production in adherent-invasive *E. coli*, a type of bacteria known for its role in inflammatory bowel diseases. Their findings revealed that phage production is blocked in the bacteria upon macrophage infection [366]. The experiment spanned 160 minutes, with images captured at 15-minute intervals to monitor the changes. The main focus was on the fluorescence signal and the count number of cells, distinguishing between those displaying dotted fluorescent foci (indicative of ongoing phage production) and non-fluorescent cells. Cells were segmented using Omnipose [116] followed by tracking with Trackmate [154], while the final image analysis was performed using ImageJ software [424]. This allowed for precise quantification and provided significant insights into how macrophage infection disrupts phage production in these bacterial cells [366].

This research aims to delve deeper into the interactions between M13 bacteriophage and its bacterial host, *E. coli*, at a single-cell level, building upon the foundational studies in phage-host dynamics. While previous investigations have offered invaluable insights into phage biology and phage-host interactions, this study specifically focuses on the interplay of M13 phage within an *E. coli* culture, using live-cell imaging to capture the detailed behavior of these entities in real-time.

To enable comprehensive observation and analysis, genetic modifications introducing fluorescent markers to both phage and host have been applied. These modifications facilitate the tracking of infection processes, allowing for the observation of phage infection rates and bacterial cell morphological changes upon infection. Through this focused approach on M13 phage and *E. coli* interactions, the study aims to contribute to our understanding of phage biology and host response mechanisms.

In addition, this study examines the correlation between host cells' size, and elongation rate, with the probability of infection by M13, highlighting how physical characteristics of individual bacterial cells influence their susceptibility to phage infection. Utilizing fluorescent microscopy, this research analyzed over 10,000 cells in each experiment, providing an unprecedented scale of data for understanding the details of phage-host interaction at the single-cell level.

Microfluidic device cultivation

Microfluidics has evolved into a well-established discipline, facilitating fluid flows at microscopic scales within microchannels [19]. The construction materials for microfluidic devices include elastomers like polydimethylsiloxane (PDMS), known for its gas permeability—an essential property for maintaining cell viability by ensuring adequate oxygenation [415, 393]. Reviews by Gale et al. [179] and Nielsen et al. [393] provide detailed insights into microfluidic chip fabrication, spotlighting the technological progress that has rendered these devices essential for contemporary biological investigations. Furthermore, Anna's discussion on fluid dynamics within microsystems clarifies how microfluidics manages small volumes of fluids to secure exact environmental parameters [30].

Maintaining precise cultivation conditions is essential for the success of time-lapse imaging experiments, crucial for accurately capturing cellular behaviors over extended periods without interference from external factors. The integration of microfluidic technology into live-cell imaging capitalizes on this need for control, enabling researchers to replicate the natural environments of cells within finely tuned microdevices. This precision is foundational to observing authentic cellular dynamics.

Recent advancements in microfluidic technology have significantly enhanced the ability to maintain exact cultivation conditions with the introduction of innovative microfluidic cultivation chambers [519]. These advanced systems have transformed live-cell imaging by providing customizable environments tailored to the specific requirements of various experiments, from colony-based setups to detailed single-cell analyses [108, 325, 96]. These chambers allow researchers to create specific culture conditions, such as controlling nutrient availability, temperature, and other environmental factors.

A variety of different microfluidic devices have been developed to address various biological problems. These devices can generally be classified into three main categories: continuous-flow, batch (or semi-batch), and droplet-based microfluidics [136]. Each category serves distinct purposes and offers unique advantages for biological research

1. **Continuous-flow Microfluidics:** in this study, we specifically utilized continuous-flow microfluidics. This category is distinguished by its capability to direct the movement of fluids through narrow microchannels, enabling the control over the flow and facilitating the detailed manipulation and analysis of biological samples. The continuous-flow system is particularly advantageous for studies requiring steady-state conditions or for processes that benefit from the controlled introduction and removal of substances.

2. **Batch or Semi-Batch Microfluidics:** These devices focus on handling discrete volumes of samples within small-scale chambers or wells. Unlike the continuous nature of the previous type, batch microfluidics allows for the isolation and study of specific sample volumes, making it ideal for assays or experiments where sample containment is crucial. Semi-batch systems may introduce or remove components during the experiment, offering a balance between continuous and discrete sample management [356].

3. **Droplet-based Microfluidics:** Specializing in the creation and manipulation of picoliter-sized droplets, this category excels in compartmentalizing reactions or processes. Each droplet acts as an independent reaction chamber, enabling high-throughput screening, single-cell analysis, and the study of minute biological systems with minimal reagent use. This approach is highly advantageous for conducting parallel experiments and for studies where isolation of reaction environments is necessary [136].

The choice between continuous-flow, batch, or droplet-based systems depends on the specific requirements of the research project, including the nature of the biological problem being addressed, the desired level of control over the experimental environment, and the throughput needed. For the purposes of this phage study, the continuous-flow microfluidic system was selected due to its ability to provide a consistent and controlled experimental environment, crucial for observing phage-bacterial interactions over time. This method's inherent design ensures a steady state of conditions, allowing for the precise manipulation of fluid streams which is essential for maintaining the viability and natural behavior of both phages and their bacterial hosts. The continuous introduction of nutrients and removal of waste products mimic the dynamic environment that these microorganisms encounter in natural settings, thereby enhancing the relevance and accuracy of the observed interactions.

Microfluidic device in single cell studies

Microfluidic devices have become pivotal in single-cell analysis, with several comprehensive reviews highlighting their development and diverse applications. Works by Anggraini et al. [29], Ou et al. [400], Wu et al. [564], Yin et al. [572], and Ling et al. [321] detail the progress and innovation within this field, showcasing how microfluidic technology has advanced our understanding of single-cell behaviors and interactions.

Among the various microfluidic designs, the following have been particularly influential in studying phage-host interactions:

1. **Microfluidic Co-Culture Systems**: Employed in this study, these designs involve creating microfluidic channels or chambers that allow the co-culturing of microbial communities under controlled conditions. The spatial arrangement and dynamic flow within these systems aim to mimic natural environmental conditions, enabling detailed study of microbial interactions and evolutionary processes. This approach allows for real-time monitoring under conditions closely resembling natural settings.

2. **Droplet-based Microfluidics**: This design involves encapsulating individual cells within picoliter-sized droplets. Each droplet acts as a discrete microreactor, enabling high-throughput analysis of interactions within microbial communities. This approach allows for the screening of a large number of individual cells in parallel [356].

3. **Nanowell Arrays**: Nanowell arrays consist of an array of nanoscale wells that can trap individual cell. This design provides a high-density platform for studying interactions within microbial communities with enhanced spatial resolution [212].

Utilizing Microfluidics in Phage Research

In exploring the dynamic interactions between bacteriophages and their bacterial hosts at the single-cell level, several key studies have employed microfluidic devices to provide insights. The pioneering work in studying phages using microfluidic devices was conducted by Mangenot et al., who utilized a microscopy flow chamber to investigate the ejection dynamics of T5 phage DNA, a tailed dsDNA virus, into its host bacterium [347]. This research aimed to elucidate whether the internal pressure built up during DNA packaging was sufficient to drive the complete ejection of the phage's genome. Through the application of fluorescence microscopy, the team was able to stain the ejected DNA and observe its release in real-time, revealing that DNA release is not a uniform process but occurs in distinct stages [347]. This foundational study set the stage for subsequent research, including the work of Grayson et al., who further utilized a microscopy flow chamber constructed with double-sided adhesive sheets for real-time measurements of DNA ejection speed from bacteriophage lambda [198]. Their investigation aimed to elucidate the real-time ejection speeds of DNA from phage lambda, focusing on the influence of genome length and the ionic conditions of the buffer on these speeds. Additionally, their work sought to understand the role of DNA-DNA interactions within the phage head, examining how these interactions affect the initiation of ejection and contribute to the friction experienced during this process [198]. These studies employed long-term time-lapse microscopy, although the exact durations were not specified, indicating a tailored approach to monitoring these interactions over necessary time frames.

In the study conducted by Pearl et al., microfluidic devices were used to investigate the interactions between *E. coli* and bacteriophage lambda [409]. Utilizing observation chambers crafted from PDMS molds, the researchers provided a controlled microenvironment to follow the fates of single infected bacteria. The goal was to unravel the impact of bacterial persistence—a phenotypic state characterized by slow growth or dormancy—on the dynamics of phage infection and prophage induction. Through long-term time-lapse microscopy, Pearl et al., observed the expression of green fluorescent protein (GFP) under the phage lytic promoter, alongside the cellular fate post-infection. The analysis of microscopy videos was conducted using ImagePro and ImageJ software. Their findings revealed that persistent bacteria, while shielded from prophage induction, remained vulnerable to lytic infection by bacteriophage lambda. Intriguingly, the expression of lytic genes was found to be suppressed in persistent cells, but resumed once these cells transitioned back to a state of normal growth, eventually leading to cell lysis [409].

In the study by Simmons et al., the interaction between phage-resistant and phage-susceptible bacteria within biofilm structures was explored to understand how biofilm architecture influences these dynamics [476]. Utilizing microfluidic devices coupled with confocal microscopy, the researchers aimed to demonstrate how biofilms promote the coexistence of both resistant and susceptible bacterial populations under various conditions, including differences in growth rate, cost of phage resistance, and phage diffusivity. This experiment involved time-lapse imaging to capture the biofilm growth and T7 phage-bacteria interactions at single-cell resolution. Their findings revealed that spatial constraints within biofilms significantly impact phage resistance dynamics, facilitating a robust coexistence of susceptible and resistant bacteria. This coexistence was attributed to the spatial protection offered to susceptible cells by resistant ones, effectively creating a barrier that limits phage access and diffusion [476].

The study by Attrill et al., not only investigated the survival strategies of *E. coli* in response to bacteriophage T4 attacks through experimental setups but also employed agent-based model simulations to further understand the dynamics of bacterial-phage interactions in structured environments [36]. The goal was to elucidate the mechanisms behind phenotypic resistance to phages, focusing on the reduced expression of phage receptors as a key survival strategy. These simulations complemented their microfluidic experiments by predicting population dynamics under various conditions, highlighting the impact of spatial refuges on the evolution of bacterial resistance. Time-lapse microscopy was used to observe individual bacterial responses to phage exposure. The agent-based simulations were designed to mirror the structured environments of the microfluidic experiments, predicting population dynamics under various conditions of phage exposure. The combination of experimental data and simulation insights offered a comprehensive view of

how phenotypic variability and spatial structure influence the outcomes of bacteria-phage encounters, suggesting a significant role for phenotypic resistance in environments where genetic resistance might be less advantageous [36].

Later on, Attrill and colleagues studied the interplay between environmental factors—specifically nutrient availability, bacterial growth rates, and phage abundance—and the evolutionary dynamics between bacteria and bacteriophages. [37]. Their research revealed that after infection by T4 phage, fast-growing bacteria often survive lysis in conjunction with their clonal kin, whereas slower-growing bacteria tend to survive in isolation. Importantly, the study identified that higher concentrations of bacteriophages trigger a phenotypic shift from solitary to collective survival strategies among bacterial populations in spatial refuges. This adaptation is thought to be driven by phage-induced lysis inhibition. The findings underscore that in structured environments, bacterial populations can manifest phenotypic resistance to phages without evolving genetic resistance, a phenomenon significantly influenced by environmental variables like nutrient availability [37].

Mabrouk et al., developed a microfluidic platform for efficiently isolating and characterizing bacteriophages, showcasing the platform's capability for detailed, long-term analysis of phage-bacteria interactions using Mimetas Organoplates[2] [345]. This approach enabled them to conduct an extensive time-lapse imaging over 40 hours, observing interactions between various lytic phages such as T4, T3, T7, phages ICP1 and ϕ29 and their respective bacterial hosts. Additionally, they utilized this innovative device to observe host responses to phage attacks, such as changes in cell shape, and facilitating the isolation of new phages from environmental samples [345].

Williams et al. [555], investigated the cooperative mechanisms between type VI CRISPR and DNA-cleaving RM systems during ϕLS59 phage infection and cell recovery using microfluidic chambers. Utilizing microfluidic chambers, they initiated the study by infecting bacterial cells with the phage and then, after a ten-minute interval, encapsulated these cells within microfluidic devices. Following this setup, phase-contrast images were captured at ten-minute intervals over a period of five hours. Image analysis was conducted using NIS Elements software v5.3, and a detailed quantitative evaluation of cell fates and phage genome loci was performed with the aid of Fiji software v2.3.0. Their study demonstrated that RM systems can cleave phage genomes, aiding bacterial recovery from Cas13-induced dormancy [555].

Despite these advancements, no studies have been conducted on the interactions between the M13 phage and its bacterial host using the specific microfluidic platform format

[2]Mimetas Organoplates are advanced microfluidic devices designed for tissue culture and high-throughput screening, allowing for the replication of human organ structures and functions [61].

employed in this study. We leverage microfluidic technologies to more extensively study M13 phage, with the aim of elucidating the dynamics of phage-host interactions. The goal of this research is to perform a comprehensive analysis of the M13 phage's interaction with its host, focusing on understanding the morphological changes in host cells and their significance in the infection process.

2.5 Simulation

2.5.1 Mathematical and computational modelling of phage-bacteria interaction

One aspect of synthetic biology is applying engineering models to optimize biological designs [194]. The functionality of these models has resulted in the accurate engineering of cells for further use in health and diseases, agriculture, biomaterial, etc. [194, 246]. *In-silico* experimentation includes the combination of biological data with mathematical modelling and computer-based models to simulate and investigate the theories that may be difficult, expensive, and time-consuming to obtain using experimental methods alone. Furthermore, they can be used to strengthen experimental knowledge, test the results of the underlying assumptions and predict system dynamics, behaviour and conditions that have not yet been explored in the laboratory settings [223, 524]. Using mathematical modelling of phage-host interactions can not only increase insights towards understanding the dynamics of phage and bacteria, but it also can provide valuable details toward better experimental design and the phage's successful practical application [479]. Mathematical modelling of the phage-bacteria interaction has a long history and has been reviewed by Krysiak-Baltyn et al. [298] and Abedon and Katsaounis [8].

Models of phage-bacteria interaction can be classified into two types, depending on the growth conditions: media with low viscosity (i.e., liquid media), and media with high viscosity (i.e., solid media). While low viscosity environments typically pose fewer spatial restrictions, spatial limitations can still occur. Conversely, in the high viscosity environment, the dynamics depend upon space and on the spatial composition of the media [478]. Models of phage-bacteria interactions include computational simulations that are categorized into continuous and discrete approaches. ODEs and PDEs, are continuous simulation approaches [164]. As will be described below, these methods have been used broadly for phage-bacteria interactions, yet, difficulty in recording and tracking individual behaviour is one of the limitation of these models. In contrast, Monte Carlo models and agent-based modelling are discrete simulation approaches. Monte Carlo simulations are computational

algorithms that use random sampling to obtain numerical results. Agent-based modelling considers individuals as agents with sets of rules describing their behaviours [268]. The overall system behaviour is given by the agents' individual dynamics and their interactions with each other. Modelling techniques for phage–bacteria dynamics are presented in Table 2.1.

Table 2.1: Modelling techniques used to study phage–bacteria dynamics.

Modelling technique	System structure		Time handling	
	Spatial distribution	Non-Spatial distribution	Continuous	Discrete
ODE		x	x	
PDE	x		x	
Monte Carlo models	x	x		x
ABM	x	x		x

Mathematical modelling using ODEs was developed by Campbell as one of the first systems that described phage-bacteria interactions in a chemostat-like condition [86] (technically, they used delay differential equations (DDEs)). Considering the nature of the habitat and impact of the availability of resources on prey growth, Levin, Stewart and Chao expanded Campbell's model to study the coexistence of two prey species and one phage predator [312]. In recent years, with major advances in understanding of the system biology, there has been an increasing amount of literature on modelling of phage-bacteria interactions. For instance, in 2016, an improved mathematical model using DDEs and combining existing models was developed to describe the effect of pH and temperature on phage-host interactions in a homogenous liquid environment in a chemostat [57]. In 2017, several groups studied lysis-lysogeny decisions, using the Gillespie stochastic simulation algorithm – a Monte Carlo model – to describe lytic/lysogenic fates [514], and to study the effect of viral replication [461]. Using agent-based models together with PDEs, Simmons et al. modelled phage infection in a bacterial biofilm [477]. Bull et al. combined mathematical and computational models to study the effect of the spatial structure of the environment on cells resistant to phage infection [78]. In more recent research, as his Ph.D. thesis, Khan studied the effects of lytic phages and antibiotics on bacterial biofilm colonies by using ODEs, and impact of evolutionary forces acting on prophage by using PDEs [283]. More details of phage-bacteria interaction studies have been explained in 'Modelling Phage-bacteria Dynamics' written by Sinha et al. [478].

Despite the fact that phages have different life cycles, the majority of these studies considered population dynamics of lytic phages [479]. As discussed in Section 2.1.1, filamentous phages follow a chronic lifecycle, in which they do not kill the host cells. Instead,

they merely decrease the growth rate of their host, while new phage progenies are continuously produced and extruded through the cell membrane. Filamentous phages are the most commonly used system for biological and biotechnological studies; yet, the number of studies using computational simulation and mathematical modelling to predict the behaviour and dynamics of filamentous phages in a population of cells are not even close to virulent and temperate phages studies. Bacteriophage M13 life cycle has been thoroughly studied in the past 50 years but only recently has been computationally modelled using ODEs [483, 482].

Agent Based Modelling

A variety of agent-based modeling (ABM) tools have been developed to elucidate the dynamics of bacterial populations and the multicellular systems they constitute. There are several ABM software packages that simulate intracellular and cellular effects. Among these, Gro [250] and CellModeller [438] stand out for their simulation of biophysical patterning in 2D environments, emphasizing physical interactions and chemical signaling within multicellular systems. Intracellular simulators like Smoldyn [28] and Stochsim [247] model molecular interactions and provide spatial dynamics of cellular mechanisms. In contrast, cell-level simulators, like AgentCell [151], BSim [194], and BNSim [548] model population dynamics of cell communities as well as simulating intracellular mechanism and interactions. Specialized tools like iDynoMiCS [305], the advanced successor of BacSim [297], focus on biofilm formation, enabling users to specify cellular properties and simulate biofilms developing on surfaces while accounting for substrate dependence and its impact on cell growth. While each platform chooses a particular abstraction level to best represent the system and address specific research questions, they share the agent-based modeling framework as a common foundation, portraying cells interacting within a dynamic environment [389].

Agent-Based Modelling is a computational approach for simulating complex systems [381]. Each individual in an ABM is considered as a software agent with sets of specific rules, conditions and behaviour [381]. Considering each agent's fate, properties, interactions and the impact of these interactions on the system properties, ABMs have become one of the most successful modelling approaches, especially in biology [450]. Compared to conventional methods like differential equations, which only account for the aggregate behaviour of a populations, ABMs can consider the spatial dynamics of interactions and the geometries of the agents at both the single-cell and population levels.

In microbiology, ABMs have been broadly used to study microbial systems and to understand the effect of the spatial environment on microbial social evolution [385], the

evolutionary dynamics of CRISPR-Cas systems [247], formation of natural biofilms [306], and emergence of antibiotic resistant among bacteria [155]. Two excellent reviews by Gorochowski [194] and Hellweger [223] provide details and studies towards ABM applications in synthetic biology. Because individual behaviours are the foundation of populations dynamics in ABM mechanisms, these model provide a promising approach in studies of phage-host cells interactions [491]. In 2006, an agent-based model named COmputing Systems of Microbial Interactions and Communications (COSMIC)-Rule was introduced which considered bacteria and phages [202, 201]. In a follow-up study, COSMIC-Rules were applied to investigate the lambda phage infection process inside bacterial populations and the effect of the restriction-modification system on phage infection [203]. Using an agent-based mathematical model for a predator-prey framework, Iranzo et al., predicted virus-host coevolution in the presence of a CRISPR-Cas system [247]. One group evaluated the impact of lytic bacteriophage on the dynamics of conjugative plasmids in a plant-associated soil bacterium and developed an ABM to explain the observed dynamics [216]. Another group used multiple infection processes of a cell and developed an ABM of phage-host cell interactions to explore the impact of spatial interactions on the dynamic of multiple infections [506]. Simmons et al., combined differential equations with agent-based methods to evaluate phage-biofilm interactions. They developed a biofilm simulation framework to study the impact of biofilm formation on the dynamics of susceptible bacteria and lytic phages [477]. Selavkumar et al., characterized the spatiotemporal dynamics of *Pseudomonas aeruginosa* biofilm and its lytic bacteriophages using Agent-based molecular dynamics framework [216]. A novel agent-based model, eco-eVolutionary mIcrobial indiViduAL-baseD sImulations (eVIVALDI), was presented by Sousa et al., to study phage-bacteria ecological interactions including population dynamics, environmental structure, genome evolution, and phage mediated horizontal transfer [376]. A year later, by combining machine-learning approaches, they developed their model to study multiple roles of virulent phages in a microbial community under different types of environments [491]. They also used eVIVALDI to study the role of transduction in temperate phage-host interactions [166].

Despite the diversity of these models, the integration of these tools into a unified platform remains unrealized. Furthermore, the implementation of computational accelerations such as multithreading, parallelization, and GPU acceleration is deemed essential for enhancing the scalability and efficiency of these platforms, especially when dealing with large-scale systems [385]. In this study, the CellModeller software package is used to stimulate the growth of bacteria cells and track the infection process of M13 bacteriophage. Several key factors motivated the choice of CellModeller as the simulation platform for modeling phage infection over other agent-based models like Gro [250] or BSim [194]. Firstly, CellModeller offers a robust and flexible framework for simulating cellular interactions with

a high degree of spatial and temporal resolution, which is crucial for capturing the dynamics of phage-bacteria interactions. It also allows for the customization and fine-tuning of model parameters to reflect the specific biological complexities and hypotheses being tested in our research.

Furthermore, CellModeller's powerful visualization tools and its ability to handle large-scale simulations efficiently make it an attractive option for exploring the emergent properties of microbial communities under phage attack. This capability is essential for understanding the ecological and evolutionary implications of phage infection at a systems level, beyond the scope of what more specialized or narrowly focused agent-based models might offer.

2.5.2 Agent based modelling in the study of phage

The study by Attrill et al., mentioned earlier, not only investigated the survival strategies of *E. coli* in response to bacteriophage T4 attacks through experimental setups but also employed agent-based model simulations to further understand the dynamics of bacterial-phage interactions in structured environments [36]. The goal was to elucidate the mechanisms behind phenotypic resistance to phages, focusing on the reduced expression of phage receptors as a key survival strategy. These simulations complemented their microfluidic experiments by predicting population dynamics under various conditions, highlighting the impact of spatial refuges on the evolution of bacterial resistance. Time-lapse microscopy was used to observe individual bacterial responses to phage exposure. The agent-based simulations were designed to mirror the structured environments of the microfluidic experiments, predicting population dynamics under various conditions of phage exposure. The combination of experimental data and simulation insights offered a comprehensive view of how phenotypic variability and spatial structure influence the outcomes of bacteria-phage encounters, suggesting a significant role for phenotypic resistance in environments where genetic resistance might be less advantageous [36].

The dissertation 'Modeling Phage-Bacteria Dynamics in Mucus: An Agent Based Approach to Phage Therapy' by Kevin L. Joiner focuses on developing a computational model to understand the interactions between bacteriophages (specifically T4 phage) and bacteria (*E. coli*) within mucus [260]. This study aims to enhance the knowledge of phage therapy as a potential treatment against antibiotic-resistant pathogens. The agent-based model simulates the dynamics of T4 phage and *E. coli* in mucus, incorporating various microbial and mucus parameters. It also employs a continuous time random walk to represent the subdiffusive movement of T4 phage due to interactions with the mucus's mucin network. The simulation uses MATLAB for its computations, aiming to provide insights into the

conditions that affect the coexistence or extinction of the phage-bacteria ecosystem within mucus environments. The research acknowledges limitations in modeling complexity and potential empirical validation challenges [260].

The study 'Modelling phage-bacteria interactions driving predation and horizontal gene transfer' introduces eVIVALDI [376], a computational model (described earlier) for simulating phage-bacteria ecological dynamics. It integrates population dynamics, environmental structure, genome evolution, and phage-mediated horizontal gene transfer. Focused on phage therapy and the spread of antibiotic resistance, the model offers insights into the ecological and evolutionary dynamics of phage-bacteria interactions in various environments. This research emphasizes the importance of environmental structure in microbial community dynamics and antibiotic resistance acquisition [376].

2.5.3 CellModeller

CellModeller is an open-source, GPU-accelerated platform for multicellular modeling, utilizing Python for environment simulation and cell behavior scripting [270]. It is a computational tool designed to simulate the growth and interaction of microbial cells, such as bacteria, within a defined environment. This software leverages the principles of cellular automata and agent-based modeling to replicate the behaviors observed in microbial communities, including biofilm formation, cellular differentiation, and pattern formation [437].

The simulation environment in CellModeller is defined by setting parameters that describe the physical and biological context in which cells exist. This includes aspects such as the spatial dimensions of the environment, the presence of nutrients or other chemical signals, and physical constraints that may affect cell growth and movement. Within this environment, cells are modeled as individual agents that can grow, divide, and interact with their surroundings and with each other according to rules specified by the user [438].

Growth and interaction in CellModeller are simulated based on principles derived from cellular and molecular biology. For instance, the software can model the process of cell division by allowing cells to grow to a certain size before dividing, and it can simulate the effects of chemical gradients on cell movement and differentiation. This enables researchers to study how bacteria grow and interact with each other under various conditions such as biofilm formation and the self-organized patterning of cell layers [438].

CellModeller has been employed in diverse studies, including the work by Nunez et al., who utilized the tool to create foundational designs for studying self-organizing patterns in bacterial populations via morphogenetic engineering and synthetic biology. Their work

demonstrates potential applications in controlling bacterial growth using CRISPRi/Cas technology [395].

In the study conducted by Kan et al., CellModeller was deployed to delve into how intercellular adhesion impacts the spatial structuring of bacterial colonies. By incorporating a model of intercellular adhesion within CellModeller, the research successfully replicated experimental outcomes, showcasing that adhesion-driven interactions are key to the spread of forces across colonies [270].

In another study leveraging the CellModeller simulation platform, the strategic importance of varied weaponry for bacterial competition and survival was highlighted, indicating how diversity in bacterial armaments plays a crucial role in their ecological success and adaptability [65].

In this research, the CellModeller platform was utilized to simulate the infection dynamics of the M13 bacteriophage, with a particular emphasis on exploring aspects of the infection process that are challenging to directly ascertain through experimental methods. A key focus of this study was to investigate the relationship between the rate of phage diffusion and the spatial distribution of infected cells in proximity to phage-producing bacteria.

Chapter 3

Project hypothesis and objectives

In previous chapters, the critical role of microbial communities in ecosystem functioning [532] has been highlighted, underscoring their impact across both natural and human-associated ecosystems [455]. This backdrop sets the stage for our research, which, while it contributes to understanding population-level dynamics, primarily zooms in on the details at the single-cell level. Traditional analyses often rely on aggregated data from populations, providing a broad overview but potentially obscuring the distinct behaviors and interactions of individual cells. In contrast, our focus is on disentangling these individual behaviors through single-cell analysis. This method reveals the diverse states and phenotypes within communities that appear homogeneous, uncovering the hidden heterogeneity within populations [231]. The distinctions observed at the single-cell level have profound implications, offering deeper insights into the health and functionality of microbial ecosystems as a whole [231].

Building upon this understanding of microbial communities, it is important to understand the influence of bacteriophages—viral entities that not only modulate bacterial population dynamics but also facilitate genetic exchanges within these communities through mechanisms such as transduction and transformation [50, 163, 69, 295]. Their compact genomes, simple structures, ease of modification, host specificity, and safety regarding mammalian cells make them invaluable in various scientific fields [263]. Thus, understanding the interactions between phages and their hosts and the factors driving infection mechanisms is essential to grasp their roles and impacts in complex ecosystems. This knowledge could allow for the strategic manipulation and control of these interactions [365].

This study primarily aims to enhance our understanding of the interactions between M13 bacteriophage and *E. coli* cultures, observed from a single-cell perspective. The general hypothesis of this study assumes that utilizing time-lapse microscopy combined

with image processing will establish a methodology for obtaining quantitative insights into the temporal and spatial patterns of M13 bacteriophage infection at the single-cell level.

To achieve the aims of this study, the project has been structured into distinct objectives encapsulated in the following chapters:

- **Chapter 4: Design, Development, and Validation of Microfluidic and Agar Pad Systems for Studying Bacterial Dynamics**: The focus of this chapter is to establish and validate an image analysis framework for the detailed observation of *E. coli* growth dynamics at the single-cell level. This involves utilizing two distinct experimental setups: the agar pad and microfluidic devices. Specific objectives include:
  - Develop and validate an image processing pipeline tailored for the analysis of single-cell activities within the acquired time-lapse images. This pipeline will utilize tools such as Ilastik and CellProfiler (explained in Section 4.3.1, focusing on segmentation and tracking of bacterial cells across successive frames.
  - Develop a data post-processing script in MATLAB to process the data from image-processing software and validate that it characterizes the radius, length and elongation rate of individual cells and tracks their motion and divisions over the course of experiment.
  - Assign characteristics or features to individual cells in the experiment and analyze the cells morphological features -radius, length and elongation rate- at different states using these features.
- **Chapter 5: Spatiotemporal Dynamics of M13 Phage Infection**:
  - Expand the image processing and analysis pipelines developed in Chapter 4 to include fluorescence imaging. This involves updating the segmentation and tracking pipelines and MATLAB scripts to process and analyze data related to phage infections.
  - Investigate the impact of cell morphological characteristics- size (radius and length) and elongation rate- as well as the cells' proximity to phage producer cells on M13 phage infection. Analyze these factors in different setups: (i) monocultures directly exposed to phages and (ii) mixed cultures of phage-producing and phage-susceptible strains.
  - Conduct computational simulations using the CellModeller framework to model the interactions between phages and their bacterial hosts. These simulations aim

to replicate the observed experimentally infection process and provide a virtual environment for testing hypotheses and exploring underlying mechanisms of the phage infection process that are challenging to observe directly in laboratory experiments.

Chapter 4

Design, Development, and Validation of Microfluidic and Agar Pad Systems for Studying Bacterial Dynamics

4.1 Introduction

This chapter is divided into two main sections. The first section revisits the development and operational specifics of two key experimental setups: the Agar Pad and Microfluidic Device, initially introduced in Section 2.4.2. This recap will emphasize their roles in facilitating the real-time observation of microbial behavior and phage-host interactions.

The second section delves into the methodologies applied in image processing, specifically focusing on segmentation and tracking techniques. It will also outline the data analysis pipeline employed to interpret the results derived from these time-lapse experiments.

4.1.1 Time-lapse Experiments

Time-lapse imaging techniques were employed within the distinct environments of the Agar Pad and Microfluidic Device to investigate the bacterial growth and phage infection processes. Each setup presents unique conditions for microbial study: the Agar Pad method

simulates a dynamic environment where nutrients gradually deplete, while the Microfluidic Device maintains a constant supply of fresh media, enabling the continuous observation of bacterial responses under steady conditions.

By contrasting these methodologies, a better understanding of how different environmental conditions impact bacterial growth dynamics and their interactions with phages was obtained. Time-lapse microscopy allowed for the documentation of dynamic processes of bacterial populations over time, providing insights into their adaptive responses to varying environmental stresses.

Through time-lapse imaging and systematic analysis, this section aims to enhance our understanding of microbial behavior, underscoring the distinct advantages of each setup in replicating both natural and controlled settings.

4.1.2 Image Processing

Time-lapse imaging enables the detailed observation of dynamic biological processes, essential for understanding cellular behaviors over time. Image segmentation, a crucial initial step in image processing, describes distinct elements within images, providing a foundation for subsequent tracking and analysis [229, 311, 314]. This study employed Ilastik [58] for pixel classification and cell body identification, followed by CellProfiler [497] for detailed morphological quantification and tracking, as outlined in Section 2.4.1. These tools, known for their precision and user-friendly interfaces, facilitate the extraction of comprehensive cellular data, including location, morphology, and dynamics, aiding in the interpretation of complex biological phenomena. Subsequent data processing and analysis were conducted using MATLAB.

4.2 Material and Methods

Strains and Media The bacterial strains used in this section are documented in Table 4.1. All strains were cultured in LB medium at 37 °C with appropriate antibiotics. The *E. coli* K12 ER2738 cells with/without the relevant plasmids were cultured on LB agar plates supplemented with appropriate antibiotics.

Table 4.1: Bacterial strains and phages used in this study

Strain	Genotype	Source
E. coli K12 ER squared738	F´proA+B+ lacIq $\Delta(lacZ)$M15 zzf::Tn10(TetR)/ fhuA2 glnV $\Delta(lac-proAB)$ thi-1 $\Delta(hsdS-mcrB)5$	NEB
$K12$ ER RFP	*E. coli* K12 ER squared738, pBR322 (mRFP, AmpR)	This study

Media The media and their respective recipes utilized in this study can be found in Appendix A. Generally, LB media, either in liquid form or solidified using 1.5 % agar and supplemented with the appropriate antibiotic, was utilized throughout the study.

Culture preparation For each trial, an inoculum was cultured until it attained the early exponential growth phase ($OD600 \sim 0.1 - 0.2$).

Agar Pad Culture Preparation To achieve optimal cell concentration, a procedure was developed based on preliminary trials and adjustments. Initially, 4 ml of the early log culture was transferred to a microcentrifuge tube and centrifuged at 8000 ×g for 3 minutes. The resulting pellet was retained, the supernatant discarded, and fresh media added. After mixing the pellet with the fresh media, centrifugation was repeated three times. The resulting pellet was then resuspended in 1 ml of fresh media.

Microfluidic Device Culture Preparation Unless otherwise stated, all cultures used for microfluidic experiments were prepared as follows. An early log-phase bacterial culture was dispensed into 2 mL microcentrifuge tubes and centrifuged at 8000 ×g for 3 minutes. The excess supernatant was removed from the pellet, and the pellet was resuspended in 1 mL of media. The tubes were centrifuged, and this washing process was repeated three times. After the third wash and collection of all supernatant, the tubes were centrifuged again to remove any remaining supernatant. Subsequently, approximately 200µL of fresh LB media was added to each tube and gently mixed with the pellet by slow micropipetting to prevent excessive shear stress on the cells ($OD600 \sim 1 - 1.2$). This culture was carefully loaded into a 1µL syringe to prevent the introduction of bubbles into the microfluidic device. Finally, the culture was loaded into the Microfluidic Device.

4.2.1 Time-lapse Experiments

Microscope Setup Imaging was conducted using an inverted fluorescence microscope, Zeiss Axio Observer, equipped with an Axiocam 506 mono camera, and image capture was automated using ZEN 2 software (ZEISS, Germany). For the 63x images, a ZEISS Plan-Apochromat 63×/1.4 oil immersion objective was used to increase the resolving power of the microscope. The microscope was also equipped with an incubation chamber (PeCon GmbH, Germany). Throughout this study, the incubation temperature was consistently set at 37°C. Utilizing time-lapse microscopy, images were captured at regular intervals, every 5-10 minutes for fluorescence with a consistent intensity set at 20% and exposure time of 200ms across all fluorescent channels, and every 3-5 minutes for phase images. The duration of observations varied depending on the experiment type and the specific setup employed, whether it was microfluidic or agar-based experiments. The selection of fields of view was determined by the cell distribution in the frame, aiming to maximize the number of cells captured. Each time point's focus was achieved using the 'Autofocus using Z values' module.

4.2.2 Agar Pad Setup

The Agar Pad setup, described in Section 2.4.2, was adapted from the system described by Joyce et al., involving the utilization of petridishes with coverslip bottoms [262]. For live-cell imaging, a bacterial strain was prepared following the protocol outlined in Section 4.2. A 1µL sample of this culture was placed in a specialized 35 mm petri dish, which features a 15 mm diameter region at the bottom where a borosilicate glass coverslip is fitted, rather than an open hole (MatTek, MA). This design creates a shallow well in the dish. Onto this surface, a thin layer of 1.5 % LB agar, marginally smaller than the well itself, was deposited. To further prevent evaporation during the experimental process, parafilm tape was wrapped around the dish's lid. Subsequently, the dish was placed in a microscope chamber, temperature-regulated at 37 °C. For a visual representation of this setup, refer to Figure 4.1.

4.2.3 Microfluidic Device

Design

The microfluidic devices used in this study were provided collaboratively by Matthew Courtney from the Carolyn Ren group at the University of Waterloo. The microfluidic

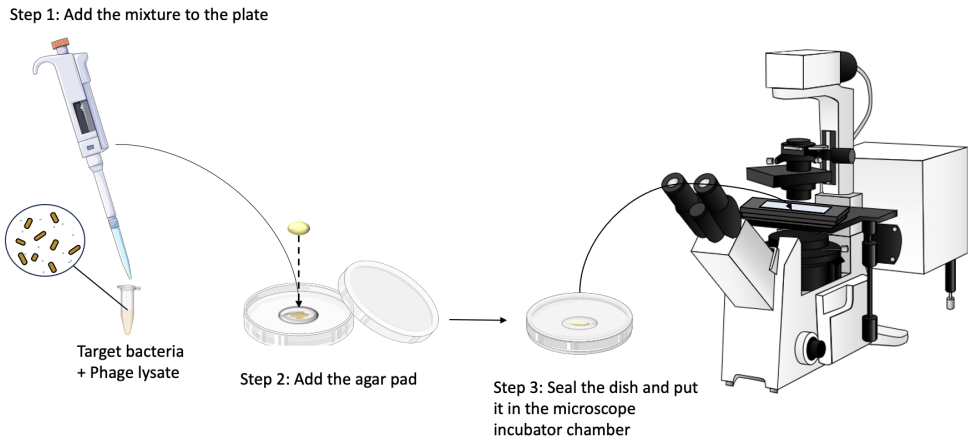


Figure 4.1: Agar pad setup. (a) 1µL of bacteria was dispensed onto the dish and covered with an agar pad. (b) The dish's lid was closed and sealed with parafilm. It was then placed in the microscopy chamber, positions were chosen, and imaging was initiated.

device fabrication involved standard multilayer soft lithography. Although the detailed specifics of the fabrication process are not the central aspect of our research, outlining these steps is essential for a clearer understanding of the discussions that follow in this thesis. To achieve varied chamber heights, a multilayer approach using SU8 photoresist [1] was adopted. This fabrication method involved a sequential layering process: initially, a layer of photoresist coated the silicon wafer, forming the monolayer traps. Subsequently, additional layers of SU8 photoresist were spin-coated onto the silicon wafer to set the desired height for the main channel. Each layer underwent patterning of microchannel features by exposure to UV light through dedicated photomasks. Achieving precise alignment among these layered levels manually presents a significant challenge. Misalignment during this process often leads to device variations, evident in our case where the misalignment caused the devices to exhibit different lengths.

After developing the photoresist layers on the silicon master, polydimethylsiloxane (PDMS) was used to create the mold. Each silicone master accommodates three chips, with multiple microfluidic devices designed on each chip (see Figure 4.3). These devices consist of a single main channel and 20-30 chambers, each connected to the main channel on one side, resulting in rectangular one-open side chambers. The chamber features an

[1]Photoresist is a light-sensitive material used in microfabrication and photolithography processes to transfer patterns onto a substrate, typically a silicon wafer. It is a key component in the creation of intricate structures at the microscale level.

approximate height of 1 µm, similar to the diameter of a single *E. coli* cell, facilitating monolayer cell growth, enabling specific studies focused on individual cells. The microfluidic device design allows continual introduction of nutrients and removal of waste and excess cells, achieved through the main channel 4.4. The main channel itself has a height of 15 µm.

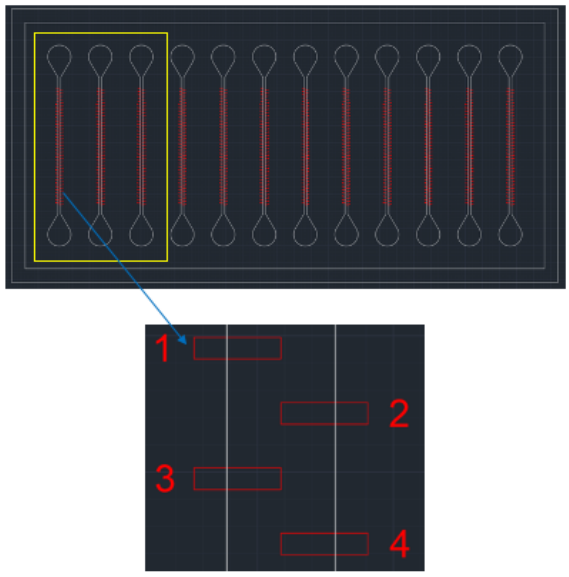


Figure 4.2: Microfluidic Design prepared by Matthew Courtney. The figure depicts a single chip containing multiple microfluidic devices. Each device has multiple rectangular one open-ended chambers

Mold preparation

To prepare the device, the protocol provided by Matthew Courtney was followed. In brief, PDMS was prepared using a Sylgard 184 silicone elastomer kit (DOW Silicones Corporation, US). A mixture of the pre-polymer base and cross-linking curing agent was made in a 10:1 ratio according to the manufacturer's recommendations. The resulting uncured PDMS mixture was degassed in a vacuum desiccator at low pressure for about 20 minutes to eliminate bubbles. It was then poured onto the silicon master provided by Courtney, ensuring it covered at least 1-2 cm above the master's surface. The PDMS was covered and left at room temperature for an additional 10-15 minutes to allow any remaining bubbles to escape.

The mold was placed in an oven at 95°C for 2-3 hours to ensure the complete curing of the PDMS. Afterward, it was allowed to cool for approximately 10 minutes. The chips were then carefully cut and separated from the master silicon, and they were immediately covered with transparent tape to prevent debris attachment. Inlets and outlets were created using a 1.5 mm biopsy punch. The PDMS layer was then bonded to glass slides (Fisher Scientific, Canada), which were prepared using a plasma wand (Electro-Technic Products, INC., US) to activate the PDMS surface. Adequate pressure was applied to ensure secure bonding of the PDMS to the glass. Finally, the device was placed in the oven at 95°C for an additional hour. Each device was subsequently examined under the microscope to verify that the chambers were not collapsed and remained in good condition (Figure 4.3).

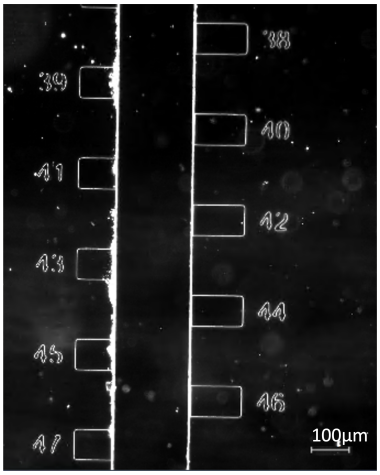


Figure 4.3: Microfluidic Device Under the Microscope at 10x Resolution. The chambers were successfully formed and connected to the main channel.

4.2.4 Microfluidic Device Preparation for Time-lapse Experiments

The initial stage of the process entailed the device's sterilization, achieved by injecting 70% ethanol into it using a sterile syringe and tubing. The ethanol was allowed to circulate for approximately ten minutes. Subsequently, a solution of 50 mg/ml sterile BSA was introduced into the device and maintained for roughly an hour. This step serves to flush out the ethanol residing in the channels and, notably, prevented the binding of PDMS functional groups to the cells.

Next, the cells, prepared as discussed in Section 4.2, were loaded into the device using a sterile syringe. The cells were pressured through the main channel, leading to several

cells entering each chamber. A syringe pipe (the syringe attached to the tubing) was utilized to gently tap the culture-containing media attached to the inlet of the device. This tapping action, presumed to increase the number of cells inside each chamber, created mechanical force dislodging cells that might have adhered to the walls or corners of the microfluidic device. Initially, attempts were made to force the cells into the chambers using a centrifugation method, as described in previous studies [20]. However, challenges such as bubble introduction were encountered, leading to deformation of the chambers or hindering cell entry. Additionally, the pressure applied during device fixation under centrifugation resulted in chamber collapse.

Once the cells were loaded into the device, a nutrient vial (connected to a 10 mL syringe containing media with the desired antibiotic) and a waste vial were connected to the inlets and outlets of the device, respectively. Positioned within the incubator chamber of the microscope (PeCon GmbH, Germany), the cells were subjected to time-lapse imaging at the study's designated temperature of 37°C. A GenieTouch flow pump (Kent Scientific Corporation, US) ensured a constant flow rate of 4 µL/minute, adjusted to provide a steady nutrient supply and efficient waste removal, and to prevent cells from exiting the chambers during experiments. The ongoing cellular activity was observed under the microscope, as depicted in Figure 4.5. The images acquired during this monitoring phase were subsequently used in the image processing techniques for the analysis of cell growth. Details regarding these methods will be further elaborated upon in Section 4.3.

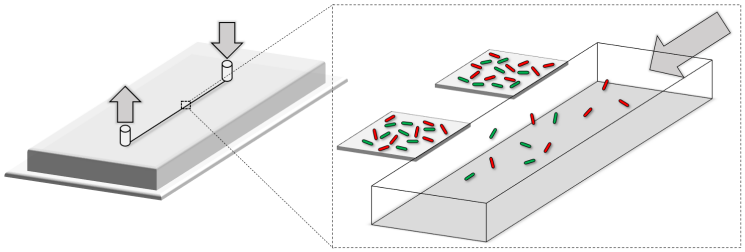


Figure 4.4: Microfluidic Operation (Matthew Courtney, 2023)

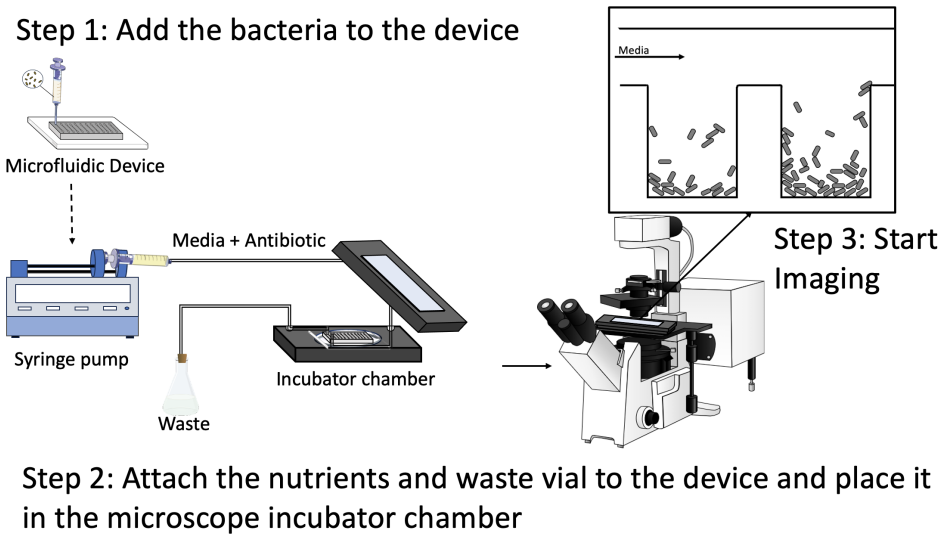


Figure 4.5: Microfluidic setup: cultures, as detailed in Section 4.2, were transferred into the device. Upon attachment of waste and nutrient vials, the setup was placed within the microscopy incubator chamber to commence the experiment promptly.

4.3 Image Segmentation

In this study, time-lapse microscopy yielded two distinct types of images: phase-contrast and fluorescent images (Figure 4.6). Phase-contrast images were used for cell identification: distinguishing cellular boundaries and shapes. In contrast, fluorescent images were exclusively employed for cell labeling and the quantification of protein intensity within the cells. The forthcoming sections will delve into the segmentation methods applied for both the microfluidic device and agar pad experiments. However, detailed insights into the segmentation pipeline are provided in Appendix D.

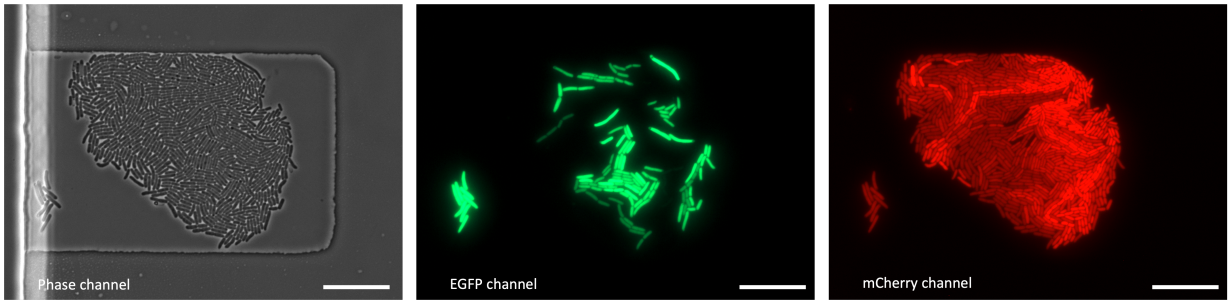


Figure 4.6: Microscopy images for a single frame in different channels. Scale bar: 20 micrometers. Left: phase channel; middle: EGFP channel represents GFP signal; right: mCherry channel represents RFP signal.

4.3.1 Segmenting Microfluidic Device Images

The initial phases of image segmentation in this research were conducted using the Ilastik toolbox for effective pixel classification and cell body identification. Opting to start with microfluidic device images for segmentation and analysis was a strategic decision, informed by the distinctive benefits provided by microfluidic environments:

- **Controlled Bacterial Population**: Microfluidic devices confine the bacterial population to a limited field of view, which significantly simplifies the manual verification process of image segmentation results. This feature is vital for the initial stages of segmentation method validation, as it minimizes the complexity and potential errors typically encountered during segmentation.
- **Prevention of Multilayer Bacterial Formation**: The engineered environments within microfluidic devices are designed to prevent the accumulation of multilayer bacterial structures, a common issue in more open systems like agar pads. This controlled environment aids in reducing the complexity related to image analysis and thus enhances the accuracy of segmentation results.

With this context, the segmentation process was undertaken as follows:

1. **Pixel Classification:** This initial phase distinguished cells from background noise (See Figure 4.7). This task involved labeling pixels as either 'cell' or 'background' to facilitate segmentation. However, densely populated images presented challenges due to the lack of clear boundaries between cells and the background, leading to

issues such as overlapping cells or misidentified background areas (e.g., cells were lost or background were considered as cells, cells were merged, etc., See Figure 4.8). To address these challenges and ensure the reliability of our segmentation, images with overly dense cell populations were selectively excluded from the dataset. This decision was based on predefined criteria assessing cell visibility and boundary distinction, ensuring reproducibility and consistency in our approach. Additional details regarding the segmentation limitations and the criteria for image exclusion are discussed in Appendix D.1. The effectiveness of segmentation for less-crowded images was validated through manual verification. This process, detailed in the corresponding sections, helped confirm that our segmentation approach effectively differentiated between cells and background in less complex scenarios.

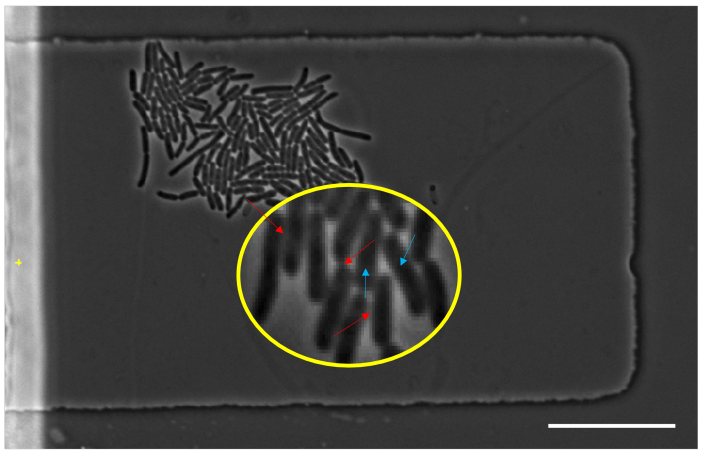


Figure 4.7: Time-lapse images of the frame with medium population density, magnified by 600x. A scale bar within the image indicates a length of 20 micrometers. Microfluidic Segmentation: Cells grew closely, yet with enough intercellular space to maintain a discernible contrast between cell and background pixel intensities. Blue arrows indicate cell pixels, while red arrows represent background pixels.

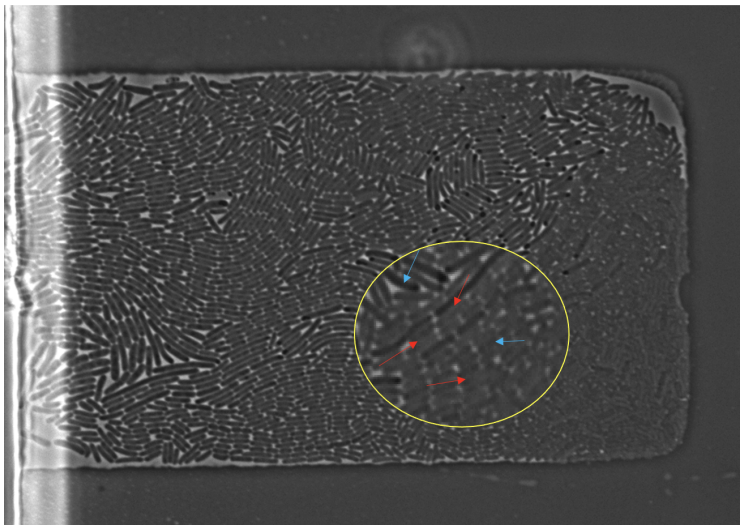


Figure 4.8: Image with high population density, magnified by 600x. Blue arrows indicate cell pixels, while red arrows represent background pixels.In the magnified part, cells displayed pixel intensities that closely aligned with the boundaries between cells, making cell identification notably challenging; hence after reaching these types of images, segmentation stopped.

2. **Object Classification**: Successfully pixel-classified images proceeded to the subsequent 'Object Classification' stage. In this stage, areas previously identified as cells in the pixel classification process were analyzed to define individual bacterial entities as distinct objects for further analysis. This step involves distinguishing individual cells from clusters and differentiating them from the surrounding environment (e.g., microfluidic walls, wastes, etc.), thereby allowing for more detailed and specific analysis of each bacterial cell's characteristics (refer to Figure 4.9 for examples).

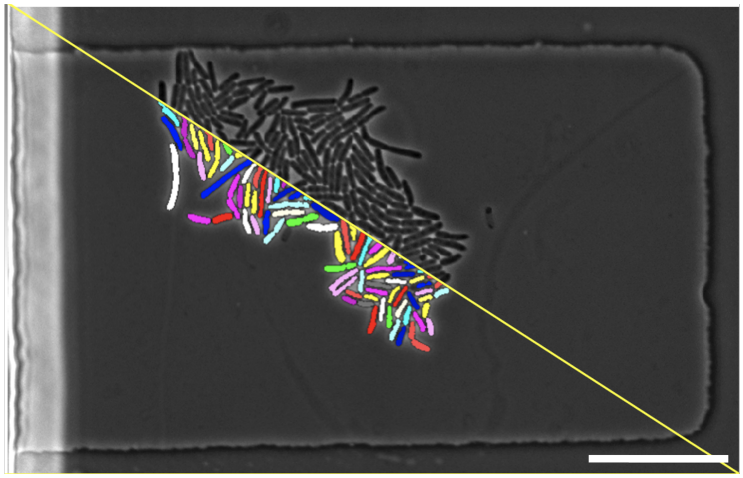


Figure 4.9: Segmented images in Ilastik. A scale bar within the image indicates a length of 20 micrometers. Above: Original image captured by the microscope. Below: Image showing identified objects after segmentation.

3. **Tracking and Processing Images**: Following object identification, CellProfiler was employed to extract cellular information and track the cells (Figure 4.10). Details about the pipeline are shared in the Appendix D, Section D.3. To ensure tracking accuracy, a manual inspection was conducted by comparing five different batches of time-lapse images (each batch containing 25-40 images) of raw and segmented/tracked images. This manual validation aimed to ascertain the precision of the tracking process, with satisfactory levels determined based on predefined criteria such as minimal misidentification rates (details and outcomes of this evaluation are illustrated in Figure 4.11). Selected information, defined based on the objective of this study, extracted from CellProfiler is as follows:

   (a) **Image number**: Sequential labeling of processed images in a time series.

   (b) **Object number**: Object count in the current frame (uniquely assigned for each image).

   (c) **Morphological features**: length, radius, and area.

   (d) **Cell location**: The x and y coordinates of cells centered position, as well as cell orientation.

   (e) **Cell orientation**: This is the measurement of the angle, ranging from -90 to 90 degrees, between the x-axis and the longest axis (major axis) of the particles.

   (f) **Fluorescence intensity**: Mean pixel intensity for fluorescently labelled cells.

(g) **Tracking Information**:

- **Label**: Each lineage receives a unique ID, persistent across all descendants of the cell.
- **Parent image number and object number**: signifying connection to the same cell in the preceding frame or to the mother cell if a division event occurred.

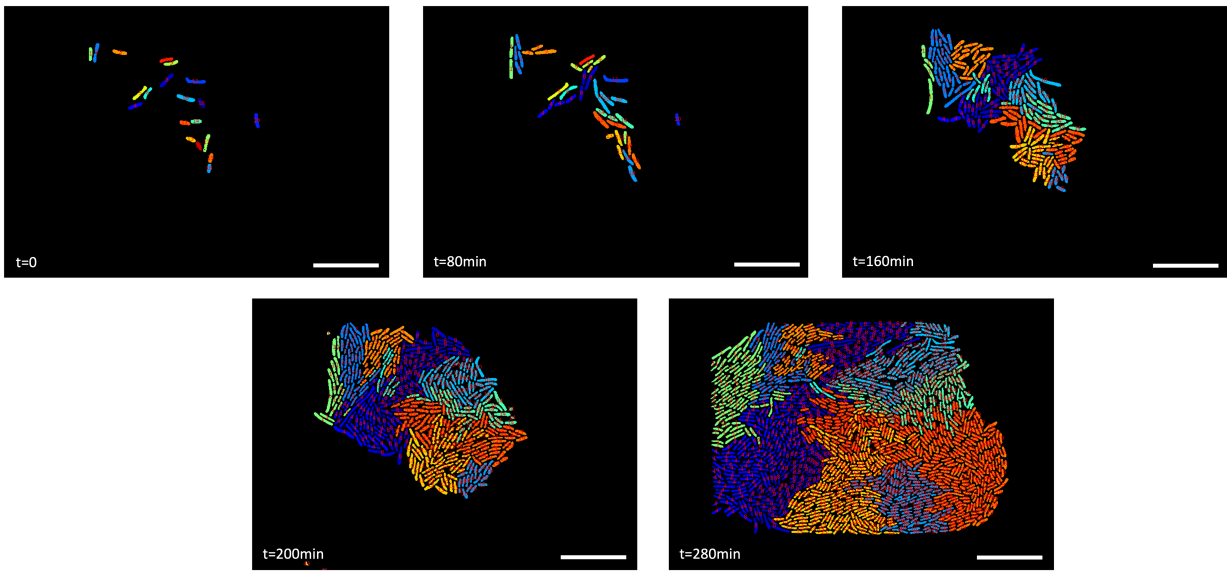


Figure 4.10: Tracked images using CellProfiler. A scale bar within the image indicates a length of 20 micrometers. Lineages are color-coded (images taken every 10 minutes a subset are shown).

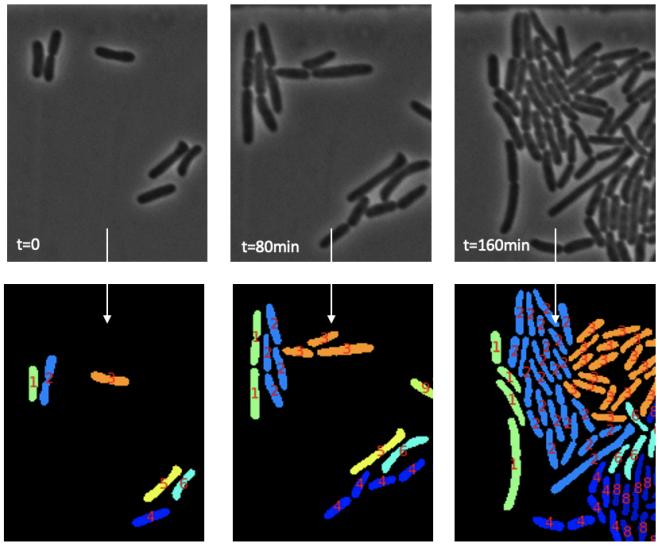


Figure 4.11: Tracked cell images. The numbers displayed within each cell represent their lineage label, which remained consistent throughout the experiment, serving as a unique identifier for each lineage.

4.4 MATLAB Script for Analyzing Microscopy Data and Cell Lineages

In this research, a crucial component of the workflow involved the development of a specialized MATLAB script for post-processing of the data derived from the segmentation and tracking software. This script relies on the tree.m package generated by Jean-Yves Tinevez [254]. The MATLAB post-processing code is available on GitHub: https://github.com/Sara-Haghayegh/MATLAB--Post-processing.git. The code is as outlined below:

1. The initial step is to create lineage trees (Figure 4.12). A tree is a hierarchical data structure that organizes data into nodes. Here, each cell at each time point correspond to a node. Each node is given a unique node index. Each cell present in the initial time frame is assigned as the root of a lineage tree. The tracking results are used to assign child nodes, corresponding to cell persistence from frame-to-frame or from mother to daughter upon cell division.

As the tree is built, the cell-specific parameters as described above are assigned to each node.

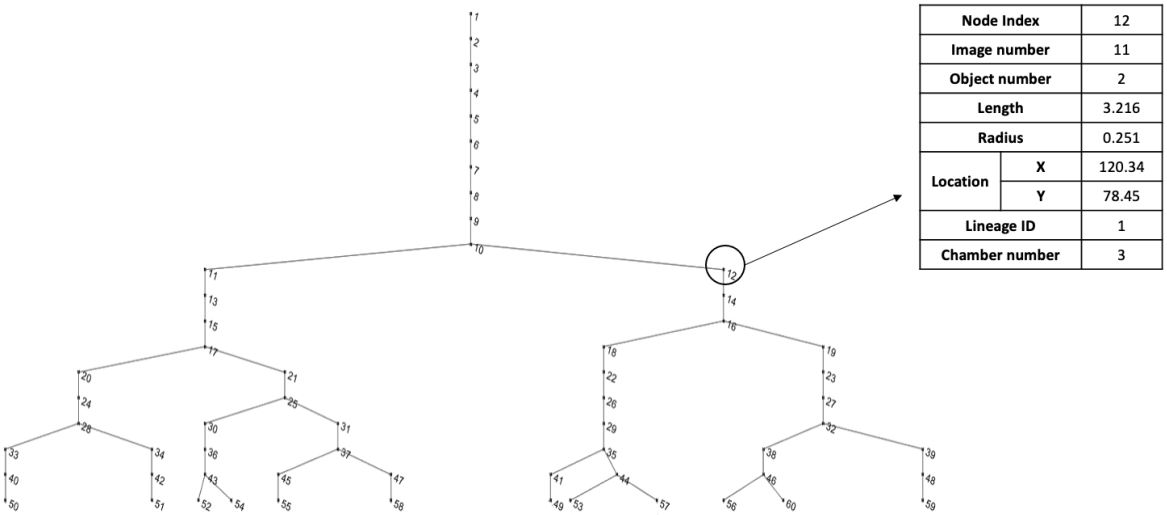


Figure 4.12: Lineage tree describing the progression of growth from an ancestor cell during an experiment. Each node is assigned a unique index as indicated. Each node is assigned a collection of parameters as indicated.

2. Each of the following were determined for each node, and assigned to the node's parameter vector.

   - **Cell Depth**: The distance of each cell from the entrance of the chamber in which it resides was calculated by comparing the x-coordinate of the cell centroid to the x-coordinate of the chamber mouth. The x-coordinate of the chamber mouth was determined by the maximum x-coordinate (centroid) found among all cells in the last frame of observation.
   - **Elongation Rate**: the average rate of length increase from frame-to-frame:

     $$\text{Elongation rate}(i) \ [\ \mu\text{m/min}] = \frac{\text{Length}(i) - \text{Length}(i-1)}{\text{Time}(i) - \text{Time}(i-1)}$$

     Not assigned for newly born daughter cells (or for ancestor cells at the first time-point).
   - **Length of cell division number**: This value represents a marker to track cell divisions. At the start, this number increments with each time step, essentially

serving as a timer. When a cell undergoes division, this count resets to zero, marking the start of a new generation.

4.5 Protocol for Unperturbed Monoculture Growth

This section details the process and observations from time-lapse experiments conducted on monocultures without the presence of phages, utilizing both agar pad and microfluidic device setups, as described in Section 4.2.1. In the agar pad setup, limitations were encountered around 6-7 hours post initiation due to desiccation of the medium, resulting in diminished cell visibility. Conversely, challenges in both setups were attributed to the high initial cell density and their rapid duplication rate, approximately 30 μm/min, complicating image segmentation efforts. This difficulty with populated images was previously addressed in Section 4.3. To maintain consistency in the analysis, time-lapse sequences were constrained to a duration of 105 minutes for agar setups and 135 minutes for microfluidic setups. This adjustment was necessary due to the inability of the microfluidic setup to sustain long-term imaging beyond these durations, highlighting a limitation in achieving extended observation periods as initially hoped. This constraint emphasizes the need for further optimization of the microfluidic environment to allow for longer-term observations of monoculture growth and interactions.

Table 4.2: Experiment Information for Unperturbed Monoculture Growth Experiment

Agar Experiment							
Experiment number	**Imaging (min)**		**Position/Chamber**[1]		**Exposure time (ms)**		
	Duration	**Frequency**	**Dimensions**[2](μm x μm)	**Number**	**Phase**	**RFP**	**GFP**
1	105	5	702.91 x 957.29	7		-	-
Microfluidic Experiment							
1	135	5	178.55 x 81.32	9	✓	✓	✓
2	135	5	153.94 x 79.07	15	✓	-	-
3	135	5	127.44 x 63.72	11	✓	-	-

[1] For Agar experiments, "positions" represent the chosen viewpoint under the microscope. This term refers to specific locations or fields of view where imaging or observations are made. In microfluidic device experiments, the term "chambers" is used. This designation refers to the compartments or chambers within the microfluidic device where cells are contained.In this setup, imaging is conducted from these chambers, making them the point of view or the specific locations of interest for observations.

[2] Length x Width

4.6 Results

4.6.1 Chamber seeding

Figure 4.13, shows the results of cell seeding at the first imaging time-point for the three experiments described in Table 4.2. As shown, the cell seeding was relatively uniform across the chambers, indicating the absence of any systematic correlation between the chambers' locations and their seeding density. Nonetheless, variations in the number of cells present in each experiment's chambers were noted, possibly due to differences in chamber capacity as outlined in Section 4.2.3 or variations in cell density, seeded according to methods described in Section 4.2.1. Moreover, potential disparities may have arisen due to the manual cell 'transfer process': as mentioned in Section 4.2.4, the transfer of bacteria into the chambers was performed manually, exerting force through a tapping method on the media to propel cells into the chamber. Despite the efficiency of this method, obtaining an optimal cell count often required repeated tapping, occasionally consuming considerable time. To adhere to the system's imaging requirements, a time restriction of 5 minutes was established to streamline this process and commence imaging promptly.

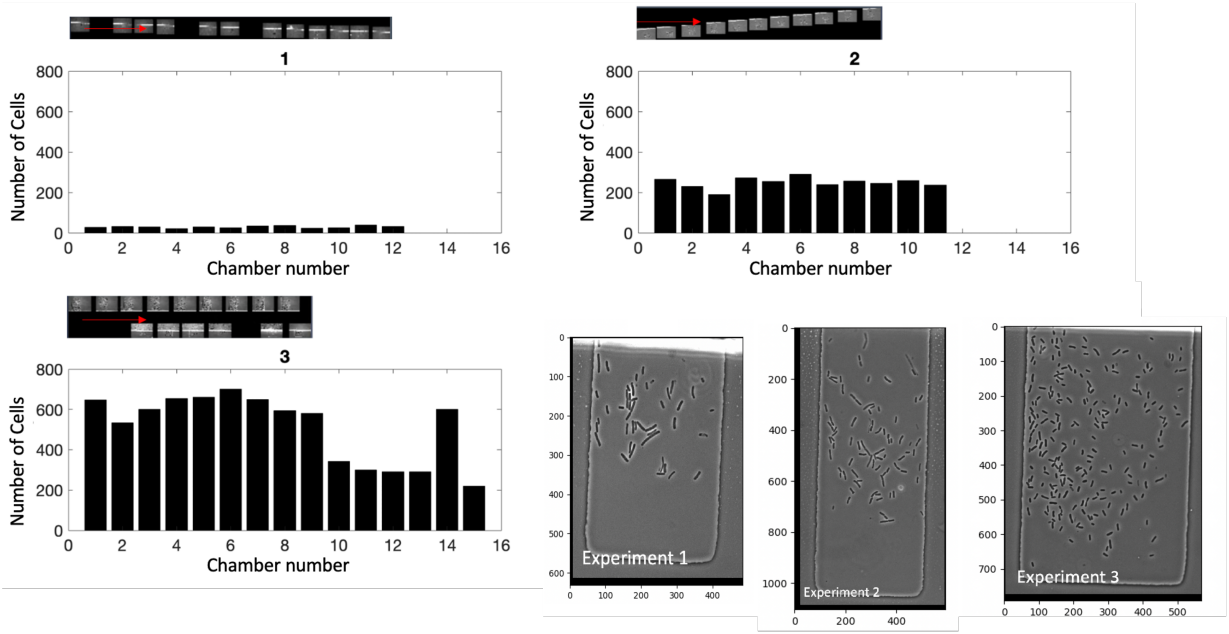


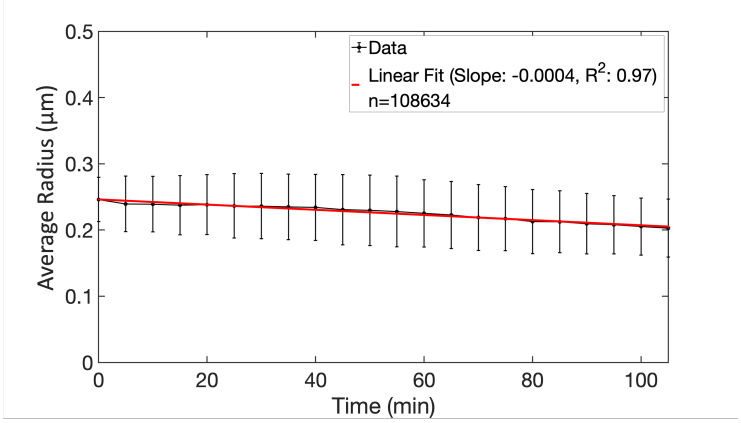
Figure 4.13: Initial cell seeding density at the start of each experiment. Above each graph: Microscopy image depicting the actual chamber positions during imaging. The red arrow indicates the flow direction in the device, originating from the lower location. In the bottom right corner, there's an individual image representing a single chamber from the device specific to that experiment.

4.6.2 Assessment of cell features through time

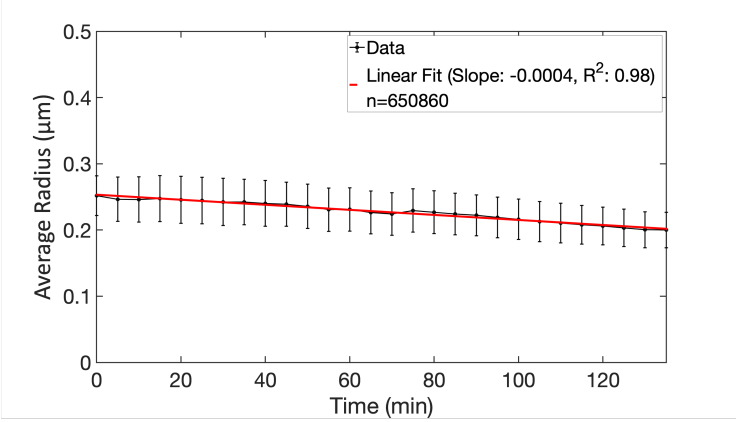
This section will illustrate the temporal and spatial trends in geometric cell features. Population averages over all experiments of each type will be shown. These observations were consistently reproducible across multiple experiments. Disaggregated results are in Appendix B.

Radius

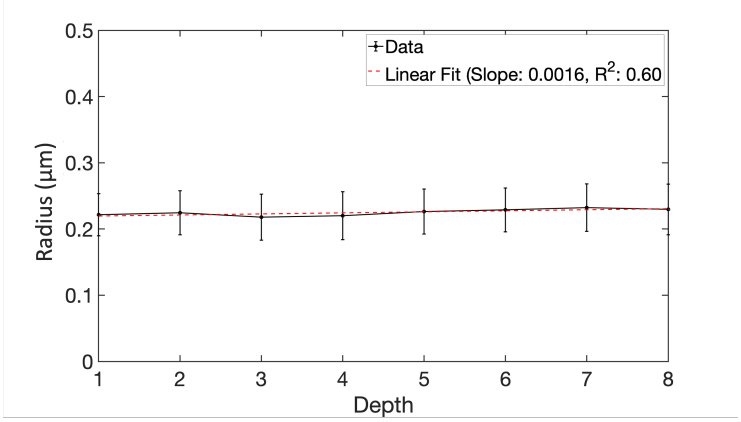
Figure 4.14 shows trends in cell radius over time and depth 4.14. The trends and R^2 values shown in the figures are based on averaged data points. Specifically, for each time interval or depth, the average radius was calculated from the data sets. The error bars in the figures represent the standard deviation of the radius within each time interval or depth. This figure illustrates the average cell radius over time in the agar setup. The linear fit shows almost no trend, with a slope of -0.0004 and an R^2 value of 0.97. The high R^2 value indicates that the linear model explains a large portion of the variability in the data. The large standard deviation in these graphs can be attributed to the inherent heterogeneity within the cultures, despite consistent genetics and environmental conditions.



(a) Agar setup



(b) Microfluidic setup



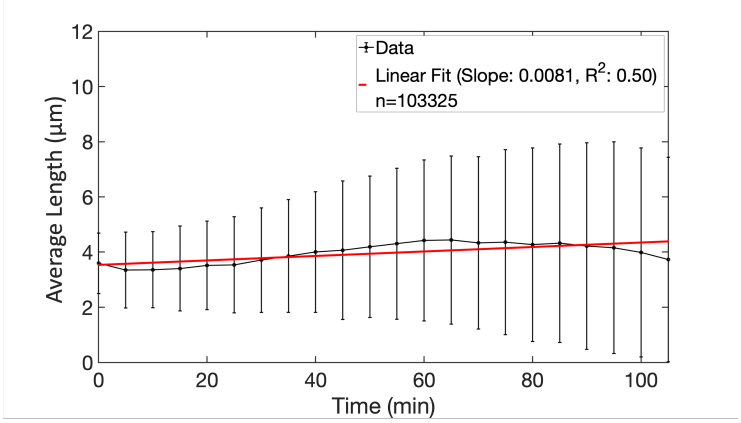
(c) Microfluidic setup

Figure 4.14: Spatiotemporal trends in cell radius. a) Change over time for agar set-up; b) hang over time for microfluidic devices. (c) The variation in space for microfluidic devices. Mean and standard deviation (bars) are shown. Best fit trend lines to the mean are shown along with slope, R squared values and sample size (n). Here, individual cells in each chamber occupy diverse positions, leading to varying depth levels within the device. The data in (c) has been binned into 10 µm intervals.

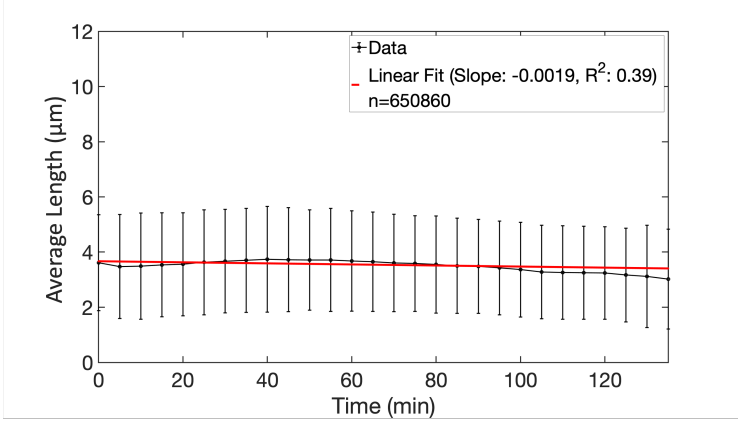
Length

In the analysis of cell length as depicted in Figure 4.15, both agar and microfluidic setups were examined for changes over time. It illustrates the trends in cell length over time, with the R^2 values based on the averaged data points for each time interval. The trends are derived from fitting a linear regression model to the average lengths at different time points. The R^2 value represents the goodness of fit for this linear model.

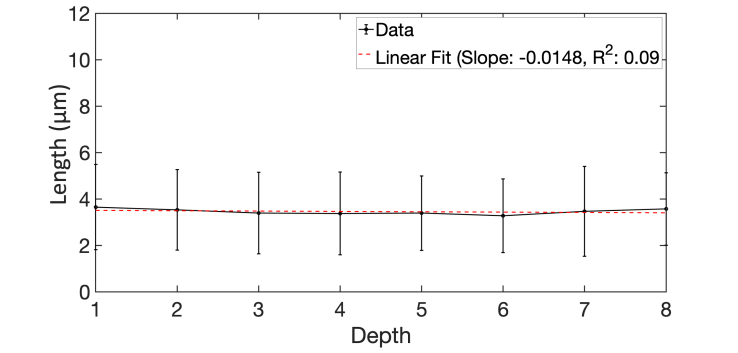
The results showed that cell length in the agar pad setup exhibited a slight increase over the experimental period, suggesting a minimal but noticeable filamentation response, potentially due to environmental stress or nutrient depletion. On the other hand, the microfluidic setup maintained a relatively stable cell length, reflecting the constant environmental conditions provided by this setup.



(a) Agar setup



(b) Microfluidic setup

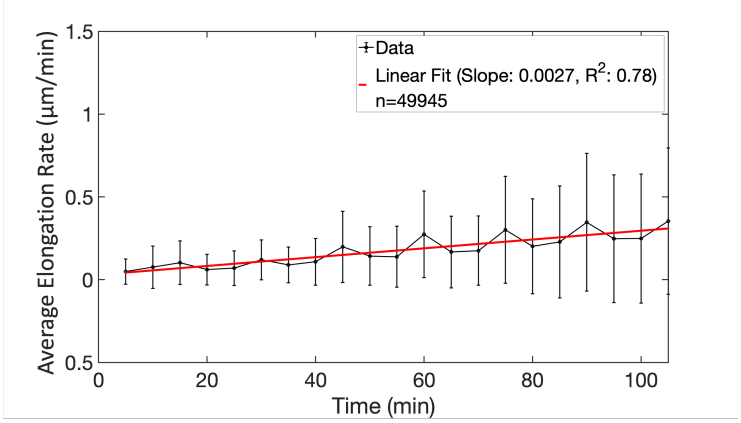


(c) Microfluidic setup

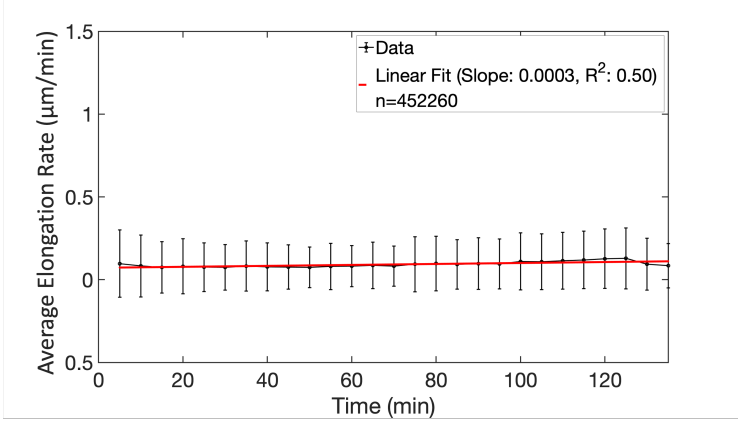
Figure 4.15: The figure illustrates the spatiotemporal changes in the average length, displaying (a) and (b) the changes over time for agar and microfluidic device respectively. (c) The variations in space for microfluidic device. Here, individual cells in each chamber occupy diverse positions, leading to varying depth levels within the device. The data has been binned into 10 µm intervals, with bars indicating the standard deviation. Best fit trend lines to the mean are shown along with slope, R squared values and sample size (n). Linear regression analysis revealed no significant trend in the length over time and space.

Elongation rate

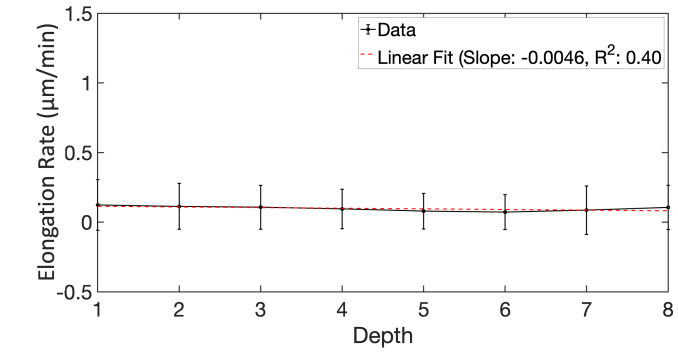
Figure 4.16 shows the spatiotemporal trends in elongation rate. In the agar experiment (refer to Figure 4.16a), the results reveal an initial lag phase, followed by a subsequent increase in the elongation rate as time progresses.The elongation rate exhibits no significant variation over time and space for microfluidic setup.



(a) Agar setup



(b) Microfluidic setup



(c) Microfluidic setup

Figure 4.16: The figure illustrates the spatiotemporal changes in the average elongation rate (um/min), displaying (a) and (b) the changes over time for agar and microfluidic device respectively. (c) The variations in space for microfluidic device. Here, individual cells in each chamber occupy diverse positions, leading to varying depth levels within the device. Best fit trend lines to the mean are shown along with slope, R squared values and sample size (n). The data has been binned into 10 µm intervals, with bars indicating the standard deviation.

RFP Intensity Figure 4.17 shows the temporal trend in RFP intensity. The consistency in RFP intensity indicates that the fluorescence exposures are sufficiently infrequent to ensure no photobleaching (from Experiment Number 3).

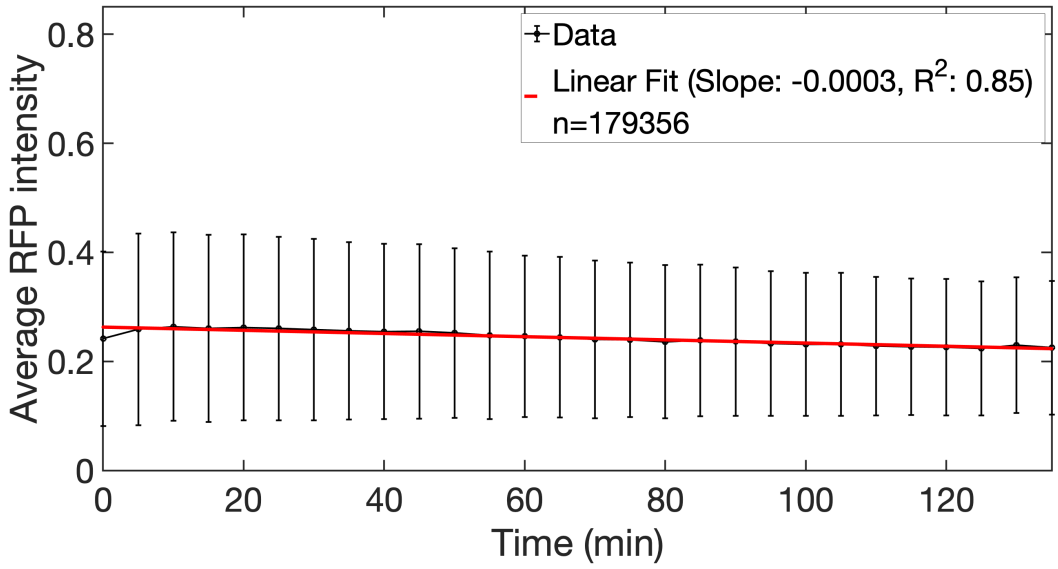


Figure 4.17: Temporal trends in RFP Intensity for cells in microfluidic device.

4.7 Discussion

The results in this chapter illustrate the pipeline for gathering single cell morphological characteristics. Cell radius showed a downward trend while length was mostly consistent. Elongation rate showed an expected lag in the agar pad setup but not in the microfluidic setup.

Dusny et al. [142], also demonstrated consistent specific growth rates of single cells *C. glutamicum* across various setups, a finding paralleled in our study where *E. coli* K12 cells showed constant elongation rates in both microfluidic and agar setups. However, the agar setup exhibited an initial lag phase, consistent with prior research [115] suggesting that the shift from liquid to solid environments can stress bacteria, causing a delay in their growth. This lag phase was absent in the microfluidic setup.

Lastly, the effect of photobleaching in the experimental setup was evaluated. Fluorescent profiling is a critical element in the processing of time-lapse images, especially when

dealing with extended experimental durations. Photobleaching poses a significant challenge in time-lapse imaging of bacteria due to its impact on fluorescent markers. These markers can degrade or lose intensity when exposed to continuous or intense illumination [182], hindering the accurate tracking and observation of bacterial behavior over time [367]. To address photobleaching, the fluorescence intensity and exposure time in our experimental setup were reduced from their initial high levels, as outlined in the Section 4.2.1. Specifically, adjustments were made from settings that typically induced photobleaching to lower levels that maintained signal clarity while minimizing light exposure. This modification effectively minimized photobleaching in our results.

Chapter 5

Spatiotemporal Dynamics of M13 Phage Infection

5.1 Introduction

This chapter employs the time-lapse imaging technique from the previous chapter to explore the dynamics of population phage infection. Beginning with an outline of the phage introduction methods employed, the chapter proceeds to detail the specific materials, methods, and ensuing results.

In previous studies, phages have been introduced into specific environments by various methods, including delivery in suspension [74], encapsulation [569], or co-cultured with bacterial hosts which could imply *in-situ* production [535]. In this study, two methods have been employed to introduce phage: direct phage introduction into the environment and *in-situ* phage production by bacterial cells (see Figure 5.1).

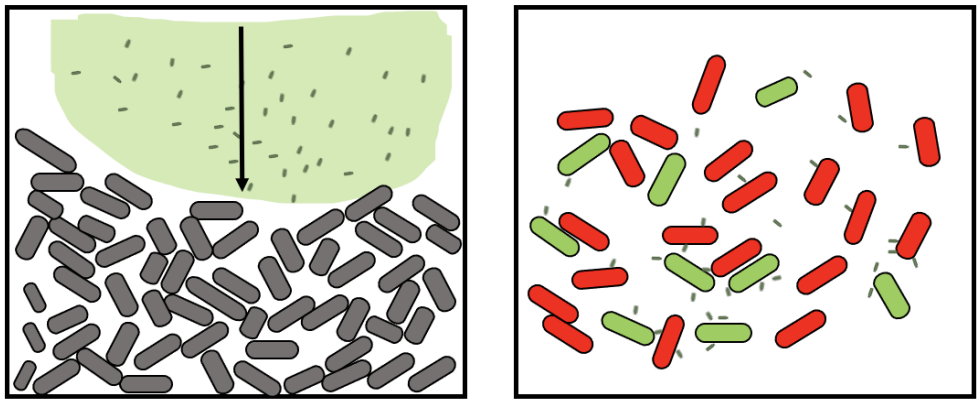


Figure 5.1: The two approaches used in this study to introduce phage to the microbial community, a) Direct phage introduction into the environment. b) *In-situ* production of phage

Direct Application of Phage In this method, phage particles are directly introduced into the environment, replicating scenarios in which phages are intentionally introduced into microbial communities for purposes like biocontrol, bioremediation, and phage therapy.

***In-situ* Production of Phage** This method involves the *in-situ* production of phages by bacterial cells within the environment. In this approach, bacterial cells were engineered to produce phages, representing a scenario where cells act as 'phage factories', continuously releasing phages into their surroundings. This method aligns with natural interactions between phage and bacteria, where phage particles are continuously produced and infect bacterial hosts.

This chapter presents results from experiments under agar pads and in microfluidic devices as growth environments as described in Chapter 4. The study begins by the direct introduction of phages to bacterial cultures that are incapable of producing new virions. This sets a baseline for understanding the initial interaction dynamics between phages and host cells without the complication of phage propagation. Subsequently, the study delves into the *in-situ* production method, where bacterial cells are engineered to produce phages within the microbial community; these are termed "phage producer cells". This approach

simulates a scenario where phages are continuously generated by the bacteria themselves. After assessing results from these two methods, the study circles back to the direct introduction approach, this time, however, with bacterial cells that are capable of producing new virions, allowing for an examination of how self-sustaining phage populations influence infection dynamics. Throughout these experiments, the primary objective is to explore the relationship between the observed morphological features of bacterial cells—namely their radius, length, and elongation rate—and their likelihood of infection by M13 phage.

5.2 Materials and Methods

The bacterial strains, phages, and plasmids used in this chapter are documented in Table 5.1 and Table 5.2. The phage and plasmid constructs were generated using *E. coli* K-12 strains, which served as the host for the production and replication of the phage and plasmid DNA.

Table 5.1: Bacterial strains and phages used in this study

Strain	Genotype	Source
E. coli K12 ER2738	F´proA+B+ lacIq $\Delta(lacZ)$M15 zzf::Tn10(TetR)/ fhuA2 glnV $\Delta(lac-proAB)$ thi-1 $\Delta(hsdS-mcrB)5$	NEB
E. coli K12 mRFP	*E. coli* K12 ER2738, pBR233, mRFP, AmpR	This study
Phage producer	*E. coli* K12 ER2738, pBlueGFP, pM13KO7, AmpR, KmR	This study
	Phages	
M13	Wild type	Gift, Slavcev group
M13KO7	M13, p15a ori, Tn903 (KmR)	NEB
Phagemid-Or	From precursor pBlueScripts II KS(+)	This study
Phagemid-GFP	From precursor pBlueGFP	This study

Table 5.2: Plasmids used in the characterization of phages

Plasmid	Genotype	Source
M13mp18 RF I DNA	M13, lacZ(α)	NEB
pM13KO7	M13, p15a ori, Tn903 (KmR)	NEB
pEB1-mGFPmut2	ProC, mGFPmut2, NeoR/KanR	Addgene 103980
pBlueScripts II KS(+)	wild-type f1 ori, pUC ori, AmpR	Gift, Slavcev's group
pBlueGFP	pBlueScripts II KS(+), mGFPmut2	This study

Buffer and Media The media used in this study, along with their respective recipes, are detailed in Appendix A. ER2738 cells were cultured in Luria Broth (LB) medium specifically formulated for phage propagation. For experiments not involving phages, standard LB medium was employed. SOC liquid medium was selected for the transformation of plasmids. Tris-buffered saline (TBS) was employed for the purification and long-term storage of phages, as detailed in the corresponding methods section.

Culture preparation The *E. coli* K12 ER2738 cells containing the respective plasmids were cultured on LB agar plates supplemented with suitable antibiotics. For each experiment, a fresh colony was cultivated until it reached the early phase of exponential growth ($(OD600 \sim 0.1 - 0.2)$).

5.2.1 Phagemid Construction

In this section, the previously discussed phagemid-based phage system, detailed in Chapter 2.2.2, was used to elucidate the interaction dynamics between bacteriophages and their bacterial hosts. Engineered phages, marked with specific fluorescent tags for easy tracking, were introduced into bacterial populations that display compatible receptors for phage attachment. As outlined in Chapter 2.2.2, these engineered phages are incapable of independent replication and depend on helper plasmids, which supply the essential genes for their life cycle. Additional experiments employed the pBluescript KS(+) phagemid: these constructs are capable of self-replication as plasmids in the absence of a helper plasmid, owing to their distinct origin of replication [23].

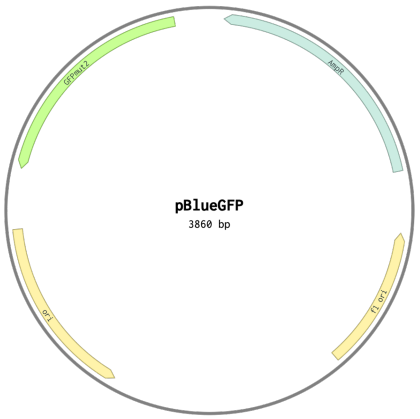
Constructing the phage vector (pBlueGFP) with fluorescent markers involved the following steps (Figure 5.2). In the first step (Figure 5.2a), the plasmid was designed with Benchling (Biology software, 2021). The primers used for the plasmid assembly were synthesized by Integrated DNA Technologies (IDT; Coralville, IA). The PCR amplification

Table 5.3: Primers used in this study

Primer	Template	Sequence (5' - 3')
BS-GFP-f	GFPmut2	GGAACGAccgtaccctaggtctagggc
BS-GFP-r	GFPmut2	GTTTACTCgccctaggtctatgagtggttg
BS-f	pBluescript KS(+)	cctagggcGAGTAAACTTGGTCTGACAGTTACC
BS-r	pBluescript KS(+)	gggtacggTCGTTCCACTGAGCGTCAGAC

process targeted segments incorporating the proC promoter, the GFPmut2 gene, and the rrnB T1 terminator. These segments were sourced from the pEB1-mGFPmut2 plasmid, as outlined by Balleza et al. [42], while also integrating sequences from the pBlueScript II KS(+) vector. The amplification was performed using Phusion High-Fidelity DNA Polymerase (New England Biolabs, Canada), following the guidelines provided by the manufacturer. Detailed primer information is presented in Table 5.3.

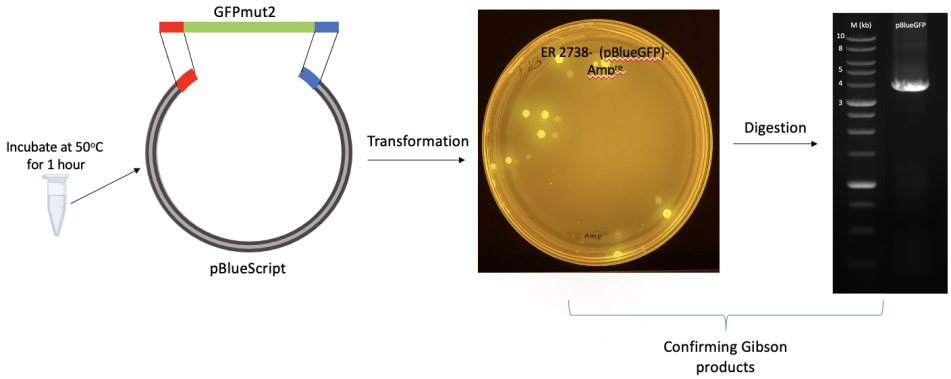
Next, the amplified fragments underwent electrophoresis and gel separation for isolation and purification (Genejet Gel Extraction Kit; Fisher Scientific, Canada), for subsequent Gibson assembly reactions (Figure 5.2b). Finally, Gibson assembly reactions were carried out using the Gibson enzymatic assembly method. The NEBuilder HiFi DNA Assembly Master Mix (New England Biolabs, Canada) was used for Gibson assembly, following the manufacturer's instructions. The resulting Gibson products were then transformed into *E. coli* K12 ER2738 chemical competent cells using a heat shock protocol, as described by Froger et al. [175], (Figure 5.2c). The bacteria were plated on agar containing suitable antibiotics for overnight growth.



(a)



(b)



(c)

Figure 5.2: Preparation of the pBlueGFP phagemid. (a) Step 1. phagemid design; (b) Step 2. Amplification of sequence and electrophoresis; (c) Step 3. Gibson assembly and plasmid transformation. Colonies were examined under blue light to validate the presence of GFP within the bacteria. Additionally, these colonies were cultured and amplified using the same primers as in the previous method to verify that the plasmids retained the desired sequence and size.

5.2.2 Phage amplification and purification

The protocols described next were employed to produce phages with desired characteristics.

M13 phages containing pBlueGFP genome Following the successful transformation of the phagemid into the cells, overnight growth was achieved, and colonies were obtained on the antibiotic-selected media. Subsequently, the following procedure was undertaken to amplify the phage. Initially, a fresh colony of *E. coli* K12 ER2738 containing the phagemid precursor plasmid was cultured in LB media with vigorous agitation (250 rpm) at 37°C until it reached a slightly turbid state ($(OD600 \sim 0.1$). After that, M13KO7 helper phage (New England Biolabs, Canada) at a final concentration of 1 x 10^8 pfu/ml was added, and the culture was further incubated with shaking for 1-2 hours. To maintain selection pressure, kanamycin was introduced into the culture, at a final concentration of 70 µg/ml. The bacterial culture was allowed to grow overnight at 37°C with continuous agitation.

Subsequently, the culture was centrifuged at 4,000 × g for 10 minutes, and the supernatant was transferred to a new tube. Then the resulting supernatant was transferred to a new tube and subjected to filtration using 0.22 µm sterile filter units (Avantor Science Central, Canada) to ensure the removal of any remaining bacterial cells or debris. To concentrate the phage particles, the filtered supernatant was mixed with a 2.5 M NaCl/20% PEG-8000 solution and then incubated at 4°C for 1-2 hours. This step allowed for the precipitation of the phage particles. Subsequently, the phage particles were recovered through a second centrifugation step at 12,000 × g for 15 minutes. The supernatant was decanted, leaving behind the phage pellet. To store the purified phage particles for an extended period, the pellet was resuspended in Tris-buffered saline (TBS); sterile glycerol was added for longer storage.

5.2.3 Phage Quantification

Spot test A spot test was conducted to identify the optimal dilution factor for obtaining a proper number of plaques, falling within the range of 10 to 300 plaques. During this procedure, 200 µL of early log-phase *E. coli* ER2738 cells were mixed with 3 mL of top agar and evenly spread on LB agar plates. Meanwhile, phage lysates underwent serial dilution in 1x TBS buffer. Aerosol-resistant pipette tips are used for dilution to prevent cross-contamination, and a fresh pipette tip was used for each dilution. Then 5 µL of each dilution were carefully spotted onto the top agar. Following an overnight incubation at 37 °C, the plates were examined to pinpoint the specific dilution that resulted in distinct

plaques across the bacterial lawn. The selected dilution was subsequently employed in the plaque assay, facilitating the determination of phage concentration.

Plaque assay A colony of *E. coli* ER2738 cells, cultured on an LB/Tet plate, was used to inoculate 5-10 mL of LB. This culture was incubated with shaking at 250 rpm until it reached the mid-log phase, ($OD600 \sim 0.1 - 0.2$). In parallel, Top Agar was melted and dispensed into sterile culture tubes, with the temperature maintained at 45-50°C. LB plates were pre-warmed to 37°C. The two last dilutions of phage lysates, as identified in the spot plating, were employed to infect the prepared culture. For this purpose, 200 µL of the culture was dispensed into individual microcentrifuge tubes, with one tube assigned per phage dilution. In the infection process, 100 µL of each phage dilution was added to the respective tubes, gently mixed, and allowed to incubate at room temperature for 1-5 minutes.

Subsequently, the infected cells were transferred one at a time to culture tubes containing warm Top Agar. After a brief vortexing to ensure thorough mixing, the culture was promptly poured onto pre-warmed LB plates. To achieve even spreading of the Top Agar, the plates were gently tilted and rotated. Following this step, the plates were left to cool for approximately 5 minutes, after which they were inverted and incubated overnight at 37°C.

Colony counting assay Colony assays were used to assess the infectivity of the phages and their ability to confer antibiotic resistance. Serial dilutions of the phage lysates were prepared in 1xTBS buffer, and 100 µL of early log-phase *E. coli* K12 ER2738 was added to each dilution. After a 30-60 min incubation at 37°C, 5 µL of each dilution was spotted onto LB agar plates supplemented with desired antibiotic. For plates with full growth, the entire dilution volume (200 µl) was spread evenly on the plates. The plates then incubated overnight at 37°C. Colony counts were conducted the following day.

5.2.4 Microscopy

Culture preparation for the microscopy experiments

Culture preparation followed the steps outlined in Section 4.2. Briefly, an inoculum was grown in the phage-specific LB Broth (recipe in Appendix A) until it reached early exponential growth ($OD600 \sim 0.2-0.4$). After centrifugation, the resulting pellet was retained, washed three times with fresh media, and resuspended in 1 ml of fresh media for the agar pad (500 µL for the microfluidic experiments).

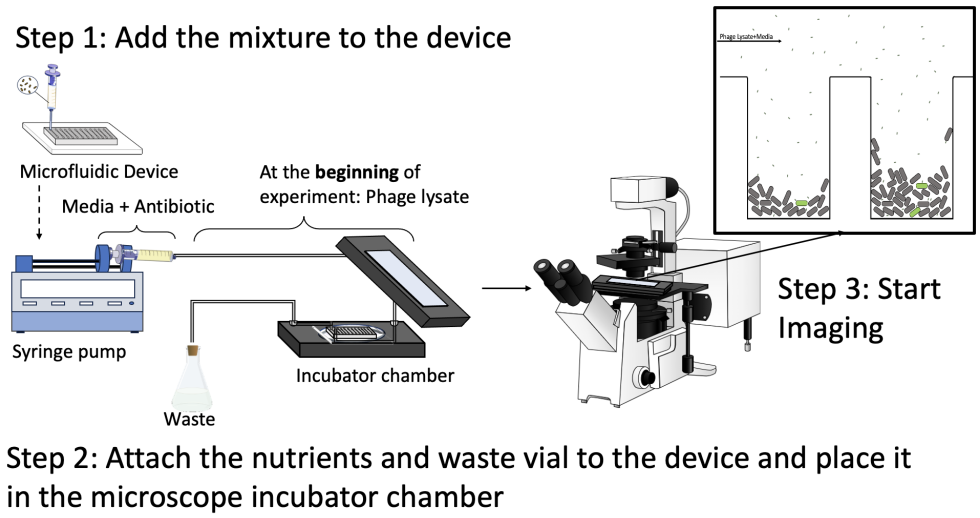


Figure 5.3: Steps required to run the experiment in the microfluidic device with direct Introduction of phage

Direct Introduction of Phage

5.2.5 Agar pad setup

The time-lapse imaging was conducted as detailed in Sections 4.2.2 and 4.2. Initially, a 500 µL aliquot of phage lysate was gently mixed with the prepared cell mixture described earlier. Then, 2µL of this mixture was dispensed into a dish with a coverslip bottom, followed by the placement of a thin agar pad layer on top. To minimize evaporation during the experiment, the dish's lid was sealed with parafilm tape. The prepared dish was then positioned in a temperature-controlled microscope chamber, maintained at 37°C.

Microfluidic Setup In this approach, after loading the cells into the device, the device was placed inside the microfluidic chamber, and the chambers to be imaged were selected. Approximately 0.5-1 µL of the phage lysate was loaded into the tube connected to the nutrient syringe. This step was taken to ensure a direct flow of phage into the device without the introduction of any potential bubbles or contamination resulting from changing the syringe source. No lysate was included in the syringe, which was filled with fresh media.

The phage lysate was loaded into the tube. Once the phage was loaded and the vial connected to the microfluidic device, the pump was activated. After activation by the syringe pump, it took approximately 30 minutes for all of the phages in the tube to enter

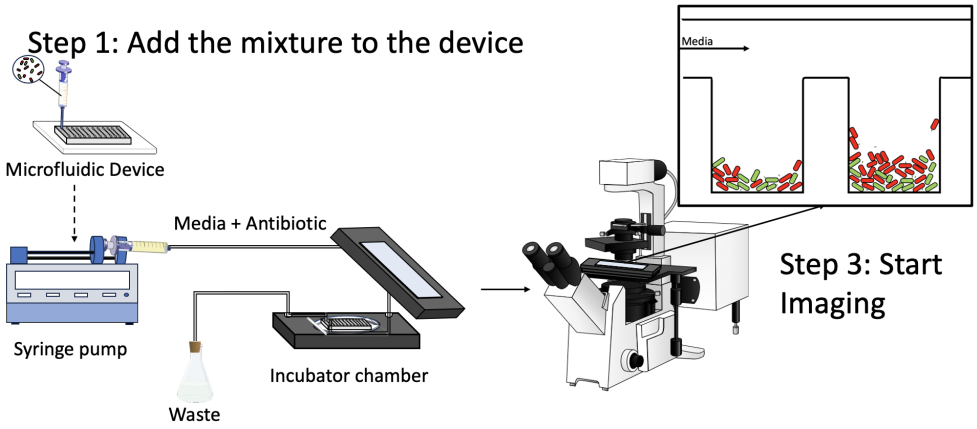


Figure 5.4: Steps required to run the experiment in the microfluidic device for cell to cell approach

the device (this time was experimentally determined; we neglect phage that may have diffused back into the nutrient syringe). Imaging began immediately to ensure real-time observation. The phage solution continued to circulate within the device for approximately 3-4 hours until the entire volume of phage supernatant was used, after which only the nutrient media was pumped through the system.

In-situ Introduction of phage

For this approach, two cell types were employed: host cells, which lack the capacity to generate new virions even after infection, and another culture consisting of cells that can produce new phages, referred to as 'phage producer cells'. For specific details on the strains, refer to Table 5.1. After washing these cell types separately, they were mixed and then introduced into a petri dish, subsequently covered with a thin layer of agar pad, or loaded into the microfluidic device, as depicted in Figure 5.4. The experiment was initiated with a slight delay of 5-10 minutes. This delay allowed for the positioning of the device under the microscope and the selection of imaging positions.

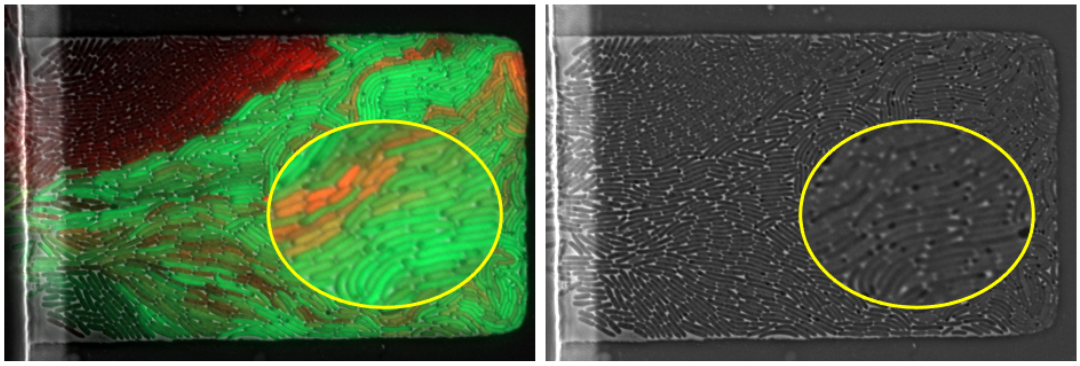


Figure 5.5: Comparing fluorescent images with phase contrast image. Fluorescent images allow for distinctly delineating cell boundaries during the segmentation process.

5.2.6 Image Segmentation and Data analysis

The image segmentation process in this chapter follows the same protocol outlined in Section 4.3, with additional steps to account for infection states.

In-situ Introduction of Phage

Fluorescent markers were incorporated into all cells used in this study to differentiate cell types during image processing. This feature also facilitated tracking of individual cells, as shown in Figure 5.5.

MATLAB data analysis

In Section 4.4, the MATLAB script used for analyzing microscopy data in this study was detailed. This script includes additional parameters specifically for assessing phage infections. Following the methodology outlined in Section 5.2.1, the M13 phage genome was engineered to express GFP within host cells upon infection, thus enabling clear differentiation between infected and non-infected cells. A specific GFP intensity threshold was established to identify newly infected cells, using the CellProfiler software. CellProfiler measures fluorescence intensity by quantifying the pixel intensity across the cell's area in digital images [497]. This was based on the minimal GFP signal identified in infected cells, calculated as the mean fluorescence intensity. This calculation helps to distinguish genuine GFP expression from autofluorescence or background noise. The robustness of the results in this chapter to variations in this threshold is documented in Appendix F.

Each cell object was categorized as follows:

1. **Infected**: Cell objects exhibiting a green fluorescent signal above the established threshold, indicative of phage infection. Additionally, as described below, temporal analysis was employed to trace the onset of infection, identifying cells as infected prior to the visible appearance of the GFP signal.
2. **Not Infected**: Cell objects that show no above-threshold green fluorescent signal.
3. **Phage Producer**: Cell objects that exhibit a GFP signal and are capable of producing new virions, characterized by the presence of both the helper plasmid and phagemid.

Figure 5.6 demonstrates a cell lineage affected by infection. Similar to the tree depicted in Figure 4.12, this lineage tree was constructed following the methodology outlined in Section 4.3.1.

Below, additional features implemented for each cell object in this analysis are discussed, aligning with the data processing approach outlined in Chapter 4. These features were not uniformly added across all cell types but were crucial for tracking the phage infection process:

1. **Infection label**: Each cell was assigned a lineage label from the three categories listed above. 'Infected' was extended back in time 25 minutes from the first appearance of above-threshold GFP signal as a consequence of the analysis in Section 5.3.2.

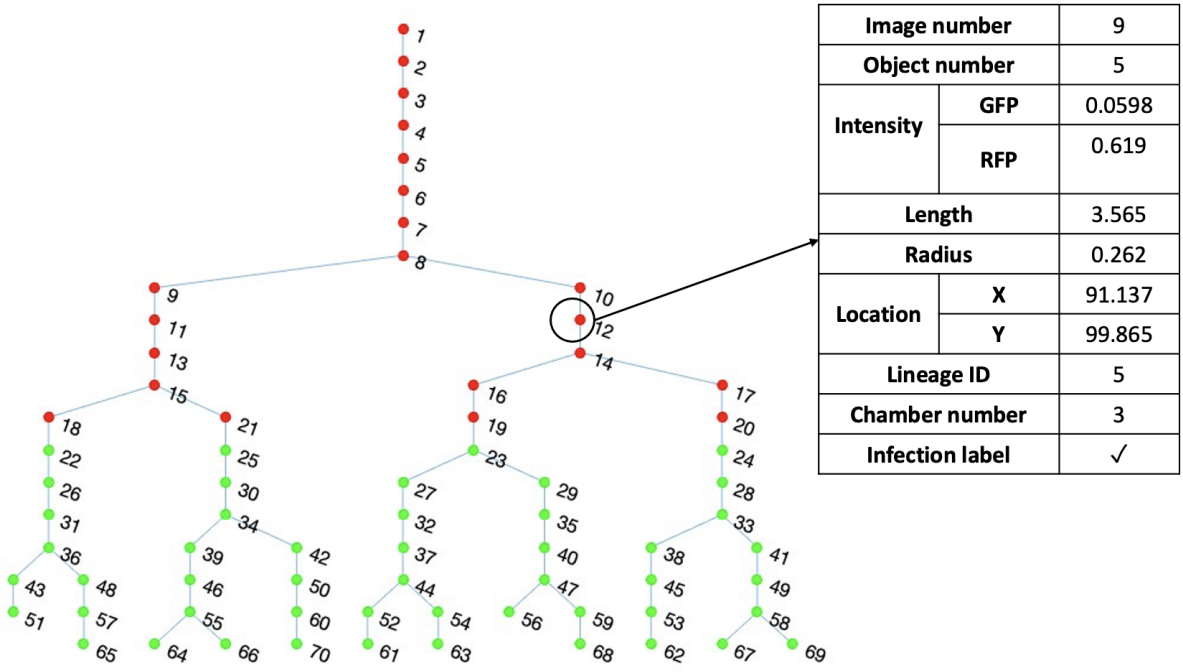


Figure 5.6: This lineage tree illustrates the progression of cells that underwent infection during the experiment. Initially, host cells contain a red fluorescent protein (RFP) plasmid, represented in red on the tree, indicating their uninfected state. Upon infection by the phage, which carries a green fluorescent protein (GFP) gene, these cells commence expressing GFP, depicted in green, signifying an infected status. This color-coding directly corresponds to the real fluorescent signals observed. Consistent with descriptions in Chapter 4, each node within the tree is uniquely indexed, denoted by numbers for easy reference.

2. **Cell morphology at the inferred time of infection**: Following the methodologies described in Chapter 4, this records the cell length, radius, and elongation rate at the inferred time of infection.

3. **Distance from phage producer population (for '*In-situ* production of phage' experiments only)**: Two complementary measure of proximity are recorded:

    a) The minimum distance to a phage producer cell object is determined based on cell object centroids.

b) An aggregate proximity from all phage producer cell objects is determined as:

$$\text{Aggregate Proximity} = \sum_{i=1}^{n} e^{-\text{Distance}_i}$$

where the sum is taken over all Phage Producer Cell objects in the frame. Nearby cell objects have a greater influence (higher weight) on the aggregate proximity, while cells that are farther away will have a smaller influence (lower weight) due to the exponential decay with distance.

5.3 Results and Discussion

5.3.1 Quantification and Infectivity Assessment of Engineered Phages

Figure 5.7 shows the results of all three quantification assay. The quantification processes determined the concentration of the phage lysate to be 1.6 x 10^8 pfu/ml. Subsequently, these customized phages were utilized in our microscopy experiments to monitor their behavior within bacterial cultures.

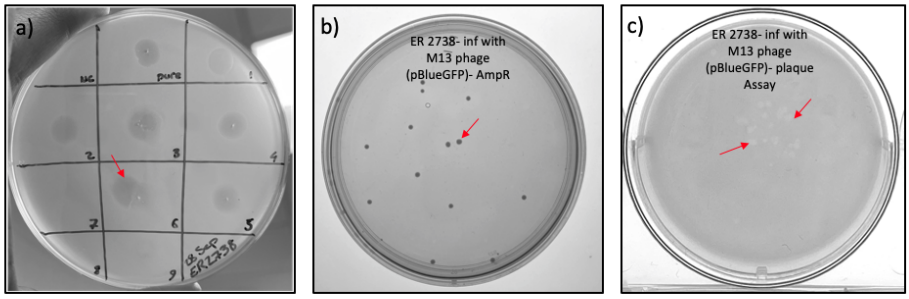


Figure 5.7: Phage Quantification results. a) Results of Spot test. 6th dilution is last dilution showing infection b) Colony counting assay results c) Plaque assay results.

5.3.2 Direct Introduction of phage

The protocols for the agar pad and microfluidic setups have been comprehensively detailed in sections 4.2.2 and 4.2, respectively. In this section, a concise summary of the microscopy setups employed for each of these methods is provided and the corresponding results are presented.

Agar Pad Setup

Detailed experimental conditions and parameters can be seen in Table 5.4.

Table 5.4: Experiment summary: Direct phage introduction, agar pad growth conditions

Imaging Duration (min)		Positions		Exposure Channel		
Total Time	**Time Interval (min)**	**Field Dimensions (µm x µm)**	**Position Index**	**Phase**	**RFP**	**GFP**
100	2	702.91 x 957.29	6	✓	-	✓

Microscopy imaging for the microfluidic setups, as outlined in Section 4.2, commenced following the introduction of phage lysate into devices pre-loaded with bacterial cells. A summary of these experiments is shown in Table 5.5.

Table 5.5: Direct introduction of phage experiment information

Experiment number	Imaging (min)		Chamber		Exposure Channel		
	Duration	**Interval**	**Dimensions (µm x µm)**	**Number**	**Phase**	**RFP**	**GFP**
1	170	15	178.55 x 81.20	23	✓	-	✓
2	170	5	144.23 x 40.94	13	✓	-	✓
3	170	5	124.22 x 78.63	19	✓	✓	✓

The results displayed below represent averages taken across all replicated experiments and imaging positions. For 'Experiment 1', a lower imaging frequency was employed due to its status as the initial attempt to capture phage infection after previous attempts had failed. This conservative approach aimed to mitigate photobleaching by extending the time intervals between each imaging session. Following the successful observation of phage infection in this initial experiment, the imaging frequency was subsequently increased for the later experiments.

Timing of GFP Detection

Figure 5.8 shows the distribution timing for GFP appearing above-threshold for direct phage introduction in each experimental environment. Simultaneous infection events were

not observed in the agar pad environment. On the other hand, as shown in Figure 5.8B, the microfluidic device experiments (Figure 5.8B) demonstrated a more clustered appearance of GFP signals around the 40-50 minute mark post phage introduction. We hypothesize that the infections happened near time zero (because the phage introduction was completed by time 30 minute). This 40-50 minutes delay between introduction and GFP signal appearance is a combination of the times required for phage infection dynamics (host recognition, receptor attachment, genome insertion, genome replication) followed by 5.6-10 minutes for GFPmut2 to mature [42].

To simplify the analysis, we assumed 25 minutes as the time delay from infection to GFP signal appearance. Sensitivity analysis (Appendix G) indicates that the assumption of a 35, 40, or 45 minute produces near-identical results.

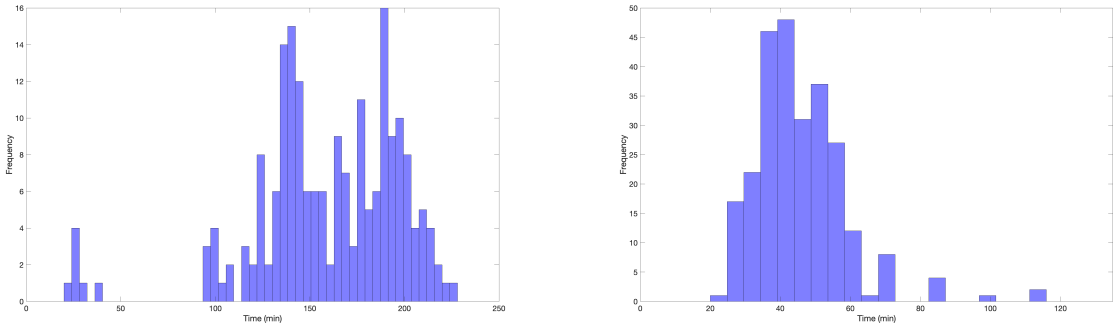


Figure 5.8: Distribution of above-threshold GFP signal appearance timing for direct phage introduction A: agar pad, B: microfluidic device. From the results in (B) we inferred a 25 minutes delay from infection to above-threshold GFP signal appearance.

5.3.3 Microfluidic device: Distribution of Infection Events

Drawing from the seeding density results in Section 4.6, where no observable correlation was found between chamber position and cell density, it was hypothesized that chamber location should not impact the distribution of infection events. The data presented in Figure 5.9 confirms this hypothesis.

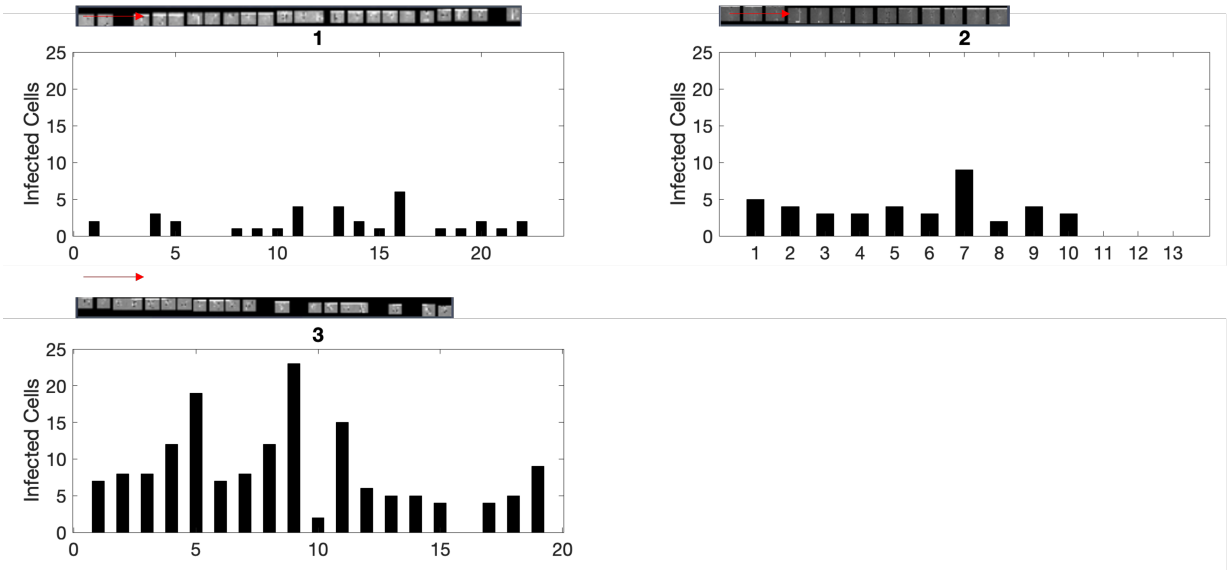


Figure 5.9: Distribution of Infection Events in Experimental Chambers: Plots show the number of infection events that occurred within each chamber. On the top left of each plot, an image displays the placement of the chambers; the red arrow indicates the direction of flow.

The relationship between initial cell density in a chamber and the subsequent rate of phage infection (at the presumed constant concentration of phage) is shown in Figure 5.10: an inverse correlation between cell density and infection probability.

These findings highlight the role that cell density plays in the dynamics of phage infection within microfluidic environments. The data suggest that the probability of infection per cell is influenced by cell density, aligning with the principles of multiplicity of infection (MOI)[1]. Measuring the MOI directly within the microfluidic device was challenging due to the difficulty in quantifying the exact number of phages within the chambers. However, assuming that the initial concentration of phages flowing into the device remains constant, the MOI would depend on the number of host cells present. This means that with fewer cells, the phages available per cell increase, thereby raising the infection likelihood per cell. Figure 5.10 demonstrate this relationship, showing how cell density inversely affects the probability of infection per cell.

[1]MOI quantifies the number of infectious agents per cell and plays a significant role in determining infection outcomes and rates within a given population of cells or organisms

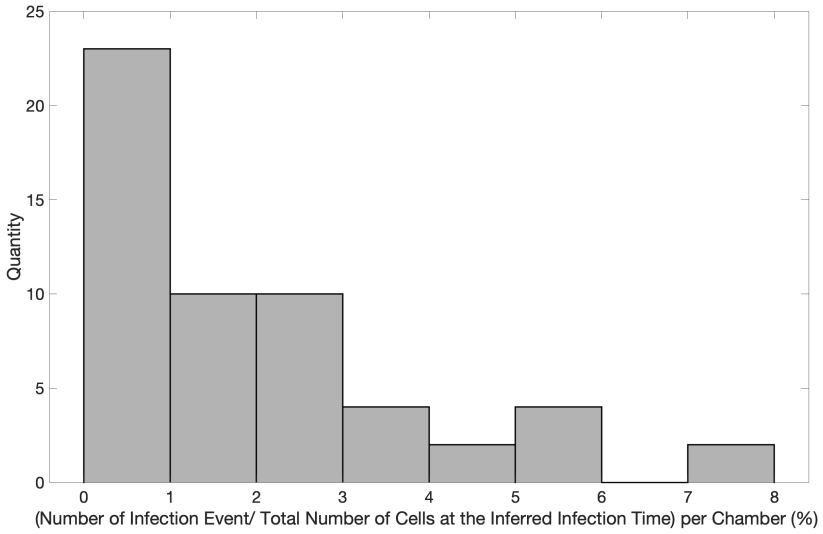


Figure 5.10: Histogram plot for Number of Infection event over total number of cells presents in the chamber at the inferred time of infection.

To explore whether phage particles were uniformly distributed throughout the chambers, particularly regarding their penetration across the full depth of each chamber, we examined the spatial distribution of infection events (with respect to depth). Figure 5.11 illustrates these infection events relative to the depth within each chamber. The lack of a pronounced trend in this spatial distribution supports the hypothesis that the phage particles are evenly distributed throughout the chamber.

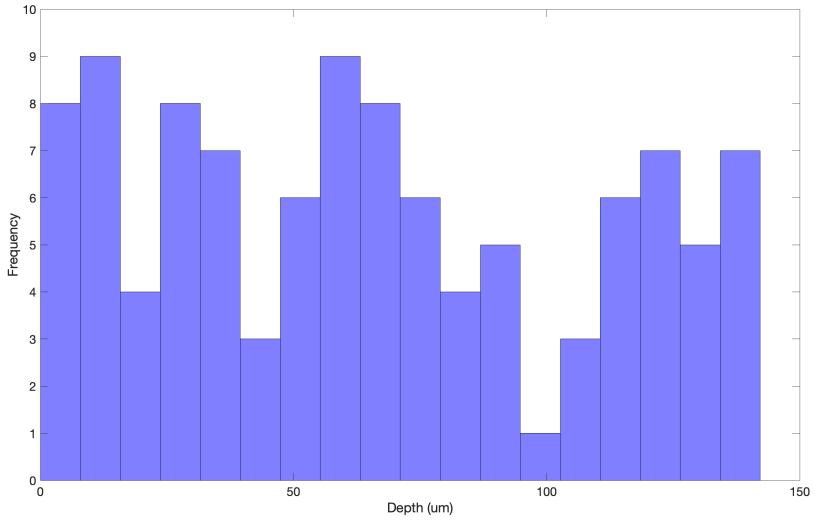


Figure 5.11: Spatial distribution of infection events within the chambers at the time of infection.

5.3.4 Distribution of phage infection events across cell states

This section presents analysis of cell elongation rate, length, and radius at the time of infection. T-tests were employed to assess statistical distinctions between different conditions [308]. The significance levels in the results are denoted as follows: not significant for $p \geq 0.05$ (ns), marginally significant for $0.01 < p < 0.05$ (*), moderately significant for $0.001 < p < 0.01$ (**), highly significant for $0.0001 < p < 0.001$ (***), and extremely significant for $p < 0.0001$ (****). Error bars, corresponding to standard deviations, signify the variability within the data.

Radius Figure 5.12 (a-d) illustrates the distribution of cell radius at the inferred time of infection.

Panels e and f indicate a significant difference in radius between cell objects involved in infection events compared to those that are not. Larger cell radii correlate with infection events. The consistency of these results across both systems underscores the reliability of the findings.

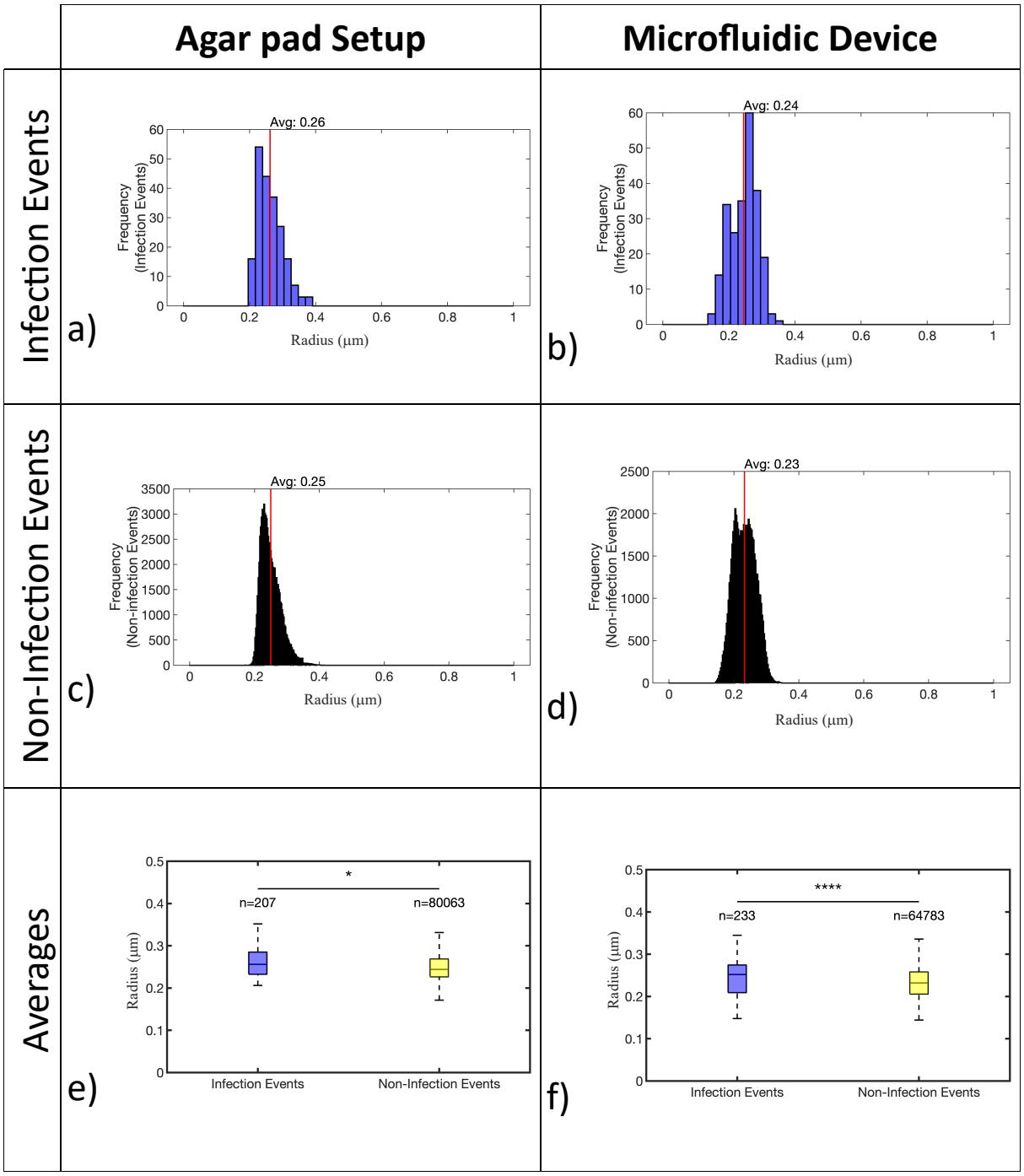


Figure 5.12: a) to d) distribution of cell radius a) and b) infection events in agar pad and microfluidic setups, and c) and d) cell-objects that were not involved in infection events. e) and f) average cell radius for infection events, and non-infection events. T-test significance is shown. Error bars represent standard deviations as described in the main text. n-values represent populations.

Length Figure 5.13 displays cell length distribution. Infection event were consistently observed in cells that were lengthier.

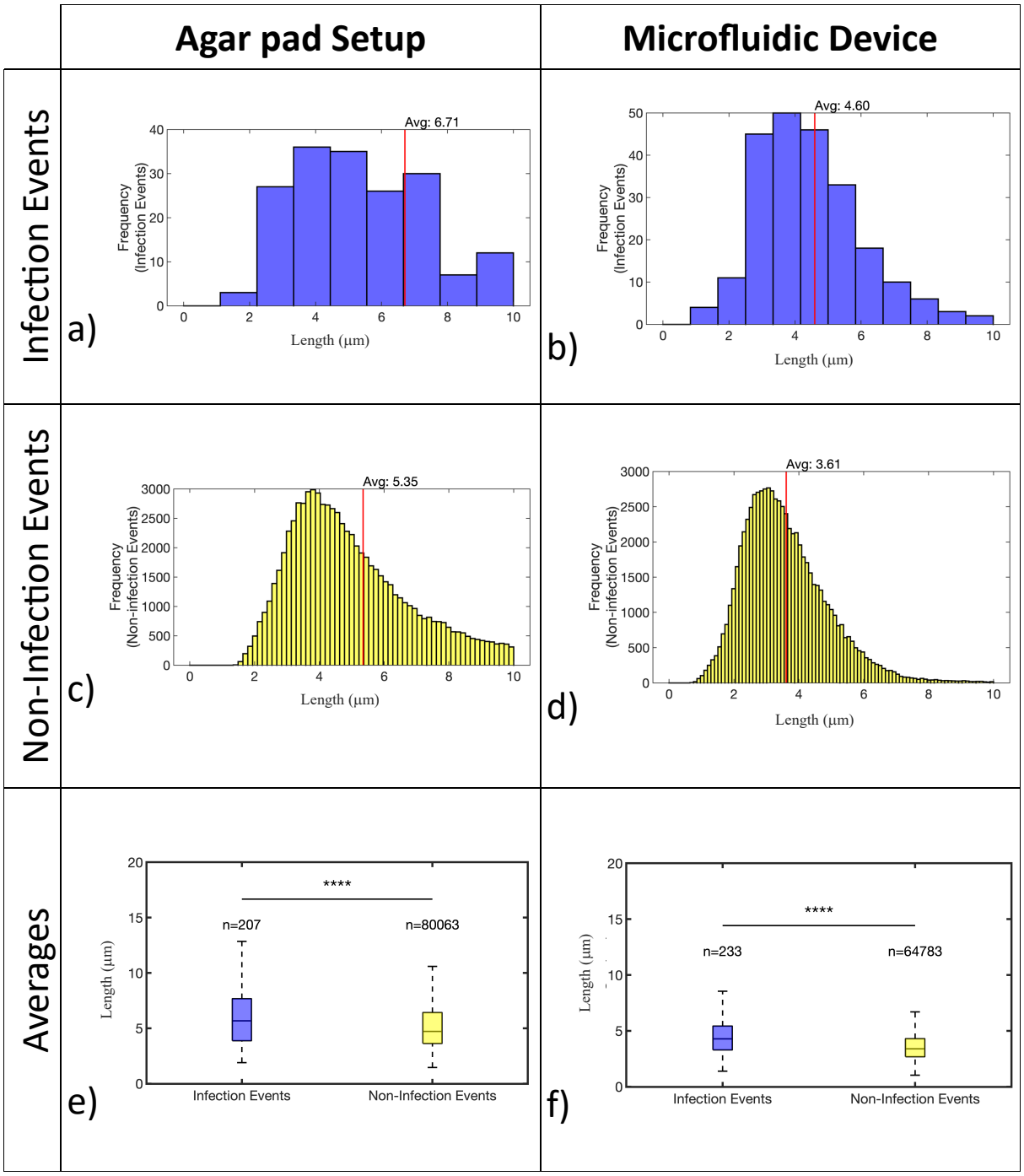


Figure 5.13: a) to d) Distribution of cell length. a) and b) infection events in agar pad and microfluidic setups,and c) and d) cell-objects that were not involved in infection events. e) and f) average cell length for infection events, and non-infection events. T-test significance is shown. Error bars represent standard deviations as described in the main text. n-values represent populations.

Elongation rate Figure 5.14 shows the elongation rate distribution. It can be seen that, cells at the inferred time of infection exhibited significantly higher elongation rates when compared to their non-infected counterparts. This trend was consistent for both the comparison between microfluidic device and agar experiments.

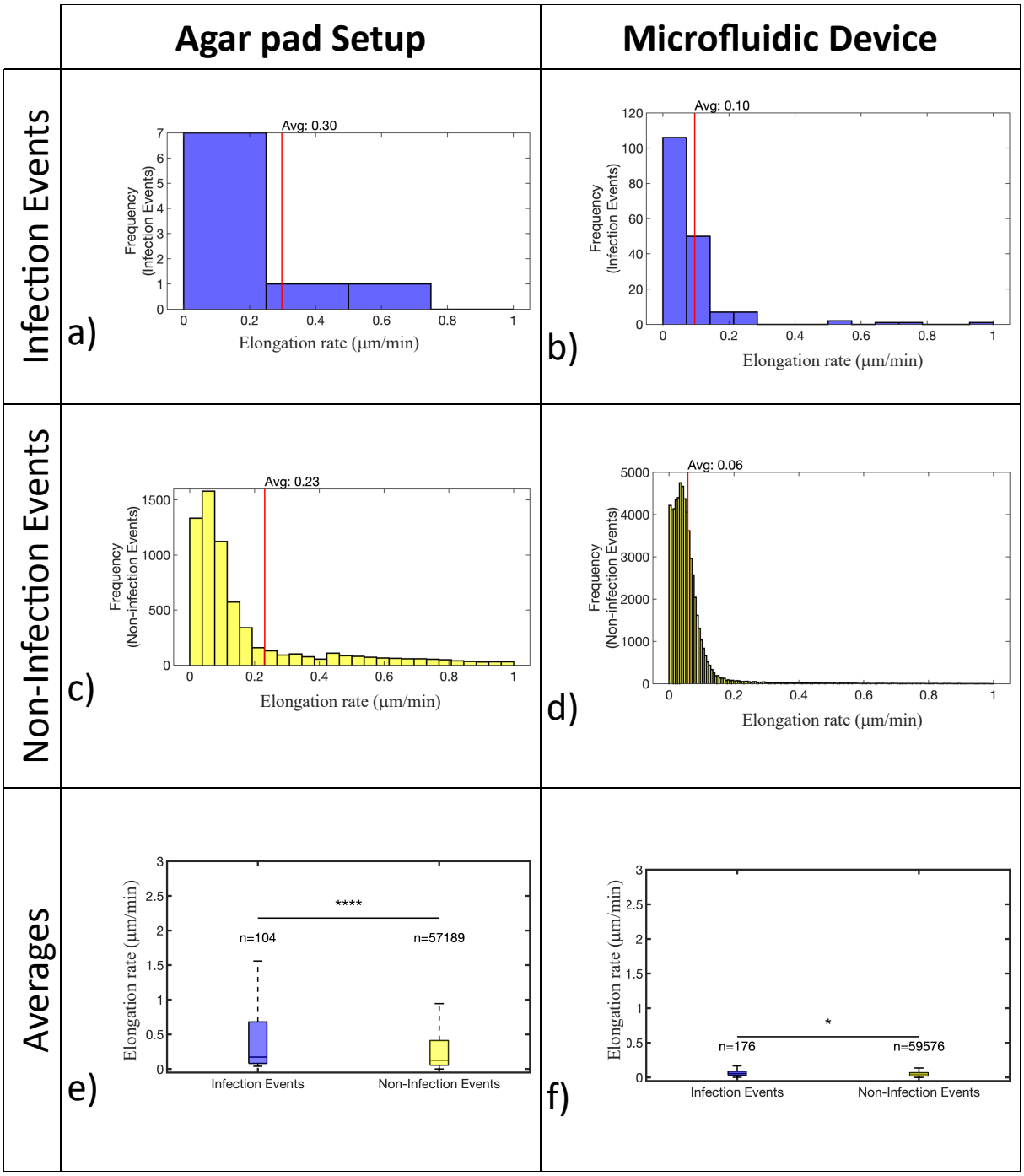


Figure 5.14: a) to d) distribution of elongation rate at the inferred moment of infection. a) and b) infection events in agar pad and microfluidic setups,and c) and d) cell-objects at the same time-point as (a)-(b) but in cell objects that were not involved in infection events. e) and f) illustrate the average cell elongation rate for both infected and non-infected cell objects, respectively, with t-test significance indicated. Error bars denote standard deviations, as detailed in the main text. The sample sizes (n-values) represent the populations of the cells examined.

Discussion

While the initiation of phage infection relies on the recognition of a specific surface receptor on the host cell, the influence of changes in host physiology on the cell's likelihood of infection remains an underexplored facet in phage biology [126]. Therefore in the current research we aimed to explore how specific bacterial morphological traits, namely length, radius, and elongation rate, impact the infection process of the M13 bacteriophage.

We found correlation between number of cells presented in the chambers and number of infection event observed in that chamber.

Consistent with previous research, studies like Kasman et al. (2002) have shown that the rate of phage infection can be dependent on host cell density [273]. However, this relationship holds true under specific, controlled conditions, which were not fully replicated in our study. Here, we observed that increasing the concentration of phage lysate did not yield the expected increase in infection rates. Consequently, elevating the multiplicity of infection (MOI) by increasing the phage concentration was not effective. This finding aligns with the research conducted by Tzagoloff et al. [518], which demonstrated that even with increased phage-to-cell ratios, a significant number of phages remained unattached. This suggests that host cells have a very limited capacity for M13 adsorption. Specifically, Tzagoloff et al. observed that the proportion of phage adsorbed was maximal at lower phage-to-cell input ratios (0.007 and 0.7) but markedly lower at higher ratios (3.5 and 7.0), indicating that simply increasing the phage concentration does not proportionally increase the adsorption efficiency [518].

Nevertheless, the primary aim of this study was to gain insights into the infection mechanism and cellular behavior at the time of infection, and in this context, precise control of the MOI was less critical. However, future research could benefit significantly from the ability to precisely control the MOI across the entire device and within each individual chamber.

Kasman et al. [273] identified four key factors dictating bacterial infection or transduction by phages: host cell density, the adsorption constant of phages, phage quantity, and the duration of their interaction. Their research highlighted that even after an average 30-minute adsorption period, a considerable number of phages remain unbound, primarily contingent on the concentration of susceptible cells [273]. This underscores the critical importance of comprehending cell susceptibility and its determinants in relation to interactions with phages.

We evaluated the correlation between cell morphology and infection frequency, discovering a direct relationship between cell size and the rate of infection. Notably, cells with larger radii and greater lengths exhibited a higher frequency of infection. These findings

align with Delbrück's data, which also indicated a higher phage adsorption constant linked cells morphological features like larger cell size [125].

The influence of host cell size on phage dynamics has been previously studied in the context of phage T4 by Hadas et al [210]. They found that larger cells, fostered in enriched media, exhibit accelerated growth due to increased protein-synthesizing system content, leading to a more rapid phage production [210]. Additionally, larger cells produced more receptors on their surface, which enhanced phage adsorption [384]. However, M13 phages, which we used in our study, employ a different attachment mechanism than T-even phages, primarily binding to the tips of F pili.

The variation in our results led us to consider two potential hypotheses. Firstly, the concept that larger cells, due to their increased surface area, might offer more points for phage interaction and thereby elevate the likelihood of infection [10], has been previously explored in the context of various phages, informing models of phage-host interactions [85]. Secondly, the larger size of cells could potentially lead to a more frequent extension and presence of F-pili per unit area, offering more potential sites for phage attachment. However, this latter hypothesis lacks support from the literature, leaving an avenue for future exploration and analysis. The study of F-pili highlights variations in the number of pili per cell, significantly impacting phage adsorption rates. Tzagoloff and Pratt observed that Hfr and F+ strains typically possess two to three F-pili [518], whereas Caro showcased Hfr strains with a striking 30 F-pili per cell, significantly increasing attachment sites [87]. This variance in F-pilus number can significantly affect the penetration of phage DNA into cells [273]. Additionally, the number of pili produced in each cell is contingent on the cell's growth rate, typically peaking during the bacterial exponential phase and diminishing in the stationary phase [521]. Therefore, the growth rate of host cells also influences their infection rate, as studies have shown an increased infection rate in cells generated during the logarithmic growth phase [441]. Moreover, Tzagoloff and Pratt highlighted that the phage adsorption rate to cells is contingent on the length of F-pili, which can vary depending on the cells' growth rate [518]. Typically, maximum piliation occurs toward the end of the exponential growth phase, suggesting cells produce more pili in enriched mediums [87, 73]. Caro et al. [87] observed this phenomenon in M9 medium, while Brinton et al. [73] reported similar results in tryptone-yeast extract-glucose medium. Further studies could potentitally shed additional light on these results.

Despite advances in understanding phage genetic control over host metabolism, data on metabolic changes from phage infection are limited [123]. Studies have shown that increased bacterial metabolism can lead to higher phage infection rates due to several interrelated factors:

1. **Enhanced Nutrient Uptake and Utilization:** Higher metabolic rates result in

increased uptake and utilization of nutrients, which supports rapid bacterial growth and replication. Phages exploit this heightened metabolic activity to facilitate their own replication within the host cells [552].

2. **Altered Cellular Physiology:** Increased metabolism can lead to changes in cellular physiology that make the host cells more susceptible to phage attachment and entry. For instance, membrane fluidity and receptor availability may be enhanced, facilitating phage adsorption [163].

3. **Energy Availability:** High metabolic activity ensures a readily available energy supply (ATP), which phages can hijack to power the processes of phage DNA replication, protein synthesis, and assembly of new virions [215].

Next in the analysis we investigated the effect of cell elongation rates on infection events. Elongation rate, which is the change of length over time, offers a more precise understanding of bacterial growth dynamics compared to growth rate measurement. Research has shown that slower or halted bacterial growth could result in smaller cells, potentially affecting adsorption rates, either slowing them down or reducing them [10, 210, 474].

The majority of previous studies on the impact of bacteria growth rate on phage adsorption were conducted at the population level. For instance, studies by Hadas et al., showcased increased T4 adsorption rates with higher growth rates in richer media. However, contrasting findings by Golec et al., suggested that bacterial growth rate had no significant impact on T4 adsorption in chemostat cultures [384, 210, 191]. Additionally, Sivec et al., demonstrated an increase in adsorption correlating with a specific growth rate increment [587]. These varying outcomes might arise from analyzing population behavior while overlooking the heterogeneity among identical cells within the population [121]. So in this study, using a single-cell analysis, we evaluated the relation of infection event and elongation rate within *E.coli* cell and M13 phage. Our investigation revealed that cells with higher elongation rates are more prone to infection, aligning with previously mentioned research at the population level.

Conclusion

The study's results consistently indicated that infected cells exhibited higher elongation rates, increased length, and larger radius at the time of infection.

5.3.5 *In-situ* production of phage

The *in-situ* protocol begins with the two cultures detailed in Section 5.2.4 introduced into the experimental configurations, namely the agar pad (Section 4.2.2) and microfluidic devices (Section 4.2).

In this section, we present results on measured elongation rates, cell length, and radius at the inferred time of infection to compare against previous findings outlined in Section 5.3.2. In addition, data is presented on the proximity from phage producer cells on the infection process.

Agar pad Setup

The relevant experimental details used in this part are summarized in Table 5.6.

Table 5.6: '*In-situ* production of phage' experiment Information for agar pad setup

Imaging (min)		**Position**		**Exposure Channel**		
Duration	**Interval**	**Dimensions (µm x µm)**	**Number**	**Phase**	**RFP**	**GFP**
250	10	702.91 x 957.29	24	✓	✓	✓

Microfluidic device

The experimental setup was established as detailed in the section 5.2.4. An outline of the setup utilized in this part is presented in Table 5.7.

Table 5.7: '*In-situ* production of phage' experiment Information for Microfluidic Devices

Experiment number	**Imaging (min)**		**Chamber**		**Exposure Channel**		
	Duration	**Interval**	**Dimensions (µm x µm)**	**Number**	**Phase**	**RFP**	**GFP**
1	250	10	178.55 x 81.32	21	✓	✓	✓
2	250	10	94.32 x 64.65	16	✓	✓	✓
3	250	5	74.89 x 40.01	19	✓	✓	✓
4	250	10	52.99 x 39.07	23	✓	✓	✓

5.3.6 Results

Distribution of phage infection events across cell states

Radius Figure 5.16 showcases the cell radius distribution. Similar to the prior 'Direct Introduction of Phage' method in section 5.3.2, larger cell radius consistently indicated higher chance of infection.

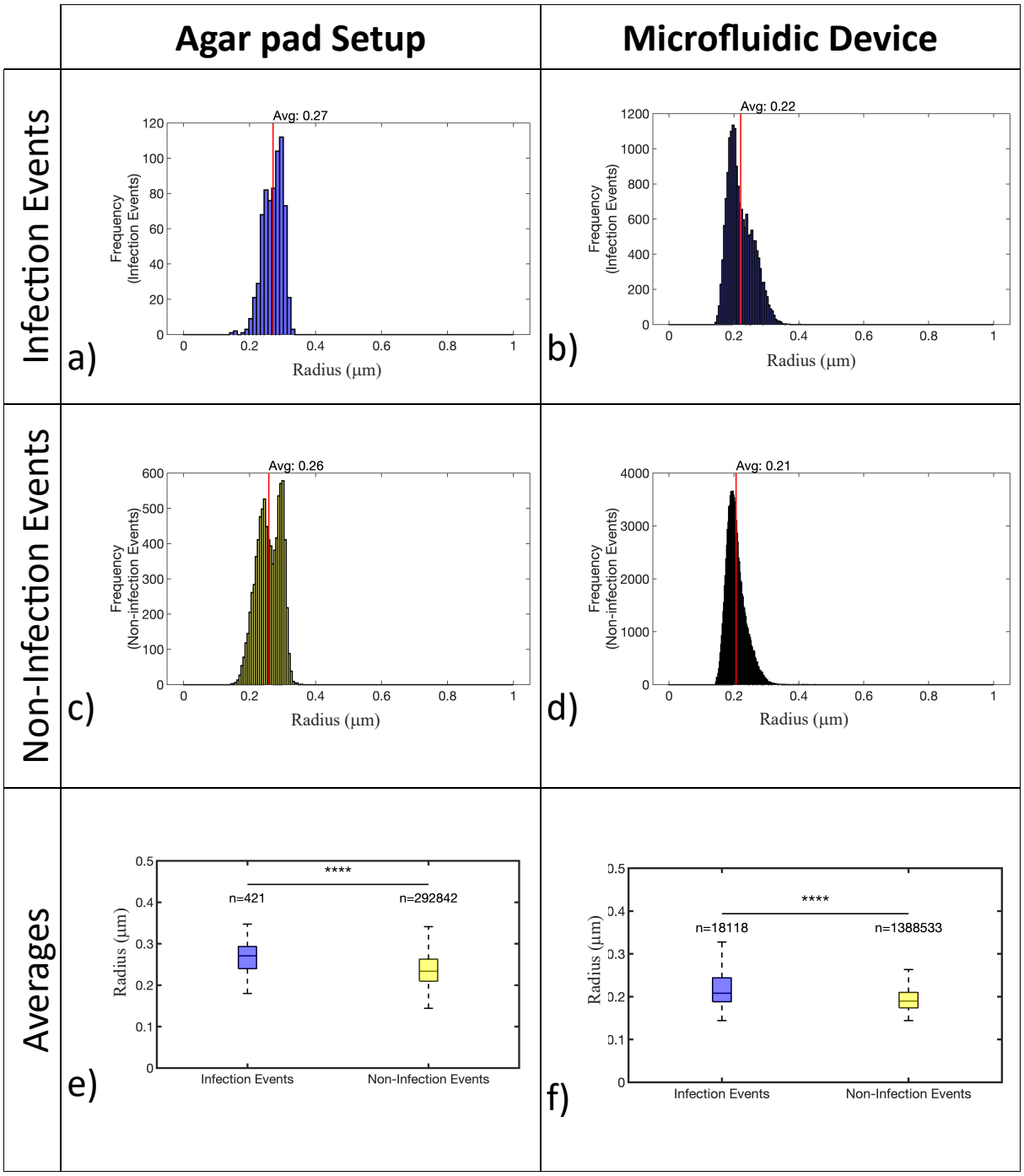


Figure 5.15: a) to d) distribution of cell radius. a) and b) infection events in agar pad and microfluidic setups,and c) and d) cell-objects that were not involved in infection events. e) and f) average cell radius for infection events, and non-infection events. T-test significance is shown. Error bars represent standard deviations as described in the main text. n-values representing the populations of the cells.

Length In Figure 5.16, the distribution of cell length at the inferred time of infection is presented. It indicates that cells with greater lengths are more vulnerable to infection, aligning with the observations from Section 5.3.2, Figure 5.13. This consistency across findings highlights the correlation between cell size, specifically length, and the likelihood of infection, confirming this pattern across different sections and figures within the study.

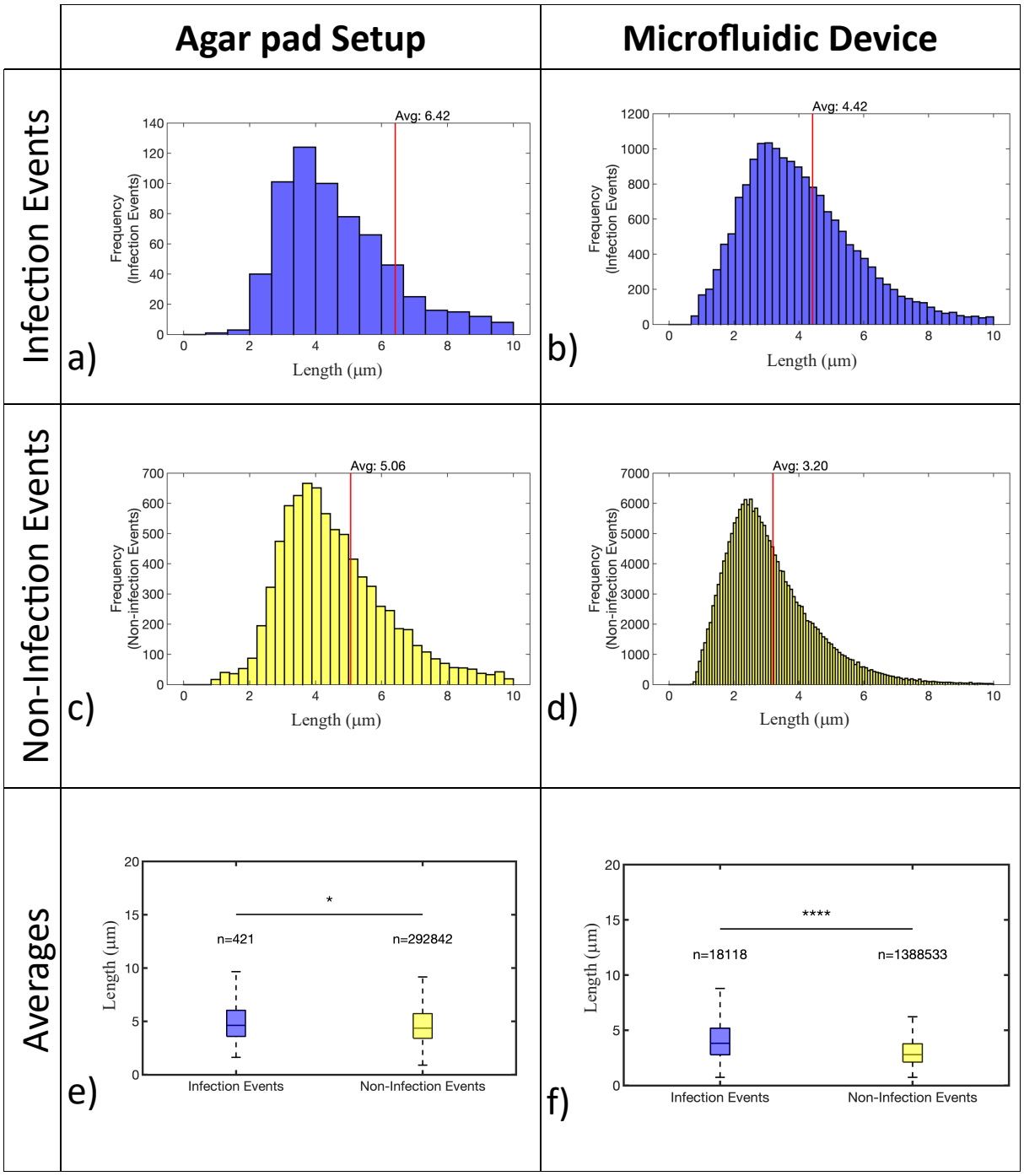


Figure 5.16: a) to d) Distribution of cell length. a) and b) infection events in agar pad and microfluidic setups,and c) and d) cell-objects that were not involved in infection events. e) and f) average cell length for infection events, and non-infection events. T-test significance is shown. Error bars represent standard deviations as described in the main text. n-vlaues representing the populations of the cells.

Elongation rate Figure 5.17 displays the distribution of elongation rates. These results exhibit a similar trend to the section 5.3.2 as in Figure 5.14, indicating that cells with higher elongation rates exhibited a higher chance of infection compared to their non-infected counterparts.

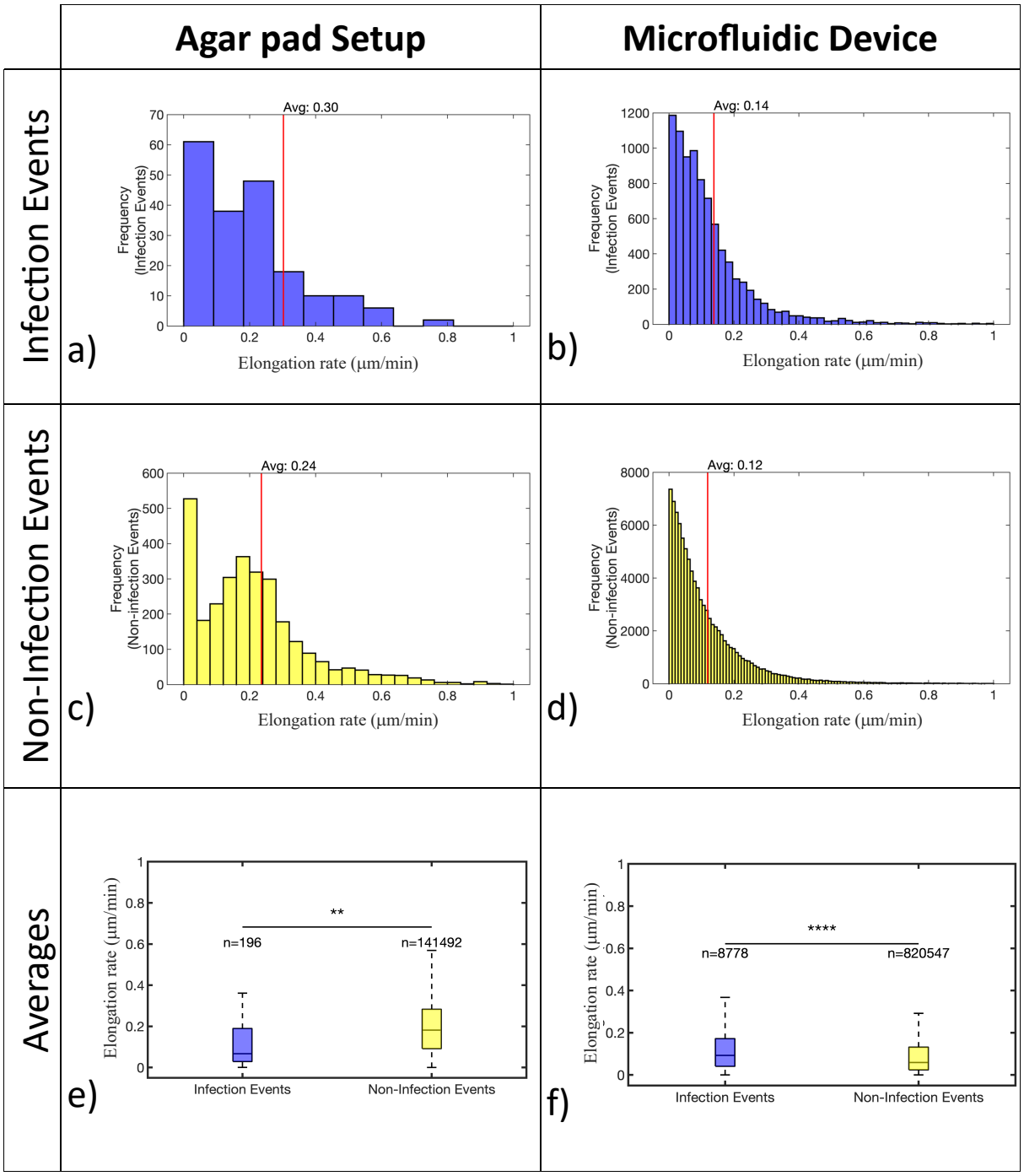


Figure 5.17: a) to d) distribution of elongation rates. a) and b) infection events in agar pad and microfluidic setups,and c) and d) cell-objects that were not involved in infection events. e) and f) illustrate the average cell elongation rate for both infected and non-infected cell objects, respectively, with t-test significance indicated. Error bars denote standard deviations, as detailed in the main text. The sample sizes (n-values) represent the populations of the cells examined.

Minimum distance Figure 5.18 shows proximity of infection and non-infection events to phage producers in both the agar pad and microfluidic devices. The non-infection events are positioned farther away from the phage producers. This observation was further validated by statistically analyzing the average minimum distances, as illustrated in panels e and f.

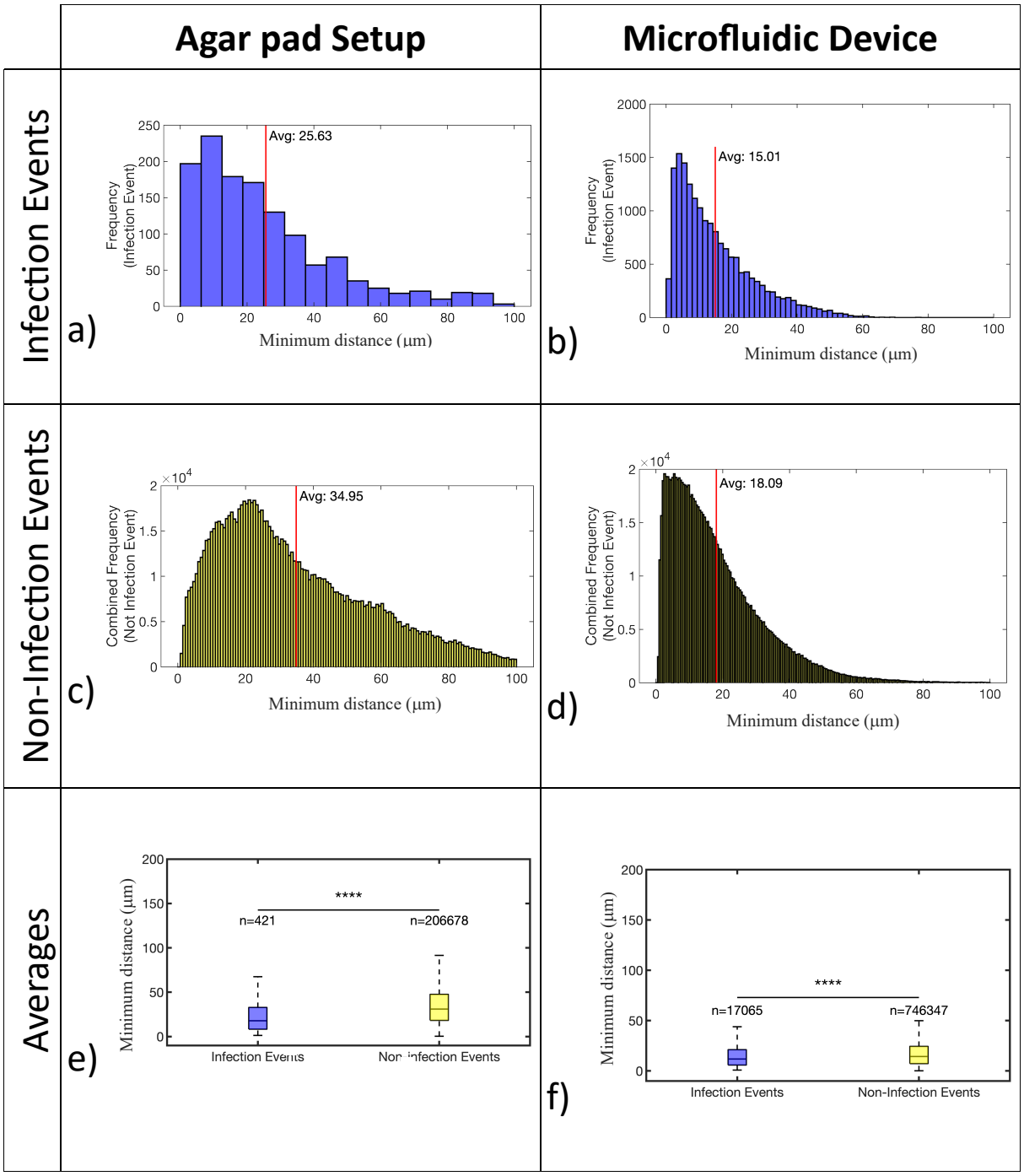


Figure 5.18: Figures a) to d) depict histograms showing the minimum distance from phage producers at the time of infection. a) and b) showcase the distribution for infection events in agar pad and microfluidic setups, while c) and d) illustrate the distribution for non infection events. Figures e) and f) are box graphs displaying the average aggregated proximity for infection events, and non-infection events. T-tests were utilized, and error bars represent standard deviations. P-values below 0.5 were considered statistically significant.

Aggregate Proximity Aggregate proximity results shown in the Figure 5.19 revealed that infected cells had higher aggregated proximity compared to non-infection events. This suggests that infected cells were, on average, closer to surrounding phage producer cells at the time of infection, which is indicative of the significance of proximity in phage infections.

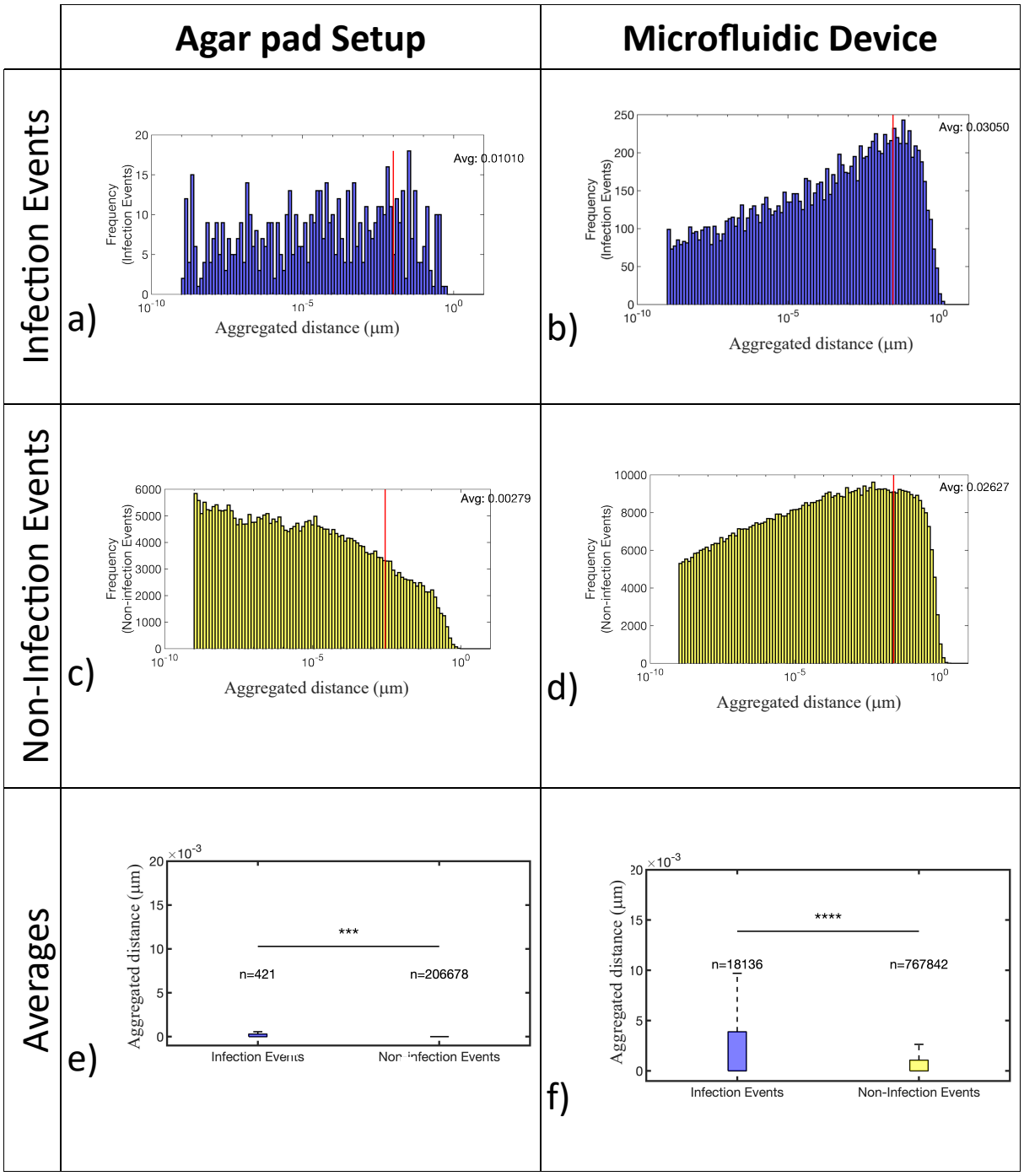


Figure 5.19: Aggregated proximity from phage producers at the time of infection. Figures a) to d) depict histograms showing the aggregated proximity from phage producers at the inferred moment of infection. a) and b) showcase the distribution for infection events in agar pad and microfluidic setups, while c) and d) illustrate the distribution for non infection events. Figures e) and f) are box graphs displaying the average aggregated proximity for infection events, and non-infection events. T-tests were utilized, and error bars represent standard deviations.

The analysis included the computation of both minimum distance and aggregated proximity from phage producer cells. Our observations strongly indicated that infection events were notably more prevalent in cells found closer to phage producer cells, suggesting diffusion limitations during the experiment.

Estimating Phage Particle Diffusion Rate To estimate the M13 phage diffusion rate, we utilized the Stokes-Einstein equation, a method previously employed by Newman et al., to calculate the diffusion rate of fd phage [390]. Our study employed this formula to estimate the diffusion rate of the M13 phage in the microfluidic device. We assumed that the viscosity of the LB media was comparable to that of water (at 37°C). We utilized diameter and radius measurements of the M13 phage (refer to Appendix E, Table E) from the research conducted by Smith et al. [488]. The values obtained were as follows:

$$D_T = \frac{KT}{3\pi\eta L}\left(\delta^{-\frac{1}{2}}(\gamma_{11}+\gamma_1)\right) \tag{5.1}$$

Where: - D_T: Translational diffusion coefficient. - K: Boltzmann's constant (1.38 x 10^{-23} J/K). - T: Absolute temperature in Kelvin (K). - η: Dynamic viscosity of the fluid. - L: Characteristic linear dimension of the particle. - δ: Dimensionality of diffusion. - γ_{11}: The translational friction coefficient (relates to how the shape and size of the particle affect its drag as it moves linearly through the fluid.). - γ_1: The rotational friction coefficient(relates to the resistance encountered by the particle as it rotates in the fluid.).

$$\delta = \ln\left(\frac{2L}{d}\right) \tag{5.2}$$

$$\gamma_{11} = 1.27 - 7.4\left(\frac{1}{\delta - 0.34}\right)^2 \tag{5.3}$$

$$\gamma_1 = 0.19 - 4.2\left(\frac{1}{\delta - 0.39}\right)^2 \tag{5.4}$$

With these parameters defined, we computed the diffusion rate, D_T, to be 258.55 μm^2/min for our specific setup. Subsequently, the approximate time it would take for the phage to diffuse through chambers with an average length of 100 um was calculated using the Einstein–Smoluchowski Diffusion Equation [248]:

$$\Delta x^2 = 2D_T\Delta t \tag{5.5}$$

The findings indicate an estimated diffusion time of around 19 minutes for phages to traverse the length of a 100 µm chamber.

Discussion

Here, phages were generated within the environment by infected phage-producing cells, mimicking natural phage-host interactions. The initial analysis focused on assessing the impact of host cell morphological features: radius, length, and elongation rate, on the infection process. The results closely mirrored those of the previous section 5.3.2.

As discussed in Section 2.1.1, M13 bacteriophages are known to continuously release from hosts without lysis [3]. Although the precise mechanism of this release is not fully understood, studies have shown that M13 bacteriophages can be produced at a rate of up to 6 phages per cell per minute [538]. These particles would be expected to accumulate around the producing cell, balanced by diffusion and possibly decay. As a result, proximity to producer cells is expected to impact infection rates, unless diffusion is so fast that phage particle concentration rapidly reaches an equilibrium distribution.

Diffusion Understanding diffusion rate is vital in exploring the correlation between proximity and phage infection dynamics. A higher diffusion rate grants phages a broader reach within a specific period, elevating the likelihood of encountering and infecting nearby cells. According to Smoluchowski's theory [489, 10], increased diffusion rates could expedite the phage's interaction with nearby cells, potentially accelerating infection events and influencing the proximity of infected cells. Different diffusion rates also influence how phages spread in the environment. Swift diffusion leads to a more even and rapid phage dispersal, potentially affecting their proximity to potential host cells across a larger area.

Fluid flow within the environment likely also influences the distribution of phage particles. While the specifics of flow within chambers are contingent upon the design and were beyond the scope of this research, we made an assumption that the flow was slow enough not to directly influence diffusion rates. Comparable results from the minimum distance and aggregated proximity assessments across both agar pad and microfluidic experiments support this assumption.

Based on the discussions in Section 5.3.2, an estimated delay of 25 minutes from the introduction of phages to the manifestation of visible GFP signals in host cells was identified. This duration encompasses various phases, including the time required for GFPmut2 to mature, estimated at approximately 10 minutes, and an additional 10 minutes allocated for phages to locate and infect their host cells. In light of these considerations, the calculated diffusion time of approximately 19 minutes for phages to traverse a 100 µm chamber aligns

with the overall estimated delay. Thus, the observed timing corroborates the predicted sequence of events leading to visible infection indicators in our experimental setup, validating the accuracy of our diffusion rate estimations and the temporal framework established for phage-host interaction dynamics.

The main focus of this research was to understand the interaction of phage and its host at a single-cell level. However, in many microbial communities, cell aggregation and phage interactions occur within more complex environments, such as biofilms. These interactions have been and continue to be analyzed in various studies.

For instance, Sutherland et al. [503], investigated the interactions between bacteriophages and biofilms, highlighting the challenges phages face in accessing host bacteria due to extracellular polymers and other microbial cells within the biofilm. Their study revealed that some phages produce polysaccharide-degrading enzymes to penetrate these barriers, while others navigate through the biofilm's open architecture and water channels [503]. Jun Hu et al., used a two-chamber diffusion method to study the diffusion properties of Myoviridae phage T4 and filamentous phage fNEL in water and agarose gel membranes, revealing that diffusion rates depend on phage morphology and biofilm density [237].

While these studies provide valuable insights into phage diffusion within biofilms and complex environments, they primarily focus on population-level observations. Our research addresses the gap by focusing on single-cell behaviors during phage infection. By integrating single-cell measurements with agent-based modeling, we inferred critical parameters such as diffusion rates and phage release patterns. The simulation-based analysis used to achieve these insights will be described in detail in Section 5.4.

5.3.7 Conclusion

In summary, our results highlight that cells displaying higher elongation rates, increased cell length, and a larger cell radius exhibited a higher incidence of M13 bacteriophage infection during the infection phase, consistent with the data from section 5.3.2. Moreover, our study underscores that cells positioned nearer to phage producer cells displayed a higher incidence of infection, possibly influenced by the constrained diffusion rate of the M13 phage.

5.3.8 Direct Application of Phage

Exploring Phage Dynamics with Direct Introduction into Virion-producing Cell

In the analysis shown above, newly infected host cells were unable to produce new virions, because they lacked the required helper plasmid. In this section we report on an experimental protocol that combines the direct phage application and *in-situ* phage production protocols. Cells carrying helper plasmids were used in the direct phage application protocol. After conducting experiments in both agar pad and microfluidic setups, we did not detect any instances of infection within the microfluidic system. Consequently, we present the results obtained from the agar pad setup summarized in Table 5.8.

Table 5.8: Direct approach, experiment information for agar experiments

Imaging (min)		**Positions**	
Duration	**Interval**	**Dimensions (µm x µm)**	**Number**
154	2	702.91 x 957.29	7

In analyzing the spread of phage infection events among cell states at the inferred infection time, there was a noticeable decline in infection occurrences: from 233 infection events in cells without the helper plasmid to 24 infection events in cells with the helper plasmid (approximately 90% decrease in the number of infection events). This significant decline likely indicates the impact of the helper plasmid in reducing the frequency of infections. This aligns with previous studies suggesting that the pIII protein present in the helper plasmid prompts pili retraction, diminishing the quantity of pili in each cell [319] and resulting in a decrease in infection events.

Distribution of phage infection events across cell states

In this phase, we conducted a parallel analysis on the impact of cell radius, length, and elongation rate as explored in Section 5.3.2, this time focusing on host cells containing the helper plasmid. Figure 5.20 displays average radius, length, and elongation rate data for infection event, not infection event (related to infection), and not infection event (not related to infection). These data represent population-based outcomes derived t-tests analysis, supported by error bars indicating standard deviation.

The findings in Figure 5.20a), 5.20b) and 5.20c) demonstrate that cells with larger radii, greater lengths and higher elongation rate at the time of infection displayed a higher incidence of infection, aligning with our previous observations from earlier sections.

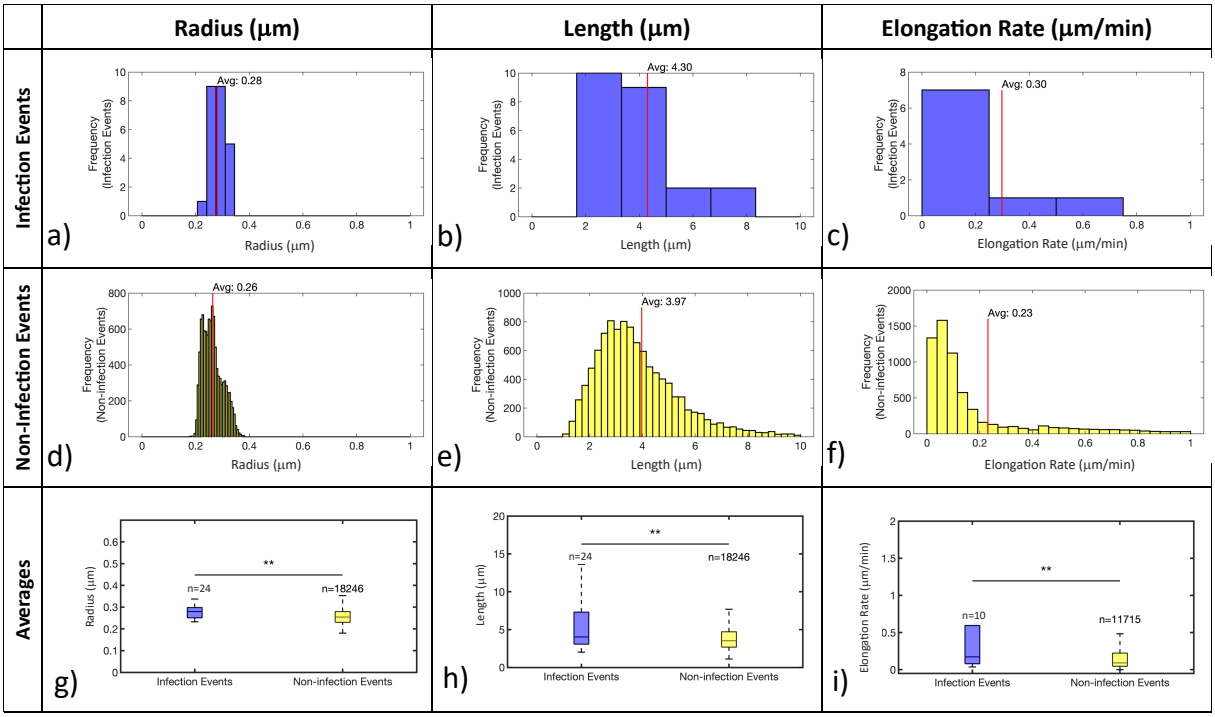


Figure 5.20: The figure shows the radius, length and elongation rate for cells containing helper plasmid at the infection time. in panel g, h and i) Atop each bar, the number of lineages in each category is displayed, with corresponding p-values determined. Similar to the hosts without helper plasmid, cells with larger length and radius, and higher elongation rate demonstrated a higher likelihood of getting infected by phages.

Longitudinal Analysis of Phage Infection Progression Within Varied Cell States

This section explored the impact of infection on cell radius, length, and elongation rate, with detailed findings presented below. Unless indicated otherwise, statistical analyses were conducted using two-sample t-tests to compare the means between groups, with error bars representing standard deviation.

Radius Figure 5.21 presents the distribution of cell radius over the course of experiment. Similar to the previous sections (Section 5.3.2, and 5.3.5, presenting in panel a) to c) we categorized lineages to two groups: a) infected cell objects, and b) Not infected cell objects. Our findings revealed a notable reduction in the radius of infected cells compared to their

non-infected counterparts. In contrast, the radius of non-infected cells remained relatively consistent throughout the experiment, with minor reductions attributed to densely packed cell growth, as observed in Section 5.6.

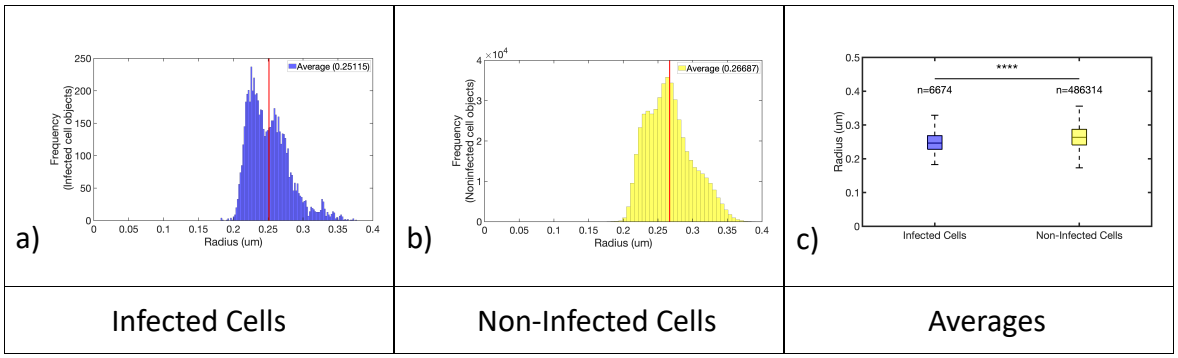


Figure 5.21: The figure consists of two key sections: (a) and (b) display histograms illustrating the distribution of radii for both infected and non-infected cells throughout the experiment; (c) features a box graph comparing the average radii of the two groups. T-tests were applied to analyze the data, and error bars indicate standard deviations. P-values below 0.05 were deemed statistically significant. The data clearly show that infected cells exhibit a decrease in radius in comparison to non-infected cells, highlighting a statistically significant difference between the groups.

Cell length Figure 5.22 displays the distribution of cell lengths throughout the experiment. Similar to the categorization used for radius analysis, lineages were divided into three groups, with results presented in panels a and b. Our analysis revealed a distinct trend: infected cells exhibited a noticeable reduction in length, contrasting with the relatively consistent length observed in their non-infected counterparts, as also noted in Section 4.5. This finding indicates that phage infection significantly influenced the length of infected cells.

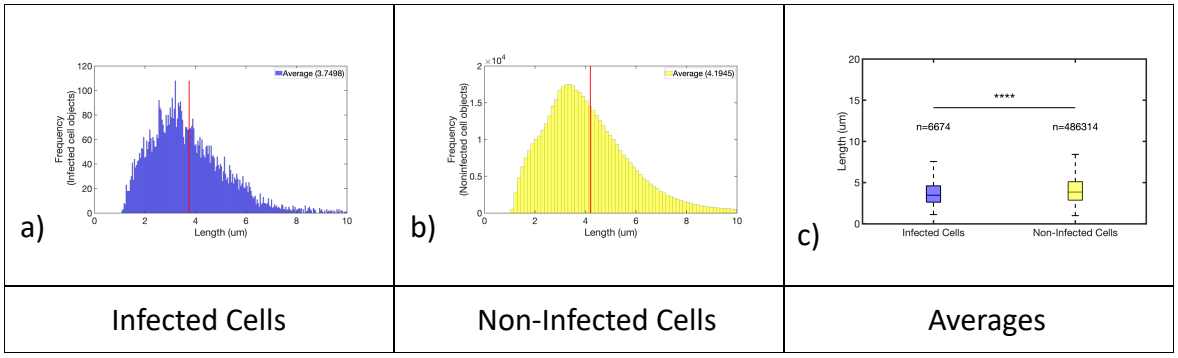


Figure 5.22: The figure comprises two key elements: (a) and (b) depict histograms illustrating the distribution of cell length among infected and non-infected cells throughout the experiment. Additionally, (c) features a box graph comparing average length. T-tests were applied to analyze the data, and error bars indicate standard deviations. Statistically significant p-values below 0.5 were observed. It's evident that infected cells exhibited lower length compared to non-infected cells, and the accompanying statistical analysis confirms this significant difference.

Elongation rate Figure 5.23 illustrates the distribution of elongation rates for cells carrying the helper plasmid across the infection period. Our analysis of elongation rates unveiled that infected cells displayed higher elongation rates compared to their non-infected counterparts.

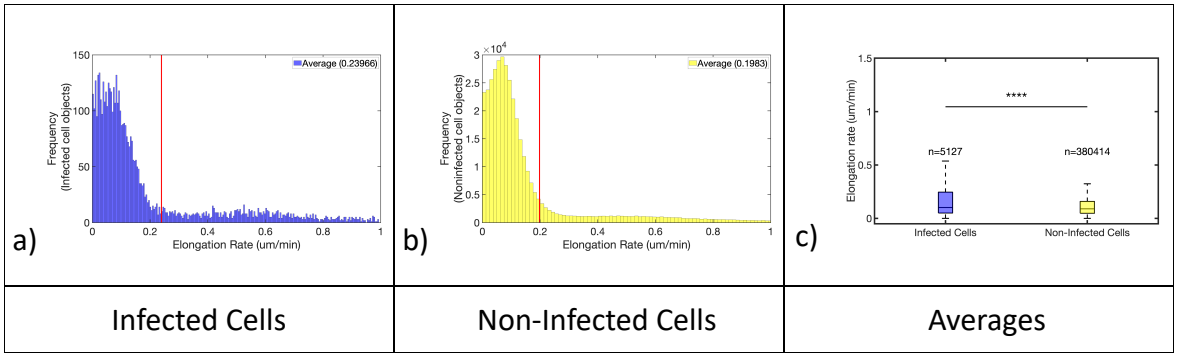


Figure 5.23: The figure comprises two key elements: (a) and (b) depict histograms illustrating the distribution of cell elongation rate among infected and non-infected cells throughout the experiment. Additionally, (c) features a box graph comparing average elongation rate. T-tests were applied to analyze the data, and error bars indicate standard deviations. A highly significant difference was observed between infected and non-infected cells, with a p-value of less than 0.001.

Discussion

In this section, we utilized a different target to explore how phage infection impacts its host using single-cell data analysis. Our goal was to determine if modifying the target influenced previously measured morphological features—specifically, cell size and elongation rate—during the inferred time of infection, similar to our earlier research. Additionally, by utilizing cells capable of producing new virions, we aimed to observe the prolonged impact of infection on cellular behavior- cell size and elongation rate— over an extended period.

Upon evaluating the results, a significant reduction in the number of infection events was observed compared to cases where cells lacked the helper plasmid. The helper plasmid, M13KO7, employed in this study, contains full-length M13 phage protein genomes and a semi-defective phage f1 origin of replication (due to an interruption of the f1 ori by a kanamycin resistance marker) [559]. Consequently, cellular resources in these hosts are already utilized to translate phage proteins within the bacterial genome. The pIII protein present in the helper plasmid has been demonstrated to triggers pili retraction, thereby reducing the quantity of pili in each cell [319]. This decrease in pili production diminishes the likelihood of phage-host interactions, consequently leading to a reduction in infection events. Consequently, superinfection with M13 phages carrying the phagemid genome might depend solely on successful attachment to the sparsely present pili within this population of cells.

The retention of self-replication capability by M13KO7, even without the presence of phagemid, owing to its plasmid origin (The p15a ori) [529], raises intriguing possibilities regarding its influence on cellular machinery. If M13KO7 self-assembles into the phages, it could have already impacted the host cell's internal processes.

Curiously, our analysis revealed that the insertion of this plasmid, accompanied by the production of self-replicating M13KO7 phages within the host, led to approximately 90% decrease in the number of infection events. This reduction was particularly noticeable when compared to cells under the same growth conditions, on agar pad setups from section 5.3.2 (from 233 infection events in cells without the helper plasmid to 24 in cells with helper plasmid). We presume that this diminishment in cell size may be indicative of the burden imposed by the phage on the cells. However, further investigation at the molecular level is required to elucidate the mechanisms underlying this size reduction phenomenon.

Our exploration into cell size supported findings from earlier sections (see Section 5.3.2, and 5.3.5), showing that larger cells demonstrated an increased frequency of infection. Upon evaluating the average elongation rate, a higher mean value was observed for infected versus non-infected events.

The investigation into the impact of phage infection on host radius, length, and elongation rate unveiled that infected lineages exhibited a reduction in size compared to their non-infected counterparts. This observation aligns with earlier findings obtained while comparing the sizes of target cells infected with M13 phage against those without it [94]. Previously, Chang et al. utilized atomic force microscopy (AFM) imaging to substantiate this claim, demonstrating that infected *E. coli* cells experienced a reduction in length [94]. Their study highlighted that this alteration is attributable to membrane damage triggered by the release of the lipopolysaccharide (LPS) layer, resulting from outer membrane damage [94].

We investigated the elongation rate of infected versus non-infected lineages. Prior studies have extensively examined the impact of M13 phage on host cells [90, 224, 287, 396]. Despite this extensive research, single-cell analysis had not directly measured the effect of M13 phage infection on host cell elongation rates. Instead, existing data were primarily derived from simulations [483, 482] or population-based analyses often conducted on agar plates or in suspension tubes. Remarkably, our work revealed that although elongation rate decreased compared to when the infection initially inferred to happen within the cells, infected cells as the time pass exhibited higher elongation rates compared to their non-infected counterparts, contrary to previous expectations.

Prior studies have established a direct correlation between cell growth rates and phage production rates [126]. For instance, faster-growing larger cells tend to exhibit faster phage

production and larger burst sizes [210]. Kick et al, shows that increasing in the growth rate of bacteria, enhanced the maximal M13 phage amplification rate [287]. Similar to other viruses described by Burrell et al. [81], the primary goal of M13 is to ensure its successful replication and dissemination to infect other host cells while avoiding immediate cell death. Acting as a parasite, M13 relies on its host's survival to continue reproducing, distinguishing itself as a non-lytic phage, thereby allowing the host cell to persist and sustain phage production over an extended period [483]. Considering recent research that suggests faster growth rates enhance the likelihood of clonal population[2] [37], the observed faster elongation rates in infected cells might be comprehensible. Indeed, a faster growth rate appears to enhance the likelihood of cell survival following infection with M13, creating conditions favorable for parasites like M13 due to the increased production rate facilitated by the host's rapid growth. Our findings align with previous research conducted by Shapiro et al. [464], which demonstrated that infected bacteria with M13 phage reproduced at an accelerated rate and reached higher population densities compared to uninfected bacteria in 96-well microplates.

Conclusion

In conclusion, our findings support prior observations, underscoring that larger cells are more often subject to phage infection. Additionally, although the average elongation rate was higher for infection events compared to non-infection events, statistical analysis did not yield a significant difference between the two. This indicates that while variations in elongation rates exist, they do not reach a level of statistical significance, suggesting inconclusive differences between the groups.

Moreover, post-infection outcomes strongly indicate that phage infection exerts a burden on bacterial hosts, evident in the reduced length and radius of infected cells compared to non-infected counterparts. However, the direct impact of phage infection on cell elongation rates remains uncertain. Further investigations are crucial to elucidate this relationship and discern whether phage infection directly influences the rate of cell elongation.

5.4 Simulating of M13 infection process

In this section, computational simulation of phage infection is explored, designed to mirror the experimental setup previously described. The primary objective is to infer unobserved

[2]Clonal population refers to the cells that are genetically identical or nearly identical because they originate from a single ancestor or parent cell

aspects of the infection dynamics, specifically diffusion rates and phage release patterns, within the context of *in-situ* phage production. Through computational analysis, this chapter aims to extract additional information from the experimental observations, with a particular focus on the minimum distances previously calculated in the experimental setups.

5.4.1 Introduction

Dynamic computational modeling tools like CellModeller have facilitated predictions regarding the spatial patterning and arrangement of cells within bacterial communities. These simulations offer insights into the complex dynamics of microbial ecosystems, underscoring the value of such models in understanding cell behavior and interactions [433].

In this study, CellModeller capabilities were employed to simulate the infection process of the M13 bacteriophage, with a specific focus on investigating aspects of the system that cannot be directly address by experimental findings: specifically how the phage diffusion rate and release rate relates to the spatial distribution of infected cells relative to phage producers. The primary aim of this study was to employ simulation data to determine the diffusion rate and uptake release rate of phage within our experimental setup. Specifically, the study examined the minimum distances of infection events from phage-producing bacteria to understand the impact of diffusion on phage spread and infection processes.

CellModeller employs biophysical models to simulate the behavior and interaction of cells within multicellular systems. These models incorporate information on cell shape, size, and mechanics—such as cell growth rate, division rates, and the forces exerted by and on cells. The software uses this data to generate dynamic simulations of how cells grow, divide, and interact with one another in a spatially explicit environment [437]. In CellModeller each cell is represented as a computational entity termed a "cellState", for which details like cell's location, orientation, length, radius, its growth rate, and the cell's specific type is available [344]. In this study, to effectively model the infection process within the CellModeller environment and to track infection data for each cell, two additional parameters were integrated into the simulation's source code: (1) an infection flag, used to indicate the initial infection event of a cell, marking the first time a cell becomes infected by the phage, and (2) the number of phage particles produced by the cell within each timestep.

The diffusion mechanism within CellModeller is used to simulate the movement of phage particles across the environment. This simulation is achieved through the implementation of partial differential equations (PDEs), specifically diffusion equations. These equations

incorporate a diffusion coefficient, thereby enabling the model to predict the dispersal patterns over time. The numerical solutions to these PDEs are obtained iteratively, with the substrate concentration at each grid point being updated at every simulation timestep just like update in the cell objects.

The infection probability equation, detailed in Section 5.4.3, was developed to estimate the likelihood of infection. This equation integrates specific aspects of cell behavior, specifically elongation rate and cell length, and phage concentration into the model. To calibrate this equation, real-time experimental data described in Section 5 were utilized. Calibration of some parameters was performed using deconvolution methods based on single-cell experimental results. However, due to inability to visualize phage particles under the microscope and measuring their concentration within microfluidic chambers, some parameters were estimated through simulations rather than directly from experimental data. Following the initial calibration, simulations were conducted to specifically estimate the phage diffusion rate and host susceptibility.

5.4.2 Deconvolution Technique

Accurate calibration of the infection probability equation is essential for ensuring that the model reliably represents biological processes. Calibration involves adjusting model parameters so that the model outputs match experimental data [516]. In this study, deconvolution techniques were employed to calibrate the kernel values for elongation rate and cell length. Deconvolution is a mathematical technique used to extract the true underlying signal from data that has been affected by a known process [122]. Kernel values represent probability density functions (PDFs), which describe the distribution and likelihood of various cell properties [124], such as elongation rate and cell length, within the population. By providing a statistical representation of the variability and distribution of these properties, PDFs enable a more precise modeling of the transformation of cell characteristics due to infection.

In essence, the deconvolution process helps us understand how the phage 'selects' hosts [3] from the entire population. For each feature, we consider the overall distribution of the feature within the population and the distribution within infected cells. The phage population can be thought of as 'selecting' cells based on certain features, and this selection process is represented as a convolution of a kernel that characterizes the phage's preference for specific host features. This kernel captures the likelihood of a phage infecting a cell

[3] Although phages do not have an active selection mechanism, the term 'select' is used to describe the probabilistic interaction between phages and host cells for the sake of simplicity.

with particular characteristics. Through deconvolution, we isolate this kernel, which allows us to understand the 'preference' pattern of phages for specific cell features and model the infection dynamics more accurately.

To achieve accurate calibration, various deconvolution methods have been introduced, each with unique properties in handling signal processing and generating accurate results. Direct deconvolution [435] is straightforward but can be highly sensitive to noise, making it less suitable for noisy datasets. Wiener deconvolution [544] incorporates a noise filter, balancing the trade-off between deconvolution accuracy and noise amplification, thus offering improved stability [522]. Regularized deconvolution [542] introduces additional constraints to stabilize the solution, making it particularly effective for noisy data by ensuring a physically meaningful and robust solution [446].

In this work, regularized deconvolution was employed to derive the selection kernel for elongation rate and length parameters. The choice of regularized deconvolution was driven by several factors. Firstly, the data consisted of single-cell measurements, where each cell exhibited unique behaviors, resulting in significant variability and noise within the dataset. Regularized deconvolution is particularly well-suited for such scenarios, as it effectively manages noise by imposing constraints that prevent overfitting and ensure stability. The deconvolution problem can be formulated as follows [446]:

$$H \cdot K = g \tag{5.6}$$

where:

- H is the convolution matrix, which is constructed from the probability density function (PDF) of the uninfected cells. It represents how the properties of uninfected cells contribute to the observed properties of infected cells.
- K is the kernel we aim to estimate. It captures the transformation applied to the properties of uninfected cells to produce the observed properties of infected cells.
- g is the observed data, represented as the PDF of the infected cells. It reflects the distribution of the measured properties of the infected cells.

Details regarding the specific of the deconvolution method employed in this study are provided in the following section, and the MATLAB code used for this process is included in Appendix H.1.

5.4.3 Methods

Defining initial conditions within simulation

The initial state of cells— positions, orientation, and initial size (length and radius)— was defined in the CellModeller environment to align the simulation with experimental conditions. Additionally, the simulation domain boundaries were defined based on the dimensions of microfluidic traps, ensuring an exact match with experimental parameters and enabling direct comparisons between simulation outcomes and empirical data. Cell size, location, fluorescent intensity, and orientation parameters for the simulations were directly imported from CellProfiler outputs, which were formatted in Excel and derived from the initial frame data (Time = 0). In the CellModeller simulation environment, three distinct cell types were defined to mirror the experimental conditions: 1) Non-infected cells, 2) Phage producer cells, and 3) Infected cells. Classification into these categories was based on GFP fluorescence intensity thresholds established in Chapter 5. Cells exceeding this GFP threshold at the initial frame were classified as phage producers, while those below the threshold were identified as Non-infected cells. The status of 'Infected cells' was assigned during the simulation process based on their response to the phage; any simulated host cell becoming infected as per simulation conditions was subsequently classified as 'Infected'. To align the simulations closely with experimental data, the elongation rates and division lengths were assigned to be equal to the averages calculated from the experimental observations as detailed in Chapter 5, reducing variability within the simulations. This calculation was carried out by a MATLAB script, detailed in Appendix H.1.

Parameter Calibration and Validation for Microfluidic Infection Dynamic Simulation

The selected experiment for simulation was the microfluidic experiment number 1, detailed in Section 5.3.5, encompassing 21 chambers. The preference for the microfluidic configuration over the agar setup stemmed from the reduced computational demand, attributable to fewer cells being visualized, thus facilitating the execution of a greater number of simulations. Additionally, this particular experiment was chosen due to the higher number of chambers (21), providing multiple similar conditions that increased the robustness of the simulation calibration.

Initially, one chamber was selected to calibrate the simulation parameters (data from this initial calibration are not reported). This step was crucial for refining the model before scaling up to all 21 chambers. Following this initial calibration, the simulation was run for all chambers, with each parameter being calibrated through a minimum of 10 replicates

per chamber. This extensive calibration process resulted in over 3000 simulations, each requiring significant computational time to simulate and analyze. Results of the simulation are presented in the Section 5.4.4.

While this approach allowed for a detailed calibration of the simulation model, it is important to acknowledge its limitation: a more robust result could be achieved by spreading the simulations across multiple experiments, rather than concentrating on a single one. Due to time constraints, this broader approach was not feasible within the scope of this thesis. However, the calibrated code can be further applied to other experiments in future work, enhancing the generalizability and robustness of the findings.

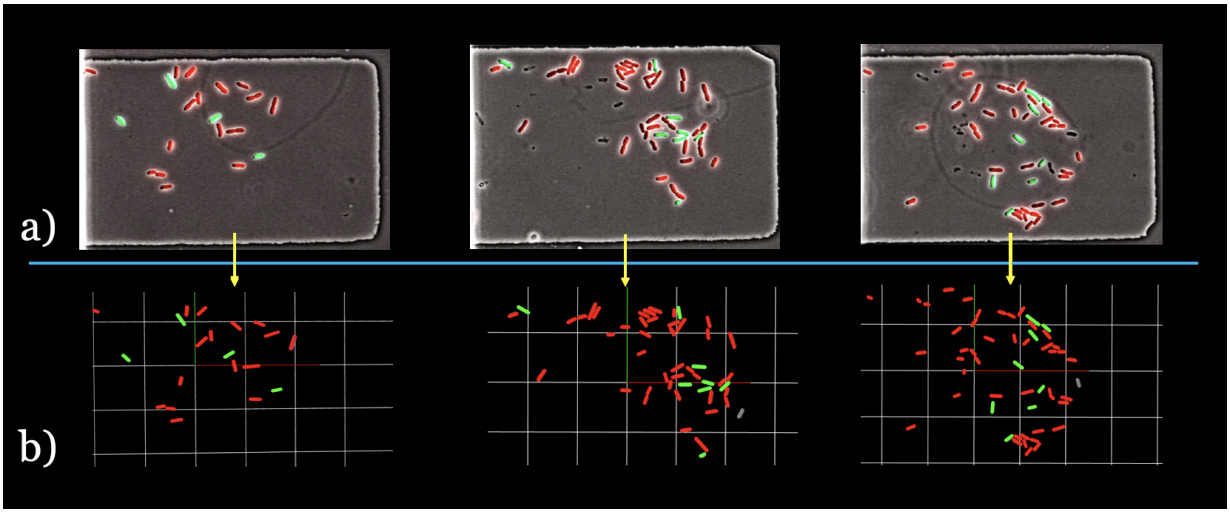


Figure 5.24: a) Experiment b) Simulation environment

Defining phage infection within simulation

The phage infection process was simulated by incorporating three steps into the CellModeller code, reflecting the interactions between bacteriophage and bacterial cells within the simulation environment. These steps are as follow:

1. **Phage Production and Release:** Building on the findings of Wan et al.[538], the model describes the phage production and release by phage-producing-cells as a continuous distribution of phage density. According to their research, the M13 phage production rate is approximately 6 particles per minute [538]. We incorporated this rate into our simulation to ensure that phage-producing cells emit phages at a consistent and steady rate. This approach captures the local density of phages in a

continuous field around the producer cells, representing the phage concentration in the environment (See Figure 5.25). The phage concentration field is updated in each time step based on the diffusion of phages through the medium and their continuous release from producer cells. K_3 is an uptake scaling factor that scales the susceptibility of host cells to infection based on the local phage concentration. By linking the continuous phage density field to the probability of infection for individual host cells, K_3 provides a comprehensive framework for modeling the infection dynamics. The introduction and calibration of K_3 are crucial steps in ensuring that the simulation accurately represents the biological processes observed experimentally.

2. **Diffusion of Phage Particles Through the Environment**: The phage particles are modeled as a continuous field released at a constant rate from the cells, and their diffusion through the environment is governed by the rules established within the CellModeller system. The simulation assumes no perturbed flow from the main channel into or through the chamber, focusing solely on the diffusion process.

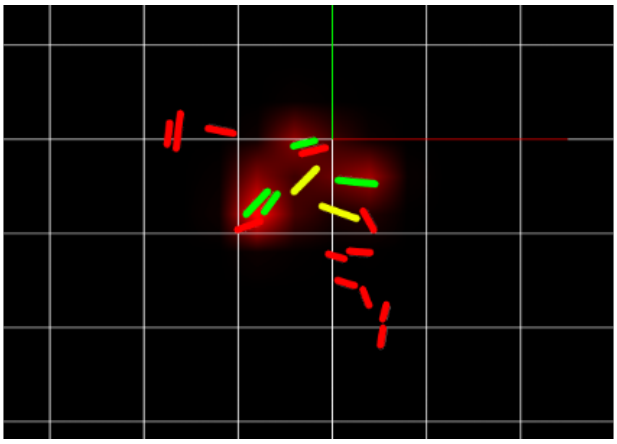


Figure 5.25: Simulation of Phage Diffusion: In the simulation environment, green cells represent phage-producing cells, red cells indicate host cells and yellow cells represent infected cells. The surrounding red cloud illustrates the concentration and spread of phage particles emanating from the producer cells, depicting their diffusion throughout the environment.

3. **Phage Infection Probability for Host Cells**: Building on experimental insights, as detailed in the Chapter 5, the model employs a straightforward method to estimate the probability of phage infection for host cells. This approach uses the established direct correlation between the host cells' physical characteristics—specifically length, radius, and elongation rate—as observed in experimental outcomes and described in

Chapter 5, and the concentration of phage virions in their vicinity, which together determine the probability of infection. These characteristics are represented by kernel distributions K_1 and K_2, which describe the probability density functions of elongation rate and cell length, respectively. The local concentration of phage virions, while generated by the simulation, influences the infection process and is scaled by K_3, an uptake scaling factor. The model calculates the likelihood of successful phage infection of a host cell by combining these kernel distributions with K_3, which adjusts the susceptibility of host cells based on the surrounding phage concentration. This approach factors in the variable efficiency of phage attachment to the cell surface, influenced by the cell's morphological state and the local phage concentration.

The kernels K_1 and K_2 were determined as follows:

$$K_1(\text{Elongation rate}) = \text{Kernel value from the distribution of elongation rates at the given elongation rate} \tag{5.7}$$

$$K_2(\text{Length}) = \text{Kernel value from the distribution of lengths at the given length} \tag{5.8}$$

These kernel values were then integrated into our infection probability model:

$$\text{Host State} = f(\text{Elongation rate}, \text{Length}) \tag{5.9}$$

The uptake probability, reflecting the chance of infection per time step and ranging between zero and one, is given by:

$$\text{Uptake probability} = \text{Host State} \times (K_3 \times \text{Surrounding Phage}) \tag{5.10}$$

In the above equations, the function $f(\text{Elongation rate}, \text{Length})$ represents the combined effect of the elongation rate and cell length, scaled by kernel distributions K_1 and K_2, respectively. K_3 is an uptake scaling factor representing the influence of surrounding phage concentration. These components are essential for accurately modeling the infection dynamics.

(a) **Calibration of K_1 and K_2 Using Experimental Data**: As described in Section 5.4.2, a regularized deconvolution method was utilized in this study to calibrate K_1 and K_2. This method is particularly suitable for our single-cell data,

as it helps derive the probability density functions (PDFs) of cell properties, represented by kernels. Kernels in this context encapsulate the transformation of uninfected cell properties to predict those of infected cells. We normalized the kernel values to one to generate probability density functions (PDFs), thereby maintaining the model's integrity.

(b) **Calibration of K_3 and Diffusion Rate Using Simulation**: As detailed in the Section 5.4.1, the estimation of the uptake scaling factor (K_3) and the diffusion rate of phage particles was achieved through simulations due to the limitations in directly measuring these factors within microfluidic chambers. An automation script, as described in the following section, was used to run a series of simulations with varying values of K_3 and diffusion rates to identify the factors that best replicated the experimental data. In the simulation framework, the diffusion rate and K_3 values were varied systematically within predefined ranges through a parameter sweep. For each combination of diffusion rate and K_3, simulations were executed using the CellModeller simulator, configured to mimic the dimensions and physical characteristics of cells within the microfluidic chambers used in the experiment as closely as possible. An automated script was employed to conduct these parameter sweeps, ensuring a comprehensive exploration of the parameter space. Each combination of diffusion rate and K_3 was tested across 10 replicas to ensure robustness and reliability of the results. The output from each simulation run was processed to extract the average minimum distances between infected and non-infected cells from phage-producing cells. This metric provided a direct measure of how well the simulations replicated the spatial distribution and interaction patterns observed in the experiments (Equation 3b). By systematically exploring the entire parameter space, we identified the combination of diffusion rate and K_3 values that best minimized the difference between the simulation results and the experimental data, thereby achieving an optimal match between the model and the observed experimental patterns. The parameter values that resulted in the closest match to the experimental data were selected as the optimal values, based on minimizing the sum of the squared differences between the simulation metrics and the corresponding experimental metrics. The formula we used for this minimization is:

$$\text{Objective Function} = \sum_{i=1}^{n} (S_i - E_i)^2$$

where: - S_i represents the simulation metric for the i-th data point, - E_i represents the corresponding experimental metric, - n is the total number of data

points.

These optimal values for the diffusion rate and K_3 were then used to run final simulations, reported in the Section 5.4.4, which were compared against the experimental data to ensure the accuracy and validity of the model.

The MATLAB code used for this calibration process is detailed in Appendix H.1. The results of the deconvolutions are presented in Section 5.4.4.

Implementing and Analyzing Simulation Data

The phage infection code utilized within the CellModeller framework is available in Appendix H.1. To explore the impact of varying diffusion rates on phage spread, a wrapper code was developed. This code facilitated the systematic alteration of diffusion values during simulations. The corresponding code is available in Appendix H.1.

Data generated by CellModeller were output in pickle format, containing an array of simulation attributes. These attributes included time stamps, image identifiers, cell dimensions (length and radius), spatial coordinates of cell (center-x and center-y), and cell status indicators (infected, non-infected, and phage-producing). Additionally, an 'infection flag' was used to identify cells newly affected by phage infection, excluding subsequent generations from this categorization. A custom Python script, detailed in Appendix H.1, was employed to extract these data points, subsequently organizing them into a structured Excel format for ease of analysis.

The processed data, now in Excel format, were then examined as described in Section 5.4.3 .

5.4.4 Results

Results of K_1 and K_2 Calibration

The initial focus of this section is on the results generated to calibrate K_1 and K_2, which represent the elongation rate and length parameters in the probability of infection equation. The deconvolution method was utilized for this calibration, with the main goal being the identification of the optimal kernels.

The deconvolution process for elongation rate (K_1) yielded a range of kernel values that represent the transformation from uninfected to infected cell elongation rates. In Figure 5.26, the green line represents the PDF of uninfected cells, the red line represents the PDF of infected cells, and the blue dashed line represents the estimated kernel PDF after deconvolution and smoothing. The PDF of uninfected cells shows a steep decline, indicating that most uninfected cells have a low elongation rate. In contrast, the PDF of infected cells shifts slightly, showing that infected cells generally exhibit higher elongation rates. The estimated kernel PDF, derived through deconvolution, aligns well between the PDFs of uninfected and infected cells, suggesting that the kernel captures the probability distribution of elongation rate changes due to infection. This kernel is crucial for the simulation model as it provides a probabilistic basis for assigning elongation rates to cells post-infection.

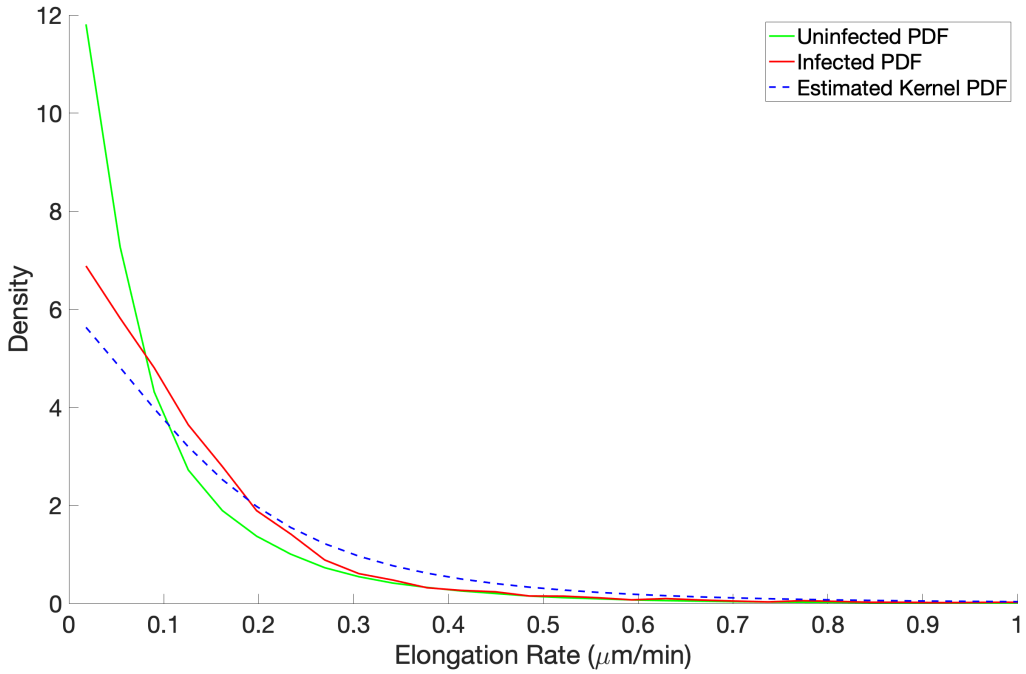


Figure 5.26: Deconvolution results for elongation rate. The green line represents the PDF of uninfected cells, the red line represents the PDF of infected cells, and the blue dashed line represents the estimated kernel PDF (K_1) (deconvolved and smoothed).

Similar to elongation rate, kernel values for cell length (K_2) were measured using the same deconvolution methods. The results are presented in Figure 5.27.

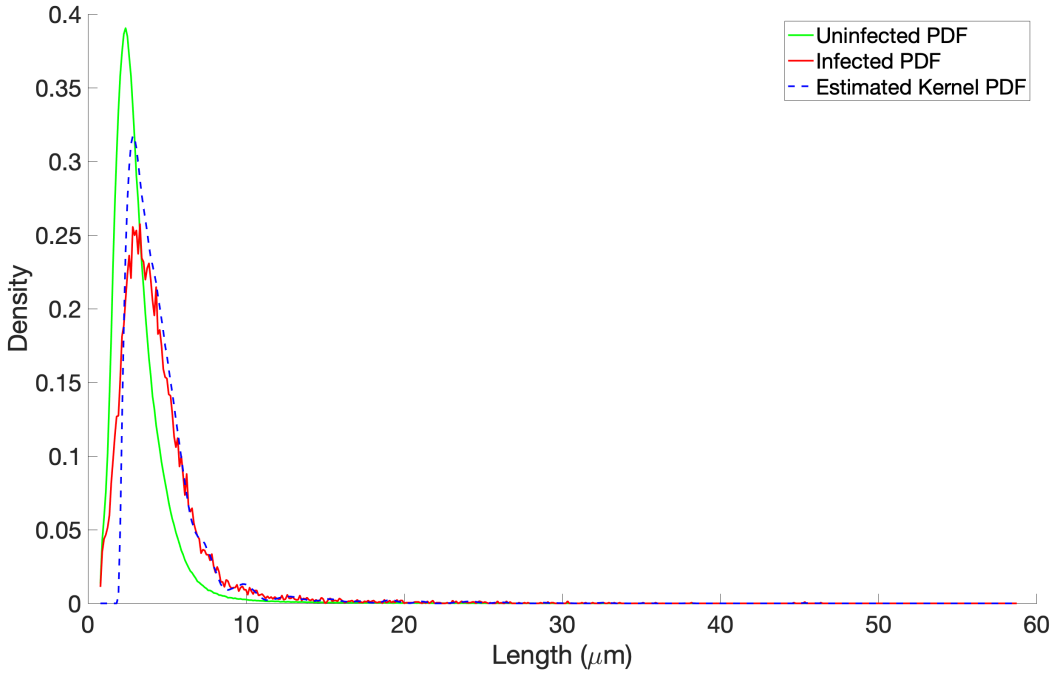


Figure 5.27: Deconvolution results for cell length. The green line represents the PDF of uninfected cells, the red line represents the PDF of infected cells, and the blue dashed line represents the estimated kernel PDF (K_2)) (deconvolved and smoothed).

These kernels were integrated into the simulation model, enabling it to closely replicate the observed infection behaviors.

Calibration of K_3 and Diffusion Coefficient

Following the calibration of the kernel values K_1 and K_2, which describe the probability density functions for elongation rate and cell length respectively, the parameter related to the phage concentration (K_3) and the diffusion coefficient were calibrated through simulations as explained in Section 5.4.3. Figure 5.28 illustrates the effect of varying K_3 and the diffusion coefficient on the squared average minimum distance between infected and non-infected cells from phage producer cells. The results indicated that the optimal diffusion coefficient was within the range of 250 to 300 μm^2/min. Smaller diffusion coefficients led to limited phage spread and lower infection rates, while larger diffusion coefficients (greater than 400 μm^2/min) caused the simulation to crash due to numerical instability in

the CellModeller framework[4]. The optimal K_3 value was within the range of 15 to 20. As K_3 increased, the minimum distance also increased. This observation is consistent with the biological significance of K_3, which corresponds to the phage concentration around host cells. A higher K_3 value indicates a larger concentration of phage particles, leading to a greater spread and increased minimum distances between infected cells.

[4]During the calibration process, it was observed that simulations with a diffusion coefficients greater than 400 consistently crashed. This issue is likely due to how the diffusion coefficient is defined within the CellModeller framework. In CellModeller, the diffusion coefficient parameter controls the spread of phage particles within the simulation environment. When set to high values, it can lead to instability in the numerical calculations, causing the simulation to crash. This instability may arise from the excessive spread of phage particles, overwhelming the computational grid and leading to numerical errors.

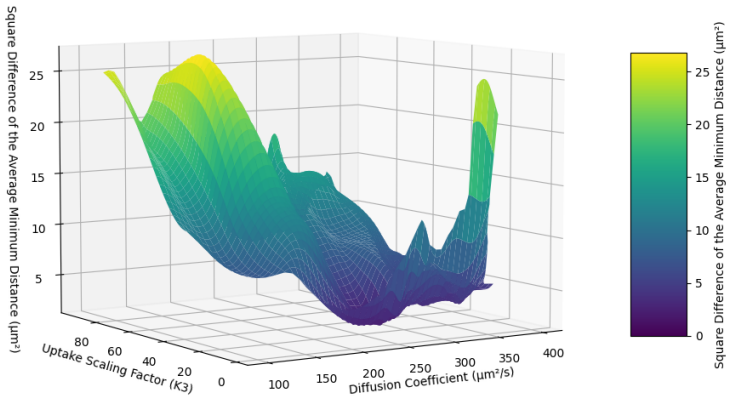


Figure 5.28: 3D surface plot depicting the relationship between uptake scaling factor (K_3), the diffusion coefficient ($\mu m^2/min$), and the square difference of the average minimum distance. The plot identifies the optimal ranges for K_3 and the diffusion coefficient, where the simulation results most closely match the experimental data. Lower values on the Z-axis indicate a better fit. The optimal diffusion coefficient is found to be in the range of 250 to 300 $\mu m^2/min$, and the optimal K_3 value is around 15 to 20. Higher diffusion coefficients lead to increased square differences and instability in the simulation, while moderate values ensure accurate phage spread and infection dynamics. Each value was tested over 10 runs.

5.4.5 Discussion and conclusion

M13 bacteriophage research is integral to multiple fields, including biotechnology and synthetic biology. Accurate determination of key parameters, such as phage diffusion rates and release patterns, is crucial for enhancing the predictive accuracy of infection models. Such models are essential for both theoretical studies and practical applications in microbiology and biotechnology. Simulations provide deeper insights into experimental work by allowing us to infer parameters that are challenging to measure directly. For instance, in this study, while single-cell analyses enabled us to measure the physical characteristics of

cells directly, parameters such as phage concentration and diffusion rates were not feasible to measure. These factors have been previously predicted and measured at the population level, often estimated through predictions of intracellular interactions and the number of plasmids produced within the cells, as well as the population-based release of phages. However, they haven't been directly predicted using single-cell data.

In this research, we integrated single-cell experimental data with agent-based modeling to estimate the diffusion rates and the uptake scaling factor (K_3) of M13 bacteriophage. This approach offers a novel perspective and potentially more accurate modeling of phage dynamics. We began by employing the deconvolution technique to calibrate the kernel values K_1 and K_2which represent the elongation rate and cell length, respectively. These kernels were then used as functions within our simulation framework to determine values for the diffusion rate and (K_3). The simulations were systematically run using our custom code, which provided a range of diffusion rates between 250-300 μm^2/min (4.17×10^{-8} to 5×10^{-8} cm^2/s).

In Section 5.3.6, we utilized the Stokes-Einstein equation to calculate the diffusion rate of the M13 phage within our microfluidic device setting and found the value to be 258.55 μm^2/min (4.31×10^{-8} cm^2/s). Comparing this value to the results generated from the simulation, which gave us a range between 250-300 μm^2/min (4.17×10^{-8} to 5×10^{-8} cm^2/s), we observe a close resemblance between the experimental calculation and the simulation, indicating that our model is consistent with empirical data.

Comparing these findings to previous studies, Newman et al. [390] calculated the diffusion rate of the fd phage using intensity fluctuation spectroscopy in an aqueous solutions at 37 °C (composed of 10mM KCl, 1mM Na phosphate and 1mM phosphate) and found a diffusion coefficient of 2.58×10^{-8} cm^2/s. Beck and Duenk [56] measured the rotational and translational diffusion coefficients of M13, finding $D_T f = 2.34 \times 10^{-8}$ cm^2/s. This lower value compared to our study (4.31×10^{-8} cm^2/s) can be attributed to differences in methodology. For instance, Beck and Duenk methodology's involved transient electric birefringence and analytical ultracentrifugation [56], both of which differ significantly from our microfluidic setup. Transient electric birefringence measures the change in light polarization as phages orient in an electric field, while ultracentrifugation measures sedimentation rates under high g-forces. These methods may not replicate the natural movement of phages in a biological environment as accurately as our microfluidic setup.

Similarly, Smith et al. [488] used fluorescence microscopy to study viral nanoparticles in semi-dilute solutions of partially hydrolyzed polyacrylamide (HPAM) in 1X PBS, finding a diffusion coefficient of 1.57 μm^2/s (1×10^{-7} cm^2/s) [488]. The higher diffusion coefficient observed in their study compared to ours might be due to the different media used, as HPAM in 1X PBS creates a more viscous environment, affecting the diffusion behavior of

M13 phages.

Additionally, Hu et al. [236], studied the diffusion properties of T4 and fNEL phages and reported apparent diffusion coefficients (D_{app}) of T4 and fNEL in water as 2.8×10^{-7} cm^2/s and 6.8×10^{-8} cm^2/s, respectively. Their methodology involved a two-chamber diffusion method where the diffusion of phages through filter paper was studied. The differences in physical properties of the phages and the experimental setup explain the variations in diffusion coefficients observed between the studies.

The discrepancy between the diffusion rates observed in our study and those reported in previous research can be attributed to the differences in methodology, phage size, shape, and the viscosity of the medium. Our study employed *in-situ* phage production within a standard media commonly used for phage-bacteria interactions, thereby closely replicating real-time conditions. By calculating the diffusion rate of M13 bacteriophage in this context, our findings provide a more accurate representation of the phage's behavior in natural environments.

Tzagoloff and Pratt [518] studied the initial steps of M13 infection, noting that the diffusion rate influenced the rate of attachment to host cells. Kasman et al. [273] explored phage replication thresholds and adsorption rates, finding that M13 phages have an adsorption rate constant of 3×10^{-11} cm^3/min. This adsorption rate is significant as it reflects the efficiency with which phages attach to host cells. Our study's K_3 value represents the uptake scaling factor, which is influenced by the concentration of phages surrounding the host cells. The adsorption rate provides a baseline for understanding the likelihood of phage-host interactions, while the K_3 value helps to model how these interactions scale with varying phage concentrations. Integrating these data allows for a more comprehensive understanding of infection dynamics and could improve the accuracy of our models in predicting phage behavior in varying environmental contexts.

In summary, while numerous studies have explored phage diffusion properties using various experimental and theoretical approaches, our research uniquely integrates single-cell data within a microfluidic environment to model phage dynamics. This approach offers a novel and potentially more accurate perspective on the diffusion rates and phage release patterns, contributing valuable insights to the field of phage biology and its applications.

Chapter 6

Conclusion and Future Work

6.1 Conclusion

In the modern age, humanity is continually engaged in a complex interaction with the microbial world. This ongoing dynamic, sometimes cooperative and sometimes antagonistic, has driven advancements in our understanding of microbial organisms. Over the years, various methodologies and technologies have been developed to probe these interactions across both population and single-cell levels. While population studies have provided broad insights into microbial behavior and its implications, single-cell analyses have pushed the boundaries further, offering a more granular view of individual microbial actions and responses.

This research focused on unveiling the relationship between bacteriophages and their bacterial hosts, exploring the mechanisms underlying phage infection processes. Bacteriophages, or phages, play a crucial role in modulating microbial populations, acting as natural regulators and potential therapeutic agents against pathogenic bacteria increasingly resistant to conventional antibiotics. In contrast, bacteria, including beneficial strains within the human microbiome, significantly influence health and disease. Understanding the interactions between phages and bacteria is not only fundamental to microbiology but also crucial for harnessing phages in medical and environmental applications.

In this study, we studied the interactions between the M13 bacteriophage and its host, *E. coli*, employing single-cell methodologies to understand their dynamic relationship. By introducing phages directly into the environment and through *in-situ* phage production within phage-capable cultures, we mirrored natural infection scenarios to deepen our understanding of their interactions.

The non-lytic, chronic lifecycle of the M13 phage enabled continuous observation of host and phage producer cells, allowing for extended analysis beyond the capabilities offered by lytic phages. Building upon population-level precedents, our findings affirm the significant role of host cell condition in determining infection susceptibility. Notably, larger cells exhibited a higher likelihood of infection, potentially due to increased surface area accessible to phages. Furthermore, we observed that cells with higher elongation rates—indicative of optimal growth conditions—were more prone to infection. Considering that in our experimental microfluidic setup, nutrients were evenly distributed and equally accessible to all cells, and temperature conditions were uniform across the device. Therefore, these environmental factors do not fully explain the observed variation in growth conditions and infection susceptibility among cells. This suggests that other factors, beyond nutrient availability and temperature, contribute to cellular growth condition, presenting an interesting avenue for future research to explore what these factors might be and how they influence phage-host interactions.

Our investigation looked at the role of spatial dynamics in infection probability. Despite the presence of flow and the resultant movement of phages, influenced by both fluid dynamics and Brownian motion, distance from the source still played a crucial role in infection probability. This phenomenon was even more pronounced in the agar-based experiments, where fluid movement is substantially slower, underscoring the importance of spatial positioning in relation to phage sources.

The primary objective of this study was to explore the ongoing phage infection process within bacterial cultures capable of producing phages, particularly focusing on cultures containing the helper plasmid. Initially, we examined the infection dynamics within these helper-plasmid-bearing cultures to understand their capacity for sustaining continuous phage production and subsequent infection processes. However, the observed infection rates within these cultures were considerably lower than anticipated (about 90%). This observation prompted a further review of existing literature, where we found studies indicating that phage protein III, produced by the helper plasmid, could interfere with bacterial pili production [319]. This prompted a shift in our experimental approach towards cultures devoid of the helper plasmid, where a significant increase in infection rates was subsequently noted.

In the final phase of this research, simulations were conducted to further investigate the role of proximity in the infection process, utilizing real-life data as a foundation. Employing the CellModeller platform, the M13 phage infection process were modeled to reflect actual experimental conditions. These simulations reaffirmed the significant impact of spatial proximity on infection likelihood. The data generated from these simulations not only validated our empirical observations but also provided deeper insights into how spatial

relationships between host cells and phages influence infection outcomes. This aspect of the study underscores the importance of considering spatial factors in understanding the complexities of phage-host interactions and contributes to a more nuanced view of infection dynamics within microbial communities.

In conclusion, this thesis not only contributes to the broader understanding of phage biology and host response mechanisms but also highlights the nuanced factors influencing phage infection dynamics. By integrating live-cell imaging with detailed morphological analysis, we offer new perspectives on how individual bacterial cells' size and growth conditions affect their interaction with phages.

6.2 Future work

6.2.1 Enhancement of Image Processing and Tracking Capabilities

One of the limitations in this study was the challenge in processing and tracking images with higher cell populations, particularly as errors increased with growing populations. While the infection process was successfully imaged for up to 48 hours, only the first 4-5 hours of data were usable due to these limitations. Future studies could benefit from the development or identification of more sophisticated image processing and tracking software. Additionally, employing a mother machine, which restricts cultures to a minimal number, might improve tracking capabilities. Although this approach may reduce the population and interaction under study, integrating this method with current findings could yield a more comprehensive understanding of the M13 infection mechanism.

6.2.2 Optimization of Microfluidic Device Design

The initial design of the in-house microfluidic device aimed to allow cell growth in one dimension. However, as populations increased, cells became compacted, leading to issues such as cell lysis and difficulties in distinguishing individual cells under the microscope, rendering manual and automated image processing unfeasible. Future work should focus on redesigning the microfluidic device to avoid these issues, drawing inspiration from studies that have successfully utilized microfluidic devices for extended periods. By addressing these design flaws, future studies could extend the duration of observable phage-bacteria interactions, providing deeper insights into the dynamics of infection processes.

6.2.3 Investigation of GFP-tagged Phage Particles

During experimental observations under fluorescent microscopy, the presence of small GFP-tagged particles was noted, visible only in the fluorescent channel. Preliminary steps, including surface panning, were undertaken to isolate these particles, leading to the hypothesis that they might be phage particles. This is intriguing because, unlike previous studies [462, 214], GFP was not intentionally displayed on the surface of these phages in our experiments. This discrepancy opens up a research avenue to determine whether these phages have inherently packed GFP within their capsid or have been genetically modified to display the protein on their surface. Initial attempts to engineer a phage using the phage display method to explore this phenomenon were made, setting a foundation for future research. Detailed descriptions of these preliminary experiments and their outcomes are provided in Appendix I.1.

6.2.4 M13 Phage Interaction with Gut Microbiome Cultures

Another research path initiated concerned the interaction of M13 phages with gut microbiome cultures. Initially, this study aimed to discern if cultures derived from patients were susceptible to M13 phage, evaluating infection rates across both isolated and communal culture setups. Surprisingly, among the various beneficial gut cultures received, one particular *E. coli* strain, identified for containing the pVR50 plasmid, showcased susceptibility to M13 infection. This discovery indicates a potential pathogenic intrusion within what is typically a beneficial gut environment, suggesting the feasibility of rectifying such imbalances through targeted phage intervention. Future research could delve deeper into this aspect, perhaps by incorporating CRISPR technology into the M13 genome for bacterial modulation. Initial blueprints for CRISPR-enhanced M13 phages were designed and developed as part of this study, setting a foundation for future research endeavors. These designs now await further testing and validation to assess their efficacy and potential applications.

Moreover, there's a pressing need to validate these engineered phages' efficacy *in-vivo* to ascertain their impact and efficiency in altering gut microbiome dynamics. This step is crucial for transitioning from theoretical to practical applications. Additionally, extending the scope of microbial cultures tested could provide broader insights into M13's infection spectrum and its utility in restoring gut microbiome balance.

References

[1] https://www.chem.agilent.com/store/biocalculators/calcODBacterial.jsp?_requestid=305051.

[2] *Bacteriophages. 2: Molecular and applied aspects*. Number 502 in Methods in molecular biology. Humana Press, New York, NY, 2009.

[3] Filamentous Bacteriophage: Biology, Phage Display and Nanotechnology Applications. *Current Issues in Molecular Biology*, 2011.

[4] Abir Abbad, Salem Abdelmalek, and Samir Bendoukha. Dynamics of a Turing-type reaction- diffusion model. 2021. Publisher: Unpublished.

[5] Stephen Abedon and Cameron Thomas-Abedon. Phage Therapy Pharmacology. *Current Pharmaceutical Biotechnology*, 11(1):28–47, January 2010.

[6] Stephen T. Abedon. Kinetics of Phage-Mediated Biocontrol of Bacteria. *Foodborne Pathogens and Disease*, 6(7):807–815, September 2009.

[7] Stephen T. Abedon, Troy D. Herschler, and David Stopar. Bacteriophage Latent-Period Evolution as a Response to Resource Availability. *Applied and Environmental Microbiology*, 67(9):4233–4241, September 2001.

[8] Stephen T. Abedon and Tena I. Katsaounis. Basic Phage Mathematics. In Martha R.J. Clokie, Andrew M. Kropinski, and Rob Lavigne, editors, *Bacteriophages: Methods and Protocols, Volume 3*, pages 3–30. Springer New York, New York, NY, 2018.

[9] Stephen T Abedon, Sarah J Kuhl, Bob G Blasdel, and Elizabeth Martin Kutter. Phage treatment of human infections. *Bacteriophage*, 1(2):66–85, 2011. Publisher: Taylor & Francis.

[10] Stephen Tobias Abedon. Bacteriophage Adsorption: Likelihood of Virion Encounter with Bacteria and Other Factors Affecting Rates. *Antibiotics*, 12(4):723, April 2023.

[11] Ana G. Abril, Mónica Carrera, Vicente Notario, Ángeles Sánchez-Pérez, and Tomás G. Villa. The Use of Bacteriophages in Biotechnology and Recent Insights into Proteomics. *Antibiotics*, 11(5):653, May 2022.

[12] Aneesha Achar, Rosemary Myers, and Chaitali Ghosh. Drug Delivery Challenges in Brain Disorders across the Blood–Brain Barrier: Novel Methods and Future Considerations for Improved Therapy. *Biomedicines*, 9(12):1834, December 2021.

[13] H.-W. Ackermann. Bacteriophage observations and evolution. *Research in Microbiology*, 154(4):245–251, May 2003.

[14] H.-W. Ackermann. 5500 Phages examined in the electron microscope. *Archives of Virology*, 152(2):227–243, February 2007.

[15] Hans-W. Ackermann. Phage Classification and Characterization. In Martha R.J. Clokie and Andrew M. Kropinski, editors, *Bacteriophages: Methods and Protocols, Volume 1: Isolation, Characterization, and Interactions*, pages 127–140. Humana Press, Totowa, NJ, 2009.

[16] Tomilola Adesina, Obinna Nwinyi, Nandita De, Olayemi Akinnola, and Emmanuel Omonigbehin. First Detection of Carbapenem-Resistant Escherichia fergusonii Strains Harbouring Beta-Lactamase Genes from Clinical Samples. *Pathogens*, 8(4):164, September 2019.

[17] Jiyoung Ahn and Richard B. Hayes. Environmental Influences on the Human Microbiome and Implications for Noncommunicable Disease. *Annual Review of Public Health*, 42(1):277–292, April 2021.

[18] Carlo Airola, Andrea Severino, Serena Porcari, William Fusco, Benjamin H. Mullish, Antonio Gasbarrini, Giovanni Cammarota, Francesca Romana Ponziani, and Gianluca Ianiro. Future Modulation of Gut Microbiota: From Eubiotics to FMT, Engineered Bacteria, and Phage Therapy. *Antibiotics*, 12(5):868, May 2023.

[19] Omnia A. Al-wdan, Omnya A. Sharallah, Nada A. Abdelwahab, Alshimaa O. Mohammed, Enas Elmowafy, and Mahmoud E. Soliman. Insights into microfabrication and implementation of microfluidics in pharmaceutical drug delivery and analysis. *OpenNano*, 12:100156, July 2023.

[20] T. Alkayyali, T. Cameron, B. Haltli, R.G. Kerr, and A. Ahmadi. Microfluidic and cross-linking methods for encapsulation of living cells and bacteria - A review. *Analytica Chimica Acta*, 1053:1–21, April 2019.

[21] Paige Allard, Fotini Papazotos, and Laurent Potvin-Trottier. Microfluidics for long-term single-cell time-lapse microscopy: Advances and applications. *Frontiers in Bioengineering and Biotechnology*, 10:968342, October 2022.

[22] Elke Allers, Cristina Moraru, Melissa B. Duhaime, Erica Beneze, Natalie Solonenko, Jimena Barrero-Canosa, Rudolf Amann, and Matthew B. Sullivan. Single-Cell And Population Level Viral Infection Dynamics Revealed By Phage, A Method To Visualize Intracellular And Free Viruses. *Environmental Microbiology*, 15(8):2306–2318, August 2013.

[23] M.A. Alting-Mees and J.M. Short. pBluescript II: gene mapping vectors. *Nucleic Acids Research*, 17(22):9494–9494, 1989.

[24] Kapil Amarnath, Avaneesh V. Narla, Sammy Pontrelli, Jiajia Dong, Jack Reddan, Brian R. Taylor, Tolga Caglar, Julia Schwartzman, Uwe Sauer, Otto X. Cordero, and Terence Hwa. Stress-induced metabolic exchanges between complementary bacterial types underly a dynamic mechanism of inter-species stress resistance. *Nature Communications*, 14(1):3165, May 2023.

[25] J. H. An, E. Goo, H. Kim, Y.-S. Seo, and I. Hwang. Bacterial quorum sensing and metabolic slowing in a cooperative population. *Proceedings of the National Academy of Sciences*, 111(41):14912–14917, October 2014.

[26] Andrew Sharpley. Fate and Transport of Nutrients: Phosphorus. Technical report, National Agricultural Water Quality Laboratory, 1995.

[27] Andrew Sharpley and Douglas Beegle. Managing Phosphorus for Agriculture and the Environment. Technical report, 2001.

[28] Steven S Andrews and Dennis Bray. Stochastic simulation of chemical reactions with spatial resolution and single molecule detail. *Physical Biology*, 1(3):137–151, September 2004.

[29] Dian Anggraini, Nobutoshi Ota, Yigang Shen, Tao Tang, Yo Tanaka, Yoichiroh Hosokawa, Ming Li, and Yaxiaer Yalikun. Recent advances in microfluidic devices for single-cell cultivation: methods and applications. *Lab on a Chip*, 22(8):1438–1468, 2022.

[30] Shelley Lynn Anna. Droplets and Bubbles in Microfluidic Devices. *Annual Review of Fluid Mechanics*, 48(1):285–309, January 2016.

[31] Esther-Maria Antão, Lothar H Wieler, and Christa Ewers. Adhesive threads of extraintestinal pathogenic Escherichia coli. *Gut Pathogens*, 1(1):22, 2009.

[32] Marco Antonio Arap. Phage display technology: applications and innovations. *Genetics and Molecular Biology*, 28(1):1–9, March 2005.

[33] John Armstrong, Richard N. Perham, and John E. Walker. Domain structure of bacteriophage fd adsorption protein. *FEBS Letters*, 135(1):167–172, November 1981.

[34] Norris Armstrong, Nils B Adey, Stephen J McConnell, and Brian K Kay. Vectors for phage display. In *Phage display of peptides and proteins*, pages 35–53. Elsevier, 1996.

[35] RJ Atterbury. Bacteriophage biocontrol in animals and meat products. *Microbial biotechnology*, 2(6):601–612, 2009. Publisher: Wiley Online Library.

[36] Erin L. Attrill, Rory Claydon, Urszula Łapińska, Mario Recker, Sean Meaden, Aidan T. Brown, Edze R. Westra, Sarah V. Harding, and Stefano Pagliara. Individual bacteria in structured environments rely on phenotypic resistance to phage. *PLOS Biology*, 19(10):e3001406, October 2021.

[37] Erin L. Attrill, Urszula Łapińska, Edze R. Westra, Sarah V. Harding, and Stefano Pagliara. Slow growing bacteria survive bacteriophage in isolation. *ISME Communications*, 3(1):95, September 2023.

[38] Simon V. Avery. Microbial cell individuality and the underlying sources of heterogeneity. *Nature Reviews Microbiology*, 4(8):577–587, August 2006.

[39] Monya Baker. Cellular imaging: Taking a long, hard look. *Nature*, 466(7310):1137–1140, August 2010.

[40] Leili Aghebati-Malekibak Bakhshinejad, Behzad Baradaran, Morteza Motallebnezhad, Ali Aghebati-Maleki, Hamid Nickho, Mehdi Yousefi, and Jafar Majidi. Phage display as a promising approach for vaccine development. *Journal of Biomedical Science*, 23, 2016. Publisher: BioMed Central.

[41] Nathalie Q Balaban, Jack Merrin, Remy Chait, Lukasz Kowalik, and Stanislas Leibler. Bacterial persistence as a phenotypic switch. *Science*, 305(5690):1622–1625, 2004. Publisher: American Association for the Advancement of Science.

[42] Enrique Balleza, J Mark Kim, and Philippe Cluzel. Systematic characterization of maturation time of fluorescent proteins in living cells. *Nature methods*, 15(1):47–51, 2018. Publisher: Nature Publishing Group US New York.

[43] Brad Larson and Peter Banks. Z-Stacking of Single Plane Digital Widefield Fluorescent Images, 2014.

[44] Hagit Bar, Iftach Yacoby, and Itai Benhar. Killing cancer cells by targeted drug-carrying phage nanomedicines. *BMC biotechnology*, 8(1):1–14, 2008. Publisher: BioMed Central.

[45] Carlos F Barbas, DR Burton, JK Scott, and GJ Silverman. Phage display. *A Laboratory Manual*, 2001. Publisher: Cold spring harbor laboratory press Cold Spring Harbor, NY, USA.

[46] Marshall Albert Barber. The rate of multiplication of Bacillus coli at different temperatures. *The Journal of Infectious Diseases*, pages 379–400, 1908. Publisher: JSTOR.

[47] Chloé S. Baron, Aditya Barve, Mauro J. Muraro, Reinier van der Linden, Gitanjali Dharmadhikari, Anna Lyubimova, Eelco J.P. de Koning, and Alexander van Oudenaarden. Cell Type Purification by Single-Cell Transcriptome-Trained Sorting. *Cell*, 179(2):527–542.e19, October 2019.

[48] Jeremy J Barr. A bacteriophages journey through the human body. *Immunological Reviews*, 279(1):106–122, 2017. Publisher: Wiley Online Library.

[49] Simona Bartkova, Marko Vendelin, Immanuel Sanka, Pille Pata, and Ott Scheler. CellProfiler: A fit tool for image analysis in droplet microfluidics. preprint, Bioinformatics, October 2019.

[50] Batinovic, Wassef, Knowler, Rice, Stanton, Rose, Tucci, Nittami, Vinh, Drummond, Sobey, Chan, Seviour, Petrovski, and Franks. Bacteriophages in Natural and Artificial Environments. *Pathogens*, 8(3):100, July 2019.

[51] Amy L. Bauer, Catherine A. A. Beauchemin, and Alan S. Perelson. Agent-based modeling of host-pathogen systems: The successes and challenges. *Information Sciences*, 179(10):1379–1389, April 2009.

[52] BD - Canada. Study Examines Clinical and Economic Impact of Antimicrobial Resistance at Acute Care Facilities, 2020.

[53] James M. Bean, Eric D. Siggia, and Frederick R. Cross. Coherence and Timing of Cell Cycle Start Examined at Single-Cell Resolution. *Molecular Cell*, 21(1):3–14, January 2006.

[54] Scott A. Beatson, Nouri L. Ben Zakour, Makrina Totsika, Brian M. Forde, Rebecca E. Watts, Amanda N. Mabbett, Jan M. Szubert, Sohinee Sarkar, Minh-Duy Phan, Kate M. Peters, Nicola K. Petty, Nabil-Fareed Alikhan, Mitchell J. Sullivan, Jayde A. Gawthorne, Mitchell Stanton-Cook, Nguyen Thi Khanh Nhu, Teik Min Chong, Wai-Fong Yin, Kok-Gan Chan, Viktoria Hancock, David W. Ussery, Glen C. Ulett, and Mark A. Schembri. Molecular Analysis of Asymptomatic Bacteriuria Escherichia coli Strain VR50 Reveals Adaptation to the Urinary Tract by Gene Acquisition. *Infection and Immunity*, 83(5):1749–1764, May 2015.

[55] Alejandro Beceiro, María Tomás, and Germán Bou. Antimicrobial resistance and virulence: a successful or deleterious association in the bacterial world? *Clinical Microbiology Reviews*, 26(2):185–230, April 2013.

[56] Konrad Beck and Rudolf M. Duenk. Flexibility of bacteriophage M13: Comparison of hydrodynamic measurements with electron microscopy. *Journal of Structural Biology*, 105(1-3):22–27, October 1990.

[57] Gabor Beke, Matej Stano, and Lubos Klucar. Modelling the interaction between bacteriophages and their bacterial hosts. *Mathematical Biosciences*, 279:27–32, September 2016.

[58] Stuart Berg, Dominik Kutra, Thorben Kroeger, Christoph N. Straehle, Bernhard X. Kausler, Carsten Haubold, Martin Schiegg, Janez Ales, Thorsten Beier, Markus Rudy, Kemal Eren, Jaime I Cervantes, Buote Xu, Fynn Beuttenmueller, Adrian Wolny, Chong Zhang, Ullrich Koethe, Fred A. Hamprecht, and Anna Kreshuk. ilastik: interactive machine learning for (bio)image analysis. *Nature Methods*, 16(12):1226–1232, December 2019.

[59] Aude G. Bernheim, Vincent K. Libis, Ariel B. Lindner, and Edwin H. Wintermute. Phage-mediated Delivery of Targeted sRNA Constructs to Knock Down Gene Expression in E. coli. *Journal of Visualized Experiments*, (109):53618, March 2016.

[60] Shweta Bhatt, Petr G. Leiman, and Nicholas M.I. Taylor. Tail Structure and Dynamics. In *Encyclopedia of Virology*, pages 186–193. Elsevier, 2021.

[61] K M. Bircsak, V Van Duinen, S J. Trietsch, A J. Van Zonneveld, T Hankemeier, A Saleh, and P Vulto. Abstract 2051: Perfusable 3D angiogenesis in a high-throughput microfluidic culture platform. *Cancer Research*, 78(13_Supplement):2051–2051, July 2018.

[62] Katie Bodner, Arin L. Melkonian, Angela I.M. Barth, Takamasa Kudo, Yu Tanouchi, and Markus W. Covert. Engineered Fluorescent E. coli Lysogens Allow Live-Cell Imaging of Functional Prophage Induction Triggered inside Macrophages. *Cell Systems*, 10(3):254–264.e9, March 2020.

[63] Katie Bodner, Arin L. Melkonian, and Markus W. Covert. A Protocol to Engineer Bacteriophages for Live-Cell Imaging of Bacterial Prophage Induction Inside Mammalian Cells. *STAR Protocols*, 1(2):100084, September 2020.

[64] Jef D. Boeke, Peter Model, and Norton D. Zinder. Effects of bacteriophage f1 gene III protein on the host cell membrane. *Molecular and General Genetics MGG*, 186(2):185–192, July 1982.

[65] Sean C. Booth, William P. J. Smith, and Kevin R. Foster. The evolution of short- and long-range weapons for bacterial competition. *Nature Ecology & Evolution*, 7(12):2080–2091, November 2023.

[66] Barbara Bortot, Maura Apollonio, Gabriele Baj, Laura Andolfi, Luisa Zupin, Sergio Crovella, Matteo di Giosia, Andrea Cantelli, Roberto Saporetti, and Luca Ulfo. Advanced photodynamic therapy with an engineered M13 phage targeting EGFR: Mitochondrial localization and autophagy induction in ovarian cancer cell lines. *Free Radical Biology and Medicine*, 179:242–251, 2022. Publisher: Elsevier.

[67] D. E. Bradley. Ultrastructure of bacteriophage and bacteriocins. *Bacteriological Reviews*, 31(4):230–314, December 1967.

[68] Dana Braff, David Shis, and James J. Collins. Synthetic biology platform technologies for antimicrobial applications. *Advanced Drug Delivery Reviews*, 105(Pt A):35–43, October 2016.

[69] Lucas P. P. Braga, Aymé Spor, Witold Kot, Marie-Christine Breuil, Lars H. Hansen, João C. Setubal, and Laurent Philippot. Impact of phages on soil bacterial communities and nitrogen availability under different assembly scenarios. *Microbiome*, 8(1):52, December 2020.

[70] Tomaž Bratkovič. Progress in phage display: evolution of the technique and its applications. *Cellular and molecular life sciences*, 67:749–767, 2010. Publisher: Springer.

[71] B.F. Brehm-Stecher. Flow Cytometry. In *Encyclopedia of Food Microbiology*, pages 943–953. Elsevier, 2014.

[72] Byron F. Brehm-Stecher and Eric A. Johnson. Single-Cell Microbiology: Tools, Technologies, and Applications. *Microbiology and Molecular Biology Reviews*, 68(3):538–559, September 2004.

[73] Charles C. Brinton. THE STRUCTURE, FUNCTION, SYNTHESIS AND GENETIC CONTROL OF BACTERIAL PILI AND A MOLECULAR MODEL FOR DNA AND RNA TRANSPORT IN GRAM NEGATIVE BACTERIA*. *Transactions of the New York Academy of Sciences*, 27(8 Series II):1003–1054, June 1965.

[74] Thomas Briot, Camille Kolenda, Tristan Ferry, Mathieu Medina, Frederic Laurent, Gilles Leboucher, and Fabrice Pirot. Paving the way for phage therapy using novel drug delivery approaches. *Journal of Controlled Release*, 347:414–424, July 2022.

[75] Jennifer A. N. Brophy, Alexander J. Triassi, Bryn L. Adams, Rebecca L. Renberg, Dimitra N. Stratis-Cullum, Alan D. Grossman, and Christopher A. Voigt. Engineered integrative and conjugative elements for efficient and inducible DNA transfer to undomesticated bacteria. *Nature Microbiology*, 3(9):1043–1053, August 2018.

[76] Ineke Brouwer, Heta Piyush Patel, Joseph Victor Willem Meeussen, Wim Pomp, and Tineke Laura Lenstra. Single-Molecule Fluorescence Imaging in Living Saccharomyces cerevisiae Cells. *STAR Protocols*, 1(3):100142, December 2020.

[77] Frank Brunton. Update of Revisions to the Early Silurian Stratigraphy of the Niagara Escarpment: Integration of Sequence Stratigraphy, Sedimentology and Hydrogeology to delineate Hydrogeologic Units. 2009. Publisher: Ontario Geological Survey.

[78] James Bull, Kelly Christensen, Carly Scott, Benjamin Jack, Cameron Crandall, and Stephen Krone. Phage-Bacterial Dynamics with Spatial Structure: Self Organization around Phage Sinks Can Promote Increased Cell Densities. *Antibiotics*, 7(1):8, January 2018.

[79] Robert Burger and Jens Ducrée. Handling and analysis of cells and bioparticles on centrifugal microfluidic platforms. *Expert Review of Molecular Diagnostics*, 12(4):407–421, May 2012.

[80] Alina Burmeister, Fabienne Hilgers, Annika Langner, Christoph Westerwalbesloh, Yannic Kerkhoff, Niklas Tenhaef, Thomas Drepper, Dietrich Kohlheyer, Eric von Lieres, Stephan Noack, and Alexander Grünberger. A microfluidic co-cultivation platform to investigate microbial interactions at defined microenvironments. *Lab on a Chip*, 19(1):98–110, 2019.

[81] Christopher J. Burrell, Colin R. Howard, and Frederick A. Murphy. Virus Replication. In *Fenner and White's Medical Virology*, pages 39–55. Elsevier, 2017.

[82] P. Bárdy, R. Pantůček, M. Benešík, and J. Doškař. Genetically modified bacteriophages in applied microbiology. *Journal of Applied Microbiology*, 121(3):618–633, September 2016.

[83] Juan C Caicedo, Sam Cooper, Florian Heigwer, Scott Warchal, Peng Qiu, Csaba Molnar, Aliaksei S Vasilevich, Joseph D Barry, Harmanjit Singh Bansal, Oren Kraus, Mathias Wawer, Lassi Paavolainen, Markus D Herrmann, Mohammad Rohban, Jane Hung, Holger Hennig, John Concannon, Ian Smith, Paul A Clemons, Shantanu Singh, Paul Rees, Peter Horvath, Roger G Linington, and Anne E Carpenter. Data-analysis strategies for image-based cell profiling. *Nature Methods*, 14(9):849–863, September 2017.

[84] Benjamin J. Cairns, Andrew R. Timms, Vincent A. A. Jansen, Ian F. Connerton, and Robert J. H. Payne. Quantitative Models of In Vitro Bacteriophage–Host Dynamics and Their Application to Phage Therapy. *PLoS Pathogens*, 5(1):e1000253, January 2009.

[85] À. Calsina and J.J. Rivaud. A size structured model for bacteria–phages interaction. *Nonlinear Analysis: Real World Applications*, 15:100–117, January 2014.

[86] Allan Campbell. Conditions For The Existence of Bacteriophage. *Evolution*, 15(2):153–165, June 1961.

[87] L G Caro and M Schnös. The attachment of the male-specific bacteriophage F1 to sensitive strains of Escherichia coli. *Proceedings of the National Academy of Sciences*, 56(1):126–132, July 1966.

[88] William Cenens, Angela Makumi, Sander K. Govers, Rob Lavigne, and Abram Aertsen. Viral Transmission Dynamics at Single-Cell Resolution Reveal Transiently Immune Subpopulations Caused by a Carrier State Association. *PLOS Genetics*, 11(12):e1005770, December 2015.

[89] CE Chan, AHY Chan, BJ Hanson, and EE Ooi. The use of antibodies in the treatment of infectious diseases. *Singapore Med J*, 50(7):663–672, 2009.

[90] Cheng Chang, Wennan Guo, Xinbo Yu, Chaoyi Guo, Nan Zhou, Xiaokui Guo, Ru-Lin Huang, Qingtian Li, and Yongzhang Zhu. Engineered M13 phage as a novel therapeutic bionanomaterial for clinical applications: From tissue regeneration to cancer therapy. *Materials Today Bio*, page 100612, 2023. Publisher: Elsevier.

[91] L. Chasteen, J. Ayriss, P. Pavlik, and A. R. M. Bradbury. Eliminating helper phage from phage display. *Nucleic Acids Research*, 34(21):e145–e145, December 2006.

[92] U.Eong Cheah, William A. Weigand, and Benjamin C. Stark. Effects of recombinant plasmid size on cellular processes in Escherichia coli. *Plasmid*, 18(2):127–134, September 1987.

[93] Mathieu F. Chellat, Luka Raguž, and Rainer Riedl. Targeting Antibiotic Resistance. *Angewandte Chemie International Edition*, 55(23):6600–6626, June 2016.

[94] Yi-Yang Chen, Chien-Chen Wu, Jye-Lin Hsu, Hwei-Ling Peng, Hwan-You Chang, and Tri-Rung Yew. Surface Rigidity Change of *Escherichia coli* after Filamentous Bacteriophage Infection. *Langmuir*, 25(8):4607–4614, April 2009.

[95] Cynthia Maria Chibani, Anton Farr, Sandra Klama, Sascha Dietrich, and Heiko Liesegang. Classifying the Unclassified: A Phage Classification Method. *Viruses*, 11(2):195, February 2019.

[96] Pei Yu Chiou, Aaron T. Ohta, and Ming C. Wu. Massively parallel manipulation of single cells and microparticles using optical images. *Nature*, 436(7049):370–372, July 2005.

[97] Steven M. Chirieleison, Taylor A. Bissell, Christopher C. Scelfo, Jordan E. Anderson, Yong Li, Doug J. Koebler, and Bridget M. Deasy. Automated live cell imaging systems reveal dynamic cell behavior. *Biotechnology Progress*, 27(4):913–924, July 2011.

[98] Huikuan Chu, Yi Duan, Sonja Lang, Lu Jiang, Yanhan Wang, Cristina Llorente, Jinyuan Liu, Selene Mogavero, Francisco Bosques-Padilla, and Juan G Abraldes. The Candida albicans exotoxin candidalysin promotes alcohol-associated liver disease. *Journal of hepatology*, 72(3):391–400, 2020. Publisher: Elsevier.

[99] I. A. Chucklova, V. S. Sotnikova, V. N. Shchipakin, and Y. V. Evtodienko. [The fragmentation and reconstruction of the oligomycin-sensitive ATPase system of liver mitochondria]. *Biokhimiia (Moscow, Russia)*, 40(2):227–232, April 1975.

[100] Kwanghun Chung, Yoosik Kim, Jitendra S Kanodia, Emily Gong, Stanislav Y Shvartsman, and Hang Lu. A microfluidic array for large-scale ordering and orientation of embryos. *Nature Methods*, 8(2):171–176, February 2011.

[101] Robert J Citorik, Mark Mimee, and Timothy K Lu. Sequence-specific antimicrobials using efficiently delivered RNA-guided nucleases. *Nature Biotechnology*, 32(11):1141–1145, November 2014.

[102] Tim Clackson and Henry B Lowman. *Phage display a practical approach*. Oxford University Press, Oxford; New York, 2004. OCLC: 1162006034.

[103] Megan Clapp, Nadia Aurora, Lindsey Herrera, Manisha Bhatia, Emily Wilen, and Sarah Wakefield. Gut Microbiota's Effect on Mental Health: The Gut-Brain Axis. *Clinics and Practice*, 7(4):987, September 2017.

[104] Margaret Clarke, Lucinda Maddera, Robin L. Harris, and Philip M. Silverman. F-pili dynamics by live-cell imaging. *Proceedings of the National Academy of Sciences*, 105(46):17978–17981, November 2008.

[105] Jose C. Clemente, Luke K. Ursell, Laura Wegener Parfrey, and Rob Knight. The Impact of the Gut Microbiota on Human Health: An Integrative View. *Cell*, 148(6):1258–1270, March 2012.

[106] Martha R.J. Clokie, Andrew D. Millard, Andrey V. Letarov, and Shaun Heaphy. Phages in nature. *Bacteriophage*, 1(1):31–45, January 2011.

[107] Martha R.J. Clokie, Thomas Erik Sicheritz-Pontén, Francesca Hodges, Anisha Thanki, Marie Vieu, Paul Robson, Andy Millardi Jill Theaker, and Melissa Haines. Urinary Tract Infections As An Urgent Need For The Clinical Deployment Of Phage Therapy A Review.

[108] David J. Collins, Belinda Morahan, Jose Garcia-Bustos, Christian Doerig, Magdalena Plebanski, and Adrian Neild. Two-dimensional single-cell patterning with one cell per well driven by surface acoustic waves. *Nature Communications*, 6(1):8686, November 2015.

[109] André M. Comeau, Denise Tremblay, Sylvain Moineau, Thomas Rattei, Alla I. Kushkina, Fedor I. Tovkach, Henry M. Krisch, and Hans-Wolfgang Ackermann. Phage Morphology Recapitulates Phylogeny: The Comparative Genomics of a New Group of Myoviruses. *PLoS ONE*, 7(7):e40102, July 2012.

[110] Callum Cooper, Shazeeda Koonjan, and Anders Nilsson. Enhancing Whole Phage Therapy and Their Derived Antimicrobial Enzymes through Complex Formulation. *Pharmaceuticals*, 11(2):34, April 2018.

[111] Michael G. Cortes, Jimmy T. Trinh, Lanying Zeng, and Gábor Balázsi. Late-Arriving Signals Contribute Less to Cell-Fate Decisions. *Biophysical Journal*, 113(9):2110–2120, November 2017.

[112] Katharine Z. Coyte and Seth Rakoff-Nahoum. Understanding Competition and Cooperation within the Mammalian Gut Microbiome. *Current Biology*, 29(11):R538–R544, June 2019.

[113] Josicelli Souza Crispim, Roberto Sousa Dias, Pedro Marcus Pereira Vidigal, Maíra Paula de Sousa, Cynthia Canêdo da Silva, Mateus Ferreira Santana, and Sérgio Oliveira de Paula. Screening and characterization of prophages in Desulfovibrio genomes. *Scientific Reports*, 8(1):9273, December 2018.

[114] A. Culot, N. Grosset, and M. Gautier. Overcoming the challenges of phage therapy for industrial aquaculture: A review. *Aquaculture*, 513:734423, November 2019.

[115] Caroline Cuny, Maïalène Lesbats, and Sam Dukan. Induction of a Global Stress Response during the First Step of *Escherichia coli* Plate Growth. *Applied and Environmental Microbiology*, 73(3):885–889, February 2007.

[116] Kevin J. Cutler, Carsen Stringer, Teresa W. Lo, Luca Rappez, Nicholas Stroustrup, S. Brook Peterson, Paul A. Wiggins, and Joseph D. Mougous. Omnipose: a high-precision morphology-independent solution for bacterial cell segmentation. *Nature Methods*, 19(11):1438–1448, November 2022.

[117] Ram Hari Dahal, Yoon-Jung Choi, Shukho Kim, and Jungmin Kim. Differentiation of Escherichia fergusonii and Escherichia coli Isolated from Patients with Inflammatory Bowel Disease/Ischemic Colitis and Their Antimicrobial Susceptibility Patterns. *Antibiotics*, 12(1):154, January 2023.

[118] Michael E. Dailey, Sidney L Shaw, Jason R. Swedlow, Paul D. Andrews, Matthias F. Langhorst, and Michael W. Davidson. Education in Microscopy and Digital Imaging. Technical report, Department of Biological Sciences and Neuroscience Program, 369 Biology Building, University of Iowa, Iowa City, Iowa, 52242.

[119] Holger Daims, Sebastian Lücker, and Michael Wagner. *daime* , a novel image analysis program for microbial ecology and biofilm research. *Environmental Microbiology*, 8(2):200–213, February 2006.

[120] Vinh T. Dang and Matthew B. Sullivan. Emerging methods to study bacteriophage infection at the single-cell level. *Frontiers in Microbiology*, 5, December 2014.

[121] Kimberly M. Davis and Ralph R. Isberg. Defining heterogeneity within bacterial populations via single cell approaches. *BioEssays*, 38(8):782–790, August 2016.

[122] Laura De Las Heras-García, Irati Zabalegui, and Olatz Pampliega. Methods to study primary cilia and autophagy in the brain. In *Methods in Cell Biology*, volume 176, pages 217–234. Elsevier, 2023.

[123] Jeroen De Smet, Michael Zimmermann, Maria Kogadeeva, Pieter-Jan Ceyssens, Wesley Vermaelen, Bob Blasdel, Ho Bin Jang, Uwe Sauer, and Rob Lavigne. High coverage metabolomics analysis reveals phage-specific alterations to *Pseudomonas aeruginosa* physiology during infection. *The ISME Journal*, 10(8):1823–1835, August 2016.

[124] Aurore Delaigle and Peter Hall. On optimal kernel choice for deconvolution. *Statistics & Probability Letters*, 76(15):1594–1602, September 2006.

[125] Max Delbrück. Adsorption of bacteriophage under various physiological conditions of the host. *The Journal of general physiology*, 23(5):631, 1940. Publisher: The Rockefeller University Press.

[126] Thomas Denes and Martin Wiedmann. Environmental responses and phage susceptibility in foodborne pathogens: implications for improving applications in food safety. *Current Opinion in Biotechnology*, 26:45–49, April 2014.

[127] Yi-Jie Deng and Shiao Y. Wang. Synergistic growth in bacteria depends on substrate complexity. *Journal of Microbiology*, 54(1):23–30, January 2016.

[128] Denis Wasley. Phosphorus: Sources, Forms, Impact on Water Quality: A general overview. Technical report, 2007.

[129] Les Dethlefsen, Sue Huse, Mitchell L Sogin, and David A Relman. The Pervasive Effects of an Antibiotic on the Human Gut Microbiota, as Revealed by Deep 16S rRNA Sequencing. *PLoS Biology*, 6(11):e280, November 2008.

[130] MF d'Herelle. Sur Un Microbe Invisible Antagoniste Des Bacilles Dysentériques. *Acta Kravsi*, 1961. Publisher: Ministerio de Asistencia Social y Salud Pública.

[131] Benjamin J. T. Dodd and Joel M. Kralj. Live Cell Imaging Reveals pH Oscillations in Saccharomyces cerevisiae During Metabolic Transitions. *Scientific Reports*, 7(1):13922, October 2017.

[132] Pilar Domingo-Calap, Lucas Mora-Quilis, and Rafael Sanjuán. Social bacteriophages. *Microorganisms*, 8(4):533, 2020. Publisher: MDPI.

[133] Xue Dong, Pei Pan, Jing-Jie Ye, Qiu-Ling Zhang, and Xian-Zheng Zhang. Hybrid M13 bacteriophage-based vaccine platform for personalized cancer immunotherapy. *Biomaterials*, 289:121763, October 2022.

[134] Xue Dong, Pei Pan, Di-Wei Zheng, Peng Bao, Xuan Zeng, and Xian-Zheng Zhang. Bioinorganic hybrid bacteriophage for modulation of intestinal microbiota to remodel tumor-immune microenvironment against colorectal cancer. *Science Advances*, 6(20):eaba1590, 2020. Publisher: American Association for the Advancement of Science.

[135] Gian Paolo Dotto, Vincenzo Enea, and Norton D Zinderi. Functional analysis of bacteriophage f1 intergenic region. *Virology*, 114(2):463–473, 1981. Publisher: Elsevier.

[136] Oliver J. Dressler, Richard M. Maceiczyk, Soo-Ik Chang, and Andrew J. deMello. Droplet-Based Microfluidics: Enabling Impact on Drug Discovery. *SLAS Discovery*, 19(4):483–496, April 2014.

[137] Andrea Du Toit. The language of phages. *Nature Reviews Microbiology*, 15(3):135–135, March 2017.

[138] Yi Duan, Ry Young, and Bernd Schnabl. Bacteriophages and their potential for treatment of gastrointestinal diseases. *Nature Reviews Gastroenterology & Hepatology*, 19(2):135–144, February 2022.

[139] Adrien Ducret, Etienne Maisonneuve, Philippe Notareschi, Alain Grossi, Tâm Mignot, and Sam Dukan. A Microscope Automated Fluidic System to Study Bacterial Processes in Real Time. *PLoS ONE*, 4(9):e7282, September 2009.

[140] Olive Jean Dunn. Multiple comparisons among means. *Journal of the American statistical association*, 56(293):52–64, 1961. Publisher: Taylor & Francis.

[141] Christian Dusny and Alexander Grünberger. Microfluidic single-cell analysis in biotechnology: from monitoring towards understanding. *Current Opinion in Biotechnology*, 63:26–33, June 2020.

[142] Christian Dusny, Alexander Grünberger, Christopher Probst, Wolfgang Wiechert, Dietrich Kohlheyer, and Andreas Schmid. Technical bias of microcultivation environments on single-cell physiology. *Lab on a Chip*, 15(8):1822–1834, 2015.

[143] Ron L Dy, Luciano A Rigano, and Peter C Fineran. Phage-based biocontrol strategies and their application in agriculture and aquaculture. *Biochemical Society Transactions*, 46(6):1605–1613, 2018. Publisher: Portland Press Ltd.

[144] Oleh Dzyubachyk, Jeroen Essers, Wiggert A. Van Cappellen, Céline Baldeyron, Akiko Inagaki, Wiro J. Niessen, and Erik Meijering. Automated analysis of time-lapse fluorescence microscopy images: from live cell images to intracellular foci. *Bioinformatics*, 26(19):2424–2430, October 2010.

[145] Oleh Dzyubachyk, Wiggert A Van Cappellen, Jeroen Essers, Wiro J Niessen, and Erik Meijering. Advanced level-set-based cell tracking in time-lapse fluorescence microscopy. *IEEE transactions on medical imaging*, 29(3):852–867, 2010. Publisher: IEEE.

[146] Mária Džunková, Soo Jen Low, Joshua N. Daly, Li Deng, Christian Rinke, and Philip Hugenholtz. Defining the human gut host–phage network through single-cell viral tagging. *Nature Microbiology*, 4(12):2192–2203, August 2019.

[147] Walead Ebrahimizadeh and Masoumeh Rajabibazl. Bacteriophage vehicles for phage display: biology, mechanism, and application. *Current microbiology*, 69:109–120, 2014. Publisher: Springer.

[148] Richard Ebright, Qianping Dong, and Joachim Messing. Corrected nucleotide sequence of M13mp18 gene III. *Gene*, 114(1):81–83, 1992. Publisher: Elsevier.

[149] Rotem Edgar, Nir Friedman, Shahar Molshanski-Mor, and Udi Qimron. Reversing Bacterial Resistance to Antibiotics by Phage-Mediated Delivery of Dominant Sensitive Genes. *Applied and Environmental Microbiology*, 78(3):744–751, February 2012.

[150] Michael B Elowitz, Arnold J Levine, Eric D Siggia, and Peter S Swain. Stochastic gene expression in a single cell. *Science*, 297(5584):1183–1186, 2002. Publisher: American Association for the Advancement of Science.

[151] T. Emonet, C. M. Macal, M. J. North, C. E. Wickersham, and P. Cluzel. AgentCell: a digital single-cell assay for bacterial chemotaxis. *Bioinformatics*, 21(11):2714–2721, June 2005.

[152] New England Biolabs. NEBuilder HiFi DNA Assembly Reaction (E2621) v2. preprint, April 2020.

[153] New England Biolabs. PCR Protocol for Phusion High-Fidelity DNA Polymerase (M0530) v3. preprint, March 2020.

[154] Dmitry Ershov, Minh-Son Phan, Joanna W. Pylvänäinen, Stéphane U. Rigaud, Laure Le Blanc, Arthur Charles-Orszag, James R. W. Conway, Romain F. Laine, Nathan H. Roy, Daria Bonazzi, Guillaume Duménil, Guillaume Jacquemet, and Jean-Yves Tinevez. TrackMate 7: integrating state-of-the-art segmentation algorithms into tracking pipelines. *Nature Methods*, 19(7):829–832, July 2022.

[155] Sylvie Estrela and Sam P. Brown. Community interactions and spatial structure shape selection on antibiotic resistant lineages. *PLOS Computational Biology*, 14(6):e1006179, June 2018.

[156] Kevin M Esvelt and Harris H Wang. Genome-scale engineering for systems and synthetic biology. *Molecular systems biology*, 9(1):641, 2013. Publisher: John Wiley & Sons, Ltd Chichester, UK.

[157] Andreas Ettinger and Torsten Wittmann. Fluorescence live cell imaging. In *Methods in Cell Biology*, volume 123, pages 77–94. Elsevier, 2014.

[158] Hyone-Myong Eun. Marker/Reporter Enzymes. In *Enzymology Primer for Recombinant DNA Technology*, pages 567–645. Elsevier, 1996.

[159] Umer Farooq, Qiaoli Yang, Muhammad Wajid Ullah, and Shenqi Wang. Bacterial biosensing: Recent advances in phage-based bioassays and biosensors. *Biosensors and Bioelectronics*, 118:204–216, October 2018.

[160] Umer Farooq, Qiaoli Yang, M Wajid Ullah, and Shenqi Wang. Principle and development of phage-based biosensors. *Biosens. Environ. Monit*, 1:1–18, 2019.

[161] Bradley J. Feilmeier, Ginger Iseminger, Diane Schroeder, Hannali Webber, and Gregory J. Phillips. Green Fluorescent Protein Functions as a Reporter for Protein Localization in *Escherichia coli*. *Journal of Bacteriology*, 182(14):4068–4076, July 2000.

[162] Peter Fekkes and Arnold J. M. Driessen. Protein Targeting to the Bacterial Cytoplasmic Membrane. *Microbiology and Molecular Biology Reviews*, 63(1):161–173, March 1999.

[163] Lucía Fernández, Ana Rodríguez, and Pilar García. Phage or foe: an insight into the impact of viral predation on microbial communities. *The ISME Journal*, 12(5):1171–1179, May 2018.

[164] Grazziela P Figueredo, Uwe Aickelin, and Peer-Olaf Siebers. Systems dynamics or agent-based modelling for immune simulation? pages 81–94. Springer, 2011.

[165] Grazziela P Figueredo, Peer-Olaf Siebers, Markus R Owen, Jenna Reps, and Uwe Aickelin. Comparing stochastic differential equations and agent-based modelling and simulation for early-stage cancer. *PloS one*, 9(4):e95150, 2014. Publisher: Public Library of Science.

[166] Alfred Fillol-Salom, Ahlam Alsaadi, Jorge A. Moura de Sousa, Li Zhong, Kevin R. Foster, Eduardo P. C. Rocha, José R. Penadés, Hanne Ingmer, and Jakob Haaber. Bacteriophages benefit from generalized transduction. *PLOS Pathogens*, 15(7):e1007888, July 2019.

[167] Michael A. Fischbach and Julia A. Segre. Signaling in Host-Associated Microbial Communities. *Cell*, 164(6):1288–1300, March 2016.

[168] Skye R. S. Fishbein, Bejan Mahmud, and Gautam Dantas. Antibiotic perturbations to the gut microbiome. *Nature Reviews Microbiology*, 21(12):772–788, December 2023.

[169] A Fleming. Penicillin's Finder Assays Its Future; Sir Alexander Fleming Says Improved Dosage Method Is Needed to Extend Use Other Scientists Praised Self-Medication Decried. *The New York Times*, 21, 1945.

[170] Marc Fransen, Paul P Van Veldhoven, and Suresh SUBRAMANI. Identification of peroxisomal proteins by using M13 phage protein VI phage display: molecular evidence that mammalian peroxisomes contain a 2, 4-dienoyl-CoA reductase. *Biochemical Journal*, 340(2):561–568, 1999. Publisher: Portland Press Ltd.

[171] Shiri Freilich, Raphy Zarecki, Omer Eilam, Ella Shtifman Segal, Christopher S. Henry, Martin Kupiec, Uri Gophna, Roded Sharan, and Eytan Ruppin. Competitive and cooperative metabolic interactions in bacterial communities. *Nature Communications*, 2(1):589, December 2011.

[172] Dan Frenkel, Odelia Katz, and Beka Solomon. Immunization against Alzheimer's -amyloid plaques via EFRH phage administration. *Proceedings of the National Academy of Sciences*, 97(21):11455–11459, 2000. Publisher: National Acad Sciences.

[173] Dan Frenkel and Beka Solomon. Filamentous phage as vector-mediated antibody delivery to the brain. *Proceedings of the National Academy of Sciences*, 99(8):5675–5679, 2002. Publisher: National Acad Sciences.

[174] Frederik SO Fritzsch, Christian Dusny, Oliver Frick, and Andreas Schmid. Single-cell analysis in biotechnology, systems biology, and biocatalysis. *Annual review of chemical and biomolecular engineering*, 3:129–155, 2012. Publisher: Annual Reviews.

[175] Alexandrine Froger and James E. Hall. Transformation of Plasmid DNA into E. coli Using the Heat Shock Method. *Journal of Visualized Experiments*, (6):253, August 2007.

[176] Germaine Fuh and Sachdev S Sidhu. Efficient phage display of polypeptides fused to the carboxy-terminus of the M13 gene-3 minor coat protein. *FEBS letters*, 480(2-3):231–234, 2000. Publisher: Elsevier.

[177] Takashi Funatsu, Tadayoshi Taniyama, Takashi Tajima, Hisashi Tadakuma, and Hideo Namiki. Rapid and Sensitive Detection Method of a Bacterium by Using a GFP Reporter Phage. *Microbiology and Immunology*, 46(6):365–369, June 2002.

[178] Luca Galbusera, Gwendoline Bellement-Theroue, Arantxa Urchueguia, Thomas Julou, and Erik Van Nimwegen. Using fluorescence flow cytometry data for single-cell gene expression analysis in bacteria. *PLOS ONE*, 15(10):e0240233, October 2020.

[179] Bruce Gale, Alexander Jafek, Christopher Lambert, Brady Goenner, Hossein Moghimifam, Ugochukwu Nze, and Suraj Kamarapu. A Review of Current Methods in Microfluidic Device Fabrication and Future Commercialization Prospects. *Inventions*, 3(3):60, August 2018.

[180] Changshou Gao, Shenlan Mao, Gunnar Kaufmann, Peter Wirsching, Richard A. Lerner, and Kim D. Janda. A method for the generation of combinatorial antibody libraries using pIX phage display. *Proceedings of the National Academy of Sciences*, 99(20):12612–12616, October 2002.

[181] Changshou Gao, Shenlan Mao, Chih-Hung L. Lo, Peter Wirsching, Richard A. Lerner, and Kim D. Janda. Making artificial antibodies: A format for phage display of combinatorial heterodimeric arrays. *Proceedings of the National Academy of Sciences*, 96(11):6025–6030, May 1999.

[182] Liang Gao, Lidai Wang, Chiye Li, Alejandro Garcia-Uribe, and Lihong V. Wang. Photothermal bleaching in time-lapse photoacoustic microscopy. *Journal of Biophotonics*, 6(6-7):543–548, June 2013.

[183] P. García, B. Martínez, J.M. Obeso, and A. Rodríguez. Bacteriophages and their application in food safety. *Letters in Applied Microbiology*, 47(6):479–485, December 2008.

[184] Chandradhish Ghosh, Paramita Sarkar, Rahaf Issa, and Jayanta Haldar. Alternatives to Conventional Antibiotics in the Era of Antimicrobial Resistance. *Trends in Microbiology*, 27(4):323–338, April 2019.

[185] Debadyuti Ghosh, Aditya G Kohli, Felix Moser, Drew Endy, and Angela M Belcher. Refactored M13 bacteriophage as a platform for tumor cell imaging and drug delivery. *ACS synthetic biology*, 1(12):576–582, 2012. Publisher: ACS Publications.

[186] Bryan Gibb, Paul Hyman, and Christine Schneider. The Many Applications of Engineered Bacteriophages—An Overview. *Pharmaceuticals*, 14(7):634, June 2021.

[187] Daniel G Gibson, Lei Young, Ray-Yuan Chuang, J Craig Venter, Clyde A Hutchison, and Hamilton O Smith. Enzymatic assembly of DNA molecules up to several hundred kilobases. *Nature Methods*, 6(5):343–345, May 2009.

[188] Jack A Gilbert, Martin J Blaser, J Gregory Caporaso, Janet K Jansson, Susan V Lynch, and Rob Knight. Current understanding of the human microbiome. *Nature Medicine*, 24(4):392–400, April 2018.

[189] Jason J. Gill and Paul Hyman. Phage choice, isolation, and preparation for phage therapy. *Current Pharmaceutical Biotechnology*, 11(1):2–14, January 2010.

[190] Nabanita Giri. Bacteriophage structure, classification, assembly and phage therapy. *Biosciences Biotechnology Research Asia*, 18(2):239–250, 2021.

[191] Piotr Golec, Joanna Karczewska-Golec, Marcin Łoś, and Grzegorz Wegrzyn. Bacteriophage T4 can produce progeny virions in extremely slowly growing *Escherichia coli* host: comparison of a mathematical model with the experimental data. *FEMS Microbiology Letters*, 351(2):156–161, February 2014.

[192] Ahmed A. Gomaa, Heidi E. Klumpe, Michelle L. Luo, Kurt Selle, Rodolphe Barrangou, and Chase L. Beisel. Programmable Removal of Bacterial Strains by Use of Genome-Targeting CRISPR-Cas Systems. *mBio*, 5(1):e00928–13, January 2014.

[193] Fernando L. Gordillo Altamirano and Jeremy J. Barr. Phage Therapy in the Postantibiotic Era. *Clinical Microbiology Reviews*, 32(2):e00066–18, March 2019.

[194] Thomas E. Gorochowski, Antoni Matyjaszkiewicz, Thomas Todd, Neeraj Oak, Kira Kowalska, Stephen Reid, Krasimira T. Tsaneva-Atanasova, Nigel J. Savery, Claire S. Grierson, and Mario di Bernardo. BSim: an agent-based tool for modeling bacterial populations in systems and synthetic biology. *PloS One*, 7(8):e42790, 2012.

[195] Thomas E. Gorochowski. Agent-based modelling in synthetic biology. *Essays in Biochemistry*, 60(4):325–336, November 2016.

[196] Cindy Govarts, Klaartje Somers, Piet Stinissen, and Veerle Somers. Frameshifting in the P6 cDNA Phage Display System. *Molecules*, 15(12):9380–9390, December 2010.

[197] Ángel Goñi-Moreno, Juhyun Kim, and Víctor de Lorenzo. CellShape: A user-friendly image analysis tool for quantitative visualization of bacterial cell factories inside. *Biotechnology Journal*, 12(2):1600323, February 2017.

[198] P. Grayson, L. Han, T. Winther, and R. Phillips. Real-time observations of single bacteriophage DNA ejections in vitro. *Proceedings of the National Academy of Sciences*, 104(37):14652–14657, September 2007.

[199] Erin R. Green and Joan Mecsas. Bacterial Secretion Systems: An Overview. *Microbiology Spectrum*, 4(1), February 2016.

[200] Michael R. Green and Joseph Sambrook. Plating Bacteriophage M13. *Cold Spring Harbor Protocols*, 2017(10):pdb.prot093427, October 2017.

[201] R. Gregory, J.R. Saunders, and V.A. Saunders. The Paton individual-based model legacy. *Biosystems*, 85(1):46–54, July 2006.

[202] R. Gregory, V.A. Saunders, and J.R. Saunders. Rule-based computing system for microbial interactions and communications: Evolution in virtual bacterial populations. *Biosystems*, 91(1):216–230, January 2008.

[203] R. Gregory, V.A. Saunders, and J.R. Saunders. Rule-based simulation of temperate bacteriophage infection: Restriction–modification as a limiter to infection in bacterial populations. *Biosystems*, 100(3):166–177, June 2010.

[204] Miller JH et al. Griffiths AJF, Gelbart WM. Bacterial conjugation. In *Modern Genetic Analysis*. New York: W. H. Freeman, 1999.

[205] Alexander Grünberger, Nicole Paczia, Christopher Probst, Georg Schendzielorz, Lothar Eggeling, Stephan Noack, Wolfgang Wiechert, and Dietrich Kohlheyer. A disposable picolitre bioreactor for cultivation and investigation of industrially relevant bacteria on the single cell level. *Lab on a Chip*, 12(11):2060, 2012.

[206] Alexander Manuel Grünberger. *Single-Cell Analysis of Microbial Production Strains in Microfluidic Bioreactors*, volume 114. Forschungszentrum Jülich, 2015.

[207] Jingmin Gu, Xiaohe Liu, Yue Li, Wenyu Han, Liancheng Lei, Yongjun Yang, Honglei Zhao, Yu Gao, Jun Song, and Rong Lu. A method for generation phage cocktail with great therapeutic potential. *PloS one*, 7(3):e31698, 2012. Publisher: Public Library of Science San Francisco, USA.

[208] Dingming Guo, Jingchao Chen, Xueyang Zhao, Yanan Luo, Menglu Jin, Fenxia Fan, Chaiwoo Park, Xiaoman Yang, Chuqing Sun, Jin Yan, Weihua Chen, and Zhi Liu. Genetic and Chemical Engineering of Phages for Controlling Multidrug-Resistant Bacteria. *Antibiotics*, 10(2):202, February 2021.

[209] Beatriz Gutiérrez and Pilar Domingo-Calap. Phage Therapy in Gastrointestinal Diseases. *Microorganisms*, 8(9):1420, September 2020.

[210] Hilla Hadas, Monica Einav, Itzhak Fishov, and Arieh Zaritsky. Bacteriophage T4 development depends on the physiology of its host Escherichia coli. *Microbiology*, 143(1):179–185, 1997. Publisher: Microbiology Society.

[211] S. Hagens and U. Blasi. Genetically modified filamentous phage as bactericidal agents: a pilot study. *Letters in Applied Microbiology*, 37(4):318–323, October 2003.

[212] Jin-Hee Han, Min S. Wang, Jayanti Das, L. Sudheendra, Erica Vonasek, Nitin Nitin, and Ian M. Kennedy. Capture and detection of T7 bacteriophages on a nanostructured interface. *ACS applied materials & interfaces*, 6(7):4758–4765, April 2014.

[213] Irshad Ul Haq, Waqas Nasir Chaudhry, Maha Nadeem Akhtar, Saadia Andleeb, and Ishtiaq Qadri. Bacteriophages and their implications on future biotechnology: a review. *Virology Journal*, 9(1):9, December 2012.

[214] Laith Harb, Karthik Chamakura, Pratick Khara, Peter J. Christie, Ry Young, and Lanying Zeng. ssRNA phage penetration triggers detachment of the F-pilus. *Proceedings of the National Academy of Sciences*, 117(41):25751–25758, October 2020.

[215] Mark Hargreaves and Lawrence L. Spriet. Skeletal muscle energy metabolism during exercise. *Nature Metabolism*, 2(9):817–828, August 2020.

[216] Ellie Harrison, A. Jamie Wood, Calvin Dytham, Jonathan W. Pitchford, Julie Truman, Andrew Spiers, Steve Paterson, and Michael A. Brockhurst. Bacteriophages limit the existence conditions for conjugative plasmids. *mBio*, 6(3):e00586, June 2015.

[217] Mahadi Hasan and Juhee Ahn. Evolutionary Dynamics between Phages and Bacteria as a Possible Approach for Designing Effective Phage Therapies against Antibiotic-Resistant Bacteria. *Antibiotics*, 11(7):915, July 2022.

[218] Graham F. Hatfull, Rebekah M. Dedrick, and Robert T. Schooley. Phage Therapy for Antibiotic-Resistant Bacterial Infections. *Annual Review of Medicine*, 73(1):197–211, January 2022.

[219] Iain D Hay and Trevor Lithgow. Filamentous phages: masters of a microbial sharing economy. *EMBO reports*, 20(6):e47427, 2019.

[220] Xuewen He, Yujun Yang, Yongcan Guo, Shuguang Lu, Yao Du, Jun-Jie Li, Xuepeng Zhang, Nelson L. C. Leung, Zheng Zhao, Guangle Niu, Shuangshuang Yang, Zhi Weng, Ryan T. K. Kwok, Jacky W. Y. Lam, Guoming Xie, and Ben Zhong Tang. Phage-Guided Targeting, Discriminative Imaging, and Synergistic Killing of Bacteria by AIE Bioconjugates. *Journal of the American Chemical Society*, 142(8):3959–3969, February 2020.

[221] Kris Heggenhougen and Stella Rodriguez Quah. *International encyclopedia of public health*. Elsevier, Amsterdam Boston, 2008.

[222] Heike A Held and Sachdev S Sidhu. Comprehensive mutational analysis of the M13 major coat protein: improved scaffolds for C-terminal phage display. *Journal of molecular biology*, 340(3):587–597, 2004. Publisher: Elsevier.

[223] Ferdi L. Hellweger, Robert J. Clegg, James R. Clark, Caroline M. Plugge, and Jan-Ulrich Kreft. Advancing microbial sciences by individual-based modelling. *Nature Reviews Microbiology*, 14(7):461–471, July 2016.

[224] Gaelen T. Hess, Juan J. Cragnolini, Maximilian W. Popp, Mark A. Allen, Stephanie K. Dougan, Eric Spooner, Hidde L. Ploegh, Angela M. Belcher, and Carla P. Guimaraes. M13 Bacteriophage Display Framework That Allows Sortase-Mediated Modification of Surface-Accessible Phage Proteins. *Bioconjugate Chemistry*, 23(7):1478–1487, July 2012.

[225] Michael E. Hibbing, Clay Fuqua, Matthew R. Parsek, and S. Brook Peterson. Bacterial competition: surviving and thriving in the microbial jungle. *Nature Reviews Microbiology*, 8(1):15–25, January 2010.

[226] Shane M. Hickey, Ben Ung, Christie Bader, Robert Brooks, Joanna Lazniewska, Ian R. D. Johnson, Alexandra Sorvina, Jessica Logan, Carmela Martini, Courtney R. Moore, Litsa Karageorgos, Martin J. Sweetman, and Douglas A. Brooks. Fluorescence Microscopy—An Outline of Hardware, Biological Handling, and Fluorophore Considerations. *Cells*, 11(1):35, December 2021.

[227] E. M. Hildebrand. Techniques for the isolation of single microorganisms. *The Botanical Review*, 4(12):627–664, December 1938.

[228] H. Rachael Hill and Peter G. Stockley. Phage presentation. *Molecular Microbiology*, 20(4):685–692, May 1996.

[229] Oliver Hilsenbeck, Michael Schwarzfischer, Stavroula Skylaki, Bernhard Schauberger, Philipp S Hoppe, Dirk Loeffler, Konstantinos D Kokkaliaris, Simon Hastreiter, Eleni Skylaki, Adam Filipczyk, Michael Strasser, Felix Buggenthin, Justin S Feigelman, Jan Krumsiek, Adrianus J J Van Den Berg, Max Endele, Martin Etzrodt, Carsten Marr, Fabian J Theis, and Timm Schroeder. Software tools for single-cell tracking and quantification of cellular and molecular properties. *Nature Biotechnology*, 34(7):703–706, July 2016.

[230] Toru Hiratsuka and Naoki Komatsu. Single-Cell Live Imaging. In Valentina Proserpio, editor, *Single Cell Methods: Sequencing and Proteomics*, pages 409–421. Springer New York, New York, NY, 2019.

[231] Emir Hodzic. Single-cell analysis: Advances and future perspectives. *Bosnian Journal of Basic Medical Sciences*, 16(4):313–314, November 2016.

[232] Ronald H. Hoess. Protein Design and Phage Display. *Chemical Reviews*, 101(10):3205–3218, 2001. _eprint: https://doi.org/10.1021/cr000056b.

[233] Hartmut Hoffmann-Berling, Donald A Marvin, and Hildegard Dürwald. Ein fädiger DNS-Phage (fd) und ein sphärischer RNS-Phage (fr), wirtsspezifisch für männliche Stämme von E. coli: 1. Präparation und chemische Eigenschaften von fd und fr. *Zeitschrift für Naturforschung B*, 18(11):876–883, 1963. Publisher: Verlag der Zeitschrift für Naturforschung.

[234] P. H. Hofschneider. Untersuchungen über kleine“ E. coli K 12 Bakteriophagen: 1. und 2. Mitteilung. *Zeitschrift für Naturforschung B*, 18(3):203–210, March 1963.

[235] Hennie R Hoogenboom, Andrew D Griffiths, Kevin S Johnson, David J Chiswell, Peter Hudson, and Greg Winter. Multi-subunit proteins on the surface of filamentous phage: methodologies for displaying antibody (Fab) heavy and light chains. *Nucleic acids research*, 19(15):4133–4137, 1991. Publisher: Oxford University Press.

[236] Jun Hu, Kazuhiko Miyanaga, and Yasunori Tanji. Diffusion properties of bacteriophages through agarose gel membrane. *Biotechnology Progress*, 26(5):1213–1221, September 2010.

[237] Jun Hu, Kazuhiko Miyanaga, and Yasunori Tanji. Diffusion of bacteriophages through artificial biofilm models. *Biotechnology Progress*, 28(2):319–326, March 2012.

[238] Chenxi Huang, Junpeng Zhao, Rongsheng Lu, Jia Wang, Sam R. Nugen, Yiping Chen, and Xiaohong Wang. A phage-based magnetic relaxation switching biosensor

using bioorthogonal reaction signal amplification for Salmonella detection in foods. *Food Chemistry*, 400:134035, January 2023.

[239] Johnny X. Huang, Sharon L. Bishop-Hurley, and Matthew A. Cooper. Development of Anti-Infectives Using Phage Display: Biological Agents against Bacteria, Viruses, and Parasites. *Antimicrobial Agents and Chemotherapy*, 56(9):4569–4582, September 2012.

[240] Simon E Hufton, Peter T Moerkerk, Els V Meulemans, Adriaan De Bruine, Jan-Willem Arends, and Hennie R Hoogenboom. Phage display of cDNA repertoires: the pVI display system and its applications for the selection of immunogenic ligands. *Journal of Immunological Methods*, 231(1-2):39–51, December 1999.

[241] Michael A Huie, Mei-Chi Cheung, Marcus O Muench, Baltazar Becerril, Yuet W Kan, and James D Marks. Antibodies to human fetal erythroid cells from a nonimmune phage antibody library. *Proceedings of the National Academy of Sciences*, 98(5):2682–2687, 2001. Publisher: National Acad Sciences.

[242] Wajid Hussain, Xiaohan Yang, Mati Ullah, Huan Wang, Ayesha Aziz, Fang Xu, Muhammad Asif, Muhammad Wajid Ullah, and Shenqi Wang. Genetic engineering of bacteriophages: Key concepts, strategies, and applications. *Biotechnology Advances*, page 108116, 2023. Publisher: Elsevier.

[243] Byungjin Hwang, Ji Hyun Lee, and Duhee Bang. Single-cell RNA sequencing technologies and bioinformatics pipelines. *Experimental & Molecular Medicine*, 50(8):1–14, August 2018.

[244] Paul Hyman and Stephen T. Abedon. Bacteriophage Host Range and Bacterial Resistance. In *Advances in Applied Microbiology*, volume 70, pages 217–248. Elsevier, 2010.

[245] AA Ilichev, OO Minenkova, SI Tatkov, NN Karpyshev, AM EROSHKIN, VI Ofitserov, ZA Akimenko, VA Petrenko, and LS Sandakhchiev. M13 Filamentous Bacteriophage In Protein Engineering. *Molecular Biology*, 24(2):435–440, 1990. Publisher: Plenum Publ Corp Consultants Bureau 233 Spring St, New York, Ny 10013.

[246] Brian P Ingalls. *Mathematical modeling in systems biology: an introduction*. MIT press, 2013.

[247] J. Iranzo, A. E. Lobkovsky, Y. I. Wolf, and E. V. Koonin. Evolutionary Dynamics of the Prokaryotic Adaptive Immunity System CRISPR-Cas in an Explicit Ecological Context. *Journal of Bacteriology*, 195(17):3834–3844, September 2013.

[248] M A Islam. Einstein–Smoluchowski Diffusion Equation: A Discussion. *Physica Scripta*, 70(2-3):120–125, January 2004.

[249] Kewal K Jain. An overview of drug delivery systems. *drug delivery systems*, pages 1–54, 2020. Publisher: Springer.

[250] Seunghee S. Jang, Kevin T. Oishi, Robert G. Egbert, and Eric Klavins. Specification and Simulation of Synthetic Multicelled Behaviors. *ACS Synthetic Biology*, 1(8):365–374, August 2012.

[251] Weronika Jaroszewicz, Joanna Morcinek-Orłowska, Karolina Pierzynowska, Lidia Gaffke, and Grzegorz Wegrzyn. Phage display and other peptide display technologies. *FEMS Microbiology Reviews*, 46(2):fuab052, 2022. Publisher: Oxford University Press.

[252] Helen P. Jarvie, Andrew N. Sharpley, Van Brahana, Tarra Simmons, April Price, Colin Neal, Alan J. Lawlor, Darren Sleep, Sarah Thacker, and Brian E. Haggard. Phosphorus Retention and Remobilization along Hydrological Pathways in Karst Terrain. *Environmental Science & Technology*, 48(9):4860–4868, May 2014.

[253] Wes Wallace Jason R. Swedlow. Introduction To Deconvolution.

[254] Jean-Yves Tinevez. MATLAB tree, 2014.

[255] Hannah Jeckel and Knut Drescher. Advances and opportunities in image analysis of bacterial cells and communities. *FEMS Microbiology Reviews*, 45(4):fuaa062, August 2021.

[256] Qi Jia and Ye Xiang. Cryo-EM structure of a bacteriophage M13 mini variant. *Nature Communications*, 14(1):5421, September 2023.

[257] Wenyan Jiang, David Bikard, David Cox, Feng Zhang, and Luciano A Marraffini. RNA-guided editing of bacterial genomes using CRISPR-Cas systems. *Nature Biotechnology*, 31(3):233–239, March 2013.

[258] Hyo-Eon Jin and Seung-Wuk Lee. Engineering of M13 bacteriophage for development of tissue engineering materials. *Virus-Derived Nanoparticles for Advanced Technologies: Methods and Protocols*, pages 487–502, 2018. Publisher: Springer.

[259] Priscilla Johanesen, Kate Mackin, Melanie Hutton, Milena Awad, Sarah Larcombe, Jacob Amy, and Dena Lyras. Disruption of the Gut Microbiome: Clostridium difficile Infection and the Threat of Antibiotic Resistance. *Genes*, 6(4):1347–1360, December 2015.

[260] Kevin L Joiner. Modeling phage-bacteria dynamics in mucus: An agent based approach to phage therapy. 2018. Publisher: San Diego State University.

[261] Jeffrey B Jones, Gary E Vallad, Fanny B Iriarte, Aleksa Obradović, Mine H Wernsing, Lee E Jackson, Botond Balogh, Jason C Hong, and M Timur Momol. Considerations for using bacteriophages for plant disease control. *Bacteriophage*, 2(4):e23857, 2012. Publisher: Taylor & Francis.

[262] Graham Joyce, Brian D Robertson, and Kerstin J Williams. A modified agar pad method for mycobacterial live-cell imaging. *BMC Research Notes*, 4(1):73, December 2011.

[263] Zhigang Ju and Wei Sun. Drug delivery vectors based on filamentous bacteriophages and phage-mimetic nanoparticles. *Drug Delivery*, 24(1):1898–1908, January 2017.

[264] Jin Woo Jun, Ji Hyung Kim, Sang Phil Shin, Jee Eun Han, Ji Young Chai, and Se Chang Park. Protective effects of the Aeromonas phages pAh1-C and pAh6-C against mass mortality of the cyprinid loach (Misgurnus anguillicaudatus) caused by Aeromonas hydrophila. *Aquaculture*, 416-417:289–295, December 2013.

[265] Vilhelmiina Juusti, Janne Kulpakko, Elizabeth Cudjoe, Ville N. Pimenoff, and Pekka Hänninen. Biophysical Properties of Bifunctional Phage-Biosensor. *Viruses*, 15(2):299, January 2023.

[266] Adam Jedrusiak, Wojciech Fortuna, Joanna Majewska, Andrzej Górski, and Ewa Jończyk-Matysiak. Phage Interactions with the Nervous System in Health and Disease. *Cells*, 12(13):1720, June 2023.

[267] Benjamin K Chan and Stephen T Abedon. Bacteriophages and their enzymes in biofilm control. *Current pharmaceutical design*, 21(1):85–99, 2015. Publisher: Bentham Science Publishers.

[268] Mozhgan Kabiri Chimeh, Peter Heywood, Marzio Pennisi, Francesco Pappalardo, and Paul Richmond. Parallelisation strategies for agent based simulation of immune systems. *BMC Bioinformatics*, 20(S6):579, December 2019.

[269] Tom Kamperman, Marcel Karperien, Séverine Le Gac, and Jeroen Leijten. Single-Cell Microgels: Technology, Challenges, and Applications. *Trends in Biotechnology*, 36(8):850–865, August 2018.

[270] Anton Kan, Ilenne Del Valle, Tim Rudge, Fernán Federici, and Jim Haseloff. Intercellular adhesion promotes clonal mixing in growing bacterial populations. *Journal of The Royal Society Interface*, 15(146):20180406, September 2018.

[271] Achillefs N. Kapanidis, Stephan Uphoff, and Mathew Stracy. Understanding Protein Mobility in Bacteria by Tracking Single Molecules. *Journal of Molecular Biology*, 430(22):4443–4455, October 2018.

[272] Mahdi Karimi, Hamed Mirshekari, Seyed Masoud Moosavi Basri, Sajad Bahrami, Mohsen Moghoofei, and Michael R Hamblin. Bacteriophages and phage-inspired nanocarriers for targeted delivery of therapeutic cargos. *Advanced drug delivery reviews*, 106:45–62, 2016. Publisher: Elsevier.

[273] Laura M. Kasman, Alex Kasman, Caroline Westwater, Joseph Dolan, Michael G. Schmidt, and James S. Norris. Overcoming the Phage Replication Threshold: a Mathematical Model with Implications for Phage Therapy. *Journal of Virology*, 76(11):5557–5564, June 2002.

[274] Tranum Kaur, Nafiseh Nafissi, Olla Wasfi, Katlyn Sheldon, Shawn Wettig, and Roderick Slavcev. Immunocompatibility of Bacteriophages as Nanomedicines. *Journal of Nanotechnology*, 2012:1–13, 2012.

[275] Brian K Kay and Ronald H Hoess. Principles and applications of phage display. *Phage Display of Peptides and Proteins. Academic Press, San Diego, CA*, pages 21–34, 1996.

[276] Mustafa Kazi and Uday S. Annapure. Bacteriophage biocontrol of foodborne pathogens. *Journal of Food Science and Technology*, 53(3):1355–1362, March 2016.

[277] Zuzanna Kaźmierczak, Agnieszka Piotrowicz, Barbara Owczarek, Katarzyna Hodyra, Paulina Miernikiewicz, Dorota Lecion, Marek Harhala, Andrzej Górski, and Krystyna Dabrowska. Molecular imaging of T4 phage in mammalian tissues and cells. *Bacteriophage*, 4(1):e28364, January 2014.

[278] Eric C. Keen. Phage therapy: concept to cure. *Frontiers in Microbiology*, 3:238, 2012.

[279] Brian Kelley, Pam De Moor, Kristen Douglas, Todd Renshaw, and Stacey Traviglia. Monoclonal antibody therapies for COVID-19: lessons learned and implications for the development of future products. *Current Opinion in Biotechnology*, 78:102798, December 2022.

[280] CD Kelly and Otto Rahn. The growth rate of individual bacterial cells. *Journal of Bacteriology*, 23(2):147, 1932. Publisher: American Society for Microbiology (ASM).

[281] Anne K. Kenworthy. Imaging Protein-Protein Interactions Using Fluorescence Resonance Energy Transfer Microscopy. *Methods*, 24(3):289–296, July 2001.

[282] Takehiko Kenzaka, Katsuji Tani, and Masao Nasu. High-frequency phage-mediated gene transfer in freshwater environments determined at single-cell level. *The ISME journal*, 4(5):648–659, 2010. Publisher: Nature Publishing Group.

[283] Amjad Khan. Phage-Bacteria Interaction and Prophage Sequences in Bacterial Genomes. 2020.

[284] Md Abu Sayem Khan and Sabita Rezwana Rahman. Use of Phages to Treat Antimicrobial-Resistant Salmonella Infections in Poultry. *Veterinary Sciences*, 9(8):438, August 2022.

[285] Zhi Y. Kho and Sunil K. Lal. The Human Gut Microbiome – A Potential Controller of Wellness and Disease. *Frontiers in Microbiology*, 9:1835, August 2018.

[286] Benjamin Kick, Samantha Hensler, Florian Praetorius, Hendrik Dietz, and Dirk Weuster-Botz. Specific growth rate and multiplicity of infection affect high-cell-density fermentation with bacteriophage M13 for ssDNA production. *Biotechnology and Bioengineering*, 114(4):777–784, April 2017.

[287] Benjamin Kick, Florian Praetorius, Hendrik Dietz, and Dirk Weuster-Botz. Efficient Production of Single-Stranded Phage DNA as Scaffolds for DNA Origami. *Nano Letters*, 15(7):4672–4676, July 2015.

[288] Samuel Kilcher, Patrick Studer, Christina Muessner, Jochen Klumpp, and Martin J. Loessner. Cross-genus rebooting of custom-made, synthetic bacteriophage genomes in L-form bacteria. *Proceedings of the National Academy of Sciences*, 115(3):567–572, January 2018.

[289] Andrew MQ King, Elliot Lefkowitz, Michael J Adams, and Eric B Carstens. *Virus taxonomy: ninth report of the International Committee on Taxonomy of Viruses*, volume 9. Elsevier, 2011.

[290] Cecile King and Nora Sarvetnick. The Incidence of Type-1 Diabetes in NOD Mice Is Modulated by Restricted Flora Not Germ-Free Conditions. *PLoS ONE*, 6(2):e17049, February 2011.

[291] Gregory Kishchenko, Hoshang Batliwala, and Lee Makowski. Structure of a foreign peptide displayed on the surface of bacteriophage M13. *Journal of molecular biology*, 241(2):208–213, 1994. Publisher: Elsevier.

[292] Hisataka Kobayashi, Mikako Ogawa, Raphael Alford, Peter L. Choyke, and Yasuteru Urano. New Strategies for Fluorescent Probe Design in Medical Diagnostic Imaging. *Chemical Reviews*, 110(5):2620–2640, May 2010.

[293] Felicitas Korn-Wendisch and Jörg Schneider. Phage typing—a useful tool in actinomycete systematics. *Gene*, 115(1-2):243–247, 1992. Publisher: Elsevier.

[294] Kaitlyn E. Kortright, Benjamin K. Chan, Jonathan L. Koff, and Paul E. Turner. Phage Therapy: A Renewed Approach to Combat Antibiotic-Resistant Bacteria. *Cell Host & Microbe*, 25(2):219–232, February 2019.

[295] Britt Koskella and Michael A. Brockhurst. Bacteria–phage coevolution as a driver of ecological and evolutionary processes in microbial communities. *FEMS Microbiology Reviews*, 38(5):916–931, September 2014.

[296] Britt Koskella and Sean Meaden. Understanding Bacteriophage Specificity in Natural Microbial Communities. *Viruses*, 5(3):806–823, March 2013.

[297] Jan-Ulrich Kreft, Ginger Booth, and Julian W. T. Wimpenny. BacSim, a simulator for individual-based modelling of bacterial colony growth. *Microbiology*, 144(12):3275–3287, December 1998.

[298] Konrad Krysiak-Baltyn, Gregory J. O. Martin, Anthony D. Stickland, Peter J. Scales, and Sally L. Gras. Computational models of populations of bacteria and lytic phage. *Critical Reviews in Microbiology*, 42(6):942–968, November 2016.

[299] Elisabeth Kutter, Raol Raya, and Karin Carlson. Molecular mechanisms of phage infection. 2005.

[300] Kyle Karhohs. CellProfiler & Ilastik: Superpowered Segmentation, January 2017.

[301] Jonas Kügler, Jonas Zantow, Torsten Meyer, and Michael Hust. Oligopeptide M13 Phage Display in Pathogen Research. *Viruses*, 5(10):2531–2545, October 2013.

[302] Jing Yi Lai, Naoya Inoue, Chuan Wei Oo, Hideya Kawasaki, and Theam Soon Lim. One-step synthesis of M13 phage-based nanoparticles and their fluorescence properties. *RSC Advances*, 11(3):1367–1375, 2021.

[303] Kathy N. Lam, Peter Spanogiannopoulos, Paola Soto-Perez, Margaret Alexander, Matthew J. Nalley, Jordan E. Bisanz, Renuka R. Nayak, Allison M. Weakley, Feiqiao B. Yu, and Peter J. Turnbaugh. Phage-delivered CRISPR-Cas9 for strain-specific depletion and genomic deletions in the gut microbiome. *Cell Reports*, 37(5):109930, November 2021.

[304] Sonja Lang, Yi Duan, Jinyuan Liu, Manolito G Torralba, Claire Kuelbs, Meritxell Ventura-Cots, Juan G Abraldes, Francisco Bosques-Padilla, Elizabeth C Verna, and Robert S Brown Jr. Intestinal fungal dysbiosis and systemic immune response to fungi in patients with alcoholic hepatitis. *Hepatology*, 71(2):522–538, 2020. Publisher: Wiley Online Library.

[305] Laurent A. Lardon, Brian V. Merkey, Sónia Martins, Andreas Dötsch, Cristian Picioreanu, Jan-Ulrich Kreft, and Barth F. Smets. iDynoMiCS: next-generation individual-based modelling of biofilms. *Environmental Microbiology*, 13(9):2416–2434, September 2011.

[306] Majid Latif and Elebeoba E. May. A Multiscale Agent-Based Model for the Investigation of E. coli K12 Metabolic Response During Biofilm Formation. *Bulletin of Mathematical Biology*, 80(11):2917–2956, November 2018.

[307] N. Le Novere and T. S. Shimizu. STOCHSIM: modelling of stochastic biomolecular processes. *Bioinformatics*, 17(6):575–576, June 2001.

[308] Sangseok Lee and Dong Kyu Lee. What is the proper way to apply the multiple comparison test? *Korean Journal of Anesthesiology*, 71(5):353–360, October 2018.

[309] Leibniz-Institut DSMZ. Brevibacillus sp, April 2007. https://bacdive.dsmz.de/#ref17082.

[310] Leibniz-Institut DSMZ. Staphylococcus capitis, July 2022.

[311] Calvin S. Leung, Oksana Kosyk, Emma M. Welter, Nicholas Dietrich, Trevor K. Archer, and Anthony S. Zannas. Chronic stress-driven glucocorticoid receptor activation programs key cell phenotypes and functional epigenomic patterns in human fibroblasts. *iScience*, 25(9):104960, September 2022.

[312] Bruce R Levin, Frank M Stewart, and Lin Chao. Resource-limited growth, competition, and predation: a model and experimental studies with bacteria and bacteriophage. *The American Naturalist*, 111(977):3–24, 1977. Publisher: University of Chicago Press.

[313] Petra Anne Levin and Esther R Angert. Small but mighty: cell size and bacteria. *Cold Spring Harbor perspectives in biology*, 7(7):a019216, 2015. Publisher: Cold Spring Harbor Lab.

[314] Kang Li, Eric D. Miller, Mei Chen, Takeo Kanade, Lee E. Weiss, and Phil G. Campbell. Cell population tracking and lineage construction with spatiotemporal context. *Medical Image Analysis*, 12(5):546–566, October 2008.

[315] Xianghui Li, Yuhua He, Zhili Wang, Jiacun Wei, Tongxin Hu, Jiangzhe Si, Guangzhao Tao, Lei Zhang, Longxiang Xie, and Abualgasim Elgaili Abdalla. A combination therapy of Phages and Antibiotics: Two is better than one. *International Journal of Biological Sciences*, 17(13):3573, 2021. Publisher: Ivyspring International Publisher.

[316] Xiaoxia Li, Min Lei, Yanli Song, Kunwei Gong, Ling Li, Hongyan Liang, and Xiaofeng Jiang. Whole genome sequence and comparative genomic analysis of multidrug-resistant Staphylococcus capitis subsp. urealyticus strain LNZR-1. *Gut Pathogens*, 6(1):45, December 2014.

[317] Yan Li, Xuewei Qu, Binrui Cao, Tao Yang, Qing Bao, Hui Yue, Liwei Zhang, Genwei Zhang, Lin Wang, and Penghe Qiu. Selectively Suppressing Tumor Angiogenesis for Targeted Breast Cancer Therapy by Genetically Engineered Phage. *Advanced Materials*, page 2001260, 2020. Publisher: Wiley Online Library.

[318] Mary E Lidstrom and Michael C Konopka. The role of physiological heterogeneity in microbial population behavior. *Nature chemical biology*, 6(10):705–712, 2010. Publisher: Nature Publishing Group US New York.

[319] Abraham Lin, Jose Jimenez, Julien Derr, Pedro Vera, Michael L. Manapat, Kevin M. Esvelt, Laura Villanueva, David R. Liu, and Irene A. Chen. Inhibition of Bacterial Conjugation by Phage M13 and Its Protein g3p: Quantitative Analysis and Model. *PLoS ONE*, 6(5):e19991, May 2011.

[320] Hua Ling, Aram Kang, Mui Hua Tan, Xiaobao Qi, and Matthew Wook Chang. The absence of the luxS gene increases swimming motility and flagella synthesis in Escherichia coli K12. *Biochemical and Biophysical Research Communications*, 401(4):521–526, October 2010.

[321] Si Da Ling, Yuhao Geng, An Chen, Yanan Du, and Jianhong Xu. Enhanced single-cell encapsulation in microfluidic devices: From droplet generation to single-cell analysis. *Biomicrofluidics*, 14(6):061508, November 2020.

[322] Sébastien Lion and Minus van Baalen. Self-structuring in spatial evolutionary ecology. *Ecology Letters*, 11(3):277–295, March 2008.

[323] Dan Liu, Jonas D. Van Belleghem, Christiaan R. De Vries, Elizabeth Burgener, Qingquan Chen, Robert Manasherob, Jenny R. Aronson, Derek F. Amanatullah, Pranita D. Tamma, and Gina A. Suh. The Safety and Toxicity of Phage Therapy: A Review of Animal and Clinical Studies. *Viruses*, 13(7):1268, June 2021.

[324] Jintao Liu, Rosa Martinez-Corral, Arthur Prindle, Dong-yeon D. Lee, Joseph Larkin, Marçal Gabalda-Sagarra, Jordi Garcia-Ojalvo, and Gürol M. Süel. Coupling between distant biofilms and emergence of nutrient time-sharing. *Science*, 356(6338):638–642, May 2017.

[325] William Liu, Nikolai Dechev, Ian G. Foulds, Robert Burke, Ash Parameswaran, and Edward J. Park. A novel permalloy based magnetic single cell micro array. *Lab on a Chip*, 9(16):2381, 2009.

[326] Jason Lloyd-Price, Galeb Abu-Ali, and Curtis Huttenhower. The healthy human microbiome. *Genome Medicine*, 8(1):51, December 2016.

[327] Jason Lloyd-Price, Cesar Arze, Ashwin N Ananthakrishnan, Melanie Schirmer, Julian Avila-Pacheco, Tiffany W Poon, Elizabeth Andrews, Nadim J Ajami, Kevin S Bonham, and Colin J Brislawn. Multi-omics of the gut microbial ecosystem in inflammatory bowel diseases. *Nature*, 569(7758):655–662, 2019. Publisher: Nature Publishing Group UK London.

[328] Catherine Loc-Carrillo and Stephen T. Abedon. Pros and cons of phage therapy. *Bacteriophage*, 1(2):111–114, March 2011.

[329] James C. W. Locke and Michael B. Elowitz. Using movies to analyse gene circuit dynamics in single cells. *Nature Reviews Microbiology*, 7(5):383–392, May 2009.

[330] James CW Locke, Jonathan W Young, Michelle Fontes, María Jesús Hernández Jiménez, and Michael B Elowitz. Stochastic pulse regulation in bacterial stress response. *science*, 334(6054):366–369, 2011. Publisher: American Association for the Advancement of Science.

[331] Belinda Loh, Andreas Kuhn, and Sebastian Leptihn. The fascinating biology behind phage display: filamentous phage assembly. *Molecular Microbiology*, 111(5):1132–1138, May 2019.

[332] Alka Lohani, Sumit Durgapal, and Pierfrancesco Morganti. Quantum dots: an emerging implication of nanotechnology in cancer diagnosis and therapy. In *Quantum Materials, Devices, and Applications*, pages 243–262. Elsevier, 2023.

[333] Dingpei Long, Zahra Alghoul, Junsik Sung, Chunhua Yang, and Didier Merlin. Oral administration of M13-loaded nanoliposomes is safe and effective to treat colitis-associated cancer in mice. *Expert Opinion on Drug Delivery*, (just-accepted), 2023. Publisher: Taylor & Francis.

[334] Zhicheng Long, Eileen Nugent, Avelino Javer, Pietro Cicuta, Bianca Sclavi, Marco Cosentino Lagomarsino, and Kevin D. Dorfman. Microfluidic chemostat for measuring single cell dynamics in bacteria. *Lab on a Chip*, 13(5):947, 2013.

[335] Anne Lopes, Paulo Tavares, Marie-Agnès Petit, Raphaël Guérois, and Sophie Zinn-Justin. Automated classification of tailed bacteriophages according to their neck organization. *BMC Genomics*, 15(1):1027, December 2014.

[336] Bradley E. Losavio, Yong Liang, Alberto Santamaría-Pang, Ioannis A. Kakadiaris, Costa M. Colbert, and Peter Saggau. Live Neuron Morphology Automatically Reconstructed From Multiphoton and Confocal Imaging Data. *Journal of Neurophysiology*, 100(4):2422–2429, October 2008.

[337] H.B. Lowman. Phage Display for Protein Binding. In *Encyclopedia of Biological Chemistry*, pages 431–436. Elsevier, 2013.

[338] Timothy K. Lu and James J. Collins. Dispersing biofilms with engineered enzymatic bacteriophage. *Proceedings of the National Academy of Sciences*, 104(27):11197–11202, July 2007.

[339] Timothy K. Lu and James J. Collins. Engineered bacteriophage targeting gene networks as adjuvants for antibiotic therapy. *Proceedings of the National Academy of Sciences*, 106(12):4629–4634, March 2009.

[340] Timothy K Lu and Michael S Koeris. The next generation of bacteriophage therapy. *Current Opinion in Microbiology*, 14(5):524–531, October 2011.

[341] Christofer Lundqvist, Antonie Giæver Beiske, Ola Reiertsen, and Ivar Sønbø Kristiansen. Real life cost and quality of life associated with continuous intraduodenal levodopa infusion compared with oral treatment in Parkinson patients. *Journal of neurology*, 261:2438–2445, 2014. Publisher: Springer.

[342] Pingli Ma, Chen Li, Md Mamunur Rahaman, Yudong Yao, Jiawei Zhang, Shuojia Zou, Xin Zhao, and Marcin Grzegorzek. A state-of-the-art survey of object detection techniques in microorganism image analysis: from classical methods to deep learning approaches. *Artificial Intelligence Review*, 56(2):1627–1698, February 2023.

[343] Sunting Ma, Xinyuan Qiao, Yigang Xu, Li Wang, Han Zhou, Yanping Jiang, Wen Cui, Xuewei Huang, Xiaona Wang, Lijie Tang, and Yijing Li. Screening and Identification of a Chicken Dendritic Cell Binding Peptide by Using a Phage Display Library. *Frontiers in Immunology*, 10:1853, August 2019.

[344] Yinyin Ma. *Consequences of microbial range expansion on the spread of plasmid-encoded functional novelty*. PhD thesis, ETH Zurich, 2022. Artwork Size: 162 p. Medium: application/pdf Pages: 162 p.

[345] Adam Sidi Mabrouk, Véronique Ongenae, Dennis Claessen, Susanne Brenzinger, and Ariane Briegel. A flexible and efficient microfluidics platform for the characterization and isolation of novel bacteriophages. preprint, Microbiology, September 2022.

[346] Anne Mai-Prochnow, Janice Gee Kay Hui, Staffan Kjelleberg, Jasna Rakonjac, Diane McDougald, and Scott A. Rice. 'Big things in small packages: the genetics of filamentous phage and effects on fitness of their host'. *FEMS Microbiology Reviews*, 39(4):465–487, July 2015.

[347] Stéphanie Mangenot, Marion Hochrein, Joachim Rädler, and Lucienne Letellier. Real-Time Imaging of DNA Ejection from Single Phage Particles. *Current Biology*, 15(5):430–435, March 2005.

[348] Pilar Manrique, Michael Dills, and Mark Young. The Human Gut Phage Community and Its Implications for Health and Disease. *Viruses*, 9(6):141, June 2017.

[349] Harold Marcotte and Lennart Hammarström. Passive immunization: toward magic bullets. In *Mucosal immunology*, pages 1403–1434. Elsevier, 2015.

[350] Florian C Marro, Frédéric Laurent, Jérôme Josse, and Ariel J Blocker. Methods to monitor bacterial growth and replicative rates at the single-cell level. *FEMS Microbiology Reviews*, 46(6):fuac030, November 2022.

[351] Francisco Martinez-Hernandez, Oscar Fornas, Monica Lluesma Gomez, Benjamin Bolduc, María José De la Cruz Peña, Joaquín Martínez Martínez, Josefa Anton, Josep M Gasol, Riccardo Rosselli, and Francisco Rodriguez-Valera. Single-virus genomics reveals hidden cosmopolitan and abundant viruses. *Nature communications*, 8(1):15892, 2017. Publisher: Nature Publishing Group UK London.

[352] DA Marvin. Filamentous phage structure, infection and assembly. *Current opinion in structural biology*, 8(2):150–158, 1998. Publisher: Elsevier.

[353] Shigenobu Matsuzaki, Mohammad Rashel, Jumpei Uchiyama, Shingo Sakurai, Takako Ujihara, Masayuki Kuroda, Masahiko Ikeuchi, Toshikazu Tani, Mikiya Fujieda, and Hiroshi Wakiguchi. Bacteriophage therapy: a revitalized therapy against bacterial infectious diseases. *Journal of infection and chemotherapy*, 11:211–219, 2005. Publisher: Springer.

[354] Shigenobu Matsuzaki, Masaharu Yasuda, Hiroshi Nishikawa, Masayuki Kuroda, Takako Ujihara, Taro Shuin, Yuan Shen, Zhe Jin, Shigeyoshi Fujimoto, M. D. Nasimuzzaman, Hiroshi Wakiguchi, Shigeyoshi Sugihara, Tetsuro Sugiura, Shigeki Koda, Asako Muraoka, and Shosuke Imai. Experimental Protection of Mice against Lethal *Staphylococcus aureus* Infection by Novel Bacteriophage MR11. *The Journal of Infectious Diseases*, 187(4):613–624, February 2003.

[355] Antoni Matyjaszkiewicz, Gianfranco Fiore, Fabio Annunziata, Claire S Grierson, Nigel J Savery, Lucia Marucci, and Mario di Bernardo. BSim 2.0: an advanced agent-based cell simulator. *ACS synthetic biology*, 6(10):1969–1972, 2017. Publisher: ACS Publications.

[356] Linas Mazutis, John Gilbert, W Lloyd Ung, David A Weitz, Andrew D Griffiths, and John A Heyman. Single-cell analysis and sorting using droplet-based microfluidics. *Nature Protocols*, 8(5):870–891, May 2013.

[357] Margaret McFall-Ngai. Care for the community. *Nature*, 445(7124):153–153, January 2007.

[358] Ross S McInnes, Gregory E McCallum, Lisa E Lamberte, and Willem Van Schaik. Horizontal transfer of antibiotic resistance genes in the human gut microbiome. *Current Opinion in Microbiology*, 53:35–43, February 2020.

[359] L McIntyre, JA Hudson, C Billington, and H Withers. Biocontrol of Foodborne Bacteria: Past, Present And Future Strategies. *Food New Zealand*, 7(5):25, 2007. Publisher: Slice Publications Ltd.

[360] Claire McQuin, Allen Goodman, Vasiliy Chernyshev, Lee Kamentsky, Beth A. Cimini, Kyle W. Karhohs, Minh Doan, Liya Ding, Susanne M. Rafelski, Derek Thirstrup, Winfried Wiegraebe, Shantanu Singh, Tim Becker, Juan C. Caicedo, and Anne E. Carpenter. CellProfiler 3.0: Next-generation image processing for biology. *PLoS biology*, 16(7):e2005970, 2018.

[361] Fabian Mermans, Valérie Mattelin, Ruben Van Den Eeckhoudt, Cristina García-Timermans, Josefien Van Landuyt, Yuting Guo, Irene Taurino, Filip Tavernier, Michael Kraft, Hira Khan, and Nico Boon. Opportunities in optical and electrical single-cell technologies to study microbial ecosystems. *Frontiers in Microbiology*, 14:1233705, August 2023.

[362] Joachim Messing. [2] New M13 vectors for cloning. In *Methods in Enzymology*, volume 101, pages 20–78. Elsevier, 1983.

[363] Joachim Messing. Phage M13 for the treatment of Alzheimer and Parkinson disease. *Gene*, 583(2):85–89, June 2016.

[364] Joachim Messing, Roberto Crea, and Peter H. Seeburg. A system for shotgun DNA sequencing. *Nucleic Acids Research*, 9(2):309–321, 1981.

[365] M. Middelboe. Bacterial Growth Rate and Marine Virus–Host Dynamics. *Microbial Ecology*, 40(2):114–124, August 2000.

[366] Pauline Misson, Emma Bruder, Jeffrey K. Cornuault, Marianne De Paepe, Pierre Nicolas, Gaëlle Demarre, Goran Lakisic, Marie-Agnès Petit, Olivier Espeli, and François Lecointe. Phage production is blocked in the adherent-invasive Escherichia coli LF82 upon macrophage infection. *PLOS Pathogens*, 19(2):e1011127, February 2023.

[367] Kota Miura. Bleach correction ImageJ plugin for compensating the photobleaching of time-lapse sequences. *F1000Research*, 9:1494, December 2020.

[368] Jeffrey R. Moffitt, Jeffrey B. Lee, and Philippe Cluzel. The single-cell chemostat: an agarose-based, microfluidic device for high-throughput, single-cell studies of bacteria and bacterial communities. *Lab on a Chip*, 12(8):1487, 2012.

[369] Christine Moissl-Eichinger, Petra Rettberg, and Rüdiger Pukall. The First Collection of Spacecraft-Associated Microorganisms: A Public Source for Extremotolerant Microorganisms from Spacecraft Assembly Clean Rooms. *Astrobiology*, 12(11):1024–1034, November 2012.

[370] R. Moldovan, E. Chapman-McQuiston, and X.L. Wu. On Kinetics of Phage Adsorption. *Biophysical Journal*, 93(1):303–315, July 2007.

[371] Moon, Choi, Jeong, Sohn, Han, and Oh. Research Progress of M13 Bacteriophage-Based Biosensors. *Nanomaterials*, 9(10):1448, October 2019.

[372] Kristin A. Moore, Sabina Altus, Jian W. Tay, Janet B. Meehl, Evan B. Johnson, David M. Bortz, and Jeffrey C. Cameron. Mechanical regulation of photosynthesis in cyanobacteria. *Nature Microbiology*, 5(5):757–767, March 2020.

[373] Zahra Moradpour, Zargham Sepehrizadeh, Fatemeh Rahbarizadeh, Abdollah Ghasemian, Mojtaba Tabatabaei Yazdi, and Ahmad Reza Shahverdi. Genetically engineered phage harbouring the lethal catabolite gene activator protein gene with an inducer-independent promoter for biocontrol of *Escherichia coli*. *FEMS Microbiology Letters*, 296(1):67–71, July 2009.

[374] Omry Morag, Gili Abramov, and Amir Goldbourt. Similarities and differences within members of the Ff family of filamentous bacteriophage viruses. *The Journal of Physical Chemistry B*, 115(51):15370–15379, 2011. Publisher: ACS Publications.

[375] Nadia Morson. Phage-Mediated Mobile Genetic Elements Identified in Dehalococcoidia, Chloroflexi Bacteria Used for Bioremediation. 2022. Publisher: University of Toronto (Canada).

[376] Jorge A. Moura De Sousa, Ahlam Alsaadi, Jakob Haaber, Hanne Ingmer, and Eduardo P.C. Rocha. Modelling phage-bacteria interactions driving predation and horizontal gene transfer. preprint, Microbiology, March 2018.

[377] S. Mukherji and D. Mondal. Lab-on-chip (LOC) devices for point of care (POC) applications. In *Medical Biosensors for Point of Care (POC) Applications*, pages 99–131. Elsevier, 2017.

[378] Paola Murgas, Nicolás Bustamante, Nicole Araya, Sebastián Cruz-Gómez, Eduardo Durán, Diana Gaete, César Oyarce, Ernesto López, Andrés Alonso Herrada, and Nicolás Ferreira. A filamentous bacteriophage targeted to carcinoembryonic antigen induces tumor regression in mouse models of colorectal cancer. *Cancer Immunology, Immunotherapy*, 67(2):183–193, 2018. Publisher: Springer.

[379] EF Murphy, PD Cotter, S Healy, Tatiana M Marques, O O'sullivan, F Fouhy, SF Clarke, PW O'toole, Eamonn Martin Quigley, and C Stanton. Composition and energy harvesting capacity of the gut microbiota: relationship to diet, obesity and time in mouse models. *Gut*, 59(12):1635–1642, 2010. Publisher: BMJ Publishing Group.

[380] Dale Muzzey and Alexander Van Oudenaarden. Quantitative Time-Lapse Fluorescence Microscopy in Single Cells. *Annual Review of Cell and Developmental Biology*, 25(1):301–327, November 2009.

[381] Omkar Swarup Krupa Sagar Mylavarapu. Agent Based Model of Biolumiescence in Vibrio fischeri. 2008. Publisher: University of Cincinnati.

[382] Jaana Männik, Matthew W. Bailey, Jordan C. O'Neill, and Jaan Männik. Kinetics of large-scale chromosomal movement during asymmetric cell division in Escherichia coli. *PLOS Genetics*, 13(2):e1006638, February 2017.

[383] Sari Mäntynen, Elina Laanto, Hanna M. Oksanen, Minna M. Poranen, and Samuel L. Díaz-Muñoz. Black box of phage–bacterium interactions: exploring alternative phage infection strategies. *Open Biology*, 11(9):210188, September 2021.

[384] Dominik Nabergoj, Petra Modic, and Aleš Podgornik. Effect of bacterial growth rate on bacteriophage population growth rate. *MicrobiologyOpen*, 7(2):e00558, 2018. Publisher: Wiley Online Library.

[385] Carey D. Nadell, Kevin R. Foster, and João B. Xavier. Emergence of Spatial Structure in Cell Groups and the Evolution of Cooperation. *PLoS Computational Biology*, 6(3):e1000716, March 2010.

[386] Sawitree Nangola, Philippe Minard, and Chatchai Tayapiwatana. Appraisal of translocation pathways for displaying ankyrin repeat protein on phage particles. *Protein Expression and Purification*, 74(2):156–161, December 2010.

[387] Paolo Natale, Thomas Brüser, and Arnold J.M. Driessen. Sec- and Tat-mediated protein secretion across the bacterial cytoplasmic membrane—Distinct translocases and mechanisms. *Biochimica et Biophysica Acta (BBA) - Biomembranes*, 1778(9):1735–1756, September 2008.

[388] Zakira Naureen, Astrit Dautaj, Kyrylo Anpilogov, Giorgio Camilleri, Kristjana Dhuli, Benedetta Tanzi, Paolo Enrico Maltese, Francesca Cristofoli, Luca De Antoni, Tommaso Beccari, Munis Dundar, and Matteo Bertelli. Bacteriophages presence in nature and their role in the natural selection of bacterial populations. *Acta Bio Medica Atenei Parmensis*, 91(13-S):e2020024, November 2020.

[389] Jonathan Naylor, Harold Fellermann, Yuchun Ding, Waleed K. Mohammed, Nicholas S. Jakubovics, Joy Mukherjee, Catherine A. Biggs, Phillip C. Wright, and Natalio Krasnogor. Simbiotics: A Multiscale Integrative Platform for 3D Modeling of Bacterial Populations. *ACS Synthetic Biology*, 6(7):1194–1210, July 2017.

[390] Jay Newman, Harry L. Swinney, and Loren A. Day. Hydrodynamic properties and structure of fd virus. *Journal of Molecular Biology*, 116(3):593–603, November 1977.

[391] Pascaline Ngweniform, Gopal Abbineni, Binrui Cao, and Chuanbin Mao. Self-Assembly of Drug-Loaded Liposomes on Genetically Engineered Target-Recognizing M13 Phage: A Novel Nanocarrier for Targeted Drug Delivery. *Small*, 5(17):1963–1969, 2009. Publisher: Wiley Online Library.

[392] Jessica Nicastro, Shirley Wong, Zahra Khazaei, Peggy Lam, Jonathan Blay, Roderick A Slavcev, and Jessica Nicastro. Overview of Bacteriophage Lifecycles and Applications. *Bacteriophage Applications-Historical Perspective and Future Potential*, pages 1–8, 2016. Publisher: Springer.

[393] Jacob B. Nielsen, Robert L. Hanson, Haifa M. Almughamsi, Chao Pang, Taylor R. Fish, and Adam T. Woolley. Microfluidics: Innovations in Materials and Their Fabrication and Functionalization. *Analytical Chemistry*, 92(1):150–168, January 2020.

[394] Franklin L Nobrega, Ana Rita Costa, Leon D Kluskens, and Joana Azeredo. Revisiting phage therapy: new applications for old resources. *Trends in microbiology*, 23(4):185–191, 2015. Publisher: Elsevier.

[395] Isaac N. Nuñez, Tamara F. Matute, Ilenne D. Del Valle, Anton Kan, Atri Choksi, Drew Endy, Jim Haseloff, Timothy J. Rudge, and Fernan Federici. Artificial Symmetry-Breaking for Morphogenetic Engineering Bacterial Colonies. *ACS Synthetic Biology*, 6(2):256–265, February 2017.

[396] R. O'Callaghan, R. Bradley, and W. Paranchych. The effect of M13 phage infection upon the F pili of E. coli. *Virology*, 54(1):220–229, July 1973.

[397] Beata Orzechowska and Manal Mohammed. The war between bacteria and bacteriophages. *Growing and handling of bacterial cultures*, page 107, 2019. Publisher: IntechOpen London, UK.

[398] Ekaterina Osmekhina, Christopher Jonkergouw, Georg Schmidt, Farzin Jahangiri, Ville Jokinen, Sami Franssila, and Markus B. Linder. Controlled communication between physically separated bacterial populations in a microfluidic device. *Communications Biology*, 1(1):97, December 2018.

[399] Lisa O'Sullivan, Colin Buttimer, Olivia McAuliffe, Declan Bolton, and Aidan Coffey. Bacteriophage-based tools: recent advances and novel applications. *F1000Research*, 5:2782, November 2016.

[400] Xiaowen Ou, Peng Chen, and Bi-Feng Liu. Single-cell Analysis with Microfluidic Devices. *Analytical Sciences*, 35(6):609–618, June 2019.

[401] Francesco Padovani, Benedikt Mairhörmann, Pascal Falter-Braun, Jette Lengefeld, and Kurt M. Schmoller. Segmentation, tracking and cell cycle analysis of live-cell imaging data with Cell-ACDC. *BMC Biology*, 20(1):174, August 2022.

[402] David Paez-Espino, Emiley A Eloe-Fadrosh, Georgios A Pavlopoulos, Alex D Thomas, Marcel Huntemann, Natalia Mikhailova, Edward Rubin, Natalia N Ivanova, and Nikos C Kyrpides. Uncovering Earth's virome. *Nature*, 536(7617):425–430, 2016. Publisher: Nature Publishing Group UK London.

[403] Ahmad Paintdakhi, Bradley Parry, Manuel Campos, Irnov Irnov, Johan Elf, Ivan Surovtsev, and Christine Jacobs-Wagner. Oufti: an integrated software package for high-accuracy, high-throughput quantitative microscopy analysis: Oufti: image analysis software. *Molecular Microbiology*, 99(4):767–777, February 2016.

[404] Ting Pan, Dengyun Lu, Hongbao Xin, and Baojun Li. Biophotonic probes for bio-detection and imaging. *Light: Science & Applications*, 10(1):124, 2021. Publisher: Nature Publishing Group UK London.

[405] Kameshpandian Paramasivam, Yuanzhao Shen, Jiasheng Yuan, Ibtesam Waheed, Chuanbin Mao, and Xin Zhou. Advances in the Development of Phage-Based Probes for Detection of Bio-Species. *Biosensors*, 12(1):30, January 2022.

[406] Stephen F. Parmley and George P. Smith. Antibody-selectable filamentous fd phage vectors: affinity purification of target genes. *Gene*, 73(2):305–318, December 1988.

[407] Matthias Paschke. Phage display systems and their applications. *Applied Microbiology and Biotechnology*, 70(1):2–11, March 2006.

[408] Dhrati V. Patangia, Cornelius Anthony Ryan, Eugene Dempsey, Reynolds Paul Ross, and Catherine Stanton. Impact of antibiotics on the human microbiome and consequences for host health. *MicrobiologyOpen*, 11(1):e1260, February 2022.

[409] Sivan Pearl, Chana Gabay, Roy Kishony, Amos Oppenheim, and Nathalie Q Balaban. Nongenetic Individuality in the Host–Phage Interaction. *PLoS Biology*, 6(5):e120, May 2008.

[410] Arezoo Pedramfar, Keivan Beheshti Maal, and Sayed Hossein Mirdamadian. Phage therapy of corrosion-producing bacterium *Stenotrophomonas maltophilia* using isolated lytic bacteriophages. *Anti-Corrosion Methods and Materials*, 64(6):607–612, November 2017.

[411] Prashant S Phale, Balaram Mohapatra, Harshit Malhotra, and Bhavik A Shah. Ecophysiological portrait of a novel Pseudomonas sp. CSV86: an ideal host/candidate for metabolic engineering and bioremediation. *Environmental Microbiology*, 24(6):2797–2816, 2022. Publisher: Wiley Online Library.

[412] Diana P. Pires, Sara Cleto, Sanna Sillankorva, Joana Azeredo, and Timothy K. Lu. Genetically Engineered Phages: a Review of Advances over the Last Decade. *Microbiology and Molecular Biology Reviews*, 80(3):523–543, September 2016.

[413] Ramiz Polić. Phase contrast microscopy principle and applications in Materials science. 2020.

[414] Benoit J. Pons, Tatiana Dimitriu, Edze R. Westra, and Stineke Van Houte. Antibiotics that affect translation can antagonize phage infectivity by interfering with the deployment of counter-defenses. *Proceedings of the National Academy of Sciences*, 120(4):e2216084120, January 2023.

[415] Witold Postek, Natalia Pacocha, and Piotr Garstecki. Microfluidics for antibiotic susceptibility testing. *Lab on a Chip*, 22(19):3637–3662, 2022.

[416] Laurent Potvin-Trottier, Scott Luro, and Johan Paulsson. Microfluidics and single-cell microscopy to study stochastic processes in bacteria. *Current Opinion in Microbiology*, 43:186–192, June 2018.

[417] P. Prabhat, S. Ram, E.S. Ward, and R.J. Ober. Simultaneous Imaging of Different Focal Planes in Fluorescence Microscopy for the Study of Cellular Dynamics in Three Dimensions. *IEEE Transactions on Nanobioscience*, 3(4):237–242, December 2004.

[418] David G. Priest, Nobuyuki Tanaka, Yo Tanaka, and Yuichi Taniguchi. Micropatterned agarose gel devices for single-cell high-throughput microscopy of E. coli cells. *Scientific Reports*, 7(1):17750, December 2017.

[419] Huan Qi, Haiqin Lu, Hua-Ji Qiu, Valery Petrenko, and Aihua Liu. Phagemid Vectors for Phage Display: Properties, Characteristics and Construction. *Journal of Molecular Biology*, 417(3):129–143, March 2012.

[420] G. Rabut and J. Ellenberg. Automatic real-time three-dimensional cell tracking by fluorescence microscopy. *Journal of Microscopy*, 216(2):131–137, November 2004.

[421] D. V. Rakhuba, E. I. Kolomiets, E. Szwajcer Dey, and G. I. Novik. Bacteriophage receptors, mechanisms of phage adsorption and penetration into host cell. *Polish Journal of Microbiology*, 59(3):145–155, 2010.

[422] Jasna Rakonjac, Nicholas J. Bennett, Julian Spagnuolo, Dragana Gagic, and Marjorie Russel. Filamentous bacteriophage: biology, phage display and nanotechnology applications. *Current Issues in Molecular Biology*, 13(2):51–76, 2011.

[423] Jasna Rakonjac, Goran Jovanovic, and Peter Model. Filamentous phage infection-mediated gene expression: construction and propagation of the gIII deletion mutant helper phage R408d3. *Gene*, 198(1-2):99–103, 1997. Publisher: Elsevier.

[424] Wayne S Rasband. ImageJ. 1997. Publisher: Bethesda, MD.

[425] Ihab Rasched and Erika Oberer. Ff Coliphages: Structural And Functional Relationships. *Microbiological Reviews*, 50(4):401–427, 1986. Publisher: Am Soc Microbiol.

[426] Jonathan M Raser and Erin K O'shea. Noise in gene expression: origins, consequences, and control. *Science*, 309(5743):2010–2013, 2005. Publisher: American Association for the Advancement of Science.

[427] Torben Sølbeck Rasmussen, Anna Kirstine Koefoed, Rasmus Riemer Jakobsen, Ling Deng, Josué L Castro-Mejía, Anders Brunse, Horst Neve, Finn Kvist Vogensen, and Dennis Sandris Nielsen. Bacteriophage-mediated manipulation of the gut microbiome – promises and presents limitations. *FEMS Microbiology Reviews*, 44(4):507–521, July 2020.

[428] S. Ratnam and Sandra B. March. Laboratory studies on salmonella-contaminated cheese involved in a major outbreak of gastroenteritis. *Journal of Applied Bacteriology*, 61(1):51–56, July 1986.

[429] G Reshes, S Vanounou, I Fishov, and M Feingold. Timing the start of division in *E. coli* : a single-cell study. *Physical Biology*, 5(4):046001, November 2008.

[430] Daniel R Rines, Dominik Thomann, Jonas F Dorn, Paul Goodwin, and Peter K Sorger. Live cell imaging of yeast. *Cold Spring Harbor Protocols*, 2011(9):pdb–top065482, 2011. Publisher: Citeseer.

[431] Gregory T. Roman, Yanli Chen, Pernilla Viberg, Anne H. Culbertson, and Christopher T. Culbertson. Single-cell manipulation and analysis using microfluidic devices. *Analytical and Bioanalytical Chemistry*, 387(1):9–12, January 2007.

[432] Carlotta Ronda and Harris H Wang. Engineering temporal dynamics in microbial communities. *Current Opinion in Microbiology*, 65:47–55, February 2022.

[433] Liam M Rooney, William B Amos, Paul A Hoskisson, and Gail McConnell. Intracolony channels in *E. coli* function as a nutrient uptake system. *The ISME Journal*, 14(10):2461–2473, October 2020.

[434] Eli Rothenberg, Leonardo A. Sepúlveda, Samuel O. Skinner, Lanying Zeng, Paul R. Selvin, and Ido Golding. Single-Virus Tracking Reveals a Spatial Receptor-Dependent Search Mechanism. *Biophysical Journal*, 100(12):2875–2882, June 2011.

[435] A. Roumboutsos and G. Stewart. A Direct Deconvolution or Convolution Algorithm for Well Test Analysis. In *All Days*, pages SPE–18157–MS, Houston, Texas, October 1988. SPE.

[436] Simon Roux, Mart Krupovic, Rebecca A. Daly, Adair L. Borges, Stephen Nayfach, Frederik Schulz, Allison Sharrar, Paula B. Matheus Carnevali, Jan-Fang Cheng, Natalia N. Ivanova, Joseph Bondy-Denomy, Kelly C. Wrighton, Tanja Woyke, Axel Visel, Nikos C. Kyrpides, and Emiley A. Eloe-Fadrosh. Cryptic inoviruses revealed as pervasive in bacteria and archaea across Earth's biomes. *Nature Microbiology*, 4(11):1895–1906, July 2019.

[437] Timothy J. Rudge, Fernán Federici, Paul J. Steiner, Anton Kan, and Jim Haseloff. Cell Polarity-Driven Instability Generates Self-Organized, Fractal Patterning of Cell Layers. *ACS Synthetic Biology*, 2(12):705–714, December 2013.

[438] Timothy J. Rudge, Paul J. Steiner, Andrew Phillips, and Jim Haseloff. Computational Modeling of Synthetic Microbial Biofilms. *ACS Synthetic Biology*, 1(8):345–352, August 2012.

[439] Roberto Rusconi, Melissa Garren, and Roman Stocker. Microfluidics Expanding the Frontiers of Microbial Ecology. *Annual Review of Biophysics*, 43(1):65–91, May 2014.

[440] Marjorie Russel, Simon Kidd, and Mark R Kelley. An improved filamentous helper phage for generating single-stranded plasmid DNA. *Gene*, 45(3):333–338, 1986. Publisher: Elsevier.

[441] Marjorie Russel, Nora A Linderoth, and Andrej Šali. Filamentous phage assembly: variation on a protein export theme. *Gene*, 192(1):23–32, 1997. Publisher: Elsevier.

[442] Masahiro Ryo, Carlos A Aguilar-Trigueros, Liliana Pinek, Ludo AH Muller, and Matthias C Rillig. Basic principles of temporal dynamics. *Trends in ecology & evolution*, 34(8):723–733, 2019. Publisher: Elsevier.

[443] E Ryu. A Simple Method of Staining Bacterial Flagella. *Kitasato Archives of Experimental Medicine*, 14:218–19, 1937.

[444] William O Salivar, Helen Tzagoloff, and David Pratt. Some physical-chemical and biological properties of the rod-shaped coliphage M13. *Virology*, 24(3):359–371, 1964. Publisher: Elsevier.

[445] Alvaro Sanchez, Sandeep Choubey, and Jane Kondev. Regulation of Noise in Gene Expression. *Annual Review of Biophysics*, 42(1):469–491, May 2013.

[446] J. Sanchez and H. Benaroya. Review of force reconstruction techniques. *Journal of Sound and Vibration*, 333(14):2999–3018, July 2014.

[447] M.E. Sanders, L. Morelli, and T.A. Tompkins. Sporeformers as Human Probiotics: *Bacillus, Sporolactobacillus* , and *Brevibacillus*. *Comprehensive Reviews in Food Science and Food Safety*, 2(3):101–110, July 2003.

[448] Jiranuwat Sapudom, Johannes Waschke, Katja Franke, Mario Hlawitschka, and Tilo Pompe. Quantitative label-free single cell tracking in 3D biomimetic matrices. *Scientific Reports*, 7(1):14135, October 2017.

[449] Sarah Sheppard. New WHO report highlights progress, but also remaining gaps, in ensuring a robust pipeline of antibiotic treatments to combat antimicrobial resistance (AMR). *World Health Organization*, May 2023.

[450] Venetia A Saunders, Richard Gregory, and Jon R Saunders. Individual-Based Modeling of Bacterial Genetic Elements. In *Encyclopedia of Information Science and Technology, Second Edition*, pages 1930–1937. IGI Global, 2009.

[451] R. Sausset, M. A. Petit, V. Gaboriau-Routhiau, and M. De Paepe. New insights into intestinal phages. *Mucosal Immunology*, 13(2):205–215, March 2020.

[452] Phei Er Saw and Er-Wei Song. Phage display screening of therapeutic peptide for cancer targeting and therapy. *Protein & Cell*, 10(11):787–807, November 2019.

[453] Johannes Schindelin, Ignacio Arganda-Carreras, Erwin Frise, Verena Kaynig, Mark Longair, Tobias Pietzsch, Stephan Preibisch, Curtis Rueden, Stephan Saalfeld, and Benjamin Schmid. Fiji: an open-source platform for biological-image analysis. *Nature methods*, 9(7):676–682, 2012. Publisher: Nature Publishing Group.

[454] Gregor W. Schmidt, Olivier Frey, and Fabian Rudolf. The CellClamper: A Convenient Microfluidic Device for Time-Lapse Imaging of Yeast. In Marco Muzi-Falconi and Grant W Brown, editors, *Genome Instability*, volume 1672, pages 537–555. Springer New York, New York, NY, 2018. Series Title: Methods in Molecular Biology.

[455] Matthias Scholz, Adrian Tett, and Nicola Segata. Computational Tools for Taxonomic Microbiome Profiling of Shotgun Metagenomes. In *Metagenomics for Microbiology*, pages 67–80. Elsevier, 2015.

[456] sciencegateway. https://www.sciencegateway.org/protocols/cellbio/cell/moipfu.htm.

[457] Patrick R. Secor, Elizabeth B. Burgener, M. Kinnersley, Laura K. Jennings, Valery Roman-Cruz, Medeea Popescu, Jonas D. Van Belleghem, Naomi Haddock, Conner Copeland, Lia A. Michaels, Christiaan R. De Vries, Qingquan Chen, Julie Pourtois, Travis J. Wheeler, Carlos E. Milla, and Paul L. Bollyky. Pf Bacteriophage and Their Impact on Pseudomonas Virulence, Mammalian Immunity, and Chronic Infections. *Frontiers in Immunology*, 11:244, February 2020.

[458] Patrick R. Secor, Johanna M. Sweere, Lia A. Michaels, Andrey V. Malkovskiy, Daniel Lazzareschi, Ethan Katznelson, Jayakumar Rajadas, Michael E. Birnbaum, Allison Arrigoni, Kathleen R. Braun, Stephen P. Evanko, David A. Stevens, Werner Kaminsky, Pradeep K. Singh, William C. Parks, and Paul L. Bollyky. Filamentous Bacteriophage Promote Biofilm Assembly and Function. *Cell Host & Microbe*, 18(5):549–559, November 2015.

[459] Hemaa Selvakumar, Yu-Hui Lin, Neeraja Gollamudi, Joshua Weitz, and Jennifer Curtis. Spatiotemporal dynamics of phage-biofilm interactions. *Bulletin of the American Physical Society*, 63, 2018. Publisher: American Physical Society.

[460] Bin Shao, Jayan Rammohan, Daniel A. Anderson, Nina Alperovich, David Ross, and Christopher A. Voigt. Single-cell measurement of plasmid copy number and promoter activity. *Nature Communications*, 12(1):1475, March 2021.

[461] Qiuyan Shao, Michael G. Cortes, Jimmy T. Trinh, Jingwen Guan, Gábor Balázsi, and Lanying Zeng. Coupling of DNA Replication and Negative Feedback Controls Gene Expression for Cell-Fate Decisions. *iScience*, 6:1–12, August 2018.

[462] Qiuyan Shao, Alexander Hawkins, and Lanying Zeng. Phage DNA Dynamics in Cells with Different Fates. *Biophysical Journal*, 108(8):2048–2060, April 2015.

[463] Jason W Shapiro and Catherine Putonti. UP phages, a new group of filamentous phages found in several members of Enterobacteriales. *Virus evolution*, 6(1):veaa030, 2020. Publisher: Oxford University Press.

[464] Jason W Shapiro, Elizabeth SCP Williams, and Paul E Turner. Evolution of parasitism and mutualism between filamentous phage M13 and Escherichia coli. *PeerJ*, 4:e2060, 2016. Publisher: PeerJ Inc.

[465] Gil Sharon, Nikki Jamie Cruz, Dae-Wook Kang, Michael J. Gandal, Bo Wang, Young-Mo Kim, Erika M. Zink, Cameron P. Casey, Bryn C. Taylor, Christianne J. Lane, Lisa M. Bramer, Nancy G. Isern, David W. Hoyt, Cecilia Noecker, Michael J. Sweredoski, Annie Moradian, Elhanan Borenstein, Janet K. Jansson, Rob Knight, Thomas O. Metz, Carlos Lois, Daniel H. Geschwind, Rosa Krajmalnik-Brown, and Sarkis K. Mazmanian. Human Gut Microbiota from Autism Spectrum Disorder Promote Behavioral Symptoms in Mice. *Cell*, 177(6):1600–1618.e17, May 2019.

[466] Natasha J. Sharp, Ian J. Molineux, Martin A. Page, and David A. Schofield. Rapid Detection of Viable Bacillus anthracis Spores in Environmental Samples by Using Engineered Reporter Phages. *Applied and Environmental Microbiology*, 82(8):2380–2387, April 2016.

[467] A. N. Sharpley, M. B. Daniels, K. R. Brye, K. VanDevender, J. Burke, L. G. Berry, and P. Webb. Fate and transport of phosphorus-containing land-applied swine slurry in a karst watershed. *Agrosystems, Geosciences & Environment*, 3(1), January 2020.

[468] Cormac Sheridan. Pivotal trials for [beta]-secretase inhibitors in Alzheimer's. *Nature biotechnology*, 33(2):115–117, 2015. Publisher: Nature Publishing Group.

[469] Ravi U. Sheth, Vitor Cabral, Sway P. Chen, and Harris H. Wang. Manipulating Bacterial Communities by in situ Microbiome Engineering. *Trends in Genetics*, 32(4):189–200, April 2016.

[470] Jae Hwan Shin, Tae Jung Park, Moon Seop Hyun, and Jong Pil Park. A phage virus-based electrochemical biosensor for highly sensitive detection of ovomucoid. *Food Chemistry*, 378:132061, June 2022.

[471] Karthik Basthi Shivaram, Pankaj Bhatt, Mohit S Verma, Kari Clase, and Halis Simsek. Bacteriophage-based biosensors for detection of pathogenic microbes in wastewater. *Science of The Total Environment*, page 165859, 2023. Publisher: Elsevier.

[472] Kshitiz Raj Shrestha and So Young Yoo. Phage-based artificial niche: the recent progress and future opportunities in stem cell therapy. *Stem Cells International*, 2019, 2019. Publisher: Hindawi.

[473] Sachdev S Sidhu. Engineering M13 for phage display. *Biomolecular engineering*, 18(2):57–63, 2001. Publisher: Elsevier.

[474] Sanna Sillankorva, Rosário Oliveira, Maria João Vieira, Ian Sutherland, and Joana Azeredo. Bacteriophage S1 infection of Pseudomonas fluorescens planktonic cells versus biofilms. *Biofouling*, 20(3):133–138, 2004. Publisher: Taylor & Francis.

[475] Peter Simmonds, Mike J. Adams, Mária Benkő, Mya Breitbart, J. Rodney Brister, Eric B. Carstens, Andrew J. Davison, Eric Delwart, Alexander E. Gorbalenya, Balázs Harrach, Roger Hull, Andrew M.Q. King, Eugene V. Koonin, Mart Krupovic, Jens H. Kuhn, Elliot J. Lefkowitz, Max L. Nibert, Richard Orton, Marilyn J. Roossinck, Sead Sabanadzovic, Matthew B. Sullivan, Curtis A. Suttle, Robert B. Tesh, René A. van der Vlugt, Arvind Varsani, and F. Murilo Zerbini. Virus taxonomy in the age of metagenomics. *Nature Reviews Microbiology*, 15(3):161–168, March 2017.

[476] Matthew Simmons, Matthew C. Bond, Knut Drescher, Vanni Bucci, and Carey D. Nadell. Evolutionary dynamics of phage resistance in bacterial biofilms. preprint, Microbiology, February 2019.

[477] Matthew Simmons, Knut Drescher, Carey D Nadell, and Vanni Bucci. Phage mobility is a core determinant of phage–bacteria coexistence in biofilms. *The ISME Journal*, 12(2):531–543, February 2018.

[478] Saptarshi Sinha, Rajdeep K. Grewal, and Soumen Roy. Modeling Bacteria–Phage Interactions and Its Implications for Phage Therapy. In *Advances in Applied Microbiology*, volume 103, pages 103–141. Elsevier, 2018.

[479] Saptarshi Sinha, Rajdeep Kaur Grewal, and Soumen Roy. Modeling Phage–Bacteria Dynamics. In Namrata Tomar, editor, *Immunoinformatics*, pages 309–327. Springer US, New York, NY, 2020.

[480] Mikael Skurnik, Maria Pajunen, and Saija Kiljunen. Biotechnological challenges of phage therapy. *Biotechnology Letters*, 29(7):995–1003, July 2007.

[481] Stefan Slopek, I Durlakowa, Beata Weber-Dabrowska, A Kucharewicz-Krukowska, Marek Dabrowski, and Regina Bisikiewicz. Results of bacteriophage treatment of suppurative bacterial infections. II. Detailed evaluation of the results. *Archivum immunologiae et therapiae experimentalis*, 31(3):293–327, 1983.

[482] Steven W. Smeal, Margaret A. Schmitt, Ronnie Rodrigues Pereira, Ashok Prasad, and John D. Fisk. Simulation of the M13 life cycle I: Assembly of a genetically-structured deterministic chemical kinetic simulation. *Virology*, 500:259–274, January 2017.

[483] Steven W. Smeal, Margaret A. Schmitt, Ronnie Rodrigues Pereira, Ashok Prasad, and John D. Fisk. Simulation of the M13 life cycle II: Investigation of the control mechanisms of M13 infection and establishment of the carrier state. *Virology*, 500:275–284, January 2017.

[484] George P. Smith. Filamentous Fusion Phage: Novel Expression Vectors That Display Cloned Antigens on the Virion Surface. *Science*, 228(4705):1315–1317, June 1985.

[485] George P Smith and Jamie K Scott. [15] Libraries of peptides and proteins displayed on filamentous phage. In *Methods in enzymology*, volume 217, pages 228–257. Elsevier, 1993.

[486] H. O. Smith, C. A. Hutchison, C. Pfannkoch, and J. C. Venter. Generating a synthetic genome by whole genome assembly: X174 bacteriophage from synthetic oligonucleotides. *Proceedings of the National Academy of Sciences*, 100(26):15440–15445, December 2003.

[487] Kevin Smith, Filippo Piccinini, Tamas Balassa, Krisztian Koos, Tivadar Danka, Hossein Azizpour, and Peter Horvath. Phenotypic Image Analysis Software Tools for Exploring and Understanding Big Image Data from Cell-Based Assays. *Cell Systems*, 6(6):636–653, June 2018.

[488] Maxwell Smith, Ryan Poling-Skutvik, Ali H Slim, Richard C Willson, and Jacinta C Conrad. Dynamics of flexible viruses in polymer solutions. *Macromolecules*, 54(10):4557–4563, 2021. Publisher: ACS Publications.

[489] M von Smoluchowski. Study of a mathematical theory of the coagulation kinetics of colloidal solutions. *Z. Phys. Chem.*, 92:129, 1917.

[490] Beka Solomon. Filamentous bacteriophage as a novel therapeutic tool for Alzheimer's disease treatment. *Journal of Alzheimer's Disease*, 15(2):193–198, 2008. Publisher: IOS Press.

[491] Jorge A. Moura de Sousa and Eduardo P. C. Rocha. Environmental structure drives resistance to phages and antibiotics during phage therapy and to invading lysogens during colonisation. *Scientific Reports*, 9(1):3149, December 2019.

[492] Matthew H. Spitzer and Garry P. Nolan. Mass Cytometry: Single Cells, Many Features. *Cell*, 165(4):780–791, May 2016.

[493] F. St-Pierre and D. Endy. Determination of cell fate selection during phage lambda infection. *Proceedings of the National Academy of Sciences*, 105(52):20705–20710, December 2008.

[494] Ruth Steinberg, Lara Knüpffer, Andrea Origi, Rossella Asti, and Hans-Georg Koch. Co-translational protein targeting in bacteria. *FEMS Microbiology Letters*, 365(11), June 2018.

[495] Craig Stephens, Tyler Arismendi, Megan Wright, Austin Hartman, Andres Gonzalez, Matthew Gill, Mark Pandori, and David Hess. F Plasmids Are the Major Carriers of Antibiotic Resistance Genes in Human-Associated Commensal Escherichia coli. *mSphere*, 5(4):e00709–20, August 2020.

[496] Eric J Stewart. Growing unculturable bacteria. *Journal of bacteriology*, 194(16):4151–4160, 2012. Publisher: Am Soc Microbiol.

[497] David R Stirling, Madison J Swain-Bowden, Alice M Lucas, Anne E Carpenter, Beth A Cimini, and Allen Goodman. CellProfiler 4: improvements in speed, utility and usability. *BMC bioinformatics*, 22:1–11, 2021. Publisher: Springer.

[498] Edel Stone, Katrina Campbell, Irene Grant, and Olivia McAuliffe. Understanding and Exploiting Phage–Host Interactions. *Viruses*, 11(6):567, June 2019.

[499] Tomas Storck, Cristian Picioreanu, Bernardino Virdis, and Damien J. Batstone. Variable Cell Morphology Approach for Individual-Based Modeling of Microbial Communities. *Biophysical Journal*, 106(9):2037–2048, May 2014.

[500] Tim Stuart and Rahul Satija. Integrative single-cell analysis. *Nature Reviews Genetics*, 20(5):257–272, May 2019.

[501] Stella Stylianidou, Connor Brennan, Silas B. Nissen, Nathan J. Kuwada, and Paul A. Wiggins. *SuperSegger* : robust image segmentation, analysis and lineage tracking of bacterial cells: Robust segmentation and analysis of bacteria. *Molecular Microbiology*, 102(4):690–700, November 2016.

[502] William C. Summers. The strange history of phage therapy. *Bacteriophage*, 2(2):130–133, April 2012.

[503] Ian W Sutherland, Kevin A Hughes, Lucy C Skillman, and Karen Tait. The interaction of phage and biofilms. *FEMS Microbiology Letters*, 232(1):1–6, March 2004.

[504] Antonet Svircev, Dwayne Roach, and Alan Castle. Framing the future with bacteriophages in agriculture. *Viruses*, 10(5):218, 2018. Publisher: MDPI.

[505] Thaysa Leite Tagliaferri, Mathias Jansen, and Hans-Peter Horz. Fighting Pathogenic Bacteria on Two Fronts: Phages and Antibiotics as Combined Strategy. *Frontiers in Cellular and Infection Microbiology*, 9:22, February 2019.

[506] Bradford P Taylor, Catherine J Penington, and Joshua S Weitz. Emergence of increased frequency and severity of multiple infections by viruses due to spatial clustering of hosts. *Physical biology*, 13(6):066014, 2017. Publisher: IOP Publishing.

[507] ThermoFisher. The Light Spectrum and its Relationship with Fluorescence.

[508] Holger Thie, Thomas Schirrmann, Matthias Paschke, Stefan Dübel, and Michael Hust. SRP and Sec pathway leader peptides for antibody phage display and antibody fragment production in E. coli. *New Biotechnology*, 25(1):49–54, June 2008.

[509] Joanna D. Thomas, Richard A. Daniel, Jeff Errington, and Colin Robinson. Export of active green fluorescent protein to the periplasm by the twin-arginine translocase (Tat) pathway in Escherichia coli. *Molecular Microbiology*, 39(1):47–53, January 2001.

[510] Xue Tian, Lloyd C. Murfin, Luling Wu, Simon E. Lewis, and Tony D. James. Fluorescent small organic probes for biosensing. *Chemical Science*, 12(10):3406–3426, 2021.

[511] N. V. Tikunova and V. V. Morozova. Phage display on the base of filamentous bacteriophages: application for recombinant antibodies selection. *Acta Naturae*, 1(3):20–28, October 2009.

[512] Helena Todorov, Tania Miguel Trabajo, and Jan Roelof Van Der Meer. STrack: A Tool to Simply Track Bacterial Cells in Microscopy Time-Lapse Images. *mSphere*, 8(2):e00658–22, April 2023.

[513] Jimmy T. Trinh, Qiuyan Shao, Jingwen Guan, and Lanying Zeng. Emerging heterogeneous compartments by viruses in single bacterial cells. *Nature Communications*, 11(1):3813, December 2020.

[514] Jimmy T. Trinh, Tamás Székely, Qiuyan Shao, Gábor Balázsi, and Lanying Zeng. Cell fate decisions emerge as phages cooperate or compete inside their host. *Nature Communications*, 8(1):14341, April 2017.

[515] null Trisilowati and D. G. Mallet. In silico experimental modeling of cancer treatment. *ISRN oncology*, 2012:828701, 2012.

[516] T.G. Trucano, L.P. Swiler, T. Igusa, W.L. Oberkampf, and M. Pilch. Calibration, validation, and sensitivity analysis: What's what. *Reliability Engineering & System Safety*, 91(10-11):1331–1357, October 2006.

[517] Peter J Turnbaugh, Ruth E Ley, Micah Hamady, Claire M Fraser-Liggett, Rob Knight, and Jeffrey I Gordon. The human microbiome project. *Nature*, 449(7164):804–810, 2007. Publisher: Nature Publishing Group UK London.

[518] Helen Tzagoloff and David Pratt. The initial steps in infection with coliphage M13. *Virology*, 24(3):372–380, November 1964.

[519] Sarah Täuber, Julian Schmitz, Luisa Blöbaum, Niklas Fante, Heiko Steinhoff, and Alexander Grünberger. How to Perform a Microfluidic Cultivation Experiment—A Guideline to Success. *Biosensors*, 11(12):485, November 2021.

[520] UKEssays. Filamentous DNA Phages & Single Stranded RNA Phages, November 2018.

[521] Raymond C. Valentine, P.M. Silverman, K.A. Ippen, and H. Mobach. The F-Pilus of Escherichia coli. In *Advances in Microbial Physiology*, volume 3, pages 1–52. Elsevier, 1969.

[522] Mirko Van Der Baan. Bandwidth Enhancement: Inverse Q Filtering or Time-varying Wiener Deconvolution? *GEOPHYSICS*, 77(4):V133–V142, July 2012.

[523] Peter Van Roessel and Andrea H. Brand. Imaging into the future: visualizing gene expression and protein interactions with fluorescent proteins. *Nature Cell Biology*, 4(1):E15–E20, January 2002.

[524] Sven Van Teeffelen, Joshua W. Shaevitz, and Zemer Gitai. Image analysis in fluorescence microscopy: Bacterial dynamics as a case study. *BioEssays*, 34(5):427–436, May 2012.

[525] Lautaro Vassallo, David Hansmann, and Lidia A. Braunstein. On the growth of non-motile bacteria colonies: an agent-based model for pattern formation. *The European Physical Journal B*, 92(9):216, September 2019.

[526] Nileena Velappan, Hugh E. Fisher, Emanuele Pesavento, Leslie Chasteen, Sara D'Angelo, Csaba Kiss, Michelle Longmire, Peter Pavlik, and Andrew R. M. Bradbury. A comprehensive analysis of filamentous phage display vectors for cytoplasmic proteins: an analysis with different fluorescent proteins. *Nucleic Acids Research*, 38(4):e22–e22, March 2010.

[527] C. Lee Ventola. The antibiotic resistance crisis: part 1: causes and threats. *P & T: A Peer-Reviewed Journal for Formulary Management*, 40(4):277–283, April 2015.

[528] Nikola Vidovic and Sinisa Vidovic. Antimicrobial Resistance and Food Animals: Influence of Livestock Environment on the Emergence and Dissemination of Antimicrobial Resistance. *Antibiotics*, 9(2):52, January 2020.

[529] Jeffrey Vieira and Joachim Messing. [1] Production of single-stranded plasmid DNA. In *Methods in Enzymology*, volume 153, pages 3–11. Elsevier, 1987.

[530] T. M. Viertel, K. Ritter, and H.-P. Horz. Viruses versus bacteria–novel approaches to phage therapy as a tool against multidrug-resistant pathogens. *Journal of Antimicrobial Chemotherapy*, 69(9):2326–2336, September 2014.

[531] Amit Vikram, Mary Tl Callahan, Joelle W Woolston, Manan Sharma, and Alexander Sulakvelidze. Phage biocontrol for reducing bacterial foodborne pathogens in produce and other foods. *Current Opinion in Biotechnology*, 78:102805, December 2022.

[532] Salom Gnana Thanga Vincent, Tim Jennerjahn, and Kumarasamy Ramasamy. Assessment of microbial structure and functions in coastal sediments. In *Microbial Communities in Coastal Sediments*, pages 167–185. Elsevier, 2021.

[533] Benjamin Volkmer and Matthias Heinemann. Condition-dependent cell volume and concentration of Escherichia coli to facilitate data conversion for systems biology modeling. *PloS One*, 6(7):e23126, 2011.

[534] Lisa R. Volpatti and Ali K. Yetisen. Commercialization of microfluidic devices. *Trends in Biotechnology*, 32(7):347–350, July 2014.

[535] Peter J. Voorhees, Carlos Cruz-Teran, Jasmine Edelstein, and Samuel K. Lai. Challenges & opportunities for phage-based in situ microbiome engineering in the gut. *Journal of Controlled Release*, 326:106–119, October 2020.

[536] Willem M. de Vos, Herbert Tilg, Matthias Van Hul, and Patrice D. Cani. Gut microbiome and health: mechanistic insights. *Gut*, 71(5):1020–1032, 2022. Publisher: BMJ Publishing Group _eprint: https://gut.bmj.com/content/71/5/1020.full.pdf.

[537] Matthew K Waldor and David I Friedman. Phage regulatory circuits and virulence gene expression. *Current Opinion in Microbiology*, 8(4):459–465, August 2005.

[538] Zhenmao Wan and Noel L Goddard. Competition Between Conjugation and M13 Phage Infection in *Escherichia coli* in the Absence of Selection Pressure: A Kinetic Study. *G3 Genes|Genomes|Genetics*, 2(10):1137–1144, October 2012.

[539] Junbiao Wang, Alessia Lamolinara, Laura Conti, Mara Giangrossi, Lishan Cui, Maria Beatrice Morelli, Consuelo Amantini, Maurizio Falconi, Caterina Bartolacci, Cristina Andreani, Fiorenza Orlando, Mauro Provinciali, Francesco Domenico Del Pizzo, Francesca Russo, Barbara Belletti, Federica Riccardo, Elisabetta Bolli, Elena Quaglino, Federica Cavallo, Augusto Amici, Manuela Iezzi, and Cristina Marchini. HER2-Displaying M13 Bacteriophages induce Therapeutic Immunity against Breast Cancer. *Cancers*, 14(16):4054, August 2022.

[540] Peng Wang, Gege Yu, Juan Wei, Xingrui Liao, Yao Zhang, Yarong Ren, Cui Zhang, Yueqi Wang, Daohong Zhang, Jianlong Wang, and Yanru Wang. A single thiolated-phage displayed nanobody-based biosensor for label-free detection of foodborne pathogen. *Journal of Hazardous Materials*, 443:130157, February 2023.

[541] Ping Wang, Lydia Robert, James Pelletier, Wei Lien Dang, Francois Taddei, Andrew Wright, and Suckjoon Jun. Robust Growth of Escherichia coli. *Current Biology*, 20(12):1099–1103, June 2010.

[542] Qing Wang and Matthias Ihme. Regularized deconvolution method for turbulent combustion modeling. *Combustion and Flame*, 176:125–142, February 2017.

[543] Quanli Wang, Jarad Niemi, Chee-Meng Tan, Lingchong You, and Mike West. Image segmentation and dynamic lineage analysis in single-cell fluorescence microscopy. *Cytometry Part A*, 9999A:NA–NA, 2009.

[544] Tao Wang, Özcan Özdamar, Jorge Bohórquez, Qian Shen, and Marie Cheour. Wiener filter deconvolution of overlapping evoked potentials. *Journal of Neuroscience Methods*, 158(2):260–270, December 2006.

[545] Ryohei Watanabe, Tetsuya Matsumoto, Go Sano, Yoshikazu Ishii, Kazuhiro Tateda, Yoshinobu Sumiyama, Jumpei Uchiyama, Shingo Sakurai, Shigenobu Matsuzaki, Shosuke Imai, and Keizo Yamaguchi. Efficacy of bacteriophage therapy against gut-derived sepsis caused by Pseudomonas aeruginosa in mice. *Antimicrobial Agents and Chemotherapy*, 51(2):446–452, February 2007.

[546] R Webster. Filamentous phage biology. *Phage display: a laboratory manual*, pages 1–1, 2001. Publisher: Cold Spring Harbor Laboratory Press Cold Spring Harbor, NY.

[547] Martijn Wehrens, Dmitry Ershov, Rutger Rozendaal, Noreen Walker, Daniel Schultz, Roy Kishony, Petra Anne Levin, and Sander J. Tans. Size Laws and Division Ring Dynamics in Filamentous Escherichia coli cells. *Current Biology*, 28(6):972–979.e5, March 2018.

[548] Guopeng Wei, Paul Bogdan, and Radu Marculescu. Efficient Modeling and Simulation of Bacteria-Based Nanonetworks with BNSim. *IEEE Journal on Selected Areas in Communications*, 31(12):868–878, December 2013.

[549] Gregory A Weiss and Sachdev S Sidhu. Design and evolution of artificial M13 coat proteins. *Journal of Molecular Biology*, 300(1):213–219, June 2000.

[550] JLM Welch, BJ Rossetti, CW Rieken, FE Dewhirst, and GG Borisy. Biogeography of a human oral microbiome at the micron scale. PNAS 113. *E791–E800*, 2016.

[551] Aimee K. Wessel, Laura Hmelo, Matthew R. Parsek, and Marvin Whiteley. Going local: technologies for exploring bacterial microenvironments. *Nature Reviews Microbiology*, 11(5):337–348, May 2013.

[552] Corey S. Westfall and Petra Anne Levin. Comprehensive analysis of central carbon metabolism illuminates connections between nutrient availability, growth rate, and cell morphology in Escherichia coli. *PLOS Genetics*, 14(2):e1007205, February 2018.

[553] Caroline Westwater, Laura M. Kasman, David A. Schofield, Phillip A. Werner, Joseph W. Dolan, Michael G. Schmidt, and James S. Norris. Use of Genetically Engineered Phage To Deliver Antimicrobial Agents to Bacteria: an Alternative Therapy for Treatment of Bacterial Infections. *Antimicrobial Agents and Chemotherapy*, 47(4):1301–1307, April 2003.

[554] William GT Willats. Phage display: practicalities and prospects. *Plant molecular biology*, 50:837–854, 2002. Publisher: Springer.

[555] Madison C. Williams, Alexandra E. Reker, Shally R. Margolis, Jingqiu Liao, Martin Wiedmann, Enrique R. Rojas, and Alexander J. Meeske. Restriction endonuclease cleavage of phage DNA enables resuscitation from Cas13-induced bacterial dormancy. *Nature Microbiology*, 8(3):400–409, February 2023.

[556] Jared L. Wilmoth, Peter W. Doak, Andrea Timm, Michelle Halsted, John D. Anderson, Marta Ginovart, Clara Prats, Xavier Portell, Scott T. Retterer, and Miguel Fuentes-Cabrera. A Microfluidics and Agent-Based Modeling Framework for Investigating Spatial Organization in Bacterial Colonies: The Case of Pseudomonas Aeruginosa and H1-Type VI Secretion Interactions. *Frontiers in Microbiology*, 9:33, 2018.

[557] Jan C. Wohlfarth, Miki Feldmüller, Alissa Schneller, Samuel Kilcher, Marco Burkolter, Susanne Meile, Martin Pilhofer, Markus Schuppler, and Martin J. Loessner. L-form conversion in Gram-positive bacteria enables escape from phage infection. *Nature Microbiology*, January 2023.

[558] Wolfe Lab, Video: https://www.youtube.com/watch?v=UqU8Mczg1Rk. Baker's yeast timelapse.

[559] Shirley Wong, Salma Jimenez, and Roderick A. Slavcev. Construction and characterization of a novel miniaturized filamentous phagemid for targeted mammalian gene transfer. *Microbial Cell Factories*, 22(1):124, July 2023.

[560] Sunny H Wong and Jun Yu. Gut microbiota in colorectal cancer: mechanisms of action and clinical applications. *Nature Reviews Gastroenterology & Hepatology*, 16(11):690–704, 2019. Publisher: Nature Publishing Group UK London.

[561] M A Woody and D O Cliver. Effects of temperature and host cell growth phase on replication of F-specific RNA coliphage Q beta. *Applied and Environmental Microbiology*, 61(4):1520, April 1995.

[562] World Health Organization. *Antimicrobial resistance: global report on surveillance*. World Health Organization, Geneva, 2014. Section: xxii, 232 p.

[563] World Health Organization. Antibiotic resistance, July 2020.

[564] Yupan Wu and Yingqi Meng. Cell manipulation and single cell characterization on microfluidic devices. *TrAC Trends in Analytical Chemistry*, 168:117301, November 2023.

[565] Jingting Xu, Ying Chau, and Yi-kuen Lee. Phage-based electrochemical sensors: A review. *Micromachines*, 10(12):855, 2019. Publisher: MDPI.

[566] Iftach Yacoby, Marina Shamis, Hagit Bar, Doron Shabat, and Itai Benhar. Targeting antibacterial agents by using drug-carrying filamentous bacteriophages. *Antimicrobial agents and chemotherapy*, 50(6):2087–2097, 2006. Publisher: Am Soc Microbiol.

[567] Da Yang, Anna D. Jennings, Evalynn Borrego, Scott T. Retterer, and Jaan Männik. Analysis of Factors Limiting Bacterial Growth in PDMS Mother Machine Devices. *Frontiers in Microbiology*, 9:871, May 2018.

[568] Li-Mei C Yang, Phillip Y Tam, Benjamin J Murray, Theresa M McIntire, Cathie M Overstreet, Gregory A Weiss, and Reginald M Penner. Virus electrodes for universal biodetection. *Analytical chemistry*, 78(10):3265–3270, 2006. Publisher: ACS Publications.

[569] Yufan Yang, Hu Du, Geng Zou, Zhiyong Song, Yang Zhou, Hao Li, Chen Tan, Huanchun Chen, Vincent A. Fischetti, and Jinquan Li. Encapsulation and delivery of phage as a novel method for gut flora manipulation in situ: A review. *Journal of Controlled Release*, 353:634–649, January 2023.

[570] Celeste Yanisch-Perron, Jeffrey Vieira, and Joachim Messing. Improved M13 phage cloning vectors and host strains: nucleotide sequences of the M13mpl8 and pUC19 vectors. *Gene*, 33(1):103–119, 1985. Publisher: Elsevier.

[571] Stephanie J Yaung, George M Church, and Harris H Wang. Recent progress in engineering human-associated microbiomes. *Engineering and Analyzing Multicellular Systems: Methods and Protocols*, pages 3–25, 2014. Publisher: Springer.

[572] Huabing Yin and Damian Marshall. Microfluidics for single cell analysis. *Current Opinion in Biotechnology*, 23(1):110–119, February 2012.

[573] So Young Yoo, Woo-Jae Chung, and Doe-Young Lee. Chemical modulation of M13 bacteriophage and its functional opportunities for nanomedicine. *International Journal of Nanomedicine*, page 5825, December 2014.

[574] Ido Yosef, Miriam Manor, Ruth Kiro, and Udi Qimron. Temperate and lytic bacteriophages programmed to sensitize and kill antibiotic-resistant bacteria. *Proceedings of the National Academy of Sciences*, 112(23):7267–7272, June 2015.

[575] Jonathan W Young, James C W Locke, Alphan Altinok, Nitzan Rosenfeld, Tigran Bacarian, Peter S Swain, Eric Mjolsness, and Michael B Elowitz. Measuring single-cell gene expression dynamics in bacteria using fluorescence time-lapse microscopy. *Nature Protocols*, 7(1):80–88, January 2012.

[576] Zi-Chao Yu, Xiu-Lan Chen, Qing-Tao Shen, Dian-Li Zhao, Bai-Lu Tang, Hai-Nan Su, Zhao-Yu Wu, Qi-Long Qin, Bin-Bin Xie, Xi-Ying Zhang, Yong Yu, Bai-Cheng Zhou, Bo Chen, and Yu-Zhong Zhang. Filamentous phages prevalent in Pseudoalteromonas

spp. confer properties advantageous to host survival in Arctic sea ice. *The ISME Journal*, 9(4):871–881, April 2015.

[577] Giuseppe Zanotti and Alessandro Grinzato. Structure of filamentous viruses. *Current Opinion in Virology*, 51:25–33, 2021. Publisher: Elsevier.

[578] Lanying Zeng, Samuel O. Skinner, Chenghang Zong, Jean Sippy, Michael Feiss, and Ido Golding. Decision Making at a Subcellular Level Determines the Outcome of Bacteriophage Infection. *Cell*, 141(4):682–691, May 2010.

[579] Jiawei Zhang, Chen Li, Md Mamunur Rahaman, Yudong Yao, Pingli Ma, Jinghua Zhang, Xin Zhao, Tao Jiang, and Marcin Grzegorzek. A Comprehensive Survey with Quantitative Comparison of Image Analysis Methods for Microorganism Biovolume Measurements. *Archives of Computational Methods in Engineering*, 30(1):639–673, January 2023.

[580] Leicheng Zhang, Peng Chen, Zhuoyue Zhou, Yawei Hu, Qiuyue Sha, Houjin Zhang, Xin Liu, Wei Du, Xiaojun Feng, and Bi-Feng Liu. Agarose-based microwell array chip for high-throughput screening of functional microorganisms. *Talanta*, 191:342–349, January 2019.

[581] Peng Zhang, Daqing Mao, Huihui Gao, Liyang Zheng, Zeyou Chen, Yuting Gao, Yitao Duan, Jianhua Guo, Yi Luo, and Hongqiang Ren. Colonization of gut microbiota by plasmid-carrying bacteria is facilitated by evolutionary adaptation to antibiotic treatment. *The ISME Journal*, 16(5):1284–1293, May 2022.

[582] Danping Zheng, Timur Liwinski, and Eran Elinav. Interaction between microbiota and immunity in health and disease. *Cell Research*, 30(6):492–506, June 2020.

[583] Yuqing Zhou, Ziyong Li, Jijie Huang, Yuxing Wu, Xinyu Mao, Yizhou Tan, Hui Liu, Dongxin Ma, Xun Li, and Xiaoye Wang. Development of a phage-based electrochemical biosensor for detection of Escherichia coli O157: H7 GXEC-N07. *Bioelectrochemistry*, 150:108345, April 2023.

[584] Michele Zuppi, Heather L. Hendrickson, Justin M. O'Sullivan, and Tommi Vatanen. Phages in the Gut Ecosystem. *Frontiers in Cellular and Infection Microbiology*, 11:822562, January 2022.

[585] Robert Zwanzig. On the relation between self-diffusion and viscosity of liquids. *The Journal of chemical physics*, 79(9):4507–4508, 1983. Publisher: American Institute of Physics.

[586] J Ørskov. Method for the isolation of bacteria in pure culture from single cells and procedure for the direct tracing of bacterial growth on a solid medium. *Journal of bacteriology*, 7(6):537, 1922. Publisher: American Society for Microbiology (ASM).

[587] Katja Šivec and Aleš Podgornik. Determination of bacteriophage growth parameters under cultivating conditions. *Applied Microbiology and Biotechnology*, 104(20):8949–8960, October 2020.

Appendix A

Media Recipes

All media utilized in this study, including their respective recipes, are documented in the Table A.1. Each was prepared using deionized water and sterilized by autoclaving. Additionally, to create agar-based media from any of the listed formulations, 15g of agar was supplemented to achieve a 1.5% agar concentration.

Table A.1: Media used in this study and their formulation

Media name	**Recipe for 1L**
LB Broth	10g tryptone, 5g yeast extract, 10g NaCl
Phage-specific LB Broth	10g tryptone, 5g yeast extract, 5g NaCl
SOC Broth	31g SOC powder
Wilkirn-Chalgern Broth	33g Wilkirn-Chalgern powder
MacConkey with Sorbitol	20g peptones, 10g D-Sorbitol, 1.5g Bile salt, 5g Sodium Chloride, 0.03g Neutral Red, 0.001g Crystal Violet
2X YT Broth	16 g tryptone, 10 g yeast extract, 5 g NaCl
Nutrient Broth	3g Beef Extract, 5g peptones, 8g NaCl

Appendix B

Single-cell analysis

The initial analysis focused on cellular morphological traits—specifically, radius, length, and elongation rate. Comparative averages of these parameters across all experiments are depicted in Figure B.1, Figure B.2, and Figure B.3 for radius, length, and elongation rate, respectively. The results exhibited consistent trends across all chambers, yet significant variations in averages were noted among experiments, as expected. This variation stemmed from the analysis being based on population averages.

Previous research has established that the length of bacteria can be affected by the composition and nutrient concentration of the culture media, as highlighted in studies like those by Levin et al. [313] and Reshes et al. [429]. In these studies, it was observed that nutrient-rich media tend to promote longer bacterial lengths when compared to slower-growth media. In this study, LB media was prepared on a weekly basis, aiming for uniformity in ingredient proportions. Nevertheless, slight variations might have arisen due to factors such as human error and device accuracy (scale). These minor differences in media preparation could contribute to the observed variations in bacterial cell length across experiments.

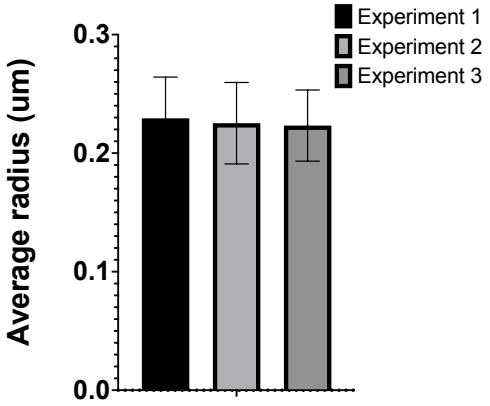


Figure B.1: The figure illustrates average radius in all the experiments analysed for control section

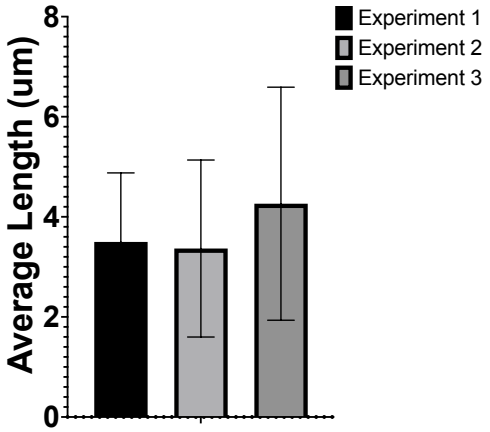


Figure B.2: The figure displays the average length across all three experiments that were utilized for the analysis.

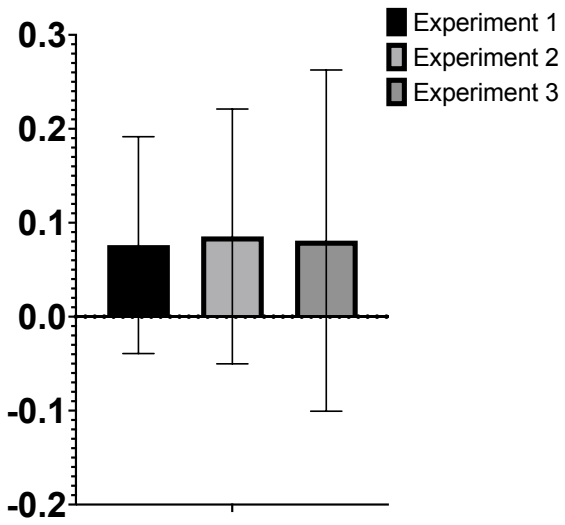


Figure B.3: Consistent Average Elongation Rate across all experiments

Appendix C

Lineage Tree

In the subsequent stage, lineages in which infection occurred were subjected to further analysis and separation. An example of how the data is analyzed for this step is illustrated in Figure C.1.

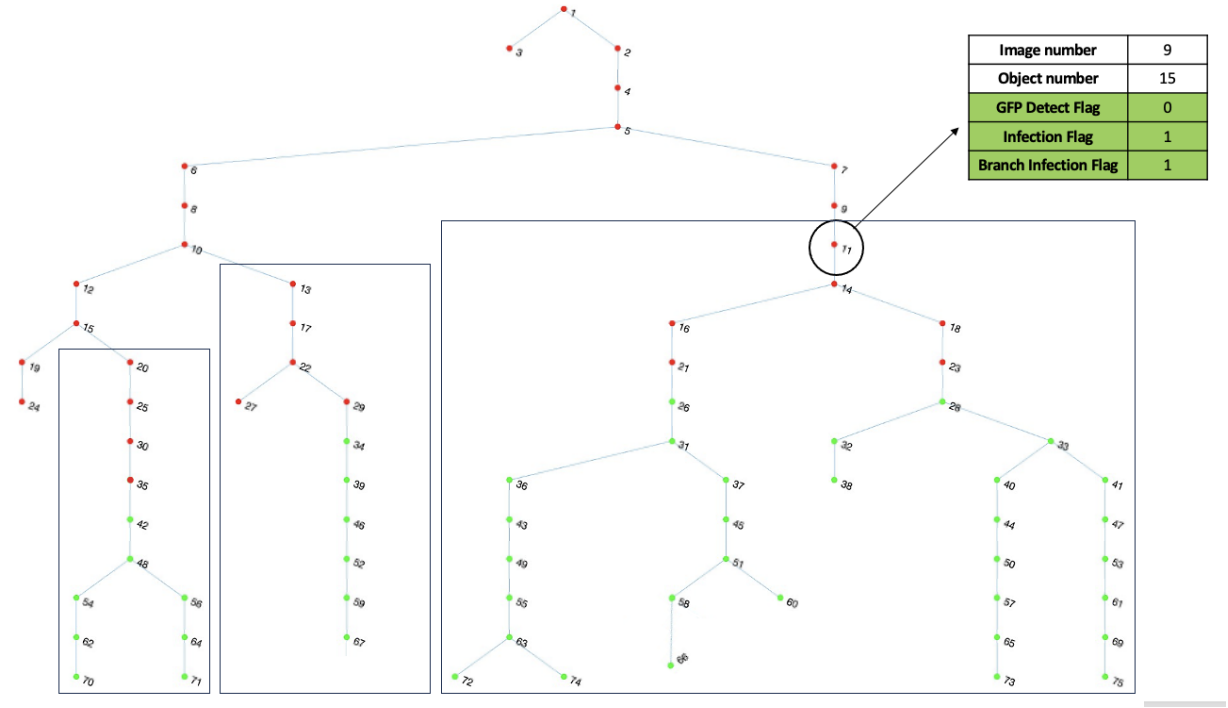


Figure C.1: This lineage tree provides a visual representation of the phenotypes associated with the points of interest. The highlighted node is the presumed point of infection origin, characterized by a GFP level exceeding a specified threshold. The "Infection Initiation" designates this node as the starting point for infection. Consequently, all connected nodes, including its descendants, inherit an "Infection Spread" characteristic. The rectangular black boxes highlight the branches displaying the "Infection Spread" within this lineage tree.

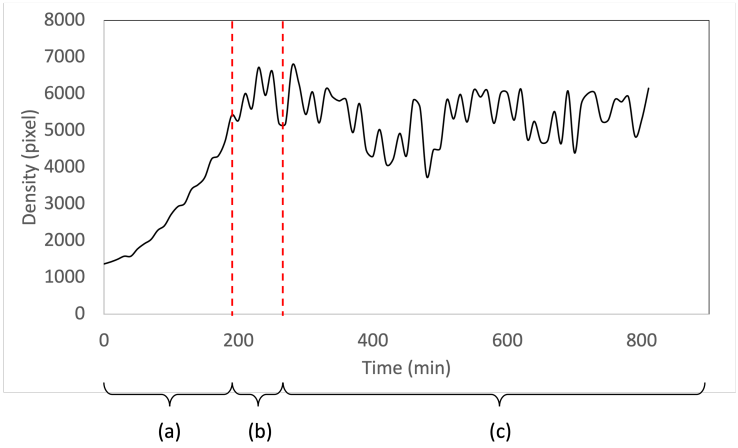
- **GFP Detect Flag**: In this section of the code, nodes with GFP intensity above the threshold are recognized, and their corresponding GFP flags will be updated.
- **Infection Flag**: In this part, nodes that initially had their GFP flags updated due to GFP intensity being a bove the threshold are analyzed. The goal is to identify the ancestor node that was initially infected with the phage.
- **Branch Infection Flag** This class was created with the purpose of distinguishing infected parent nodes and their corresponding daughter nodes within the entire lineage tree. For instance, if a cell's Infection flag is set to 1, this flag is also assigned to all of its descendant nodes in the lineage tree (See figure C.1).

Appendix D

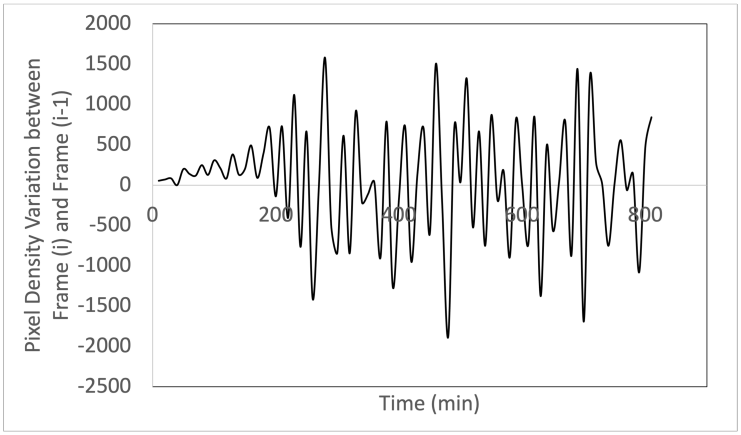
Segmentation

The initial image segmentation phase aimed to identify the latest image where the software effectively separated cells from background noise using pixel classification. Employing the "Cell Density Counting" class, images were categorized based on their population density. As cell populations increased, distinguishing cells from the background became challenging due to pixel similarity (See Figure D.5, leading to erroneous segmentation, particularly detrimental for subsequent tracking purposes.

To mitigate this issue, we segregated highly populated images, prone to increased segmentation errors, from those with lower errors using the "Cell Density Counting" class. Time-lapse images were subjected to this classification, and the outcomes are depicted in Figure D.1.



(a)



(b)

Figure D.1: Initial step of Segmention in Ilastik: Measuring Intensity Density (a) Density of Cells Intenity, a, b and c representing low populated, medium populated and over populated frames, respectively (b) Fluctuation in the intensity density of the current frame compared to its previous frame

The fluctuation in density measurements corresponds to the increasing population within frames. In summary, three categories of images were generated based on population density:

a) Low-density images: These depict sparsely populated cell populations, allowing clear differentiation between cell and background pixels due to significant intensity differences. See Figure D.2 for further clarification.

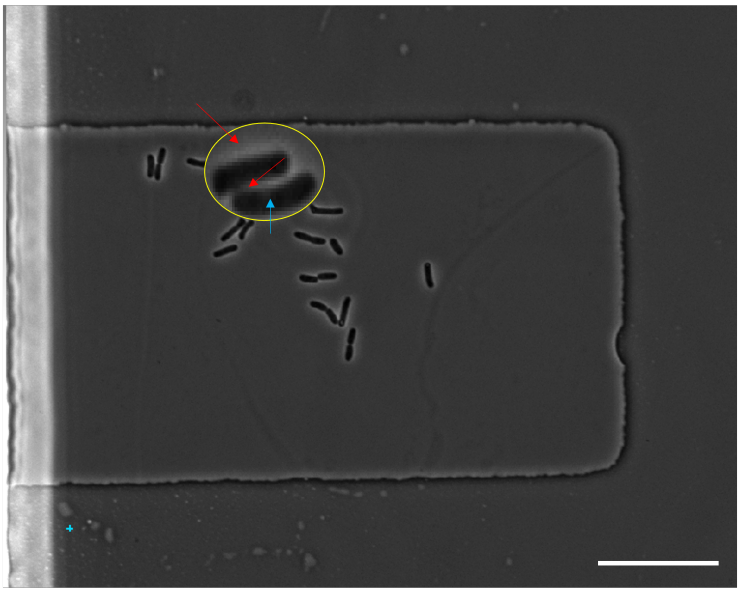


Figure D.2: Image with low population density, magnified by 600x. A scale bar within the image indicates a length of 20 micrometers. Blue arrows denote cell pixels, while red arrows indicate background pixels. Evidently, the pixel intensity of cells starkly contrasts with that of the background, rendering the differentiation between cells and background straightforward in this image type.

b) Medium-density images: Cells in this scenario grew closely, yet with enough intercellular space to maintain a discernible contrast between cell and background pixel intensities (Figure D.3). However, some cells still exhibited intensities resembling the background, necessitating more refined training for accurate segmentation (Figure D.4.

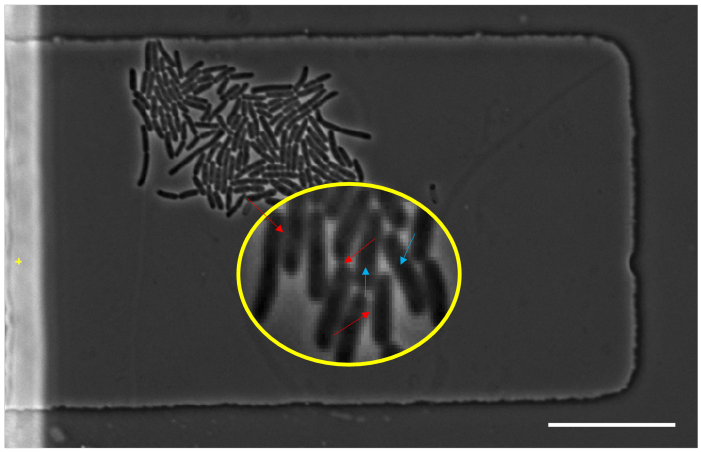


Figure D.3: Image with medium population density, magnified by 600x. A scale bar within the image indicates a length of 20 micrometers. Blue arrows indicate cell pixels, while red arrows represent background pixels. Cells in this context exhibited close adjacency, maintaining enough intercellular space for distinct differentiation between cell and background pixel intensities.

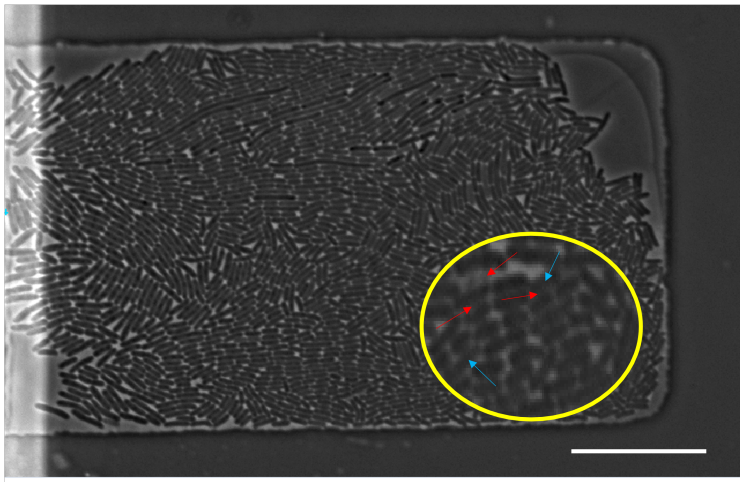


Figure D.4: Image with medium population density, magnified by 600x. A scale bar within the image indicates a length of 20 micrometers. Blue arrows indicate cell pixels, while red arrows represent background pixels. Certain cells displayed intensities resembling the background, highlighting the need for meticulous training to achieve accurate segmentation.

c) High-density images: These images displayed densely populated cell arrays, resulting in minimal disparity between cell surface and background intensities. Cells were situated closely, making individual separation unfeasible due to closely matched pixel intensities. Moreover, multilayer growth atop deceased cells hindered segmentation. Images of this category were excluded from segmentation due to these challenges (Figure D.5).

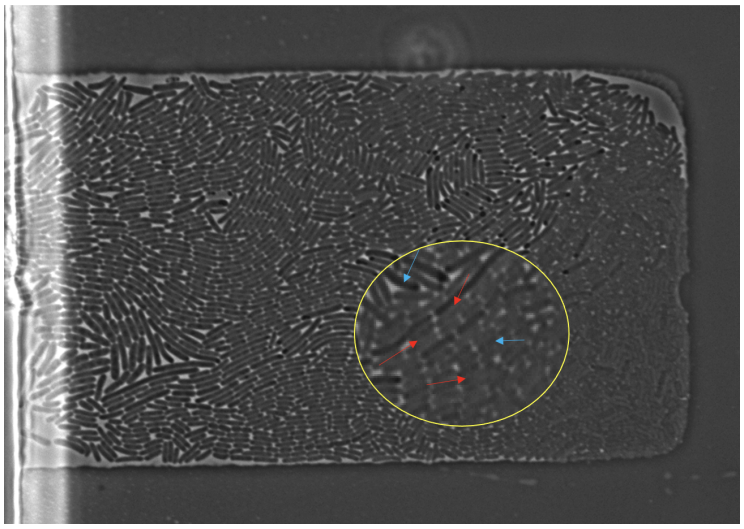
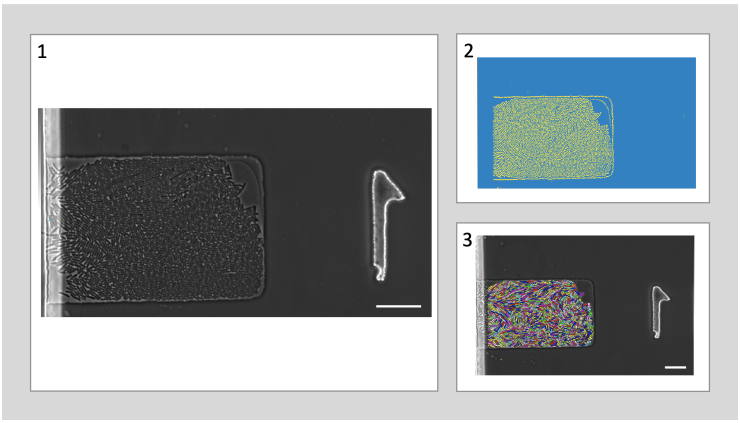
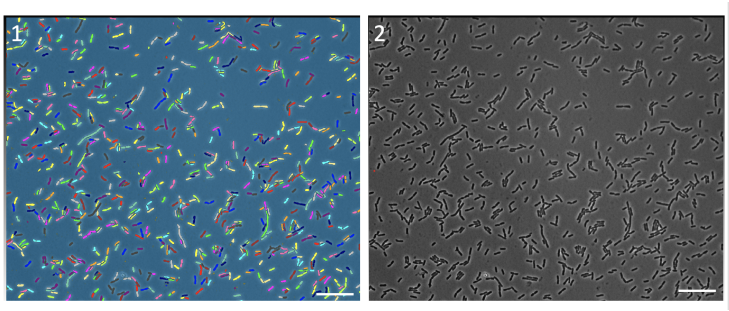


Figure D.5: Image with high population density, magnified by 600x. Blue arrows indicate cell pixels, while red arrows represent background pixels. In this instance, specific cells displayed pixel intensities that closely aligned with the boundaries between cells, making cell identification notably challenging and largely unattainable.

2. Successfully pixel-classified images proceeded to the subsequent "Object Classification" stage. Here, pixels categorized as cells were further classified as objects based on their sizes (Figure 4.9). A specific size threshold (details are explained in Appendix D) was established, ensuring that only objects falling within the predefined cell size range were retained, thereby eliminating undesired objects. For instance, in microfluidic device images, chambers walls shared pixel intensity characteristics with bacterial cells . Size-based filtration effectively eliminated the wall features, retaining only the cell-related information (See Figure D.6a).



(a)



(b)

Figure D.6: Segmented images in Ilastik. (a) Microfluidic Segmentation: 1)Original phase image obtained through microscopy. 2) Pixel-classified image, where cells are denoted in yellow, while background pixels are marked in blue. 3) After the object filtration stage, cells within a defined size range were identified as primary objects, while those outside this range, like chambers walls, were excluded and not considered as objects. (b) Agar pad Segmentation: 1) Successful Segmentation of image 2, where the background is represented in blue and individual cells are colorfully differentiated.

Following object identification, CellProfiler was employed to extract cellular information and track the cells. A dedicated pipeline was established and applied to all processed images. Details about the pipeline is shared in the Section D.3. This pipeline incorporated Ilastik-segmented images (representing identified objects) and raw fluorescent channel images for fluorescent intensity information extraction. The pipeline utilized MeasureObjectShapeSize, MeasureObjectIntensity, and TrackObject modules to extract parameters outlined in the Section 4.3.1. After segmentation, the selected information is extracted from the software to excel document using the ExportToSpreadSheet module.

D.1 Segmenting Limitation in Agar Pad Setup

In the Agar setup, image segmentation followed a process similar to the one employed in the microfluidic device. It entailed dividing images into three parts, determined by the degree of cell compaction. However, the Agar setup presented several challenges that required careful consideration.

Firstly, cells were observed to move out of the focal plane (Figure D.8), even when situated within colonies that hadn't experienced significant growth. This displacement from the focal plane led to a decrease in pixel intensity, causing cell intensities to more closely resemble background intensity (See figure D.7). Secondly, instances were noted where individual cells were in very close proximity to each other, as if they were forced into such proximity makes little sense: also packing occurs in MF devices. In the early stages of the experiment, cells typically underwent an adjustment phase and displayed limited movement suggesting they're motile?. In these cases what cases?, the close cells shared nearly identical intensity profiles, making their separation during the segmentation process highly challenging. An example of this scenario can be observed in figure D.7.

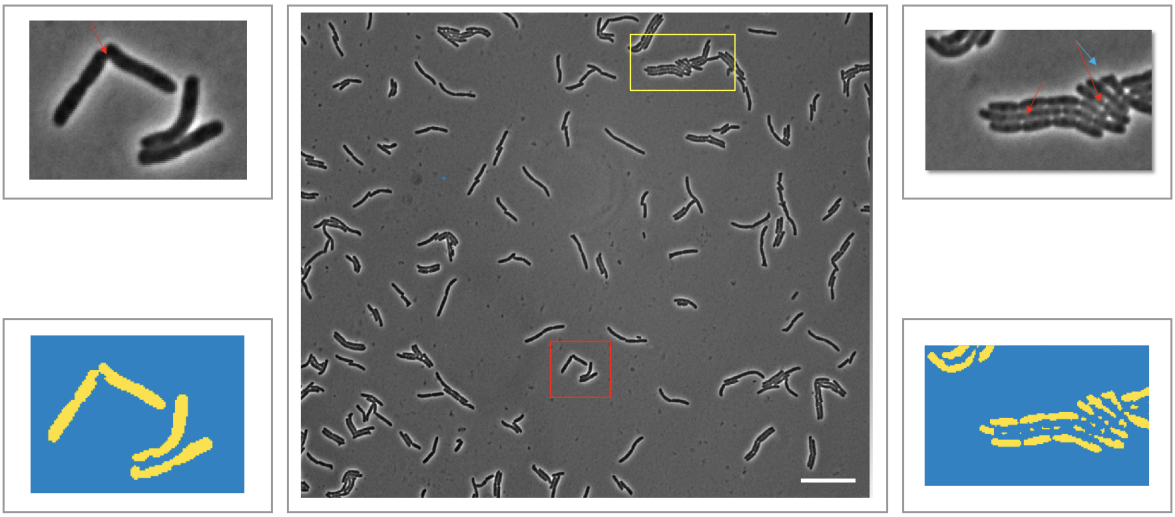


Figure D.7: Agar Experiment Segmentation Challenge: Middle Image: Represents the raw image captured during the agar experiment.Left Image: Depicts a scenario where cells are situated too closely to each other, complicating their differentiation based on pixel intensity.Right Image: Illustrates a situation where cells at the center of the colony have moved out of the focal plane, making their accurate segmentation challenging.

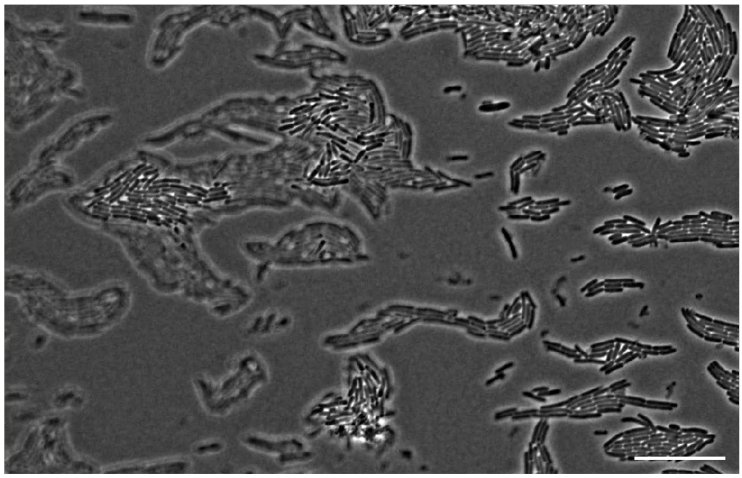


Figure D.8: Figure illustrating the Impact of Variable Z-locations of Cells within a Colony

Thirdly, in the context of the Agar system, the formation of multilayer cell structures can indeed be a significant challenge for image segmentation and analysis. When cells aggregate into multilayer structures, they overlap in the z-direction, making it difficult impossible, no? to distinguish and segment individual cells in a single 2D image plane (See figure D.9). To accurately segment such images and separate cells at different heights, it often requires is this what you did?? acquiring images at different z-directions (z-stacks) to capture the entire three-dimensional structure. However, this process can be time-consuming and technically challenging.

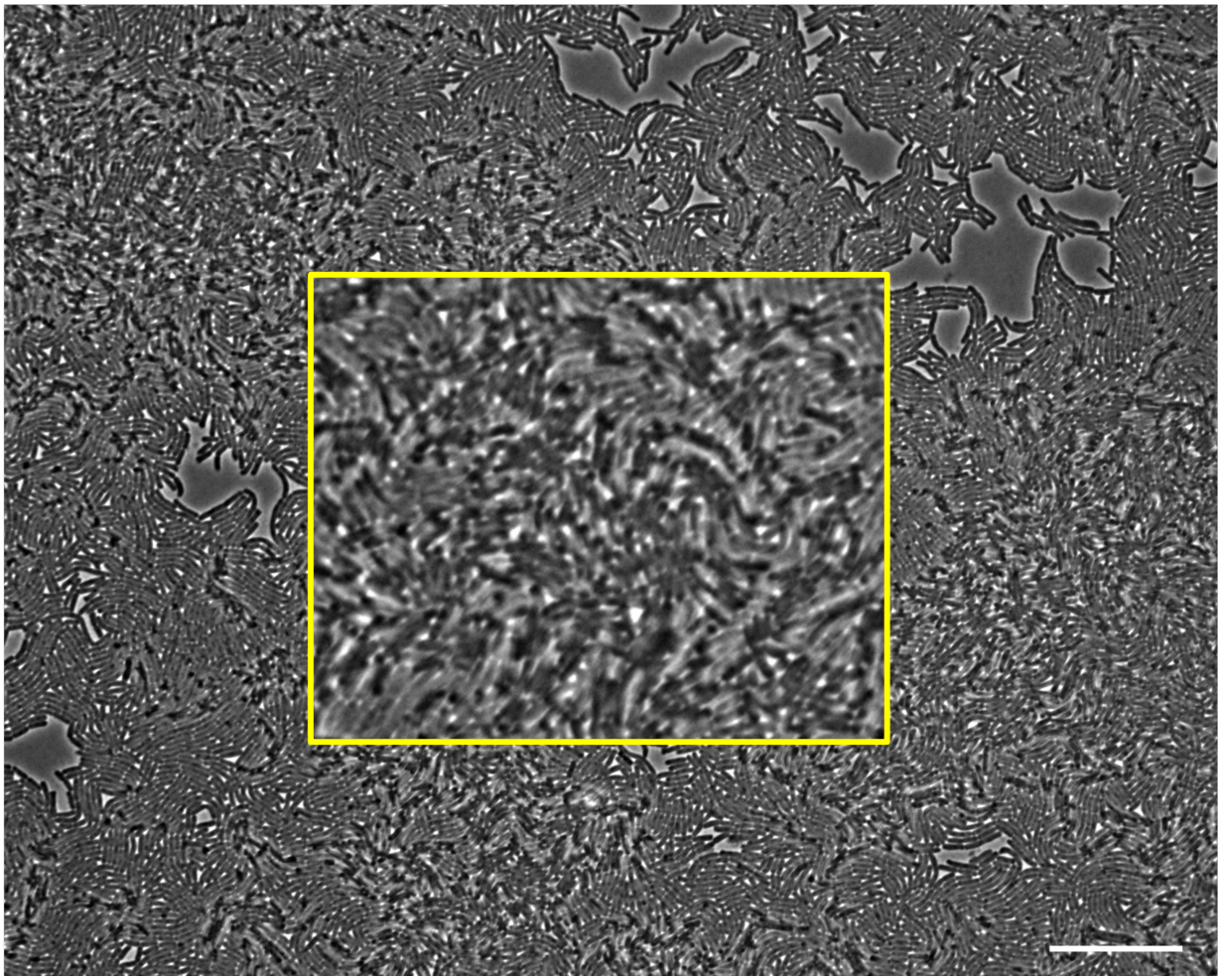


Figure D.9: This figure illustrates the Formation of Multilayers in the Agar Experiment. As evident in the figure, the overlapping cell layers make it challenging to distinguish individual cells.A scale bar within the image indicates a length of 20 micrometers.

In this work, addressing multilayer formations and acquiring z-stacks to separate cells in different heights was a complex and avoided aspect of the study. Imaging was paused when cells began to form multilayer structures due to the difficulties associated with segmentation and the limitations of the experimental setup. This approach was taken to ensure the accuracy and efficiency of the image analysis process.

These challenges, which included variations in focal plane positioning, cell clumping, and close proximity of cells with similar intensity profiles, demanded careful handling during the image segmentation and analysis processes to ensure the reliability and accuracy

of the results. Indeed, the segmentation of agar images required more time and careful attention compared to the microfluidic experiment, given the specific limitations of the agar system. However, these challenges were effectively addressed through manual adjustments HOW!!??? (Figure D.10, and the segmented images were subsequently processed using CellProfiler to extract the information as previously described for the Microfluidic device.

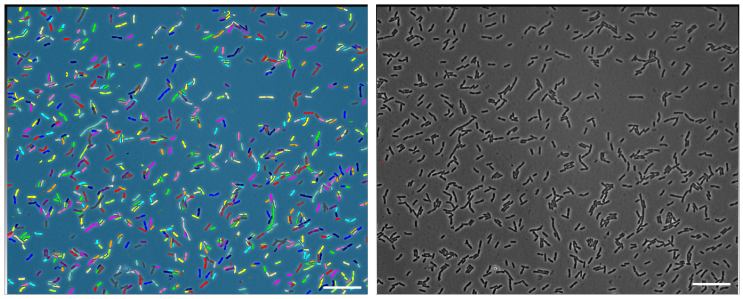


Figure D.10: Right: Successful Segmentation of Left Images, where the background is represented in blue and individual cells are colorfully differentiated. A scale bar within the image indicates a length of 20 micrometers.

the preceding section can be shortened considerably. too much detail about things that you're not focusd on.

D.2 Ilastik Pipeline

D.2.1 Population

To Investigate how populate images are "Cell Density Counting" class was used. Initially, raw images depicting various cell densities, generated from Zen2 software, were employed in the "Input Data" module. Within the "Select Features" Module, all Sigma values for Color/Intensity, Edge, and Texture were chosen, as recommended by the developer for achieving high-quality segmentation. In the "Counting" module, cells were chosen as the "Foreground" and background was chosen as "Background". In the "Density Export" Module "Probability" source with tif format was chosen as export images and Density values for each images were also exported into CSV file.

D.2.2 Segmentation

The Pixel classification + Object classification module formed the basis of our approach. Initially, raw images depicting various cell densities, generated from Zen2 software, were employed in the "Input Data" module. Within the "Select Features" Module, all Sigma values for Color/Intensity, Edge, and Texture were chosen, aligning with the developer's recommendation for achieving high-quality segmentation.

Moving to the "Training" Module, the differentiation between cell and background labels was facilitated by software-based pixel differentiation. Per the developer's guidelines, I exclusively labeled cells and background components, relying on the software's guidance.

In the subsequent "Thresholding" module, the "Simple" method was applied to the "Cells" input, utilizing a Smooth filter ranging from 1 to 0.8 and a Threshold value set at 0.6. Additionally, a "Size Filter" with a minimum of 50 and a maximum of 1000 was utilized. The intent behind this filter was to eliminate small unwanted particles, erroneously identified as cells, and larger entities such as microfluidic device chamber walls within the microfluidic images.

Moving forward to "Object Feature Selection," all recommended features were selected based on the developer's guidelines. Notably, the "Object Classifier" module wasn't utilized in our segmentation setup since our study involved only one cell type, negating the need for segregating various shapes or objects.

The subsequent step involved the "Object Information Export" module, where "Object Identities" were selected as the image source, and the images were exported in the TIFF format, a compatible format for CellProfiler's use. Throughout this study, a consistent pipeline was employed for all images, facilitated by the "Batch Processing" module, ensuring uniformity in the segmentation process.

The resulting extracted images were saved and subsequently utilized in the succeeding segmentation steps.

D.3 CellProfiler pipeline

In CellProfiler, two types of images were imported: 1. Object images created via Ilastik. 2. Raw time-lapse images obtained from microscopy using Zen2 software.

The Object images were employed to create masks on the raw images, effectively eliminating undesired intensity noise from the background. This process was executed using

the "MaskImage" module. Subsequently, modules like MeasureObjectShapeSize, MeasureObjectIntensity, and TrackObject were configured based on these masked images. For the "TrackObject" module, a distance-based tracking method was implemented, with a maximum distance set at 50 pixels. Finally, the ExportToSpreadSheet and SaveImage modules were utilized to extract relevant information and save the processed images, respectively.

Appendix E

Diffusion Variables

Variables used for diffusion rate calculations are presented in the Table E.

Parameter	Value
K (J/K)	1.38×10^{-23}
T (K)	330.15
L (nm)	900
d (nm)	6
δ	5.703782475
γ_{11}	1.069
γ_1	-0.004
η (mPa.s)	0.691
Δx (um)	100

Appendix F

GFP threshold

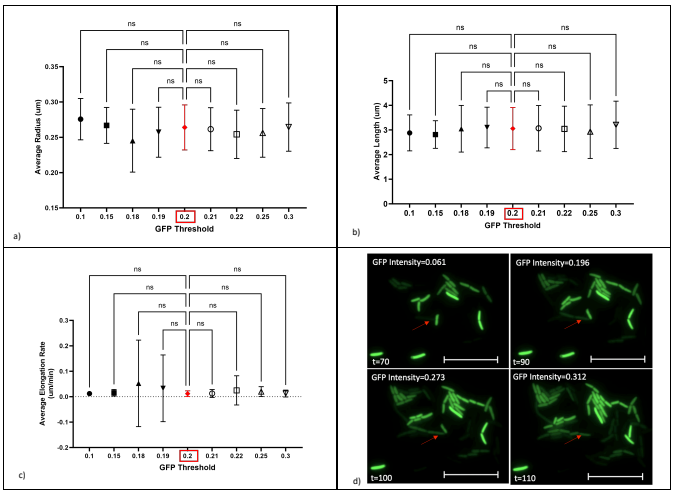


Figure F.1: The information was processed using different GFP thresholds to examine: a) The mean cell radius b) The mean cell length c) The average rate of elongation d) Time-lapse sequences capturing cell growth and phage infection, with images captured in the EGFP channel. The EGFP intensity was quantified for individual cells, indicated by an orange arrow. As the GFP levels rose within the cell, its intensity also increased. The initial detectable GFP intensity was selected as a threshold for subsequent measurements.

Appendix G

Different Delay Time

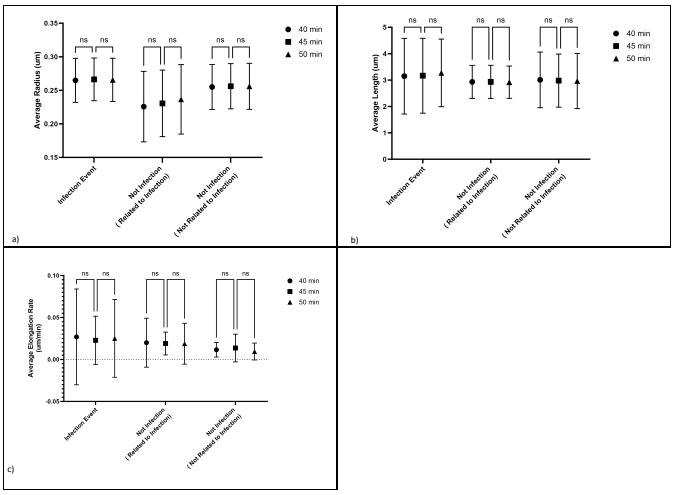


Figure G.1: The information was processed using three different delay time to examine: a) The mean cell radius b) The mean cell length c) The average rate of elongation

Appendix H

Simulation

H.1 Simulation Code

H.1.1 Calibration code

Below is the Matlab code used for calibration of Elongation rate/Length:

```
    % Clear workspace
clc;
clear;
% Read data from the Excel file
filename = '';
infected_lengths = readmatrix(filename, 'Sheet', 1);
uninfected_lengths = readmatrix(filename, 'Sheet', 2);
% Remove NaN values from the data
infected_lengths = infected_lengths(~isnan(infected_lengths));
uninfected_lengths = uninfected_lengths(~isnan(uninfected_lengths));
% Define evaluation points (bins) for histograms
num_bins =; % Adjusted number of bins
data_min = min([infected_lengths; uninfected_lengths]);
data_max = max([infected_lengths; uninfected_lengths]);
bins = linspace(data_min, data_max, num_bins);
% Compute histograms and normalize to get PDFs
[infected_hist, ~] = histcounts(infected_lengths, bins, 'Normalization',
    'pdf');
[uninfected_hist, ~] = histcounts(uninfected_lengths, bins, '
    Normalization', 'pdf');
% Center the bins for correct plotting
bin_centers = (bins(1:end-1) + bins(2:end)) / 2;
```

```
% Normalize histograms to get PDF
infectedPDF = infected_hist / trapz(bin_centers, infected_hist);
uninfectedPDF = uninfected_hist / trapz(bin_centers, uninfected_hist);
% Define the convolution matrix for the problem
H = toeplitz([uninfectedPDF(1), zeros(1, num_bins-2)], uninfectedPDF);
% Regularization parameter
lambda = 50; % Further increased regularization parameter
% Define the regularization matrix (identity matrix scaled by lambda)
L = lambda * eye(num_bins-1);
% Construct the augmented system
A = [H; L];
b = [infectedPDF'; zeros(num_bins-1, 1)];
% Solve the regularized least squares problem with non-negative
    constraints
K_optimized = lsqnonneg(A, b);
% Normalize the kernel to get a PDF
K_optimized = K_optimized / trapz(bin_centers, K_optimized);
% Apply Gaussian smoothing to the kernel
sigma = ; % Further increased standard deviation for Gaussian smoothing
K_smoothed = imgaussfilt(K_optimized, sigma);
% Apply a moving average filter
window_size = ; % Moving average window size
K_smoothed = movmean(K_smoothed, window_size);
% Normalize the smoothed kernel to get a valid PDF
K_smoothed = K_smoothed / trapz(bin_centers, K_smoothed);
% Manually shift the kernel to the left
shift_amount = ; % Adjust this value to shift the kernel to the left
K_shifted = [K_smoothed(shift_amount+1:end); zeros(shift_amount, 1)];
% Normalize the shifted kernel to get a valid PDF
K_shifted = K_shifted / trapz(bin_centers, K_shifted);
% Print kernel values
disp('Kernel Values (K_shifted):');
disp(K_shifted);
% Verify normalization
normalized_sum = trapz(bin_centers, K_shifted);
disp('Sum of K_shifted:');
disp(normalized_sum);
% Adjust K_shifted to be normalized if it's not
if abs(normalized_sum - 1) > 0.01
    K_shifted = K_shifted / normalized_sum;
    disp('Re-normalized Sum of K_shifted:');
    disp(trapz(bin_centers, K_shifted));
end
% Plotting the results
figure;
hold on;
```

```
plot(bin_centers, uninfectedPDF, 'g', 'LineWidth', 2, 'DisplayName', '
    Uninfected PDF');
plot(bin_centers, infectedPDF, 'r', 'LineWidth', 2, 'DisplayName', '
    Infected PDF');
plot(bin_centers, K_shifted, 'b--', 'LineWidth', 2, 'DisplayName', '
    Estimated Kernel PDF');
legend show;
xlabel('Elongation Rate (\mum/min)');
ylabel('Density');
xlim([0 1])
grid off;
set(gca, 'FontSize', 28);

% % % Save kernel values to a CSV file
%  csvwrite('kernel_values_Elong.csv', K_shifted);
```

Below is the Python code used for the simulation:

```
import random
import pandas as pd
import numpy as np
import math
from CellModeller.Regulation.ModuleRegulator import ModuleRegulator
from CellModeller.Biophysics.BacterialModels.CLBacterium import
    CLBacterium
from CellModeller.GUI import Renderers
from CellModeller.Signalling.GridDiffusion import GridDiffusion
from CellModeller.Integration.CLCrankNicIntegrator import
    CLCrankNicIntegrator

# Constants for conversion
PIXELS_TO_UM = 6.96
simulation_step_minutes = 10  # Equivalent to dt in min (timestep (dt) is
    0.005 day- Simulator.py)
SPATIAL_SCALING_FACTOR = 1.5  #  m  per simulation length unit

# Load experimental data from CSV file
file_path = ''
data = pd.read_csv(file_path)

# Reading elongation rates and converting them (time and length units)
    for simulation
elongation_rates = {
    0: [0.14 * simulation_step_minutes / SPATIAL_SCALING_FACTOR],
    1: [0.1 * simulation_step_minutes / SPATIAL_SCALING_FACTOR],
    2: [0.12 * simulation_step_minutes / SPATIAL_SCALING_FACTOR]
}
```

```
26
27 # Filter rows for initial and final states of the simulation
28 image_1_data = data[data['ImageNumber'] == 1]
29 max_image_number = data['ImageNumber'].max()
30 last_image_data = data[data['ImageNumber'] == max_image_number]
31
32 # Calculate cell count
33 max_cell_count_last_image = last_image_data['ObjectNumber'].max()
34
35 # Adjusting Microfluidic device dimensions and cell positions
36 device_x_length = ((image_1_data['Location_Center_X'].max() -
       image_1_data['Location_Center_X'].min()) / PIXELS_TO_UM) /
       SPATIAL_SCALING_FACTOR
37 device_y_length = ((image_1_data['Location_Center_Y'].max() -
       image_1_data['Location_Center_Y'].min()) / PIXELS_TO_UM) /
       SPATIAL_SCALING_FACTOR + 5
38 center_x_last_image = float(((image_1_data['Location_Center_X'].max() +
       image_1_data['Location_Center_X'].min()) / (2 * PIXELS_TO_UM))) /
       SPATIAL_SCALING_FACTOR - 40
39 center_y_last_image = float(((image_1_data['Location_Center_Y'].max() +
       image_1_data['Location_Center_Y'].min()) / (2 * PIXELS_TO_UM))) /
       SPATIAL_SCALING_FACTOR - 10
40
41 # Define simulation grid and parameters
42 grid_size = (4, 4, 4)
43 grid_dim = (128, 32, 4)
44 grid_orig = (-128, -40, -4)
45
46 max_cells = max_cell_count_last_image
47 max_cells = 700
48
49 n_signals, n_species = 1, 1
50
51 # Microfluidic device entrance
52 left_boundary_x = -device_x_length / 4
53
54 # Cell properties
55 cell_lens = {0: 6.34 / SPATIAL_SCALING_FACTOR, 1: 6.8 /
       SPATIAL_SCALING_FACTOR, 2: 6.95 / SPATIAL_SCALING_FACTOR}
56
57 # Assign initial lengths to each cell from experimental data
58 initial_lengths = {}
59 for index, row in image_1_data.iterrows():
60     initial_length = row['AreaShape_MajorAxisLength'] / PIXELS_TO_UM /
       SPATIAL_SCALING_FACTOR  # Adjusting for spatial scale
61     initial_lengths[index] = initial_length
```

```
62
63 # Read kernel values from CSV files
64 kernel_length_file_path = ''
65 kernel_elongation_file_path = ''
66 kernel_length_values = np.loadtxt(kernel_length_file_path, delimiter=',')
67 kernel_elongation_values = np.loadtxt(kernel_elongation_file_path,
       delimiter=',')
68
69 # Ensure kernels are normalized to represent PDFs
70 kernel_length_values = kernel_length_values / np.sum(kernel_length_values
       )
71 kernel_elongation_values = kernel_elongation_values / np.sum(
       kernel_elongation_values)
72
73 # Define bins for the kernel PDFs
74 kernel_length_bins = np.linspace(min(initial_lengths.values()), max(
       initial_lengths.values()), len(kernel_length_values))
75 kernel_elongation_bins = np.linspace(min(elongation_rates[0] +
       elongation_rates[1] + elongation_rates[2]), max(elongation_rates[0] +
        elongation_rates[1] + elongation_rates[2]), len(
       kernel_elongation_values))
76
77 # Filter data to only include the first and third images
78 data_filtered = data[data['ImageNumber'].isin([1, 3])]
79 dead_cell_ids = set()  # Initialize set to store ids of dead cells
80
81 # Simulation setup function
82 def setup(sim, Diffusion_Rate=100.0, K3=1):
83     global k3_global
84     try:
85         with open("diffusion_rate.txt", "r") as file:
86             Diffusion_Rate = float(file.read().strip())
87     except (FileNotFoundError, ValueError):
88         pass
89     try:
90         with open("K3.txt", "r") as file:
91             K3 = float(file.read().strip())
92     except (FileNotFoundError, ValueError):
93         pass
94     k3_global = K3  # Set the global variable for K3
95     print(f" Diffusion: {Diffusion_Rate}, K3: {K3}")
96
97     biophys = CLBacterium(sim, jitter_z=False, gamma=10.0, compNeighbours
       =True, max_planes=5)
98     right_boundary_x = device_x_length / 2
99
```

```
    # Define planes
    top_boundary_plane = (center_x_last_image, (device_y_length / 2 - 10), 0)
    bottom_boundary_plane = (center_x_last_image, -(device_y_length / 2 + 20), 0)
    right_boundary_plane = (device_x_length / 4, center_y_last_image, 0)

    biophys.addPlane(right_boundary_plane, (-1, 0, 0), 1.0)
    biophys.addPlane(top_boundary_plane, (0, -1, 0), 1.0)
    biophys.addPlane(bottom_boundary_plane, (0, 1, 0), 1.0)

    sig = GridDiffusion(sim, n_signals, grid_dim, grid_size, grid_orig, [Diffusion_Rate])
    integ = CLCrankNicIntegrator(sim, n_signals, n_species, max_cells, sig)
    regul = ModuleRegulator(sim, sim.moduleName)
    sim.init(biophys, regul, sig, integ)

    for index, row in image_1_data.iterrows():
        cell_id = int(row['ObjectNumber'])
        if cell_id not in dead_cell_ids:
            cell_type = 1 if row['Intensity_MeanIntensity_GFP'] > 0.4 else 0
            x = (row['Location_Center_X'] / PIXELS_TO_UM) / SPATIAL_SCALING_FACTOR - center_x_last_image
            y = (row['Location_Center_Y'] / PIXELS_TO_UM) / SPATIAL_SCALING_FACTOR - center_y_last_image
            dir_x, dir_y = math.sin(math.radians(row['AreaShape_Orientation'])), math.cos(math.radians(row['AreaShape_Orientation']))
            if x <= right_boundary_x / 2:
                sim.addCell(cellType=cell_type, pos=(x, -y, 0), dir=(dir_x, -dir_y, 0), length=initial_lengths[index] / SPATIAL_SCALING_FACTOR)
            else:
                print(f"Discarded cell at ({x}, {y}) out of boundary.")
    sim.addRenderer(Renderers.GLBacteriumRenderer(sim))
    sim.pickleSteps = 2
    sim.saveOutput = True



def init(cell):
    cell.targetVol = cell_lens[cell.cellType] + random.uniform(0.0, 0.0)
    cell_id = cell.id
    initial_length = initial_lengths.get(cell_id)
```

```
135
136     if initial_length is None:
137         print(f"No initial length found for cell ID: {cell.id}")
138         return
139
140     if cell.cellType in elongation_rates:
141         experimental_elongation_rate = np.random.choice(elongation_rates[
    cell.cellType])
142     else:
143         experimental_elongation_rate = 2.0 / SPATIAL_SCALING_FACTOR
144
145     cell.growthRate = experimental_elongation_rate / initial_length
146
147     cell.species[:] = [0.0] * n_species
148     cell.signals[:] = [0.0]
149     if cell.cellType == 0: cell.color = (1.0, 0.0, 0.0)
150     elif cell.cellType == 1: cell.color = (0.0, 1.0, 0.0)
151     cell.justInfected = 0
152     cell.stepsSinceInfection = 0
153
154 cl_prefix = '''
155     const float Da = 1.0f;
156     const float ka = 6.0f;
157     float alpha_in = species[0];
158     float alpha = signals[0];
159 '''
160
161 def specRateCL():
162     global cl_prefix
163     return cl_prefix + '''
164         if (cellType==1){
165             rates[0] = ka + Da*(alpha-alpha_in)*area/gridVolume;
166         } else {
167             rates[0] = Da*(alpha-alpha_in)*area/gridVolume;
168         }
169     '''
170
171 def sigRateCL():
172     global cl_prefix
173     return cl_prefix + '''
174         rates[0] = -Da*(alpha-alpha_in)*area/gridVolume;
175     '''
176
177 def update(cells):
178     delay_steps = 2
179     global dead_cell_ids, k3_global
```

```
    for (id, cell) in cells.items():
        if cell.id in dead_cell_ids:
            del cells[cell.id]
            continue
        if cell.pos[0] <= left_boundary_x:
            del cells[cell.id]
            continue
        if cell.justInfected:
            cell.stepsSinceInfection += 1
            if cell.stepsSinceInfection >= delay_steps:
                cell.justInfected = 0

        if cell.volume > cell.targetVol:
            cell.divideFlag = True

        if (cell.cellType == 0) and (cell.signals[0] >= 0.1):
            uptake_prob = calculate_uptake_probability(cell, get_K1(cell.
    growthRate), get_K2(cell.length), k3_global)
            if random.uniform(0, 1) < uptake_prob:
                cell.cellType = 2
                cell.justInfected = 1
                cell.stepsSinceInfection = 0

        if cell.cellType == 0: cell.color = (1.0, 0.0, 0.0)
        elif cell.cellType == 1: cell.color = (0.0, 1.0, 0.0)
        elif cell.cellType == 2: cell.color = [np.clip(1-(cell.species
    [0]/1.0), 0.0, 1.0), 1.0, 0.1]

def get_K1(elongation_rate):
    bin_index = np.digitize(elongation_rate, kernel_elongation_bins) - 1
    # Find the appropriate bin for the cell elongation rate
    bin_index = max(0, min(bin_index, len(kernel_elongation_values) - 1))
     # Ensure index is within bounds
    return kernel_elongation_values[bin_index]

def get_K2(length):
    bin_index = np.digitize(length, kernel_length_bins) - 1
    bin_index = max(0, min(bin_index, len(kernel_length_values) - 1))
    return kernel_length_values[bin_index]

def calculate_uptake_probability(cell, K1, K2, K3):
    elongation_rate = cell.growthRate
    length = cell.length
    surrounding_phage = cell.signals[0]
    host_state = get_K1(elongation_rate) * get_K2(length)
    uptake_probability = K3 * host_state * surrounding_phage
```

```
    return uptake_probability

def divide(parent, d1, d2):
    d1.targetVol = cell_lens[parent.cellType] + random.uniform(0.0, 0.0)
    d2.targetVol = cell_lens[parent.cellType] + random.uniform(0.0, 0.0)

def run_simulation(platform, device, run, diffusion, K3):
    print(f"Running simulation with Diffusion_Rate: {diffusion}, K3: {K3}")  # Debug statement
    import CellModeller.Simulator as Simulator
    sim = Simulator.Simulator('simulator', 0.025, clPlatformNum=platform, clDeviceNum=device)
    setup(sim, diffusion, K3)  # Ensure setup is called with the correct arguments
    while len(sim.cellStates) < max_cell_count_last_image:
        sim.step()
        update(sim.cellStates)
    print("Simulation completed.")  # Debug statement

if __name__ == "__main__":
    import sys
    if len(sys.argv) != 6:
        print("Usage: simulator.py <platform> <device> <run> <diffusion> <K3>")
        sys.exit(1)

    platform = int(sys.argv[1])
    device = int(sys.argv[2])
    run = int(sys.argv[3])
    diffusion = float(sys.argv[4])
    K3 = float(sys.argv[5])

    run_simulation(platform, device, run, diffusion, K3)
```

H.1.2 Wrapper code

```
import os
import numpy as np
import pandas as pd
import scipy.optimize as optimize
import CellModeller.Simulator as Simulator
from simulator import setup
from process_results import convert_pickles_to_excel
```

```
from analyze_simulation_results import analyze_simulation_results,
    read_experimental_data
import shutil

# Fixed steps for exploration
diffusion_steps = np.arange(0, 400, 25).tolist()
K3_steps = np.arange(1, 100, 1).tolist()
max_cells = max_cell_experiment
num_runs = 10

# Read experimental data
exp_data = read_experimental_data()

def run_simulation(modfilename, platform, device, run, diffusion_rate, K3
    ):
    print(f"Running simulation with Diffusion_Rate: {diffusion_rate}, K3:
    {K3}")  # Debug statement
    with open("diffusion_rate.txt", "w") as file:
        file.write(str(diffusion_rate))

    with open("K3.txt", "w") as file:
        file.write(str(K3))

    base_path = ''
    modname = modfilename.split('.')[0] if '.' in modfilename else
    modfilename

    # Ensure unique directory name
    output_directory_name = f"{modname}-diffusion_{diffusion_rate}-K3_{K3
    }-run_{run}"
    output_directory_path = os.path.join(base_path, output_directory_name
    )
    suffix = 1
    while os.path.exists(output_directory_path):
        output_directory_path = os.path.join(base_path, f"{
    output_directory_name}_{suffix}")
        suffix += 1

    try:
        sim = Simulator.Simulator(modname, 0.025, clPlatformNum=platform,
     clDeviceNum=device, saveOutput=True, outputDirName=
    output_directory_path)
        while len(sim.cellStates) < max_cells:
            sim.step()
    except Exception as e:
        print(f"An error occurred during simulation: {e}")
```

```
        return None  # Return None to indicate an error

    return output_directory_path

def discrete_value(value, steps):
    return min(steps, key=lambda x: abs(x - value))

def save_results_to_excel(results, file_path):
    new_row = pd.DataFrame([results])
    print(f"Saving results to {file_path}")  # Debug statement
    if os.path.exists(file_path):
        df = pd.read_excel(file_path, engine='openpyxl')
        df = pd.concat([df, new_row], ignore_index=True)
    else:
        df = new_row

    df.to_excel(file_path, index=False, engine='openpyxl')
    print(f"Results saved to {file_path}")  # Debug statement

def objective_function(x, num_runs):
    diffusion_rate = discrete_value(x[0], diffusion_steps)
    K3 = discrete_value(x[1], K3_steps)

    platform = 0
    device = 0
    infected_min_distances = []
    non_infected_min_distances = []
    infected_agg_distances = []
    non_infected_agg_distances = []

    base_path = ''
    for run_number in range(1, num_runs + 1):
        output_directory = run_simulation('simulator', platform, device,
    run_number, diffusion_rate, K3)

        # Check if the Excel file exists in the main directory for all
    simulation runs
        excel_file_name = f"{os.path.basename(output_directory)}_CellData
    .xlsx"
        excel_file_path = os.path.join(base_path, excel_file_name)

        if not os.path.exists(excel_file_path):
            print(f"Excel file {excel_file_path} not found, converting
    pickle files to Excel...")
            convert_pickles_to_excel(base_path)
            print("convert_pickles_to_excel called successfully.")
```

```
        else:
            print(f"Excel file {excel_file_path} already exists. Skipping conversion.")

        print("Calling analyze_simulation_results...")
        avg_distances = analyze_simulation_results(base_path)
        print("analyze_simulation_results called successfully.")

        if avg_distances is None:
            print(f"No valid data to analyze for Diffusion Rate {diffusion_rate} and K3 {K3}")
            continue

        infected_min_distances.append(avg_distances['infected_min'])
        non_infected_min_distances.append(avg_distances['non_infected_min'])
        infected_agg_distances.append(avg_distances['infected_agg'])
        non_infected_agg_distances.append(avg_distances['non_infected_agg'])

        # Calculate the square differences between simulation and experimental results
        min_distance_diff = ((avg_distances['infected_min'] - exp_data['expAvgMinDistanceInfected']) ** 2 +
                             (avg_distances['non_infected_min'] - exp_data['expAvgMinDistanceNonInfected']) ** 2)
        agg_distance_diff = ((avg_distances['infected_agg'] - exp_data['expAvgAggDistanceInfected']) ** 2 +
                             (avg_distances['non_infected_agg'] - exp_data['expAvgAggDistanceNonInfected']) ** 2)

        results = {
            "Diffusion rate": diffusion_rate,
            "K3": K3,
            "Run number": run_number,
            "Average minimum distance for infected cells": avg_distances['infected_min'],
            "Average minimum distance for non-infected cells": avg_distances['non_infected_min'],
            "Total difference (min distance)": min_distance_diff,
            "Average aggregated distance for infected cells": avg_distances['infected_agg'],
            "Average aggregated distance for non-infected cells": avg_distances['non_infected_agg'],
            "Total difference (agg distance)": agg_distance_diff
        }
```

```
        save_results_to_excel(results, "")

        # Clean up the folder after processing
        try:
            shutil.rmtree(output_directory)
            print(f"Deleted folder: {output_directory}")
        except OSError as e:
            print(f"Error deleting folder {output_directory}: {e}")

    if not infected_min_distances or not non_infected_min_distances:
        return np.nan

    avg_infected_min_distance = np.nanmean(infected_min_distances)
    avg_non_infected_min_distance = np.nanmean(non_infected_min_distances
    )
    avg_infected_agg_distance = np.nanmean(infected_agg_distances)
    avg_non_infected_agg_distance = np.nanmean(non_infected_agg_distances
    )

    return avg_infected_min_distance + avg_non_infected_min_distance +
    avg_infected_agg_distance + avg_non_infected_agg_distance

def callback_func(xk, convergence):
    # Extract current best result
    current_diff = objective_function(xk, num_runs)
    print(f"Current best difference: {current_diff}")
    # Check if the current best result is close to 0.1 micrometer
    if current_diff <= 0.1:
        print(f"Stopping early as the objective function value is close
    to 0.1 with Diffusion Rate: {xk[0]} and K3: {xk[1]}")
        return True  # Returning True will stop the optimizer
    return False

def main():
    bounds = [(275, 410), (1, 10)]  # Adjust the range based on desired
    values

    print("Starting initial quick exploration...")
    initial_result = optimize.differential_evolution(lambda x:
    objective_function(x, num_runs), bounds, maxiter=1, popsize=1, disp=
    True, polish=False, strategy='best1bin')
    print(f"Initial optimized Diffusion Rate: {initial_result.x[0]}")
    print(f"Initial optimized K3: {initial_result.x[1]}")
    print(f"Initial best result value (closest to zero): {initial_result.
    fun}")

```

```
    print("Starting final detailed exploration...")
    final_result = optimize.differential_evolution(lambda x:
    objective_function(x, num_runs), bounds, maxiter=10, popsize=10, disp
    =True, polish=True, strategy='best1bin', callback=callback_func)
    print(f"Final optimized Diffusion Rate: {final_result.x[0]}")
    print(f"Final optimized K3: {final_result.x[1]}")
    print(f"Final best result value (closest to zero): {final_result.fun}
    ")

if __name__ == "__main__":
    main()
```

H.1.3 MATLAB code

```

clc;
clear;
% --- Experimental Data Setup ---
expFilePath = '';
expInfected = readtable(expFilePath, 'Sheet', 'Sheet1');
expUninfected = readtable(expFilePath, 'Sheet', 'Sheet2');
expInfectedArray = table2array(expInfected);
expUninfectedArray = table2array(expUninfected);
expInfectedArray = expInfectedArray(isfinite(expInfectedArray));
expUninfectedArray = expUninfectedArray(isfinite(expUninfectedArray));
expAvgMinDistanceInfected = mean(expInfectedArray, 'omitnan');
expAvgMinDistanceNonInfected = mean(expUninfectedArray, 'omitnan');
expRatio = expAvgMinDistanceNonInfected / expAvgMinDistanceInfected;
%For agg data
expFilePath_agg = '';
expInfected_agg = readtable(expFilePath_agg, 'Sheet', 'Sheet1');
expUninfected_agg = readtable(expFilePath_agg, 'Sheet', 'Sheet2');
expInfectedArray_agg = table2array(expInfected_agg);
expUninfectedArray_agg = table2array(expUninfected_agg);
expInfectedArray_agg = expInfectedArray_agg(isfinite(expInfectedArray_agg
    ));
expUninfectedArray_agg = expUninfectedArray_agg(isfinite(
    expUninfectedArray_agg));
expAvgAggDistanceInfected = mean(expInfectedArray_agg, 'omitnan');
expAvgAggDistanceNonInfected = mean(expUninfectedArray_agg, 'omitnan');
expRatio_agg = expAvgAggDistanceNonInfected / expAvgAggDistanceInfected;
% --- Simulation Data Setup ---
folderPath = '';
```

```
files = dir(fullfile(folderPath, 'Phage_Infection_Main-diffusion_*-run_*_CellData.xlsx'));
avgMinDistances = struct();
avgAggDistances = struct();
for k = 1:length(files)
filePath = fullfile(folderPath, files(k).name);
tokens = regexp(files(k).name, 'Phage_Infection_Main-diffusion_(\d+(?:\.\d+)?)-run_(\d+)_CellData\.xlsx', 'tokens');
if isempty(tokens)
continue;
end
diffusionRate = str2double(tokens{1}{1});
runNumber = str2double(tokens{1}{2});
data = readtable(filePath);
if iscell(data.CellType)
data.CellType = cellfun(@str2double, data.CellType);
end
if iscell(data.ImageNumber)
data.ImageNumber = cellfun(@str2double, data.ImageNumber);
end
data.CellType = standardizeMissing(data.CellType, NaN);
data.ImageNumber = standardizeMissing(data.ImageNumber, NaN);
data.CellType = double(data.CellType);
data.ImageNumber = double(data.ImageNumber);
minDistancesType0 = [];
minDistancesType2 = [];
aggDistancesType0 = [];
aggDistancesType2 = [];
imageNumbers = unique(data.ImageNumber);
for imageIndex = 1:length(imageNumbers)
imageNumber = imageNumbers(imageIndex);
if any(data.CellType == 1 & data.ImageNumber == imageNumber)
cellsType1 = data(data.CellType == 1 & data.ImageNumber == imageNumber, :);
else
continue;
end
if any(data.CellType == 0 & data.ImageNumber == imageNumber)
cellsType0 = data(data.CellType == 0 & data.ImageNumber == imageNumber, :);
for i = 1:height(cellsType0)
distances = sqrt((cellsType0.X_Position(i) - cellsType1.X_Position).^2 + ...
(cellsType0.Y_Position(i) - cellsType1.Y_Position).^2);
minDistancesType0(end+1) = min(distances);
aggDistancesType0(end+1) = sum(exp(-distances));
```

```
end
end
if any(data.CellType == 2 & data.ImageNumber == imageNumber)
cellsType2 = data(data.CellType == 2 & data.ImageNumber == imageNumber &
    data.JustInfected == 1,:);
for i = 1:height(cellsType2)
distances = sqrt((cellsType2.X_Position(i) - cellsType1.X_Position).^2 +
    ...
(cellsType2.Y_Position(i) - cellsType1.Y_Position).^2);
minDistancesType2(end+1) = min(distances);
aggDistancesType2(end+1) = sum(exp(-distances));
end
end
end
avgMinDistanceType0ForFile = mean(minDistancesType0, 'omitnan');
avgMinDistanceType2ForFile = mean(minDistancesType2, 'omitnan');
avgAggDistanceType0ForFile = mean(aggDistancesType0, 'omitnan');
avgAggDistanceType2ForFile = mean(aggDistancesType2, 'omitnan');
rateKey = ['rate_' strrep(num2str(diffusionRate), '.', '_')];
if isfield(avgMinDistances, rateKey)
avgMinDistances.(rateKey).type0 = [avgMinDistances.(rateKey).type0,
    avgMinDistanceType0ForFile];
avgMinDistances.(rateKey).type2 = [avgMinDistances.(rateKey).type2,
    avgMinDistanceType2ForFile];
avgAggDistances.(rateKey).type0 = [avgAggDistances.(rateKey).type0,
    avgAggDistanceType0ForFile];
avgAggDistances.(rateKey).type2 = [avgAggDistances.(rateKey).type2,
    avgAggDistanceType2ForFile];
else
avgMinDistances.(rateKey).type0 = avgMinDistanceType0ForFile;
avgMinDistances.(rateKey).type2 = avgMinDistanceType2ForFile;
avgAggDistances.(rateKey).type0 = avgAggDistanceType0ForFile;
avgAggDistances.(rateKey).type2 = avgAggDistanceType2ForFile;
end
end
%% Data Processing for Plotting
diffusionRates = fieldnames(avgMinDistances);
avgMinDistancesType0 = [];
avgMinDistancesType2 = [];
avgAggDistancesType0 = [];
avgAggDistancesType2 = [];
stdDeviationsType0 = [];
stdDeviationsType2 = [];
stdDeviationsAggType0 = [];
stdDeviationsAggType2 = [];
labels = {};
```

```
numericRates = [];
ratiosDiff = [];
ratioStd = [];
ratiosAggDiff = [];
ratioAggStd = [];
for i = 1:length(diffusionRates)
rateStr = strrep(diffusionRates{i}, 'rate_', '');
rateStr = strrep(rateStr, '_', '.');
numericRate = str2double(rateStr);
numericRates(end+1) = numericRate;
labels{end+1} = rateStr;
avgDistType0 = mean(avgMinDistances.(diffusionRates{i}).type0, 'omitnan')
    ;
avgDistType2 = mean(avgMinDistances.(diffusionRates{i}).type2, 'omitnan')
    ;
avgAggDistType0 = mean(avgAggDistances.(diffusionRates{i}).type0, '
    omitnan');
avgAggDistType2 = mean(avgAggDistances.(diffusionRates{i}).type2, '
    omitnan');
stdDevType0 = std(avgMinDistances.(diffusionRates{i}).type0, 'omitnan');
stdDevType2 = std(avgMinDistances.(diffusionRates{i}).type2, 'omitnan');
stdDevAggType0 = std(avgAggDistances.(diffusionRates{i}).type0, 'omitnan'
    );
stdDevAggType2 = std(avgAggDistances.(diffusionRates{i}).type2, 'omitnan'
    );
avgMinDistancesType0(end+1) = avgDistType0;
avgMinDistancesType2(end+1) = avgDistType2;
avgAggDistancesType0(end+1) = avgAggDistType0;
avgAggDistancesType2(end+1) = avgAggDistType2;
stdDeviationsType0(end+1) = stdDevType0;
stdDeviationsType2(end+1) = stdDevType2;
stdDeviationsAggType0(end+1) = stdDevAggType0;
stdDeviationsAggType2(end+1) = stdDevAggType2;
ratiosDiff(end+1) = avgDistType0 / avgDistType2;
ratioStd(end+1) = stdDevType0 / stdDevType2;
ratiosAggDiff(end+1) = avgAggDistType0 / avgAggDistType2;
ratioAggStd(end+1) = stdDevAggType0 / stdDevAggType2;
end
[sortedNumericRates, sortIndex] = sort(numericRates);
sortedLabels = labels(sortIndex);
sortedAvgMinDistancesType0 = avgMinDistancesType0(sortIndex)*2;
sortedAvgMinDistancesType2 = avgMinDistancesType2(sortIndex)*2;
sortedAvgAggDistancesType0 = avgAggDistancesType0(sortIndex);
sortedAvgAggDistancesType2 = avgAggDistancesType2(sortIndex);
sortedStdDeviationsType0 = stdDeviationsType0(sortIndex);
sortedStdDeviationsType2 = stdDeviationsType2(sortIndex);
```

```
sortedStdDeviationsAggType0 = stdDeviationsAggType0(sortIndex);
sortedStdDeviationsAggType2 = stdDeviationsAggType2(sortIndex);
sortedRatiosDiff = ratiosDiff(sortIndex);
sortedRatiosStd = ratioStd(sortIndex);
sortedRatiosAggDiff = ratiosAggDiff(sortIndex);
sortedRatiosAggStd = ratioAggStd(sortIndex);
% Adjust labels for including experimental results
adjustedLabels = ['Experimental', sortedLabels];
%% Plotting for Minimum Distances
expData = [expAvgMinDistanceNonInfected; expAvgMinDistanceInfected];
simDataMin = [expData, [sortedAvgMinDistancesType0;
    sortedAvgMinDistancesType2]];
figure;
bar(simDataMin', 0.4, 'grouped');
xticks(1:length(adjustedLabels));
xticklabels(['Experimental', sortedLabels]);
xtickangle(90);
ylabel('Average Minimum Distance (um)');
xlabel('Diffusion Rate (um^2/min)');
legend({'Non-Infection Events', 'Infection Events'}, 'Location', '
    northeast');
set(gca, 'FontSize', 30);
% --- Plotting with Error Bars ---
figure;
errorbar(sortedNumericRates, sortedRatiosDiff, sortedRatiosStd, '-ok', '
    LineWidth', 2, 'Color', 'k', 'MarkerFaceColor', 'k', 'DisplayName', '
    Simulation');
hold on;
% Add the experimental ratio line
yline(expRatio, '--r', 'DisplayName', 'Experimental', 'LineWidth', 2); %
    Plot experimental ratio
xlabel('Diffusion Rate (um^2/min)');
ylabel({'Ratio of Avg Min Distances',' (Non-Infection Events / Infection
    Events)', 'from Phage producers'});
legend('Location', 'northeast');
xticks(sortedNumericRates);
xtickangle(90);
set(gca, 'FontSize', 30);
hold off;
%% Plotting for Aggregated Distances
expData_agg = [expAvgAggDistanceNonInfected; expAvgAggDistanceInfected];
simDataAgg = [expData_agg, [sortedAvgAggDistancesType0;
    sortedAvgAggDistancesType2]];
figure;
bar(simDataAgg', 0.4, 'grouped');
xticks(1:length(adjustedLabels));
```

```
xticklabels(['Experimental', sortedLabels]);
xtickangle(90);
ylabel('Average Aggregated Distance(um)');
xlabel('Diffusion Rate (um^2/min)');
legend({'Non-Infection Events', 'Infection Events'}, 'Location', '
    northeast');
set(gca, 'FontSize', 30);

% --- Plotting with Error Bars for Aggregated Distances ---
figure;
errorbar(sortedNumericRates, sortedRatiosAggDiff, sortedRatiosAggStd, '-
    ok', 'LineWidth', 2, 'Color', 'b', 'MarkerFaceColor', 'b', '
    DisplayName', 'Aggregated Simulation');
hold on;
% Add the experimental ratio line
yline(expRatio, '--r', 'DisplayName', 'Experimental', 'LineWidth', 2); %
    Plot experimental ratio
xlabel('Diffusion Rate (um^2/min)');
ylabel({'Ratio of Avg Aggregated Distances',' (Non-Infection Events /
    Infection Events)', 'from Phage producers'});
legend('Location', 'northeast');
xticks(sortedNumericRates);
xtickangle(90);
set(gca, 'FontSize', 30);
hold off;
```

Appendix I

Phage Display

I.1 Introduction

In the experiments detailed in Chapter 5, the introduction of phage led to the detection of small fluorescent entities, visible solely in the fluorescent channel and illustrated in Figure I.1. These observations prompted inquiries into the actual composition of these minute particles: were they phage entities encapsulating GFP molecules, or merely green fluorescent proteins disseminated into the surroundings due to bacterial disintegration, or even packaged within the phage genomes themselves?

Inspired by previous research by Shao et al, Harb et al., etc. [462, 214], where fluorescent markers were attached to the surface of phages for easy observation under a microscope, this study utilized the phage display technique. By attaching the GFP marker to the surface of the M13 bacteriophage, the aim was to explore if these GFP-tagged particles could be used to track these particles during time-lapse imaging to observe if they attach to or enter host cells, thereby suggesting infectivity. This strategy was intended to facilate direct, real-time observation and analysis of phage-host interactions, thereby expanding our comprehension of phage behavior and infection dynamics under direct microscopic observation.

The chapter begins with an overview of the phage display technique and the application of green fluorescent proteins (GFP) in biological studies. It then proceeds to present and discuss the outcomes of this experimental approach, focusing on whether the GFP-tagged phage particles exhibit behaviors indicative of infection and tracking within the host environment.

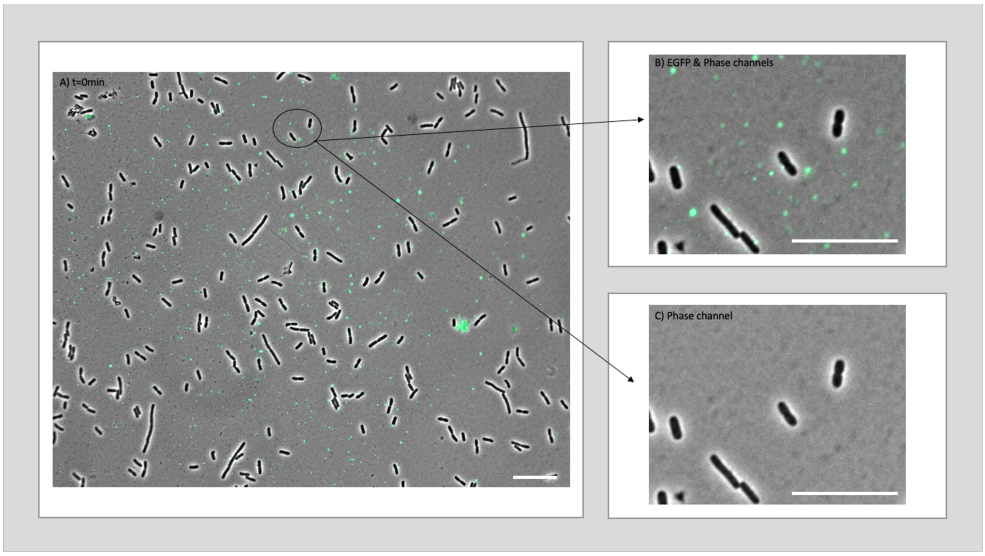


Figure I.1: The figure offers an observation of small green fluorescent particles in the direct introduction of phage approach within the agar experiment. This observation is made under 63x resolution in both the phase and EGFP channels. Images were taken using Zeiss Fluorescence Microscopy (Carl Zeiss Promenade, Germany)

I.2 Phage Display Overview

Phage display is a versatile technique utilized to analyze and manipulate specific protein or ligand interactions by displaying polypeptides on the surface of bacteriophages [176]. Filamentous phages, particularly M13, are predominantly used due to their high titration capabilities and structural flexibility. This method involves the fusion of polypeptides to the phage coat protein, allowing the corresponding genome to reside within the same viral particles [554]. The choice of display method often depends on the size and type of peptide or protein libraries intended for display, including gene fragments, random oligonucleotides, and antibody sequences [554]. The most common display system involves attaching the displayed protein to the N-terminus of pIII using a Sec-based leader. However, display vectors that rely on the C-terminus of pIII have been proposed as more suitable for displaying cytoplasmic proteins since the C-terminus of these proteins is located in the bacterial cytoplasm prior to phage assembly [526].

I.2.1 Display on pIII

The filamentous phage consists of five coat proteins, each contributing to its structural stability. Among these proteins, pIII has three distinct domains, making it the largest and most complex. pIII is often used as a basis for displaying peptide and protein libraries [228], and plays an essential role in the infection of the host cell[423] .The N-terminal domain helps in the translocation of the viral DNA into the *E. coli* during infection. The second domain of pIII is responsible for the recognition of the host cell, which it accomplishes by binding to the F pilus. The C-terminal domain interacts with other phage coat proteins and is necessary for the incorporation of pIII into the phage coat[34, 473]. For display purpose all three domain of pIII has been used and analysed for the better results.

I.2.2 Display Domains

The initial phage display systems were based on fusion with the N-terminus of pIII or pVIII in the viral genome [473]., However several studies have reported that certain sequences may not be effectively displayed on the surface of M13 phage, likely due to issues with the assembly, stability, and infectivity of the viral particles [34, 473]. Display vectors that utilize the C-terminal end of pIII or pVI have been suggested as being more effective for displaying cytoplasmic proteins since these proteins are located in the bacterial cytoplasm before phage assembly, allowing for proper folding of the displayed protein to occur within the cytoplasm[526].

One drawback of the filamentous M13 phage system is that if they use their natural pathway, they transport the fusion proteins in an unfolded state into the periplasm, which may have different effects on the folding of various proteins. As GFP is a fluorescent protein marker that expressed naturally in the cytoplasm, using M13 phage or Sec pathway , commonly used pathway for trasformin proteins via M13 phage, is not recommended[161] as studies shown that they are not capable of active, folded proteins such as GFP[509, 161]. To address this, the Tat pathway can be utilized to secrete the folded cytoplasmic proteins of interest, with coupling to phage protein III achieved through the use of a zipper domain in the periplasm [301].The TAT pathway only translocates folded proteins across the inner membrane and has been used to transport folded and fluorescent GFP from the cytoplasm to the periplasm. A study demonstrates that active green fluorescent protein (GFP) can be successfully exported to the periplasm of *Escherichia coli* using the twin-arginine translocase (Tat) pathway. This suggests that the Tat pathway could be a useful tool for producing functional recombinant proteins in *E. coli* [509].

I.3 Materials and Methods

otherwise stated strain *E.coli* K12 ER2738 was used in all parts of this study and prepared as discussed in Chapter 5.

Table I.1: Bacterial strain

Strain	Genotype	Source
E. coli K12 ER2738	F´proA+B+ lacIq (lacZ)M15 zzf::Tn10(TetR)/ fhuA2 glnV (lac-proAB) thi-1 (hsdS-mcrB)5	NEB

Table I.2: Phage used in this study

Strain	Genotype	Source
M13KO7	M13, p15a ori, Tn903 (KmR)	NEB
Phagemid-Or	From precursor pBlueScripts II KS(+)	addgene
Phagemid-GFP	From precursor pBlueGFP	This study
Phagemid-CLGFP-TorA	From precursor pBlue-CpIII-GFP	This study
Phagemid-CGFP-TorA	From precursor pBlue-CpIII-GFP	This study

Table I.3: Plasmids used in this study

Plasmids	Genotype	Source
pEB1-mGFPmut2	sth	[42]
pEB1-mGFPmut2-Linker	sth	[42]
pBlueScripts II KS(+)	wild-type f1 ori, pUC ori, ApR	addgene
pBlueGFP	pBlueScripts II KS(+), mGFPmut2 inserted in somewhere	This study
pBlue-CpIII	pBlueScripts II KS(+), mGFPmut2 inserted in somewhere	This study
pBlue-CpIII-TorA	pBlueScripts II KS(+), mGFPmut2 inserted in somewhere	This study
CpIII-LGFP-TorA	pBlueScripts II KS(+), mGFPmut2 inserted in somewhere	This study
CpIII-NLGFP-TorA	pBlueScripts II KS(+), mGFPmut2 inserted in somewhere	This study

I.3.1 Phagemid Preparation and Amplification

The procedures employed in this chapter closely mirrored those discussed in previous Chapter 5. In summary, the primers, as detailed in Table 1, were used for PCR to amplify the desired sequence, which was subsequently utilized in Gibson assembly to construct the circular phagemid plasmids. These phagemid plasmids were then introduced into *E. coli* K12 ER2738 competent cells to amplify the plasmids. Once amplified, the plasmids underwent sequencing to verify the correctness of the design. Following confirmation, *E. coli* K12 ER2738 cells containing the phagemid genome underwent the steps outlined in Chapter 5 to generate phage stocks.

I.4 Results

In the initial phase of the study, surface panning was utilized to ascertain whether the observed particles were phages, a process detailed in Chapter 5. Upon microscopic examination of the phage-containing solution post-panning (refer to Figure I.2), it was noted that the small green fluorescent particles were significantly reduced, by approximately 95%, yet still detectable. This observation suggested the possibility that these particles could be phage-related, prompting further investigation through time-lapse microscopy to track potential infection events linked to these particles.

Despite the visibility of GFP-tagged particles under the fluorescence microscope, subsequent time-lapse imaging failed to establish a connection between these particles and actual infection events. Manual tracking revealed that cells proximal to these green particles did not exhibit signs of infection, while infection occurrences within the system were observed independently of these identifiable GFP-tagged entities.

I.5 Discussions

In this chapter, we explored the utilization of fluorescent protein fusions to visualize individual phage particles, building on the methodologies and findings from earlier investigations. Previous research, as cited in references such as Shao et al. (2015) and Harb et al. (2020)[462, 214], has shown that tagging phage particles with fluorescent proteins enables their microscopic observation. This technique has facilitated the tracking of infected bacterial cells, shedding light on the infection mechanisms.

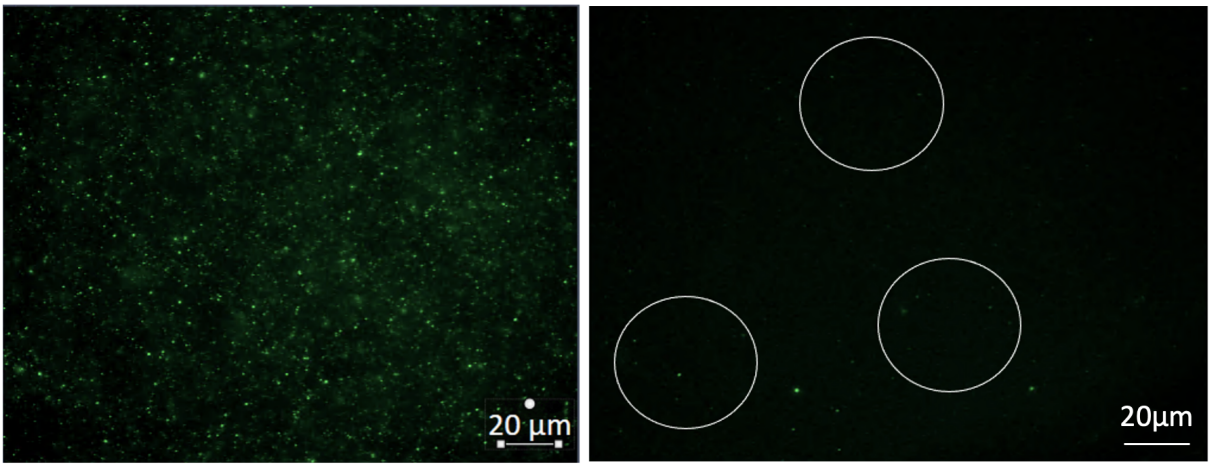


Figure I.2: The figures represent: Left: 1uL of phage lysate used in the experiments, Right: Results of surface panning of the same stock phage lysate. As depicted in the figure, the concentration of green particles has decreased, but they are still observable under the 63x objective in the EGFP channel. Images were taken using Zeiss Fluorescence Microscopy (Carl Zeiss Promenade, Germany)

The primary aim of this segment was to extend this observation technique to individual M13 phage particles by fusing the GFPmut2 protein to the C domain of the M13 phage pIII coat protein. This experiment utilized the TolA leader sequence to enhance the secretion of properly folded proteins, with the anticipation that cells infected by these genetically modified phages would display GFP on their periplasmic membranes.

Despite the successful fusion and expression of GFP within the phage structure, the direct tracking of individual phage particles remained elusive. While there was a reduction in the visibility of green fluorescent particles, this did not conclusively correlate with increased phage detection or infectivity.

Appendix J

Evaluating M13 Phage Infectivity within Gut Microbiome Cultures: Single-Species and Co-Culture

J.1 Introduction

In this chapter experiments were designed to assess the infectivity of various wild-type gut bacterial strains by the M13 phage. Following this, the study explored the impact of co-culturing different bacterial species on the infectivity rates of the M13 phage. By concentrating on the natural host, *E. coli*, this investigation sought to shed light on how mixed bacterial cultures affect phage infection rate. The primary aim was to provide insights into the potential interactions within the gut microbiome when exposed to bacteriophages and to explore the feasibility of employing M13 phage as a tool for targeting specific bacteria within mixed microbial communities.

J.2 Material and methods

The gut bacterial strains utilized in this study were generously provided by professor Emma Allen-Vercoe from the University of Guelph and are fully documented in Table J.1. The strains were named and identified by professor Allen-Vercoe's lab, and in this study, had been employed without additional scrutiny. For simplicity, they have been assigned numbers, and henceforth, they will be referenced using these assigned numbers. M13 phages used in this section are listed in Table J.2.

Table J.1: Bacteria culture used in this section

Strain Number	Strain ID[1]	Identity[1]	% Identity[1]	Source
4	22-5-S 1 D6 FAA	*Brevibacillus agri*	99.57	Gift, Allen-Vercoe lab
6	16-6-S BF 7	*Klebsiella aerogenes*	100	Gift, Allen-Vercoe lab
9	32-6-S 1 MET AER	*Staphylococcus capitis*	99.71	Gift, Allen-Vercoe lab
10	32-6-S 14 BHI	*Escherichia fergusonii*	100	Gift, Allen-Vercoe lab
15	22-5-S 10 D5 FAA	*Parastutterella excrementihominis*	99.57	Gift, Allen-Vercoe lab
		Synthetic Culture		
-	-	*E. coli* ER2738	-	NEB
-	-	ERGFP	-	This study Chapter 5
-	-	ERRFP	-	This study Chapter 4

[1] Strain ID, Identity, and % Identity were provided by Dr. Allen-Vercoe's lab. They used 16S rRNA gene sequencing to identify the bacteria.

Table J.2: Phages used in this section

Name	Genotype	Source
M13KO7	M13, p15a ori, Tn903 (KmR)	NEB
Phagemid-GFP	pBlueScript KS(+), GFPmut2, (AmpR)	This study Chapter4

Media The medium employed in this study was Wilkins-Chalgren (Sigma-Aldrich, Canada), broth and agar, recommended by Professor Allen-Vercoe.

J.2.1 Protocol

Culture preparation All the bacterial strains, including *E. coli* ER2738, were thawed from frozen stocks and cultured overnight at 37°C. The resulting overnight cultures were then utilized to generate early log-phase cultures (OD600 $\tilde{0}$.2-0.3) under continuous agitation at 250 rpm.

Control experiments All cultures underwent testing in both suspension and solid media, exposing them to different antibiotics, ampicillin, and kanamycin, to assess their resistance. Strains displaying resistance to both ampicillin and kanamycin were excluded from further use in this study due to uncertainties about their susceptibility to the phage produced in our setting. Additionally, a plate reader was employed to measure the OD600 of the growing bacterial cultures. Using a 48-well plate (Fisher Scientific, Canada) with 1 mL of culture per well, the plate reader was configured to operate at a temperature of

37°C, with continuous shaking at a moderate speed. OD600 readings were taken every 10 minutes using the BioTek Gen5 software (Agilent Technologies, Inc., USA), which was utilized to record and save the OD measurements obtained from the plate reader.

Phage infection The "Phage infection" section involved two distinct methods to assess susceptibility and interactions:

1. **Single culture infection:** This approach aimed to evaluate the susceptibility of individual gut microbiome cultures to two different phages—Phagemid-GFP (constructed in Chapter 5) and M13KO7 (commercially available). The standard procedure for M13 phage infection in suspension, detailed in Chapter 5, was employed. Briefly, a mixture comprising 200 µL of early log-phase culture and 100 µL of phage lysate underwent incubation at room temperature for 1-2 hours. Subsequently, 100 µL of the mixture was spread onto Wilkins-Chalgren Agar plates supplemented with Ampicillin or Kanamycin, corresponding to the specific phage used. The plates were sealed and incubated at 37°C for each culture, within a range of 24 to 72 hours.
2. **Two-culture infection (*E. coli* ER2738 and a gut bacteria):** This method sought to examine whether any of the gut cultures impacted the infectivity of the Phagemid-GFP phage on *E. coli* ER2738. Early log-phase cultures were utilized in this procedure. A mixture comprising 20µL of *E. coli* ER2738, 20µL of a gut bacteria, and 20µL of Phagemid-GFP phage underwent incubation at room temperature for 1-2 hours. The resulting mixture was spread onto Wilkins-Chalgren Agar plates. Subsequent observation of green colonies indicated successful infection of *E. coli* ER2738 with Phagemid-GFP phage.

Microscopy imaging

1. **Image Capture:** To capture images, 1µL of the bacterial culture was deposited onto a glass slide (Fisher Scientific, Canada) and observed under phase-contrast channel using a 63x resolution. Image acquisition was performed using Zen2 software.

J.3 Results

The outcomes of control experiments are detailed in Table J.3. Strains exhibiting resistance to both kanamycin and ampicillin (except for 15) were omitted from the infection experiments. The remaining strains were subjected to microscopic imaging to validate their morphology based on available references.

J.3.1 Microbiome Culture Analysis: Growth Behaviors of Different Strains in Varying Culture Conditions.

Strain 4 (*Brevibacillus agri*) In Figure J.1, the outcomes for strain 4 in both mono-, di-, and tri-culture conditions, with or without other cultures, are illustrated. The findings revealed that neither the gut microbiome cultures employed in this investigation nor ER2738 had an inhibitory effect on the growth of strain 4. In fact, the OD growth curve revealed an increase in growth when this strain was cultured alongside other microorganisms.

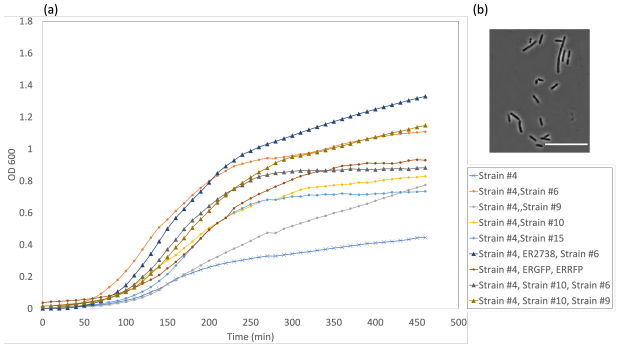


Figure J.1: Growth Behavior and Microscopic Image of Strain 4 (*Brevibacillus agri*). a) OD600 growth curves of strain 4 when cultivated individually and in co-culture with one or two additional bacterial strains. b) Microscopic image of strain 4, shown at a scale bar of 20 µm. The images correspond with those documented in previous research on Brevibacillus species [309].

Strain 6 (*Klebsiella aerogenes*) In Figure J.2, the outcomes for strain 6 in mono-, di-, and tri-culture conditions are depicted. The observations revealed diverse growth behavior of this strain in the presence of different bacteria. Notably, when co-cultured with Strain 9 (*Staphylococcus capitis*), its growth was significantly promoted, exhibiting a faster growth rate compared to its individual growth. This enhanced growth was consistent in both Strain 6 and Strain 9 co-cultures, as well as when co-cultured with Strain 10 (*Escherichia fergusonii*). Conversely, when in the presence of *E. coli* ER2738, a notable reduction in the OD growth curve of Strain 6 was evident. Interestingly, this reduction was more pronounced when Strain 6 was mixed with Strain 10 (*Escherichia fergusonii*).

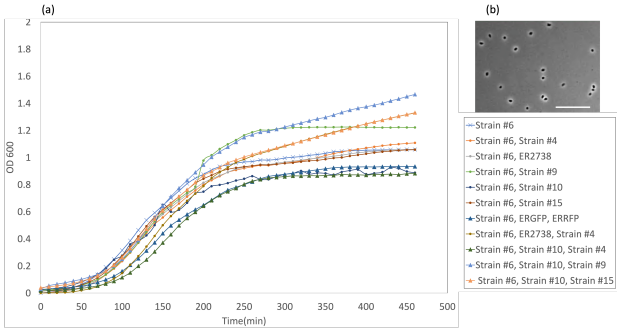


Figure J.2: Growth Behavior and Microscopic Image of Strain 6 (*Klebsiella aerogenes*). a) OD600 growth curves of strain 6 when cultivated individually and in co-culture with one or two additional bacterial strains. b) Microscopic image of strain 6, shown at a scale bar of 20 µm. The images correspond with those documented in previous research on the Klebsiella aerogenes [4].

Strain 9 (*Staphylococcus capitis*) In Figure J.3, the outcomes for strain 9 in mono-, di-, and tri-culture conditions are portrayed. The OD600 readings revealed growth patterns. Notably, in most di-culture settings (except when co-cultured with strain 6), there was a reduction in the OD600 growth curve. For instance, co-culturing with *E. coli* ER2738 exhibited a faster exponential phase but reached the stationary phase sooner. Conversely, with strain 4, the exponential phase extended longer, while in the presence of strain 10, a quicker reduction in OD600 was observed compared to other cultures. Interestingly, when co-cultured with two other strains, an increase in OD measurement was observed across all co-cultures.

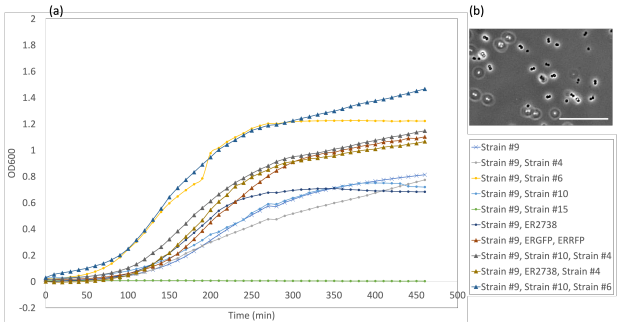


Figure J.3: Growth Behavior and Microscopic Image of Strain 9 (*Staphylococcus capitis*). a) OD600 growth curves of strain 6 when cultivated individually and in co-culture with one or two additional bacterial strains. b) Microscopic image of strain 9, shown at a scale bar of 20 µm. The images correspond with those documented in previous research on the Staphylococcus capitis [310].

Strain 10 (*Escherichia fergusonii*) Figure J.4 presents the findings for strain 10 across mono-, di-, and tri-culture conditions. The results suggested that when co-cultured with two other strains, the OD600 increased more rapidly, contrasting with lower OD values observed when co-cultured with a single strain compared to its individual growth. However, an exception emerged in the co-culture scenario with strain 6. In this case, the exponential phase occurred at an accelerated rate, yet the stationary phase also commenced sooner and was more prolonged compared to the individual growth of strain 10. Additionally, strain 9 exhibited a reduction impact on the OD growth measurement of this strain.

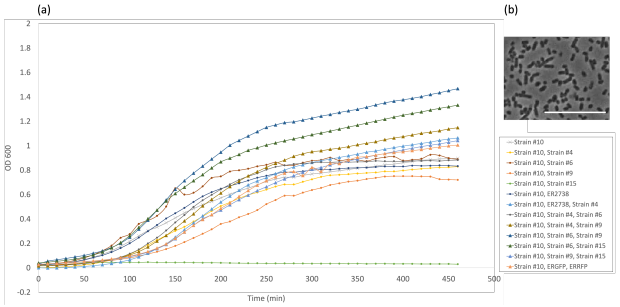


Figure J.4: Growth Behavior and Microscopic Image of Strain 10 (*Escherichia fergusonii*). a) OD600 growth curves of strain 10 when cultivated individually and in co-culture with one or two additional bacterial strains. b) Microscopic image of strain 10, shown at a scale bar of 20 µm.

Strain 15 (*Parastutterella excrementihon*) Figure J.5 illustrates the outcomes for strain 15 in mono-, di-, and tri-culture conditions. Initial microscopic observations (Figure J.5b) revealed a structural similarity to members of the yeast family ([76, 131, 430, 454]. Given the focus of this research, delving into the specifics of yeast-related characteristics remained beyond its scope. Despite this unexpected nature, we investigated its growth to explore its impact on bacterial growth dynamics. Our observations indicated a significant reduction in the OD growth curve when this strain was mixed with strain 4. Conversely, when in the presence of other bacteria, the growth curve exhibited an increase compared to when this strain grew alone.

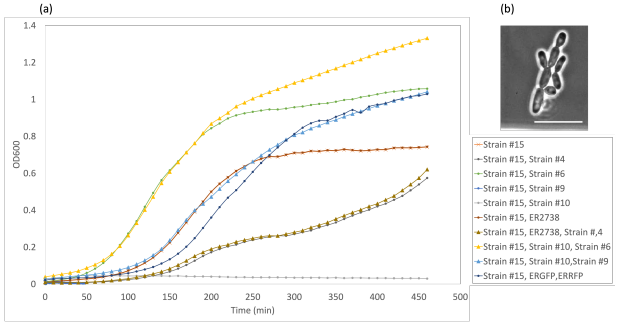


Figure J.5: Growth Behavior and Microscopic Image of Strain 15 (*Parastutterella excrementihon*). a) OD600 growth curves of strain 15 when cultured individually and in co-culture with one or two additional bacterial strains. b) Microscopic image of strain 15, displayed with a scale bar of 20 µm.

Strain *E. coli* ER2738 Figure J.6 depicts the outcomes for *E. coli* ER2738 in mono-, di-, and tri-culture conditions. The observations revealed accelerated OD growth curves, particularly in the presence of strains 4 and 6, compared to when cultured individually with either of these strains. Notably, in the case of strain 6, while the growth rate was faster, it also entered the stationary phase earlier. Contrarily, when co-cultured with strain 4, it exhibited a more extended exponential phase. The presence of other strains appeared to stimulate the growth of ER2738.

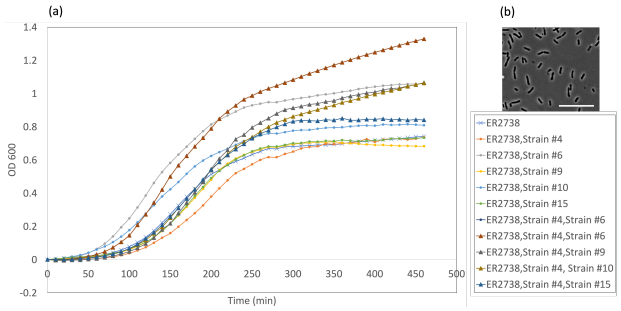


Figure J.6: Figure: Growth Behavior and Microscopic Image of Strain *E. coli* ER2738. a) OD600 growth curves illustrating the growth patterns of strain ER2738 when cultured individually and in co-culture with one or two additional bacterial strains. b) Microscopic image showcasing ER2738, with a scale bar of 20 µm for reference

J.3.2 Susceptibility to M13 phage

Table J.3 displays the outcomes of M13 phage infection experiments conducted on the wild-type gut bacterium and lab strain *E. coli* ER2738. using Phagemid-EGFP and M13KO7. Among the tested strains, only strain 10 exhibited susceptibility to the M13 bacteriophage, as indicated in Table J.3 and Figure J.7a. Initially identified as *E. fergusonii* by Professor Allen-Vercoe's lab, further tests using the Sorbitol-MacConkey Agar Test and the *E. coli* detection kit from AquaVial (a gift from Bill Anderson's lab, University of Waterloo) (See Figure J.7) revealed its affiliation with the *E. coli* family. To delve deeper into this strain's characteristics, a miniprep was performed, and subsequent plasmid sequencing (Figure J.7e) revealed a striking 99.9% similarity to the well-known pathogenic plasmid, pVR50, found in natural pathogenic *E. coli* strains within the gut [54].The genomic sequence data for pVR50 can be accessed at the National Center for Biotechnology Information (NCBI) GenBank under the accession number CP011143.1 [54].

Table J.3: Results of Control and Phage susceptibility experiments

Strain Number	Control Experiment			Phage Experiment	
	PC	Amp	km	Amp	km
4	✓	-	✓	-	-
6	✓	✓	-	-	-
7	✓	-	-	-	-
8	✓	-	-	-	-
9	✓	-	-	-	-
10	✓	-	✓	✓	✓
15	✓	✓	✓	-	-
18	✓	-	-	-	-

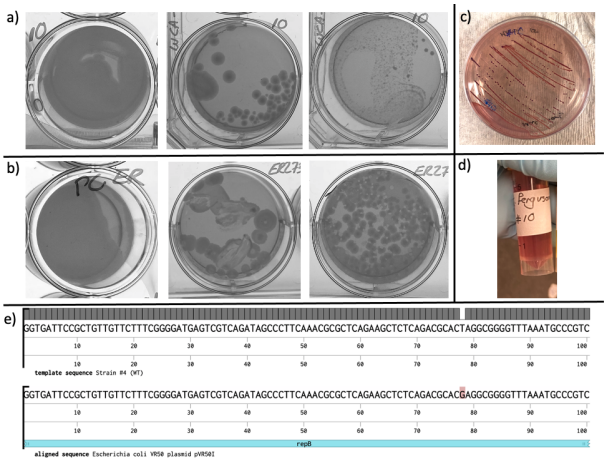


Figure J.7: Results of M13 Phage Infection. a) Cultures of wild-type *E. coli* and b) *E. coli* ER2738. c) Overnight growth of Strain 10 on Sorbitol-MacConkey Agar. Red colonies indicate sorbitol fermentation, distinguishing it from pathogenic *E. coli* 0157:H7, which ferments lactose but not sorbitol. d) Aquavill test for lactose fermentation. *E. fergusonii* does not ferment lactose, thus strain 10 classified as *E. coli*. e) Plasmid alignment results from Strain 10 against pVR50. These plasmids exhibit a 99.9% similarity, differing in only one base.

J.3.3 Impact of Co-culturing Wild Type Culture with Lab Strain ER2738 on M13 phage Infectivity

The subsequent investigation focused on the influence of this culture on the infectivity of *E. coli* ER2738 used in this study. The outcomes are presented in the Figure J.8. With the exception of strain 10, the count of infected cells was diminished. In the case of strain 10, this count exhibited an increase, possibly indicating susceptibility to phage infection. Nonetheless, additional research is imperative to comprehensively understand the behavior of this strain.

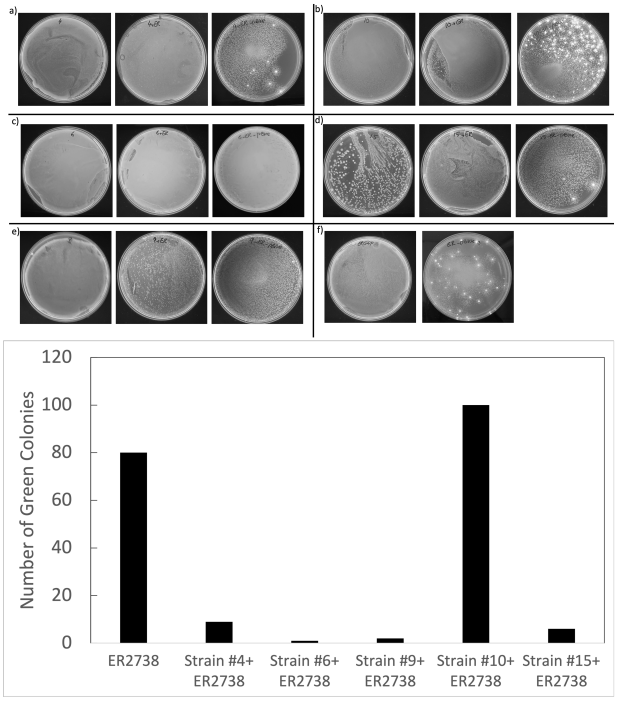


Figure J.8: Infectivity of M13 Phage. The left and center plates depict the growth of the culture without the presence of phage. The right plate in each panel illustrates the co-culture's growth in the presence of M13 phage. Shiny colonies observed in the right plate represent instances of infection by Phagemid-EGFP phage. The bar graph shows the number of green colonies in each culture. *E. coli* ER2738 is the strain that can infected with phage. rests are the wt gut microbiom

J.4 Discussion

In this chapter, our primary objective was to evaluate the infectivity potential of M13 phagemid within the human gut microbiome's natural bacterial community.

Understanding the behaviors of individual species arises from their complex interactions within the microbial community and the surrounding environment, which poses a challenge in discerning specific interactions. Consequently, quantifying microbial interactions within the mammalian microbiome remains a complex task [112]. To address this complexity, our investigation initially started by observing individual behaviors in a controlled laboratory setting.

Several studies have elucidated the crucial role of gut microbiota in human health [582], employing diverse methods to characterize these communities and their effects on gut homeostasis. The wild-type strains provided to our lab were predominantly aerobic cultures isolated from the human gut microbiome. Our initial analysis centered on assessing the individual influences of distinct cultures on each other's growth dynamics. This involved evaluating the growth patterns of each culture in isolation, in co-culture with a single bacterial strain, and subsequently when co-cultured with two different strains. The objective was to discern whether these cultures exhibited antagonistic or synergistic effects on each other's growth behaviors, laying the groundwork for understanding complex microbial interactions.

Strain 4, *Brevibacillus agri*, known to be associated with human infections [447], displayed a distinctive growth pattern in the presence of other bacterial strains. When combined with two additional cultures, the growth curve demonstrated the most significant increase, followed by a moderate rise in the presence of a single culture, and the least growth observed when cultured in isolation. Such observations of increased growth rates in the presence of various bacterial combinations shed light on potential synergistic relationships that influence the proliferation of this particular strain.

Strain 6, *Klebsiella aerogenes*, a Gram-negative bacterium recognized for its colonization ability within the human gastrointestinal tract, exhibited an intriguing behavior when in the presence of strain 9. Surprisingly, co-culturing these two strains resulted in an even greater increase in the OD growth curve compared to strain 6 alone. Notably, even when strains 6 and 9 were co-cultured with either strain 10 or ER2738—both known to typically reduce the growth rate of strain 6—this combination still displayed an accelerated growth rate. This suggests a potential synergistic or cooperative interaction between strains 6 and 9, potentially involving mutually beneficial metabolic processes or cooperative mechanisms that promote heightened growth.

Strain 9, *Staphylococcus capitis*, classified as Gram-positive cocci [316], exhibited intriguing growth behavior when co-cultured. Interestingly, when in a tri-culture setup, an increase in growth was observed. However, in dual-culture scenarios with each of those cultures, the growth rate was lower compared to its individual growth (except for strain 6). Notably, when co-cultured with ER2738, an accelerated exponential growth phase was evident. However, this phase transitioned to the stationary phase more rapidly, potentially indicating a modification in the growth dynamics due to the interaction between strain 9 and ER2738.

Strain 10, *E. coli*, exhibited an interesting pattern in its growth dynamics. In the triculture setup, it displayed a notably faster growth rate. However, in dual-culture scenarios, the growth was relatively lower compared to its individual growth, indicating potential inhibitory effects or altered growth dynamics due to the presence of other strains. An intriguing exception was observed in the co-culture with strain 6, where there was a rapid exponential growth phase. Nonetheless, this phase reached the stationary phase earlier and maintained a longer duration compared to when strain 10 was growing individually. This discrepancy might be attributed to various factors, including the interactive effects of different strains on their growth patterns or potential competition for resources within the environment. Further analysis is necessary to elucidate the specific mechanisms driving these observed growth dynamics.

Strain 15, Unknown strain of yeast, displayed mixed growth behavior when subjected to different co-culture conditions. Notably, when in the presence of strain 6 or in combination with strains 6 and 10, the growth curve showed an increase compared to its individual growth. Similarly, co-culturing with strain 9 and subsequently with both strains 9 and 10 also resulted in faster growth compared to its solitary growth phase. However, the presence of strain 4 caused a reduction in the growth curve of strain 15 compared to its growth when cultured alone. The varying growth patterns indicate complex interactions among these strains, possibly influenced by competitive dynamics or synergistic effects within the co-culture environment. Further investigation is required to decipher the precise mechanisms driving these distinct growth responses.

Finally, we examined the impact of co-culturing any of the aforementioned wild-type bacteria on *E. coli* ER2738. Our findings consistently revealed that the presence of these wild-type cultures led to an increased growth curve in *E. coli* ER2738. This observation suggests a positive influence or a supportive role of these wild-type cultures on the growth dynamics of *E. coli* ER2738 within the co-culture setting. Understanding these interactions could offer insights into potential collaborative relationships or niche-related dynamics among these bacterial strains.

As observed from the results, the mixed microbial communities demonstrated diverse in-

teractions, encompassing both favorable and adverse effects. These occurrences necessitate further investigation, delving deeper into factors that determine these patterns—however, these details extend beyond the confines of this research. Below, we've outlined several scenarios, both positive and negative, that potentially contribute to the observed OD growth patterns. Each scenario holds the potential to elucidate the outcomes we observed and presents an intriguing avenue for further exploration."

Table J.4: Factors Influencing OD Changes in Bacterial Cultures

OD Increase	**OD Decrease**
Synergistic Growth: Certain bacterial species exhibit improved growth in the presence of others, benefiting from shared resources or metabolic byproducts, leading to increased OD measurements [127].	Competition for Resources: Bacteria compete for essential resources like nutrients or space, resulting in inhibited growth or reduced population density.
Complementary Metabolism and Cross-Feeding: Some bacteria metabolize nutrients discarded by others, fostering an environment conducive to mutual growth [24].	Inhibition: Certain bacterial species produce inhibitory substances (e.g., antibiotics or metabolites) impeding the growth of others [225].
Cooperative Interactions: Bacteria release substances stimulating the growth of other species or engage in quorum sensing, regulating gene expression based on cell density, thereby augmenting growth rates [171].	
Competition Dynamics: Competitive interactions might lead to increased growth rates for one species at the expense of others, reducing overall population density.	

It's important to note that while our laboratory setup allows for controlled observations, microbial behavior within this setup might not entirely replicate their actions within the gut culture. The gut environment is complicated, influenced by diverse factors [584] including environmental conditions [17]. Therefore, direct translation of laboratory findings to the complex gut environment warrants cautious consideration.

Next, we explored the wt gut cultures' vulnerability to the M13 bacteriophage. As previously described, M13 specifically infects male-specific *E. coli* strains that produce f

pili [234], which has been shown to be the primary carriers of antibiotic resistance genes in human-associated commensal *E. coli* [495]. These F-pili are involved in horizontal gene transfer, enabling bacteria to acquire antibiotic resistance genes [358]. While transfer of antibiotic genes offers advantages, it can also have burden on the bacteria [581] and can cause imbalance in the microbial community. For instance, dysbiosis of the gut microbiota, attributed to these factors, can lead to severe health complications in humans [168, 259, 105].

Preserving the normal gut microbiome by treating these bacteria without lysing them, thus minimizing endotoxin release associated with bacterial lysis, could have significant benefits in maintaining gut ecosystem stability [90]. Therefore, utilizing the non-lytic cycle of the M13 phage could be a promising approach [211]. Additionally, owing to its non-lytic nature, M13 phage demonstrated the ability to persist within the culture for numerous generations, consistently producing new virions, thereby maintaining a high viral titre [331]. An insightful recent review conducted by Chang et al. [90] comprehensively detailed the diverse applications of the M13 phage in the realm of medicine. The study by Lam et al. explored the utilization of the M13 phage for delivering CRISPR-Cas9 into the gut microbiome of mice. However, it's crucial to note that rather than employing a wild-type culture, they introduced mice to E. coli cells susceptible to the M13 phage [303].

Among the tested strains, only strain 10 displayed susceptibility to the M13 bacteriophage. Initially classified as *E. fergusonii* by professor Emma Allen-Vercoe lab, further analysis using specialized tests revealed its alignment with the *E. coli* family. *E. coli* and *E. fergusonii*, genetically similar, pose challenges in differentiation based solely on 16S rRNA gene sequencing [117]. Identifying them hinges on their ability to ferment sorbitol and lactose, but this becomes complicated with pathogenic strains like *E. coli* O157:H7 that do not ferment sorbitol. *E. fergusonii* is non-lactose fermenting and does not ferment sorbitol [16]. We conducted two tests to identify this strain, but for more accurate identification, further testing is highly recommended. We used the *E. coli* detection kit from AquaVial, which confirmed the strain's ability to hydrolyze lactose, ruling out its classification as *E. fergusonii*. Additionally, the Sorbitol-MacConkey Agar Test affirmed the strain's capacity to ferment sorbitol, eliminating its classification as the pathogenic *E. coli* 0157:H7 [428]. Upon genetic investigation, the extracted plasmid from this strain exhibited a 99.9% genetic similarity (only 1bp different) to the pathogenic plasmid, pVR50, commonly found in disease-causing *E. coli* strains within the gut. This plasmid contain a multidrug resistance cluster containing genes such as *strAB* and *folP*, conferring resistance to specific antibiotics [54].

As previously demonstrated [10], it was evident that heterogeneity within the culture significantly reduces phage absorbance. Subsequently, we investigated the impact of each

gut culture's presence on the infection rate of *E. coli* ER2738. The results notably showed that even the presence of a single gut culture substantially reduced the infection rate. However, in scenarios where both strains were susceptible to phage infection, this reduction wasn't observed. Notably, in the presence of strain 10, an *E. coli* variant containing pVR50, the infection rate of *E. coli* ER2738 was increased compared to when either of the strains was independently infected by the M13 phage. Further analysis is required to gain deeper insights into this scenario.

J.5 conclusion

In this section, our focus was to elucidate the infection mechanism of bacteriophage M13 within the wild-type culture and compare it with the laboratory strain *E. coli* ER2738, known for its susceptibility to M13. Initially, our investigations delved into the impact of co-culturing these wild-type bacteria on each other's growth. Except for a few exceptions, co-culturing generally improved the growth rates of all strains. The reasons behind these enhancements or inhibitions could be investigated, although this study didn't encompass a detailed exploration of these factors.

Following this, we aimed to assess the susceptibility of these wild-type strains to the M13 bacteriophage. As these strains were provided by the lab and considering M13's specificity to *E. coli* F-plasmids, we did not anticipate infection in any of these strains. However, strain 10 exhibited susceptibility to the M13 phage. Further investigation unveiled that this strain, belonging to the *E. coli* family, contains pVR50, an F-plasmid, explaining its susceptibility to the M13 phage due to the presence of the M13 receptor.

Continuing our analysis, we investigated the infection rate of *E. coli* ER2738 in the presence of each wild-type strain. Except for strain 10, when mixed with other strains, a reduced number of infected cells was observed. co-culturing *E. coli* ER2738 with strain 10 increased the number of infected colonies.